6-2021

Improving the Stability and Operability of a Small-Scale Rotating Detonation Engine

Nathan T. Fiorino

IMPROVING THE STABILITY AND OPERABILITY OF A SMALL-SCALE
ROTATING DETONATION ENGINE

THESIS

Nathan T. Fiorino, 2nd Lieutenant, USAF

AFIT-ENY-MS-21-J-100

DEPARTMENT OF THE AIR FORCE

AIR UNIVERSITY

AIR FORCE INSTITUTE OF TECHNOLOGY

Wright-Patterson Air Force Base, Ohio

AFIT-ENY-MS-21-J-100

The views expressed in this document are those of the author and do not reflect the official policy or position of the United States Air Force, the United States Department of Defense or the United States Government. This material is declared a work of the U.S. Government and is not subject to copyright protection in the United States.

IMPROVING THE STABILITY AND OPERABILITY OF A SMALL-SCALE ROTATING
DETONATION ENGINE

THESIS

Presented to the Faculty

Graduate School of Engineering and Management

Air Force Institute of Technology

Air University

Air Education and Training Command

in Partial Fulfillment of the Requirements for the

Degree of Master of Science in Aeronautical Engineering

Nathan T. Fiorino, B.S.

Second Lieutenant, USAF

June 2021

IMPROVING THE STABILITY AND OPERABILITY OF A SMALL-SCALE ROTATING
DETONATION ENGINE

Nathan T. Fiorino, B.S.
Second Lieutenant, USAF

Committee Membership:

Fred R. Schauer, Ph.D.

Chairman

Marc D. Polanka, Ph.D.

Member

S. Alex Schumaker, Ph.D.

Member

Lieutenant Colonel Jeffrey R. Komives, Ph.D.

Member

Abstract

Current interest resides in investigating the operable limits of rotating detonation engines (RDEs) with low mass flows and small channel diameters. Such RDEs would offer a research tool that could be quickly and cheaply modified. Furthermore, due to the small geometry, the detonation wave would be forced to operate near the edge of common reactants' detonability. The characterization of the operating behavior on the small scale could then be used to inform the limits of larger RDEs, on which exploration of such behavior would be expensive and slow. Therefore, the objectives of this research were to further characterize the operating envelope and improve the detonation wave stability of a recently developed small scale, "Micro" RDE. The Micro-RDE was designed with an outer diameter of 28 mm and channel gap of 2 mm and operated on nitrous oxide (N_2O) and ethylene (C_2H_4). Previously, unstable wave modes with a peak frequency of 14.0 kHz were achieved using a Jets in Crossflow (JIC) injection scheme and spark plug initiation at mass flows as low as 0.025 kg/s. Non-ideal mixing and flow field interactions with the spark plug were blamed for the unstable wave behavior [1]. In response, the current work implemented a new injection scheme to improve mixing and installed a pre-detonation device as the ignition mechanism to reduce the destabilizing interactions encountered with the spark plug.

Testing with the modifications showed successful operation was possible over a range of mass flows (0.035-0.068 kg/s) and equivalence ratios (Φ = 0.6-1.4). These operating ranges were similar to those in previous work, where mass flows of 0.025-0.075 kg/s and equivalence ratios of Φ = 0.8-1.5 were observed [1]. Significant erosion of the RDE hardware required iteration on the pre-detonator placement and different materials, such as Inconel, to improve durability. Issues with flow controllers were present throughout testing and limited the size of the tested operating space. With the new injection scheme, plenum to chamber pressure ratios greater than three were required

to achieve reliable detonation and a stable, single wave mode was observed for the first time in an RDE of this size. Observed frequencies ranged from 13-19.1 kHz, an increase over the previous range of frequencies (11.7-14 kHz) [1]. A decrease in the prevalence of unstable wave behavior, such as clapping, indicated improved wave stability. Fill height was determined to govern trends in wave frequency and mode.

Acknowledgments

Thank you to my advisor Dr. Fred Schauer and predecessor Major Joe Dechert for getting me started on the Micro-RDE, this was truly a special opportunity. To Nathan Snow, Riley Huff, Kavi Muraleetharan, and Jonathan Wyatt, who helped me build and test well after it was time to go home, thank you, I owe you. Thank you to the D-Bay cadre, Brian, Matt, Andrew, Rob, Curtis, and John, who let me into the fold at the lab and put up with my questions. Lastly, to my committee members Dr. Marc Polanka, Dr. Alex Schumaker, and Lt Col Jeffrey Komives, whose editing help, advice, and mentorship made this process challenging, productive, and possible, thank you. I am grateful and excited to pay it forward.

Nathan T. Fiorino

Table of Contents

List of Figures

Figure   Page

Figure   Page

List of Tables

List of Abbreviations

List of Symbols

I. Introduction

This document presents the research effort made to improve the stability and operability of a previously developed small-scale Rotating Detonation Engine (RDE) known as the "Micro-RDE" [1]. Improvements to detonation wave stability were based on the observed wave behavior while changes to the operability were based on the observed ranges of operating mass flows and equivalence ratios. Parameters which governed changes to wave behavior were then determined. The Micro-RDE was designed with a channel diameter of 28 mm and channel gap of 2 mm and operated on nitrous oxide (N_2O) and ethylene (C_2H_4) as the oxidizer and fuel respectively. Changes to the original Jets in Crossflow (JIC) injection scheme and spark plug ignition method were implemented to counteract previously observed wave instabilities [1]. Successful detonation was observed over a range of mass flows (0.035-0.068 kg/s) and equivalence ratios ($\Phi = 0.6$-1.4) and a stable single wave mode with frequency up to 16.8 kHz was observed for the first time. Injection pressure ratios and fill height were driving parameters in the ignition and operability characteristics observed.

Section 1.1 Introduction to Rotating Detonation Engines

Detonation is a mode of a combustion in which a leading shock/compression wave couples to a combustion reaction. The energy release from the shock compressed reaction occurs at a near constant volume and subsequently is able to propel the shock wave forward. Ideally, coupling between the shock and reaction continues indefinitely as long as the wave propagates into a reactive medium and the reaction stays close to the wave. Due to the coupling, detonation waves can move at velocities many times greater than the speed of sound in the medium through which they move [2]. High Mach speeds, in the range of 5-8, cause strong shock compressions in the

reacting gas creating a substantial pressure rise over the course of the reaction. This is distinct from the more common mode of combustion known as deflagration in which pressure remains nearly constant or decreases slightly. As a result, the amount of work extractable from a thermodynamic cycle using detonation is theoretically greater than that of a similar cycle using deflagration [2, 3]. Figure 1 illustrates this advantage by comparing P-v diagrams of the common Brayton cycle to a propagating detonation cycle. In the figure, both a Humphrey cycle and Fickett-Jacobs cycle are shown [4]. Importantly, the detonation must be propagating, and not stationary, in order for these cycles to be representative, a result expanded on in Chapter 2 [4]. Harnessing this thermodynamic advantage is one of the main objectives in detonation engine research [5].
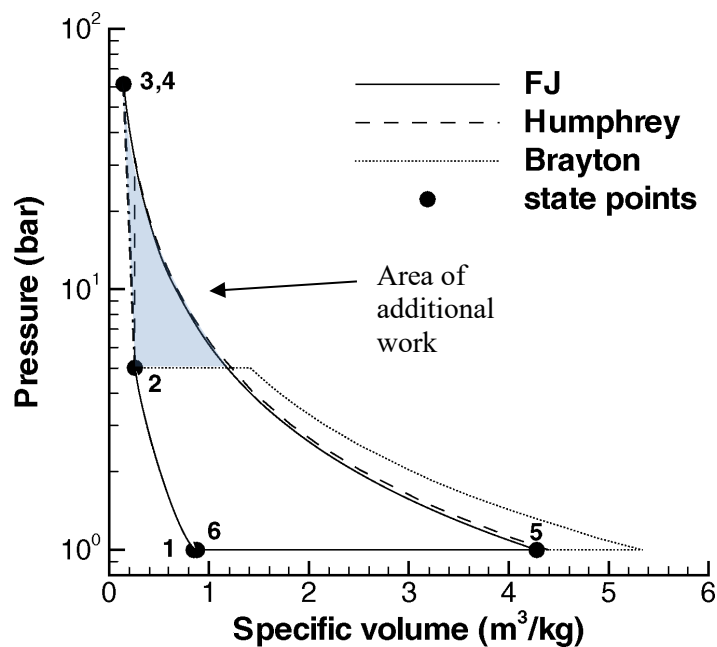
Fig. 1 Comparison of Brayton Cycle to a Propagating Detonation Cycle approximated by both a Humphrey and Fickett-Jacobs cycles for a $\pi_c = 5$. [4]

Under the umbrella of detonation engines is the Rotating Detonation Engine (RDE). The RDE is a device which harnesses the self-sustaining nature of a detonation by propagating it continuously around an annulus where the reactants are always available. To accomplish this, product gases are exhausted while new reactants are simultaneously replenished through an

injection scheme. Reactants must enter the combustion chamber before the detonation wave completes a rotation, otherwise the wave does not have new fuel and oxidizer to sustain itself [5, 6]. Fundamentally, the RDE does not require any moving parts.

While conceptually and mechanically elegant, the actual flow field inside an RDE is complex and makes operable design choices difficult. A main consequence of poor design choices (beyond a simple failure to detonate) are detonations with unstable propagation modes and wave velocities well below their theoretical values, known as the Chapman-Jouguet (CJ) velocity. In an effort to unravel this complexity, Bykovskii et al. documented sizing parameters for RDE geometry that were found critical to the production of a stable detonations with velocities at or near their CJ speeds [7]. In their work they found guidelines, based on the detonation cell size (λ), for channel length (l_d), channel gap (Δ), and reactant fill height (*h*) were required in order to successfully produce a stable detonation wave [7]. Figure 2 shows these parameters and their relationship to the Micro-RDE cross-section. Details on the Micro-RDE design are covered in Chapter 3. The reactants are also a major consideration as they determine the detonation's cell size (λ), which as mentioned was the basis for the parameters that Bykovskii et al. used to define their guidelines [7]. Some fuel and oxidizer combinations have larger detonation cells than others and as a result will not detonate if used in small geometries such as those in the current research. Further discussion on cell size can be found in Chapter 2.
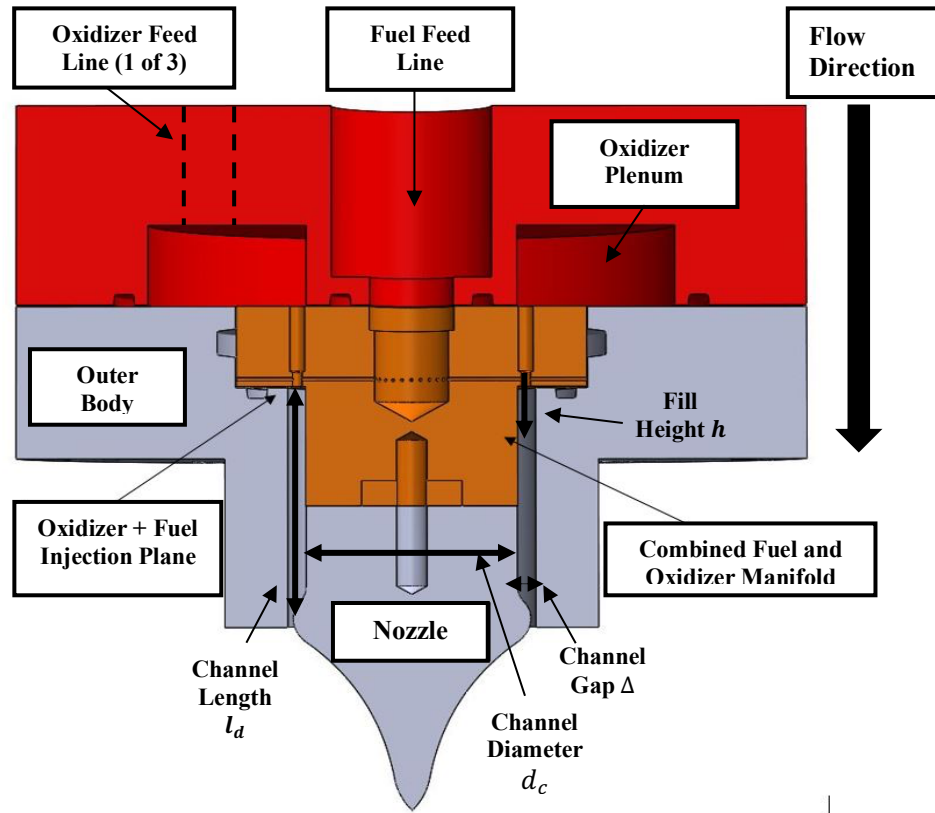
Fig. 2 Cross section view of Micro-RDE highlighting RDE components and geometric parameters

Section 1.2 Motivation for Research into Small Scale RDEs

Integration of RDE technology into propulsion systems that will operate over a wide range of conditions requires a good understanding of the limits of detonability and operability. Unfortunately, the combustion physics occurring inside the RDE are the result of a complicated interrelationship of geometric and flow field parameters which only become more complicated at the limit [7,8]. As a result, analytical relationships are usually not available, and computational approaches are cumbersome. Therefore, interest resides in investigating the limits experimentally. One way to approach these limits is to size the geometric parameters of channel length, channel gap, fill height, and channel diameter smaller than what is considered ideal [7]. Doing so creates less space for the detonation cells to form, less time for reactants to enter and mix, and in general

reduces the detonation's ability to propagate continuously. The behavior in this restrictive geometry could then be used to characterize the potential limit behavior in larger RDEs because the physics would remain consistent between devices and therefore the behavior in one could be extended to the other. Furthermore, the small scale of the RDE would allow for low flow rates and low-cost modifications resulting in rapid testing capabilities. Additional applications include use as a small standalone thruster on account of the pressure gain potential in RDEs. The small-scale detonation inside the annulus could also offer a stable flame holder in extreme environments. Lastly, the small channel diameter would necessarily produce high operating frequencies, that could potentially exceed audible limits (>20 kHz). This would allow the device to be operated in a wider range of laboratories. Driven by these motivations, the goal of the current research was to create a small scale RDE that would reliably detonate at low mass flows and high frequencies.

Previously, Dechert et al. designed the first iteration of the Micro-RDE and sized it to produce wave frequencies of 20 kHz at mass flow rates between 25-75 g/s [9]. Their Micro-RDE had a channel diameter of 28 mm, a channel gap of 2 mm, and a channel length of 30 mm. Because the RDE was designed near the edges of the Bykovskii criteria, and therefore near the limit of detonability it was expected to be difficult to operate [7,9]. To combat this, nitrous oxide and ethylene were used as reactants. This fuel-oxidizer combination had a small cell size estimated between 0.5 mm to 1.75 mm and high reactivity which helped combat the limited space in the RDE and thus improve chances of successful detonation [9]. The design was tested over a range of equivalence ratios from 0.5 to 1.5 and mass flows of 0.025 kg/s to 0.075 kg/s. Successful detonations were achieved exhibiting unstable clapping behavior with frequencies between 11.7-14 kHz [1]. High speed video showed that clapping modes were influenced by the presence of the spark plug and ¼" hole needed to hold it. Additionally, the spark plug's electrodes consistently eroded during detonations requiring constant replacement. It was hypothesized that removal of the

spark plug may allow for continuous single wave propagation by removing sources of instability as well as increase the durability of the RDE [1].

The consistent clapping mode also indicated that local mixing was likely non ideal which would have also contributed to the low frequency [1]. For example, research on injections schemes, showed that poor mixing lead to severely limited wave stability on account of the lower available heat release [10]. In addition, the ~13 kHz frequency led to fill times on the order of 70 μs for reactants to enter the channel, reach the required fill height (h) and be adequately mixed before the next wave passed. Faster waves would only decrease this time further. These considerations reinforced the need of an adequate injection scheme which could meet these requirements and suggested that the observed instability and velocity deficits may be improved with changes to the current scheme.

Section 1.3 Research Objectives

In the current research, the goal to produce a small scale RDE that could reliably detonate at low mass flows and high frequencies remained the same. To accomplish this, the previous design was modified through the implementation of a new injection scheme and ignition method. The new injection scheme was designed to address issues of mixing quality by moving the point of fuel injection from inside the detonation chamber to inside the oxidizer injection holes. This design partially mixed reactants before entering the chamber and was predicted to decrease the required mixing length. Additionally, the spark plug was removed and replaced by a pre-detonator device. With these changes, the impacts to the RDE's operability and wave stability could then be determined.

Therefore, the first objective of the current work was to characterize the operating space of the Micro-RDE with the new injection scheme. The impact of the pre-detonator needed to be

known as well, and so tests with the new injection scheme were run using both a spark plugs and a pre-detonator. The second research objective was to improve the wave stability so that unstable wave modes, such as clapping, were minimized. Increasing frequency closer to the original 20 kHz design goal was also desired. Once accomplished, the results could be compared to the previous work to make an assessment on how the modifications had impacted the operability and stability. Based on the assessment, recommendations for future work could be made.

Section 1.4 Research Approach

From here, Chapter 2 will cover applicable literature on the topics of detonation thermodynamics, detonation wave structure, RDE designs, RDE injector designs, and RDE ignition considerations. These topics were used during the design and test campaign of the new injection scheme and pre-detonator integration.

Next, Chapter 3 will cover the methodology of the work. It will begin with a review of the injection scheme design and the subsequent components that were built and installed into the Micro-RDE. Then a review of the pre-detonator will be covered. However, integration of the pre-detonator was complicated by persistent erosion of the tube used to enter the channel, and iterations were made on the optimum axial location to minimize its susceptibility to damage. Outerbodies made of Inconel were eventually incorporated to further improve the RDE's durability during testing. The mass flow control methods are presented next. Flow controllers were found to not supply flow conditions equivalent to those requested and therefore estimation methods were used to back out true mass flows and equivalence ratios. Those methods are also outlined. The instrumentation used is then introduced along with the high-speed camera equipment required to capture the detonation wave's behavior.

In Chapter 4, the results obtained with these changes in place are presented. The RDE's operating space was tested by sweeping through mass flows from 0.025 kg/s to 0.075 kg/s and equivalence ratios from 0.6 to 1.4. Successful detonation was observed over a range of mass flows from 0.035-0.068 kg/s and a range of equivalence ratios from $\Phi = 0.6$-1.4. The mass flow control issues restricted the set of condition which could be tested and therefore the space of mass flows and equivalence ratios tested was limited. Flow conditions before and after detonation were found to be significantly different as well, and therefore the operating space was broken into two categories: an ignition space and an operating space. Data for the ignition space revealed that detonability was increased when pressure ratios between the chamber and plenum were above 3 and 3.5 for the oxidizer and fuel respectively. A new range of frequencies from 13-19.1 kHz was observed along with numerous new wave propagation modes. Most significantly, multiple instances of stable, single wave modes were observed for the first time in an RDE of this size and had frequencies up to 16.8 kHz. Fill height was determined to be a mechanism for variations in wave frequency but a mechanism for wave mode proved more elusive. Erosion during detonation was found to influence both frequency and wave mode.

Finally, Chapter 5 summarizes the results with respect to the research objectives and introduces avenues for future work. Ideas for future work include improving mass flow control into the RDE so that a more accurate and comprehensive operating space could be explored. Further hardware modifications could also be pursued to improve erosion resistance and durability. An optically accessible detonation channel using quartz outerbodies and highspeed imagery is also proposed so that wave behavior and fill height could be directly observed. Estimations of fill height and theories on wave mode mechanisms could then be proven or disproven. Lastly, new injection schemes could be designed and used in combination with the optical access to further define the interactions between injector stiffness and detonability both during ignition and operation.

II. Background

Recent research into the development of a small-scale Rotating Detonation Engine (RDE) has yielded promising results on the operability of high frequency and low mass flow designs [1]. Typical RDEs in current literature have diameters of 100-200 mm with mass flows in the range of 1-10 kilograms per second. Due to their widespread use, these RDEs have a significant operational knowledge base. Unfortunately, there is not a similar knowledge base for smaller scale RDEs such as those with a diameter of ~30mm. In an initial investigation, Dechert was able to demonstrate detonation across multiple mass flows and equivalence ratios for a small scale RDE. However, Dechert's RDE detonated at frequencies around 14 kHz, which were well below the original design frequency of 20 kHz [1]. The reactant mixing and ignition mechanism were identified as the most probable causes of the wave instability that slowed down the operating frequency [1].

The current research therefore aims to stabilize the detonation by improving the reactant mixing via changes to the injection scheme and ignition mechanism. A more stable wave will detonate closer to, and potentially above, the 20 kHz design goal while also revealing the range of mass flows and equivalence ratios an RDE of this scale will operate successfully over as well as the characteristic wave behavior. Before changes can be made, a range of background knowledge must be understood. This includes detonation thermodynamics, which will be discussed in Section 2.1, and rotating detonation wave structure in an RDE, which will be covered in Section 2.2. These topics will allow an in-depth investigation of RDE geometry design in Section 2.3, RDE injection design in Section 2.4, and detonation initiation considerations in Section 2.5. The following is an overview of these core competencies. Each section will highlight concepts which were used to make and inform the design decisions discussed in Chapter 3.

2.1 Detonation Thermodynamics

Combustion reactions come in two stable forms: deflagration and detonation. Deflagration combustion is the more familiar form and consists of a subsonic reaction that occurs at constant pressure [11]. Deflagration therefore is the type of combustion used in common thermodynamic cycles, such as the Brayton cycle, where heat is assumed to be released at a near constant pressure. Detonation on the other hand, is a locally sonic reaction preceded by a strong leading shock wave which causes a large increase in pressure [11]. This increase in pressure during the combustion reaction is attractive because it allows for an increase in pressure across the heat addition stage of a thermodynamic cycle using detonation. The increased pressure at which heat is released then generates less entropy when compared to the deflagration process (for the same amount of heat release). The lower entropy rise is what ultimately allows for more usable work [4,12].

2.1.1 Chapman-Jouguet Theory and the Zeldovich-von Neumann-Doring Model

There have been attempts to theoretically model a detonation since the first attempts to observe the phenomenon were made in the late 1800s [11]. These observations led researchers such as Mallard and Le Chatelier (1883) to suggest that the reactions sustaining the detonation were initiated by the detonation shock wave front [11]. Such observations inspired Chapman (1889) and Jouguet (1904, 1905) to create a quantitative theory which could predict the wave front speed of a detonation [11]. The Chapman-Jouguet theory, as it became known, was derived from solving the mass, momentum, and energy equations across a shock wave while also considering the energy release due to the detonation combustion reaction. Their analysis showed that for a given detonation, there were two distinct regimes along the equilibrium Rankine-Hugoniot curve where solutions fell: a strong detonation regime, and a weak detonation regime. Strong detonations had relative subsonic flow downstream of the leading shock, while weak detonations had

supersonic flow relative to the shock [11]. Each regime was shown to converge where the flow was at a sonic velocity (again relative to the wave) behind the wave [11]. With two regimes, the problem then became which one to choose. Without any physical or mathematical basis, Chapman and Jouguet suggested that the convergence point, which corresponded to the sonic condition behind the wave, be chosen. The speed corresponding to this solution has become known as the Chapman-Jouguet (CJ) wave velocity and their method became known as CJ theory [11]. Coincidentally, this solution was shown to correspond to the minimum entropy state as well, however this still did not explain the actual mechanism behind the natural preference for the sonic condition [11]. Application of the CJ theory involves finding the tangency point of the equilibrium Hugoniot curves with the Rayleigh line for a set of given thermodynamic properties. This tangency point represents the thermodynamic state after the combustion wave and the slope of the Rayleigh line can be directly related to the Mach number of the combustion wave [11].

Since CJ theory was first presented other researchers have attempted to fill in the mathematical and physical reasons for the sonic speed solution. Three different researchers, Zeldovich, von Neumann, and Doring independently determined the true mechanisms behind a detonation by considering its substructure. Their model, which became the Zeldovich-von Neumann-Doring (ZND) model, showed that a detonation consisted of a leading shock wave followed by a chemical reaction zone [11]. Additionally, these two subcomponents existed far enough away from each other to decouple them analytically while being close enough that the wave which ignited the reaction zone was maintained by the energy released by the following reaction zone [11]. Their model also revealed that the solution for the wave speed was not necessarily the tangency point to the Rayleigh line described earlier. Instead the true wave speed was defined by an iterative equilibrium analysis which considered the reaction zone. Ultimately, this analysis showed a solution that was below the CJ point on the Hugoniot curve could exist.

However, even though the CJ and ZND solutions are not always the same, the difference in the wave speed is on the order of a few percent [11]. As a result, the CJ theory in practice provides a quick and accurate estimation, even if it is not completely physical. Use of CJ theory precludes the need to go through the more detailed and involved equilibrium analysis of the ZND model across the reaction zone to determine a detonation's wave speed.

2.1.2 Detonation Thermodynamic Cycle Analysis

With the ZND model defined, proper thermodynamic analysis was conducted on cycles proposed for detonation combustion devices, such as the RDE. A caveat, engines such as the RDEs and Pulsed Detonation Engines (PDE) (which preceded the RDE), use unsteady, propagating detonations instead of steady stationary detonations. As a result, cycle analysis produces substantially different results depending on which type is considered, the stationary wave or the propagating wave [12]. The analyses in this section only considers the propagating wave.

The ZND model is fairly complex and as such other models have been used as surrogates in cycle analysis. Examples are the Humphrey cycle, which models detonations as the heat release occurring in a constant volume, and the Fickett-Jacobs (FJ) model proposed by Wintenberger and Shepherd [4]. This new cycle replaces the constant volume heat release of the Humphrey cycle with straightforward application of CJ detonation theory [4]. The FJ model differs from the ZND model because it ignores the shock compression step that occurs between the initial state and the CJ point [4]. Figure 3 below shows the FJ cycle alongside the Humphrey and Brayton cycles [4]. Notice how closely the Humphrey and FJ cycles are to each other even though their thermodynamic processes are different.
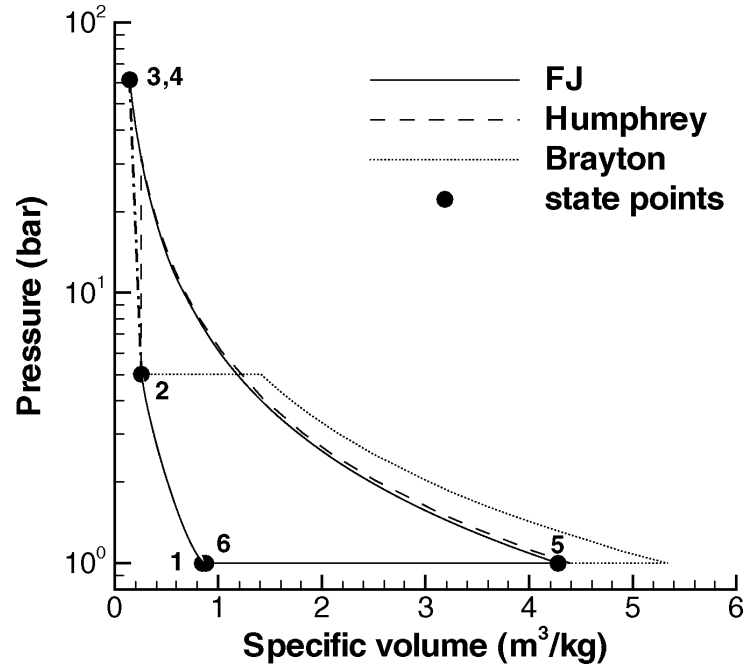
Fig. 3 P-v Diagram of Fickett-Jacobs, Humphrey, and Brayton Cycles for stoichiometric propane-air mixture at 300k and 1 bar initial conditions ($\pi_c = 5$). FJ cycle jumps from points 2-3 to account for the CJ theory application [4].

Wintenberger and Shepherd used their cycle in a comparative analysis with the Humphrey and Brayton cycles. Due to the large pressure spike characteristic of a detonation, both the FJ and Humphrey cycles produced more work than the Brayton cycle, as can be seen in Figure 3 [4]. Their results also showed that the FJ and Humphrey cycles had similar thermal efficiencies which were higher than the Brayton cycle when efficiency was a function of compression ratio. The inverse was true when efficiency was a function of combustion pressure ratio [4]. Wintenberger and Shepherd also showed that in order to extract the increased thermodynamic potential of detonations, the cycle analysis had to consider unsteady propagating detonations, not steady flow, stationary detonations [12]. They found that when stationary detonations were considered, the thermodynamic benefits over constant pressure heat release were no longer available due to changes in the amount of entropy generated [12].

Vutthivithayarak and Lu compared performance of just the combustion processes of the

ZND, FJ, and Humphrey cycles [13]. The P-v and T-s diagrams from their analysis is shown in Figure 4. In their analysis, the CJ point was used to define point 2CJ in Figure 4a and represented the peak pressure and temperature of the FJ cycle. This point was also used as the peak temperature of the ZND cycle [13]. Comparing the three detonation cycles there was much more area under the ZND P-v curve, and therefore more work, than the other two. This is confirmed by the values in Table 1 which show the performance of each cycle. However, if the FJ and Humphrey models were to be useful surrogates, they should behave similarly. In Table 1 the ZND model has significantly more heat input and work output than the other two models while having similar efficiency [13].

(a)   **(b)**
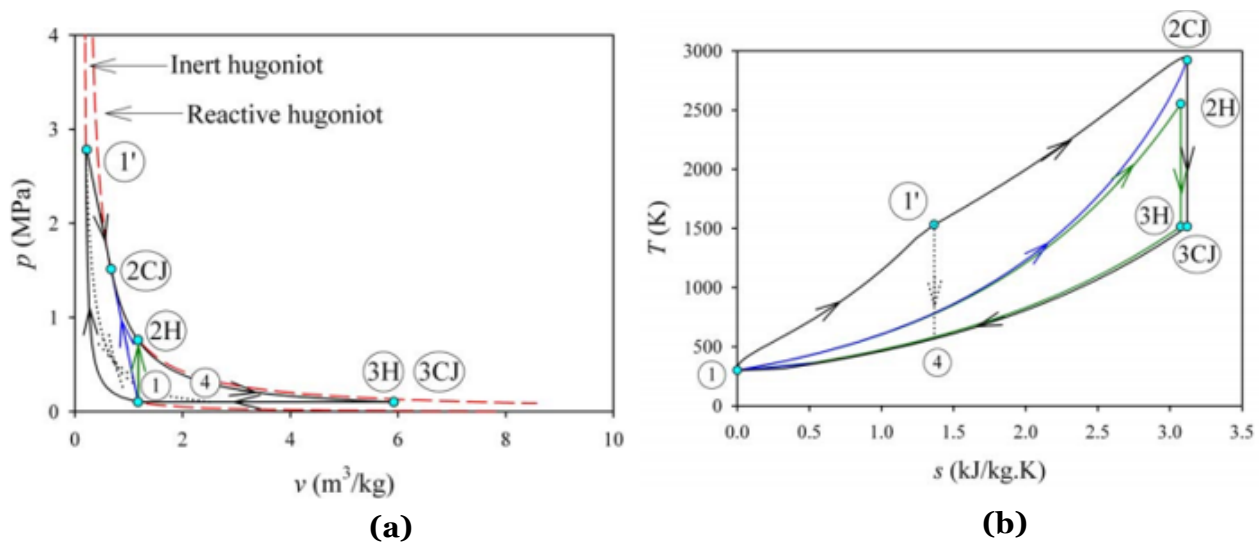
Fig. 4 Ideal Humphrey (1→ 2H → 3H → 1), FJ (1 → 2CJ → 3CJ → 1), and ZND (1 → 1'→ 2CJ → 3CJ → 1) for stoichiometric hydrogen/air mixtures at STP initial conditions P-v (**a**) and T-s (**b**) diagrams [13]

Table 1: Performance comparisons of the Humphrey, FJ, and ZND models [13]

	Humphrey	Fickett–Jacobs	Zel'dovich–von Neumann–Döring
Work out (MJ/kg)	0.709	0.834	1.40
Heat in (MJ/kg)	1.07	1.3	2.29
Efficiency (%)	66.5	64.3	61.2

The discrepancy is best explained by considering the two-step process that occurs inside the ZND model and the work actually extractable from it. Vutthivithayarak and Lu proposed that in the ZND model some of the work being produced must contribute to the momentum of the leading shock wave [13]. This internal work is unavailable for use in a cycle because it is occupied by sustaining the shock wave [13]. In Figure 4, the internal work is the area under the path 1-1'-4-1. Whereas the usable, 'external' work can be calculated by taking the total area captured by the path 1-1'-2CJ-3CJ-1 and subtracting from it the internal work. This external work is less than the total work of the ZND model, and has a value more closely related to the areas under the Humphrey and FJ model curves. This interplay is why the heat and work values are larger for the ZND model [13]. The efficiencies calculated by Vutthivithayarak, and Lu imply the two surrogate models will slightly overestimate the detonation performance, with the FJ model closer to the ZND model than the Humphrey model.

Heiser and Pratt performed a full thermodynamic cycle analysis with the ZND model as the combustion component and compared their results to similar analyses of the Humphrey and Brayton cycles [14]. Figures 5 and 6 compare their results [14]. For their calculations, the cycle using the ZND model was identical to the Brayton cycle except for during the heat addition process. Additionally, they considered both ideal and real cycles and quantified performance through T-s and P-v diagrams as well as thermal efficiency calculations [14]. Figure 5 shows the normalized T-s diagrams of the three cycles considered [14].
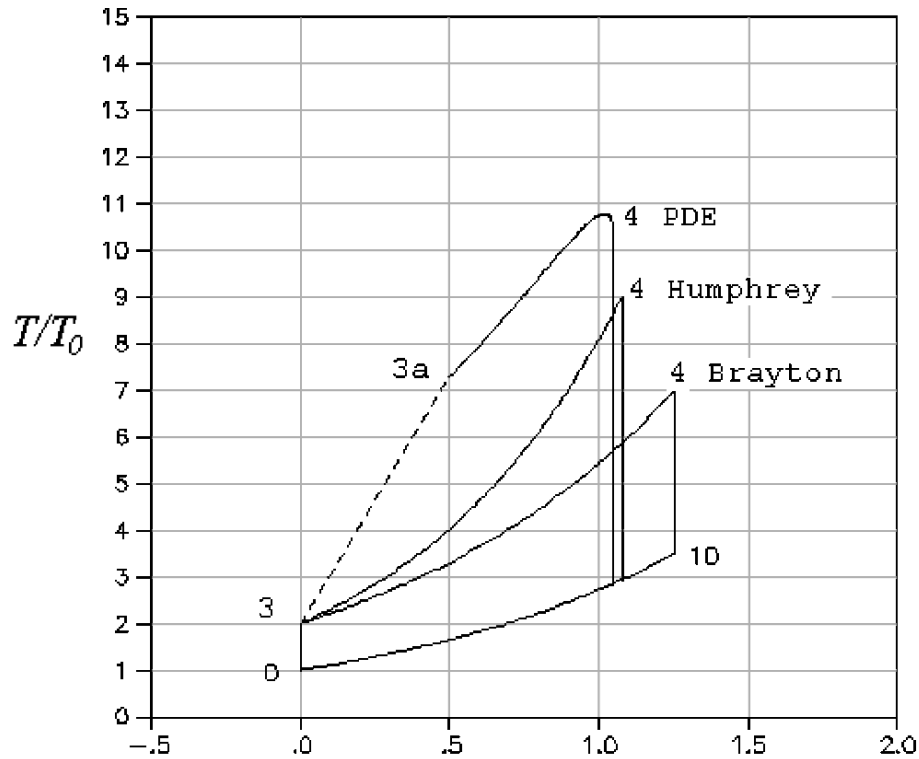
Fig. 5 Temperature-entropy diagrams for the ideal PDE/RDE, Brayton, and Humphrey
cycles compared in analysis by Heiser and Pratt. [14].

For the ZND cycle it was assumed Point 4 was the CJ condition where the flow is sonic

behind the shock wave [14]. Based on the previous discussion, the ZND model does not reach this

condition exactly but the difference is negligible. From Point 4 to 10 it was assumed that the true

non-steady expansion behind a propagating detonation was isentropic [14]. In Figure 5, the ZND

model, labeled PDE, clearly reaches temperatures greater than either of the other two cycles and

therefore the ideal expansion assumption significantly improves the cycle's work output [14]. The

thermal efficiency of the three cycles was calculated analytically for the ideal case using Equations

1-3. Numerical solvers were used to solve the cycles' real processes with pre-selected component

loss efficiencies and the results are presented in Figure 6. In Equations 1-3 $\tilde{q}$ was the non-

dimensional heat addition, γ is the ratio of specific heats, ψ was the static temperature ratio from

initial to pre-combustion, and M_{CJ} was the Mach number at the CJ condition [14].

$$M_{CJ}^2 = (\gamma + 1)\left(\frac{\tilde{q}}{\psi}\right) + 1 + \sqrt{\left[(\gamma + 2)\left(\left(\frac{\tilde{q}}{\psi}\right)\right) + 1\right]^2 - 1} \qquad (1)$$

$$\tilde{q} = \frac{f h_{PR}}{C_p T_o} \qquad (2)$$

$$\eta_{th} = 1 - \frac{\left[\frac{1}{M_{CJ}^2}\left(\frac{1+\gamma M_{CJ}^2}{1+\gamma}\right)^{\frac{\gamma+1}{\gamma}} - 1\right]}{\tilde{q}} \qquad (3)$$
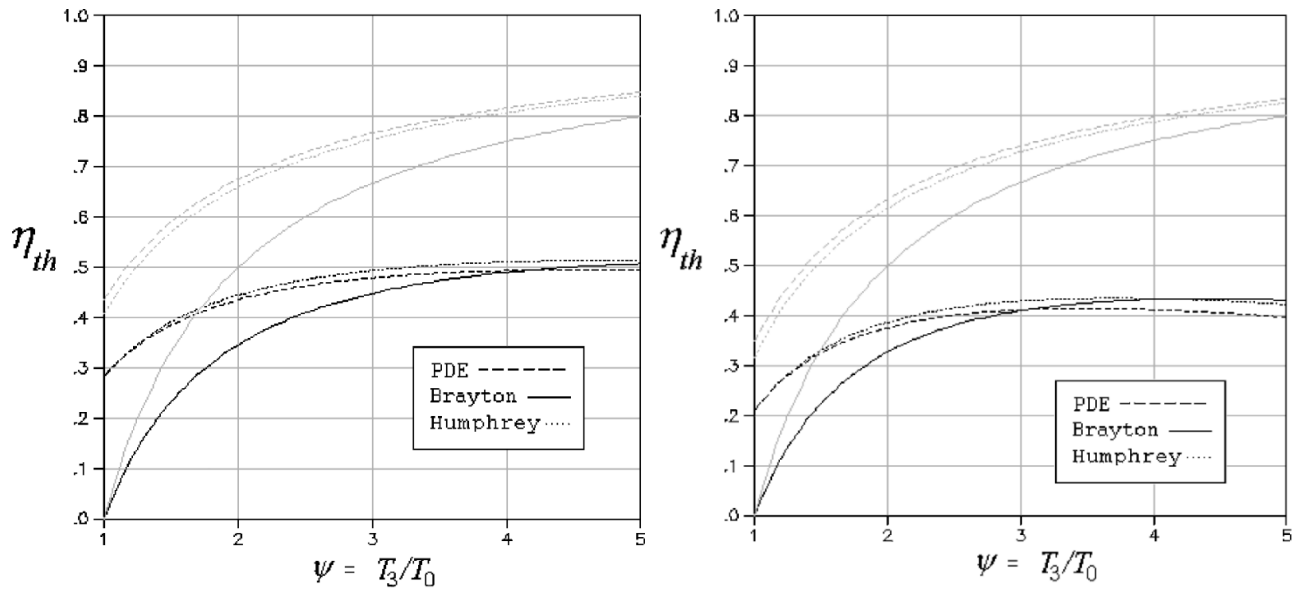
Fig 6. (a). Ideal (Grey) and Real (black) thermal efficiencies of the PDE/RDE, Brayton, and Humphrey cycles. $\tilde{q} = 5$, $\eta_{burner} = 0.9$, $\eta_{comp} = 0.9$, $\eta_e = 0.9$
(b). Ideal (Grey) and Real (black) thermal efficiencies of the PDE/RDE, Brayton, and Humphrey cycles. $\tilde{q} = 10$, $\eta_{burner} = 0.9$, $\eta_{comp} = 0.9$, $\eta_e = 0.9$ [14]

From Figure 6, the ZND augmented model (labeled PDE) had superior ideal performance over the Brayton and Humphrey cycles. However, once real component losses were considered the performance gains over the Brayton cycle decreased as the static temperature ratio increased [14]. The Humphrey cycle slightly outperformed the ZND model in all cases which was consistent with the findings of Vutthivithayarak and Lu [13,14]. Based on Figure 6, the cross over temperature ratio, where the efficiency of the Brayton cycle equaled that of the Humphrey/PDE

17

cycle, increased from three to four depending on the heat added from the combustion reaction [14]. Lastly, the use of the Humphrey cycle as a surrogate for the full ZND model appeared conservative when the ideal performance was considered, but with real losses considered overestimated performance [14]. This overestimation was later found by Paxson and Kaemming to be a function of the component losses used at station 4, and when appropriate losses were implemented, the PDE/RDE cycle had a higher thermal efficiency than the Brayton cycle for all ψ [15].

These thermodynamic analyses showed that detonation combustion may offer theoretical advantages over conventional constant pressure cycles such as the Brayton cycle. Due to the large pressure rise and peak temperature during detonation that can be estimated using the CJ point, the amount of work extractable is increased [4,14]. The improved thermal efficiency diminished as the static temperature ratios increased but was found to always stay higher than deflagrative cycles [14,15]. The type of fuel used in the detonation also impacted both the work output and the thermal efficiency [4]. Additionally, the ZND model of detonations was shown to be closely approximated by simpler models such as the Humphrey constant volume model and the Fickett-Jacobs model [4,13]. Both of these surrogates had the tendency to overestimate performance in analysis with losses considered [14]. Lastly, in all analysis it was important to remember that the true physical mechanism behind the detonation process, as defined by the ZND model, consisted of a leading shock wave adiabatically compressing the reactants which then combusted [11]. Some of the energy from the reaction was required to sustain the leading shock while the rest was available to produce work [13].

Section 2.2 Detonation Wave Propagation inside an RDE

With the thermodynamics and physical mechanism of a detonation covered, the details of the wave's structure and how it propagates in an RDE can be investigated. In general, RDEs look

very similar to the model in Figure 7. For this type of design, the detonation wave is propagated

via an annular channel (labeled annular combustor in the figure) with a width much smaller than

the diameter of the RDE [16]. Inside this small channel, fuel and oxidizer are continuously mixed

and exhausted axially. As mixing occurs, the detonation is triggered and the reaction propagates

in the direction of fresh reactants with a leading shock wave and entrained reaction zone, as

described by the ZND model [11]. The wave will circle the chamber radially near the injection

holes where the fresh reactants are located. Behind the wave, post combustion products are

expanded and exhausted axially out of the chamber. Therefore, if fuel and oxidizer can be injected

and mixed sufficiently fast enough, the wave always sees fresh reactants ahead of it and can

propagate continuously [16]. Thus, the fundamental crux of the RDE design lies in the continuous

supply of well mixed reactants in front of the wave [16].
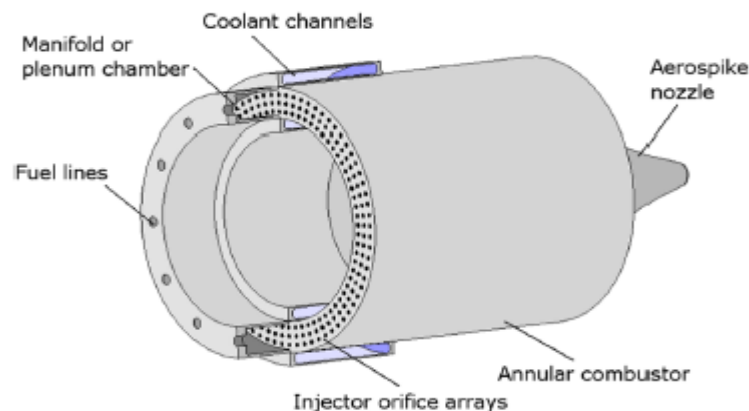
Fig. 7 Simple conceptual schematic showing basic design components of an RDE [16].

Section 2.2.1 Detonation Wave Macro Structure

Although conceptually simple, the actual flow field that results in the chamber is quite

complex and can be best visualized by unwrapping the annular chamber of the RDE as shown in

Figure 8 [16]. When interpreting the figure keep in mind the flow is moving from bottom to top

and the radial direction is right to left.

nozzle

flow proceeds
to nozzle

attached shock

mixed products from prior wave

contact surface burning

fresh reactants ← detonation wave

reactants enter annulus from
manifold chamber and mix

injector flow blockage from
detonation wave

refueling when wave
pressure decreases
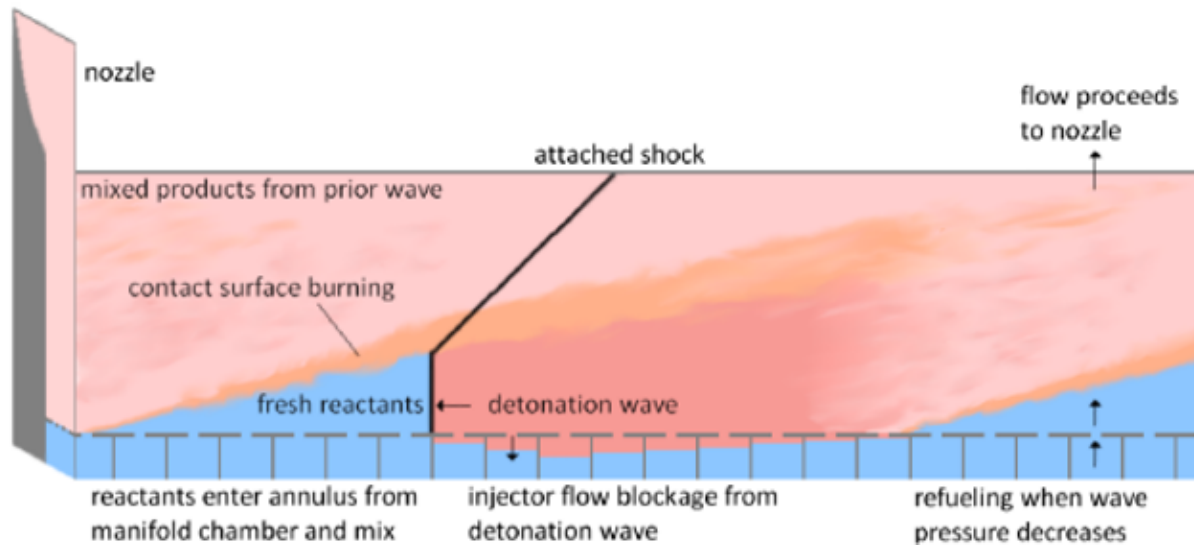
Fig 8. Sketch of a rotating detonation structure inside an RDE annulus [16].

From Figure 8, many of the important features of the detonation wave's macro-structure are shown, including the detonation wave, attached shock, reactant and product zones. Only a single wave is shown for simplicity, however, multiple waves can exist inside the chamber at once [16]. Additionally, the actual detonation wave is shown simply as a line, however it too has its own complex sub-structure and will be discussed in depth in Section 2.2.2. Importantly, the detonation wave is a wave and therefore does not "flow" through the injected reactants. Instead it propagates like a sound wave through air. As a result, not much of the injected flow field is disturbed from its axial trajectory as the wave passes [16].

Notice that the detonation wave is only as tall as the height of the fresh reactants ahead of it. Keeping in mind that there is a physical constraint on how "short" a detonation can be, a concept explained further in Section 2.2.2, this relationship hints that there is minimum height the reactants must fill to before the wave comes back around [16]. In fact, this minimum height is a significant feature in RDE design known as fill height and will be discussed at length in Section 2.3. If the wave propagates too fast, or the reactants fill too slowly, the wave will complete a rotation to the

20

same point before a sufficient amount, or height, of fresh reactants are available again.

This balance between speed of propagation and fill height is exasperated by other features shown in Figure 8 such as contact surface burning and injector flow blockage [16]. Both of these features tend to decrease the fill height by either burning available reactants before the wave arrives or by increasing the amount of time it takes for a given injector to "recover" from the overpressure of the previous wave passage [16]. Interestingly, the ideal fill height is a function of the reactants and in instances where mass flows/injection recovery allow for fill heights larger than the ideal the wave will split into multiple waves, each with a fill height near the ideal value [16]. As a result, RDE design philosophy must consider that an optimum fill height exits for stable detonations and that the wave will naturally attempt to propagate at this fill height under varying conditions.

Further, Figure 8 shows that an attached shock at the top of the detonation wave. The point of attachment is known as the triple point [16]. The attached shock appears because detonation products directly behind and near the top of the wave experience expansion due to "side relief" from the cooler, and thus lower pressure, products further behind, above and in front of the wave [16]. An expansion fan that centers on the triple point then forms which propagates into the combustion products decreasing their pressure until it equalizes with the injector pressures [17]. This point of pressure equalization can be seen in Figure 8 where the injection flow begins to enter the chamber behind the detonation wave. The expansion fan also turns the velocity of the unburnt reactant flow relative to the detonation wave upwards [17]. Remembering that the flow of the burnt products ahead of the wave, relative to the wave, must therefore also be turned to satisfy the conservation of mass and momentum, a compression wave/oblique shock will form. Figure 9 further illustrates this compressible flow field around the triple point [17]. In this figure the "inert" zone is analogous to cooler combusted products in Figure 8, while the "combustion product" zone is analogous to the hotter combusted products in Figure 6 [16,17].
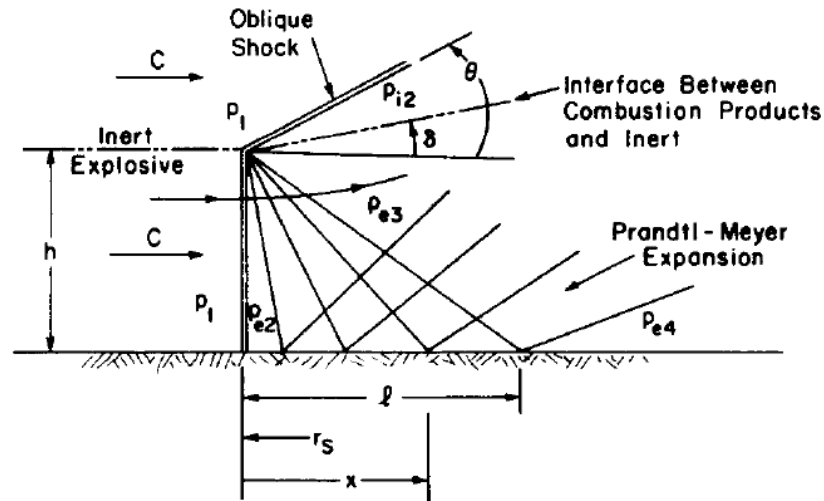
Fig 9. Inviscid compressible flow field interaction as a result of side relief due to inert combustion product boundary conditions [17].

The characteristic interactions between the detonation wave and the annular flow field described above help define areas interest, such as the fill height. However, they also offer analytical insight into the pressure directly behind a propagating detonation wave. Sichel and Foster showed that inviscid compressible analysis of the flow field in Figure 9 yields similar results to experimental results for the impulse from a plane fuel-air explosion [17]. As a result, their technique, based in the compressible flow features in Figure 9, provides a relatively simple approximation for the theoretical pressure rise across a propagating detonation [17].

Section 2.2.2 Detonation Wave Micro-Structure

With the macro-structure of the detonation wave understood, the internal micro-structure of just the detonation wave can be considered. The first fundamental observation of this internal structure is that it is unstable and unsteady [18]. Meaning, the structure is not a nice solid region of intense density change like a standard shock wave. Intuitively this is consistent with the ZND model which predicts a coupling between a leading compression zone and a reaction zone. It turns out this coupling is inherently unsteady. Research from the past two decades has uncovered a range

of unstable behaviors for propagating detonations, including weakly unstable and strongly unstable waves [18]. In weakly unstable detonations the wave is nearly laminar with an unsteady periodic flow. In strongly unstable detonations the wave's instability is chaotic and has turbulent flow characteristics [18].

A linear perturbation analysis of the leading shock shape and speed mathematically grounds the unstable nature of a detonation wave [18]. Shepard explained that physical mechanisms for the instability in the wave front arise from a coupled set of factors [18]. First there is an amplification of acoustic waves inside the region between the lead shock and the end of the reaction zone. Second, the chemical reactions comprising the reaction zone are sensitive to temperature and pressure changes. Lastly, there is a hydrodynamic instability inherent to propagating reaction fronts [18]. In total, the instability causes almost all propagating detonation wave fronts to break down into a set of multiple smaller wave fronts which are constantly being formed and destroyed by nonlinear, large amplitude, perturbations in three dimensions [18]. Most importantly, these multiple wave fronts create the building block of the full propagating detonation known as the detonation cell, and ultimately create an internal wave structure that has a spatially non-uniform and unsteady reaction zone. However, statistically this zone is stationary and moving at the speed predicted by the ZND model, which is near the CJ velocity [18]. Figure 10 shows a Schlieren image of propagating detonation wave [19]. The striations along the height of the wave are known as transverse waves and are a result of the multiple wave fronts (cells) inside the larger overall wave. [18].
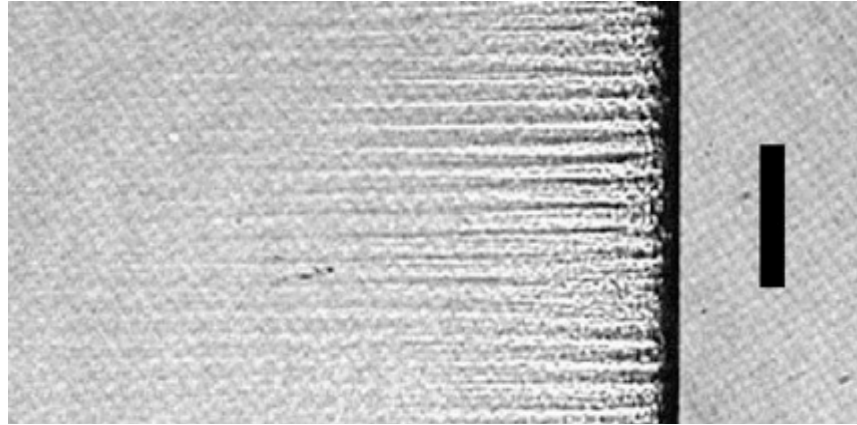
Fig 10. Schlieren image of a reaction/detonation front. Length of black bar in front of wave is 10mm. [19].

The unsteady and three-dimensional formation of the wave fronts/cells inside the dark black region of Figure 10 are hard to observe, but recent research has allowed high fidelity imaging to take place. Figure 11 shows examples of both a strongly unstable detonation wave and a weakly unstable detonation wave [18]. Next to each image of the wave front is what is known as a soot foil fish scale pattern. This pattern is caused by the soot traces left behind by the passing wave front. It is a useful tool in visualizing the anatomy of the wave's interior structure by preserving the time history of the transverse waves. Image set (b), in Figure 11, is the weakly unstable wave with smooth laminar waves and fish scale patterns, while image set (c) has clear evidence of turbulence both in its wave front and soot foil pattern indicative of a more chaotic nature [18,20]. These images were also taken in a high aspect ratio channel, eliminating much of the three-dimensional behavior of the cells. This restriction simplifies visualization.

Soot foil patterns also reveal a useful way to measure the special wavelength called the detonation cell size denoted by (λ), which is the width of a single cell [18]. It turns out that cell size is a governing factor in many of the practical applications of detonation wave technologies, including RDEs. Specifically, it enforces certain sizing constraints on the annular chamber through which the wave propagates. If the physical area is too small to contain a minimum of a single cell, the detonation simply cannot form [18]. Importantly, cell sizes vary based on the

reactants used, pressure, temperature and equivalence ratio for a given detonation. Even within

the same wave front, cells are not always perfectly consistent. In some cases, there may be two

dominate cell sizes within a single wave [18].
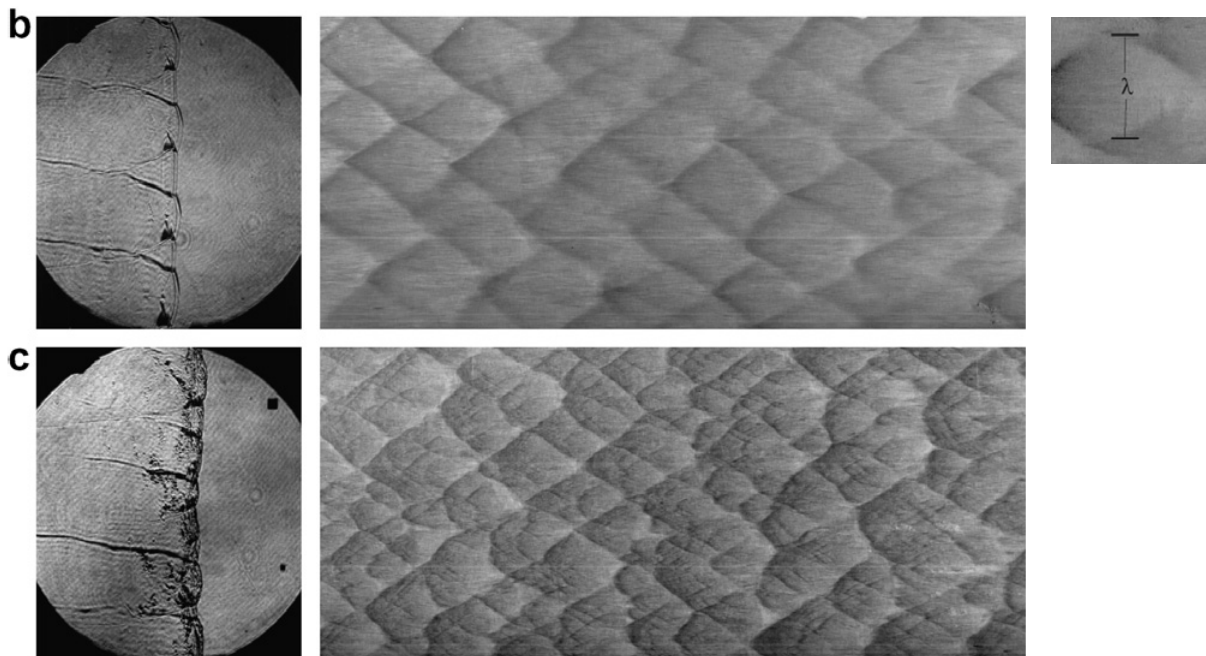
Fig 11. Zoomed in Schlieren images of two different propagating detonations with corresponding soot foils and Cell Size (λ) definition. Images show same scale with height of 150mm initial pressure of 20 kPa [20].

Lastly, the anatomy of this unsteady behavior can be further defined by schematics such as

those shown in Figure 12 [18]. The three major subcomponents of the cell structure are the

transverse waves, incident wave, and Mach stem. In Figure 12, the transverse waves are labeled,

but the incident waves are those labeled as "slow", while the Mach stem/wave is labeled as "fast".

Mach stems can be viewed as the active, or energetic portion of the wave front, while the incident

waves are older Mach stems that are no longer close enough to their local reaction zone to stay

energized. The point labeled as the "Triple Point" is the location where all three components

intersect [18]. This triple point is distinct from the macro-structure where the triple point was the

location of where the oblique shock attached to the top of the detonation wave [16,18].
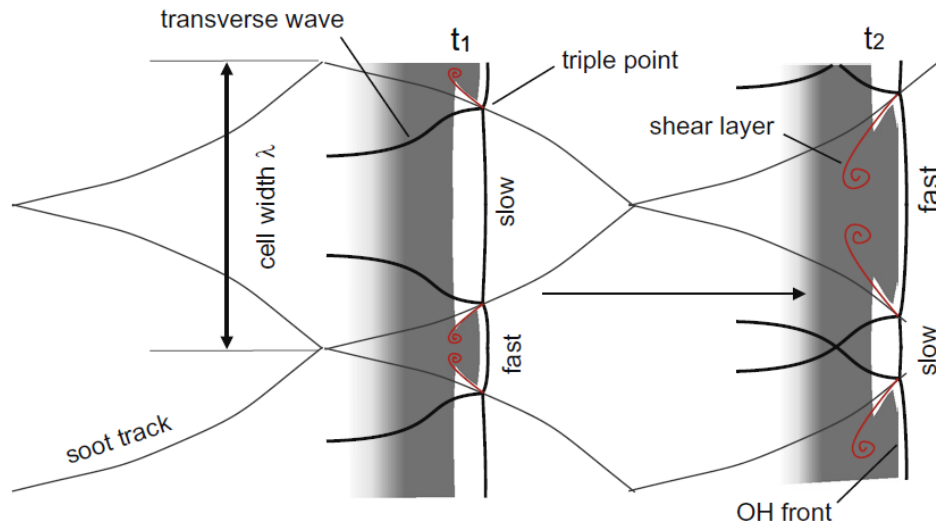
Fig 12. Sketch of the sub-components of a detonation wave front overlaid with a soot foil pattern to illustrate the unsteady interactions between the Transverse waves, incident waves, and Mach stems [18].

The transverse waves always travel such that they move along the incident wave until they collide in pairs. At this collision point the increase in pressure and temperature locally ignites the reactants, propelling the transverse waves away from each other to new corresponding pairs where the process will repeat. At the same time/point where the transverse waves collided, the corresponding incident wave, over which they had moved, vanishes (incident waves decrease in length as the transverse waves approach each other) and the corresponding Mach wave behind them then becomes the new incident wave. The new Mach wave forms when the recently ignited reaction propels the transverse waves away creating a new, energetic wave front in the process. A shear layer forms between the newly formed reaction zone and the older, cooler reaction zone behind it [18]. The dynamic and complex interplay of these subcomponents contribute to the difficulties associated with analytically and numerically modeling detonation wave behavior for use in RDE designs [18].

Section 2.2.3 Impact of Channel Curvature on Wave Propagation

So far wave propagation has been discussed in the context of a linear propagation path. However, in an RDE the wave must negotiate a curved channel. Furthermore, in a small scale RDE such as the one in this thesis, effects due to curvature will be even more significant. There exists a limit on how much curvature a wave can overcome because of an increasing normal pressure gradient acting on the detonation wave front [16]. This normal pressure gradient further destabilizes the already unstable and unsteady wave structure detailed in Section 2.2.2 by constantly forcing the coupled reaction zone and wave front interactions to re-align with the changing normal direction [16].

Kudo et al. investigated the behavior of the wave as this limit on curvature was approached and found that the constant re-alignment had the general effect of causing the propagation speed of the wave to decrease [21]. Additionally, they took these characteristics and defined regimes that corresponded to either stable, critical, or unstable wave propagation [21]. Waves which moved above 80% the CJ velocity were said to be stabilized, waves between 60%-80% CJ speed were critically stable, and waves below 60% CJ velocity were unstable [21]. Guidelines on how large a curvature was allowable were defined using the inner radius to cell size ratio, $\frac{r_i}{\lambda}$. Later, Nakayama et al. performed a series of experiments to produce the plot shown in Figure 13 to define quantifiable limits based on this ratio [22]. From this they recommended that the ratio stay between or above 21-32. As can be seen, below these minimum ratio values shown as the slope of the lines, only 1-2 test points resulted in a fully stable wave [22]. Dechert designed the Micro-RDE with a $\frac{r_i}{\lambda}$ ratio of ~7-24 and experimentally documented wave speeds near 55% of the predicted CJ velocity of an ethylene and nitrous oxide mixture [1]. Subsequent high-speed camera footage showed unstable wave behavior as well, validating the predictions of both the guidelines discussed [1,21,22]. Ultimately these results emphasized the potential impact the small-scale geometry was

having on wave stability and propagation.

Lastly, these ratios do not fully account for the impact of channel width. In an oblique wave, such as the one in a curved channel of an RDE, the amount the wave must re-align itself is affected by the channel gap. Smaller channel gaps limit the curvature in the wave by limiting the radial space available for the wave to curve. In very thin channels where waves may only be a single cell wide, the oblique wave simply does not have enough space to curve enough to impact stability. However, channels with gaps small enough to see this effect do not usually fall within the standard sizing guidelines for RDEs and as a result, the ratios described above hold well in general. Thin channels may be an avenue to improve the design by Dechert [1].
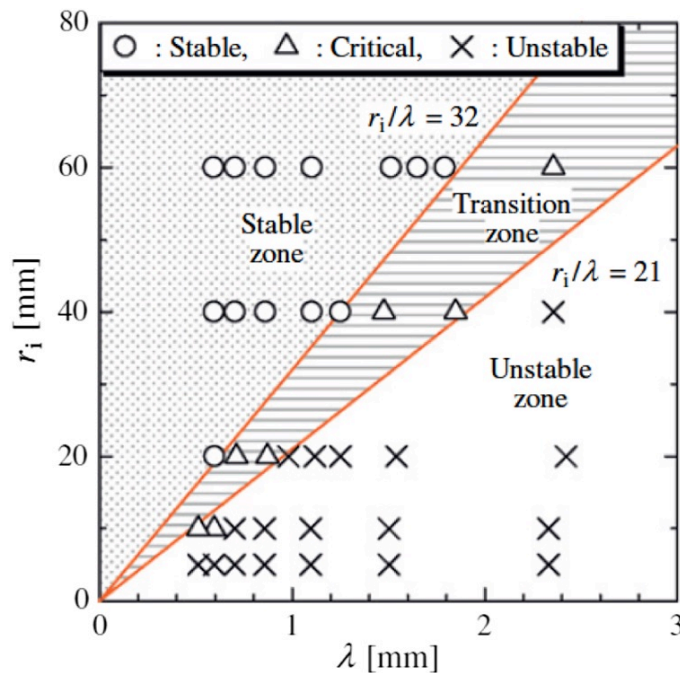
Fig. 13 Detonation wave behavior in terms of propagation modes detailed in Nakayama et al. showing a relationship between inner radius of the curved channel and cell width [22].

Section 2.3 Rotating Detonation Engine Design

From the discussion above, the detonation thermodynamics and wave propagation must be taken into account when designing an RDE. The current section will cover how previous designers

have handled making their design decisions with these considerations in mind and what guidelines they have used to justify them. As will be seen, the starting points for RDE design is the geometry of the device and the injection scheme. Details about the injection scheme will be handled in Section 2.4. Additionally, as this work is a follow on to work by Dechert, the decisions and results of that research will also be reviewed [1].

Section 2.3.1 Rotating Detonation Engine Geometric Sizing

In a comprehensive study of Spin Detonation Engines by Russian researchers Bykovskii et al., a set of guidelines to calculate nominal values for the desired fill height (h), channel gap (Δ), channel diameter (d_c), and channel length (l_c) was put forth [7]. Figure 14 shows the relationship between the geometric parameters of interest in a nominal RDE [1,7]. Their derivation of these guidelines came from a culmination of experiments with C_2H_2-O_2, C_3H_8-O_2, and CH_4-O_2 gaseous mixtures in various chamber diameters of 40 and 100 mm. Along with diameter, the channel length and channel gaps were also varied between 20-100 mm and 2.5-10 mm, respectively [7]. By understanding the reasoning behind how their results led to their guidelines, use or deviation from them in design decisions can be explained and supported.
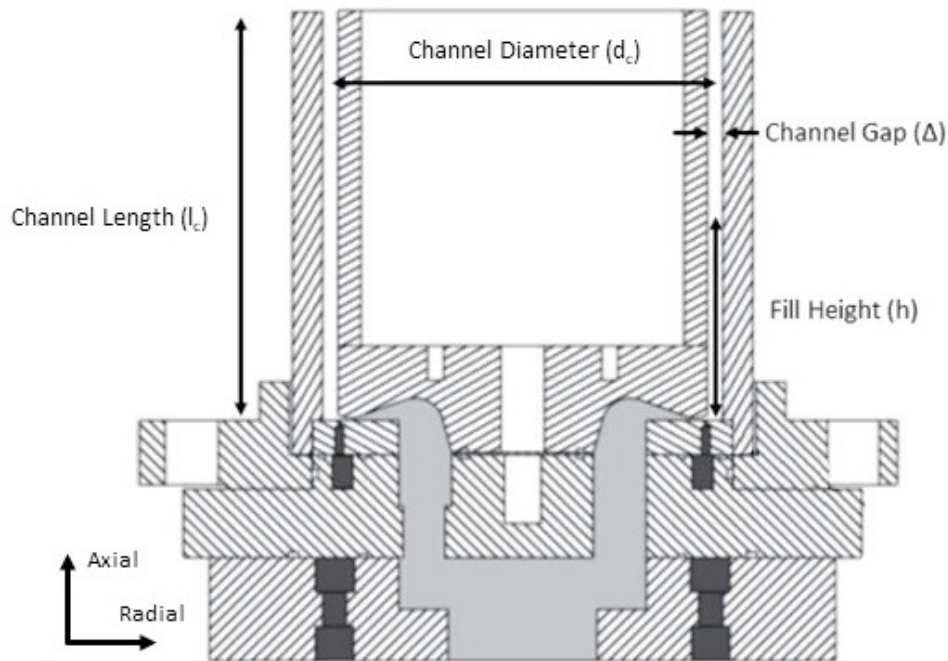
Fig. 14 Sketch of major RDE design features studied by Bykovskii et al. [1, 7]

From their results, Bykovskii et al. noted five characteristics of continuous spin detonation that separated it from other detonation processes. First, the mixture in front of the detonation wave was not pre-heated by the leading normal shock, but instead by either the hot product gases left over or contact burning [7]. This mixture was also rarely mixed ideally, as the fill time between waves passing was so short. As a result, the wave impacted upstream mixing through the left-over products [7]. The large pressure of the passing wave was observed to back flow injectors, particularly when the injection flow was subsonic. Lastly, stable/steady waves only propagated in a single direction [7]. This last point on wave direction seemed to imply that if a wave was in a clapping mode i.e., if the wave ran in both directions around the chamber, it was not stable.

Bykovskii et al. also noted that the single most important physical factor to a successful detonation was effective local mixing directly in front of the wave [7]. Proper mixing was found to be so significant because the detonation reaction would only occur within a specific range of equivalence ratios. In fact, optimum detonation and maximum propagation speed was found to occur around stoichiometric values for a given mixture [7]. Deviations from this value tended to

30

increase wave instability and contribute to an increase in cell size [7, 23].

From the discussion in Section 2.3.2 cell size drives the propagation characteristics of the wave. So, it intuitively makes sense that as the equivalence ratio moves away from the stoichiometric value, the detonation cell begins to grow in both size and turbulence as a result of increased instability. Subsequently, the wave propagates poorly. Figure 15 shows the cell size versus equivalence ratio for a H_2-Air mixture [23]. As can be seen the relationship is strictly parabolic with a clear optimum near the stoichiometric value. Furthermore, the Detonation Database [23], from which this figure was produced, shows that this shape occurs for most mixtures. This implies the relationship is fundamental for detonable mixtures, which validates the observations of Bykovskii et al [23].
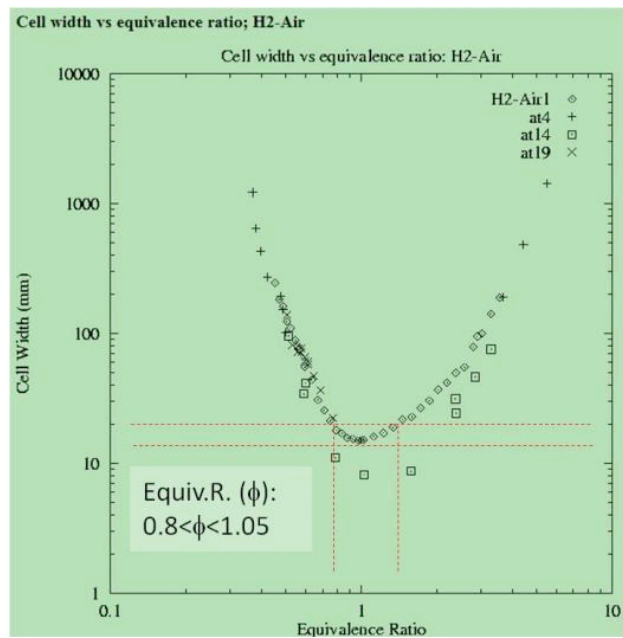
Fig. 15 Equivalence Ratio versus Cell Width for H2-Air mixture at 1 atm initial pressure [23]

Almost all of the Bykovskii et al. guidelines act as functions of cell size, which is a function of equivalence ratio which is a function of mixing [7]. If proper local mixing was attained then the necessary condition became the critical fill height, h^* [7]. As discussed in Section 2.2.1, if this fill height is not reached, then the wave cannot sustain itself. It was noticed that wave reflections from

disturbances in the channel wall or a constriction of the exit flow could hinder the formation of constant height fill layers, disrupting wave formation [7]. In general fill heights in stably operating RDEs fell between *h** and *2h** [7]. It was from these observations that the following relationships were proposed.

The first quantitative guideline comes from combining observations on fill height and cell size and relating them via Equation 4 [7]. If channel length was considered along with fill height, the ratio of the two was found to be reasonably constant across most gaseous RDEs. This constant was defined as K and can be calculated using Equation 5 [7]. Equation 5 can also be used to find the minimum channel diameter as shown in Equation 6 [7]. By examining the relationship of Equations 4-6, it can be seen that increasing the minimum diameter, holding all else equal, will increase the number of waves inside the chamber [7].

$$h \cong (12 \pm 5)\lambda \qquad (4)$$

$$K = \pi(d_c)_{min}/nh \qquad (5)$$

$$(d_c)_{min} = \frac{hK}{\pi} \qquad (6)$$

Numerical simulations and experimental data showed a pressure ratio of 10 ± 4 across the detonation wave was a good rule of thumb but was also dependent on propellent combination [7]. The post detonation pressure was also estimated to be 4 ± 1 times the average chamber pressure [7].

The next major guideline regarded the channel gap (Δ). As with fill height, there also exists a minimum channel gap that depends on the cell size of the reactants and is given in Equation 7 [7]. Due to the dependence on cell size, if the mixing quality diminishes, the minimum channel gap requirement increases for the same reason as the fill height. Importantly, if the channel gap is designed significantly larger than the minimum value (Δ^*) determined in Equation 7, then changes will not impact wave stability [7].

$$\Delta \geq \Delta^* \cong (.2)h \tag{7}$$

Lastly, knowledge of the fill height, number of waves, and channel diameter can allow estimation of both the minimum and optimum channel length (l_c) as shown in Equations 8 and 9. Ultimately changes to channel length have weak effects on the wave's propagation [7]. However, excessive changes away from the optimum value can be detrimental. In the case of a channel length which is too long, a boundary layer can form and significantly shrink the effective channel gap. If the channel length is too short, pressure relief through the exit may take away too much pressure ahead of the wave, causing it to stop propagating [7].

$$l_{c_{min}} \cong 2h \cong \frac{(d_c)_{min}}{n} \tag{8}$$

$$l_{opt} \geq 4h \cong \frac{2d_c}{n} \tag{9}$$

From these proposed relationships RDE design should start with the cell size of the reactants and march through estimations of necessary fill height, channel length, channel gap, and minimum diameter. However, it must be emphasized that these are guidelines, and the presence of both ranges in the equations and approximate symbols suggest that there is room to deviate from the suggested values. Specifically, deviation from suggested fill height is examined in the current research.

Section 2.3.2 Review of the Micro-RDE Design

It was with the philosophy to push the boundaries of the guidelines of Bykovskii that Dechert designed the first version of the Micro-RDE [1]. To meet the design goal of a single propagating detonation with a 20 kHz frequency, a reactant combination with a small cell size was desirable. This led to nitrous and ethylene being chosen as the reactants [1]. However, this combination did not have a documented cell size in sources such as the detonation database [23].

Therefore, Dechert used a soot foil from a nitrous and ethane detonation and correlated the measurements to get an estimate of the nitrous and ethylene value. This technique yielded a cell size between 0.5 and 1.75 mm [1]. From this cell size the following values for the sizing parameters in Figure 14 were found. These results are placed in Table 2. Refer to Dechert for full details on the process through which they were derived using the guidelines from Section 2.3.1 [1].

Table 2: Summary of Micro-RDE sizing Parameters [1]

Cell Size	0.5-1.75 mm
Fill Height	Estimated: 3.5-12 mm Experimentally Calculated: 3.2-8.1 mm
Channel Gap	2 mm
Channel Length	30 mm
Channel Diameter	28 mm

Initial success at detonation proved difficult in this size of an RDE across all mass flows (0.025-0.075kg/s) and equivalence ratios (0.5-1.5) [1]. Reactant flow in the channel reached axial velocities nearly six times the turbulent flame speed for ethylene and nitrous oxide. This made ignition via a spark plug located just outside the exhaust plane of the channel impossible [1]. To slow this flow to the point where detonation could occur, an aerospike nozzle was placed at the end of the detonation channel and used to increase the pressure in the chamber, slowing the flow. Additionally, the ignition spark plug was moved from just outside the detonation channel, to inside it. The subsequent increase in chamber pressure, decrease in exhaust flow speed and proximity of spark to freshly mixed reactants led to successful detonation [1]. The resultant operating maps for the Micro-RDE are shown in Figures 16 and 17. Dechert used two aerospike nozzles, one with a throat to chamber area ratio (ε) of 0.14 and another with a ratio of 0.40 [1]. Each point on the

figure was tested twice, if detonation occurred each time, it was solid green. If detonation occurred once the RDE was heated by a previous successful test, but not when it was cold, it was marked as a green open circle.
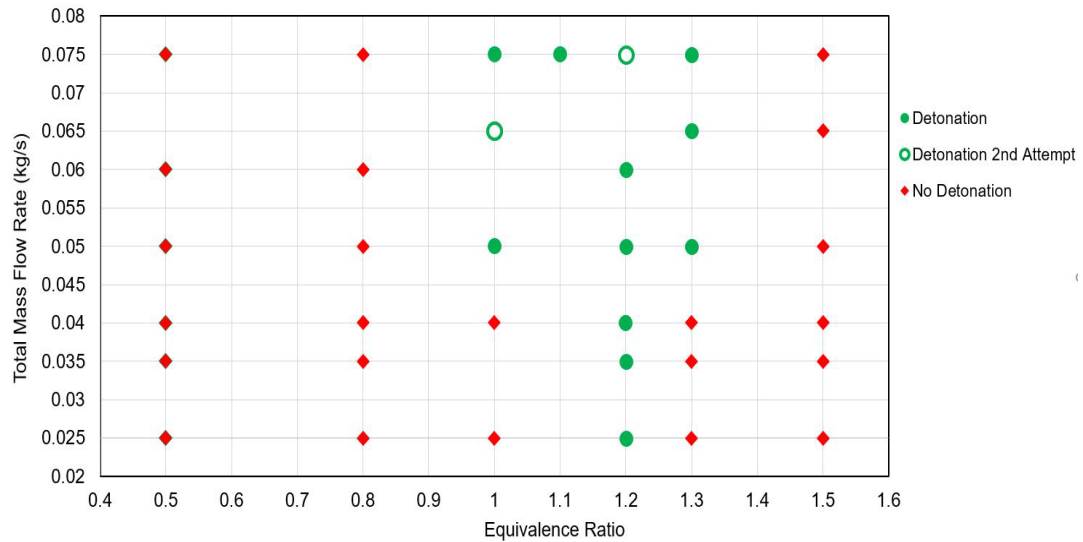
Fig. 16 Operating Map from Dechert using $\varepsilon = 0.14$ nozzle [1]
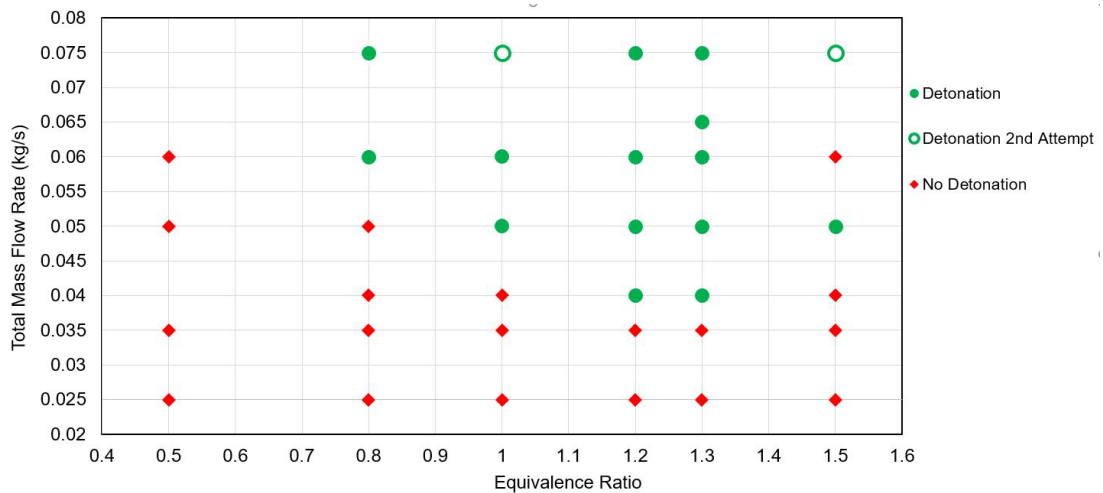
Fig. 17 Operating Map from Dechert using $\varepsilon = 0.40$ nozzle [1]

Significantly, both these operating maps showed an optimum equivalence ratio (Φ) of $\Phi = 1.2$. This conflicted with the expected optimum of $\Phi = 1.0$ for N_2O and C_2H_4 mixtures [1]. Dechert explained this difference by suggesting that there was a discrepancy between global and local equivalence ratios. So, while the global Φ, measured by the flow controllers, was around 1.2, the local value, which was not directly measured, was likely closer to the true optimum of 1.0. This indicated that not all the fuel being injected was being mixed [1]. As has been discussed local mixing is arguably the single most influential aspect of RDE design [7]. In the Micro-RDE design a Jets in Cross Flow injection scheme was used [1]. Modification of this scheme may allow for better local mixing and is one of the major areas of interest for the current research. Injection schemes will be covered further in Section 2.4.
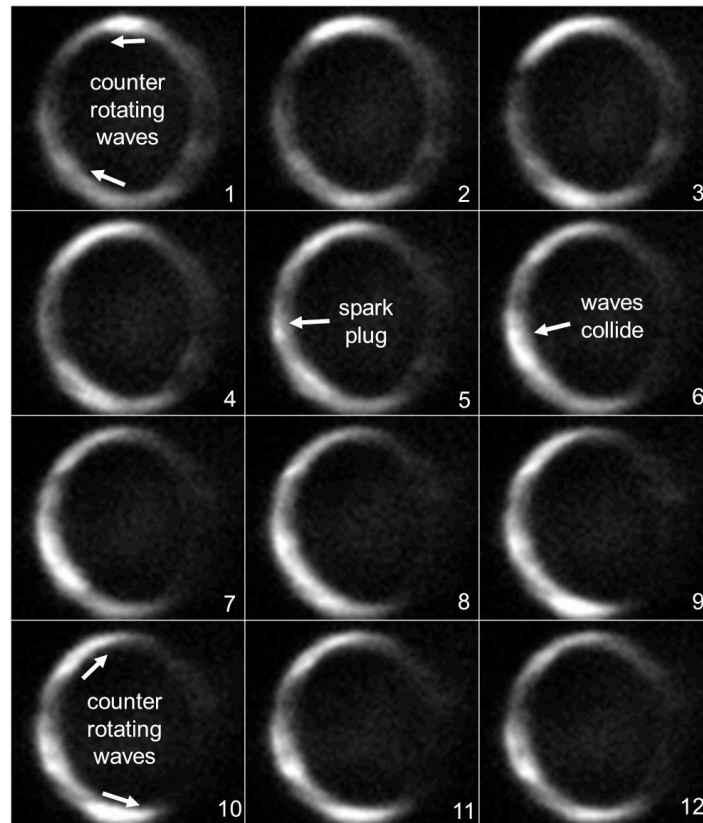
Fig. 18 Detonation wave behavior at 0.075kg/s mass flow rate and $\Phi = 1.2$ using $\varepsilon = 0.40$ nozzle [1]

The detonation wave behavior was captured via a high-speed camera [1]. The video from the camera was then used to examine the wave's propagation. Figure 18 below shows 12 frames of a typical detonation. It was not uncommon for the detonation wave to seemingly gravitate towards the spark plug in the detonation channel, and it was suspected the protrusion increased the odds for a clapping mode to initiate [1].

Another indication of the spark plug's influence on the detonation wave was its condition after each run. For many spark plugs, after one detonation it was destroyed with its entire electrode tip completely eroded away [1]. Additionally, over the entirety of the testing campaign, the hole through which the spark plug was inserted into the chamber eroded significantly. This was believed to contribute to the wave's instability for tests which occurred later [1].

Section 2.4 RDE Injection Scheme Design

The importance of properly mixed reactants inside an RDE cannot be overemphasized [1,7,11]. Due to its importance, particularly to the current research, the injection scheme was a major design focus. When considering a potential design, the aspects of injection geometry and mixing scheme, injection stiffness, and pressure recovery become major areas of interest. As will be discussed in the following sections, choices regarding each of these areas will have to be made to balance the advantages and disadvantages of the many options available. For the current research, the main interest is in a stable and reliable detonation in a small-scale geometry. Therefore, priority will be given to design choices which optimize these key characteristics.

Section 2.4.1 Injection Geometries and Mixing Schemes

Duvall et al. looked into the impact of three different injection geometries in an effort to characterize their effects on RDE operation [10]. To help qualify their results, the authors defined

5 modes of combustion which covered the range of behaviors seen from each of the injection geometries [10]. These modes have been put into Table 3. The injection geometries used were the Pintle Injector, Jets in Crossflow (JIC), and Semi-Impinging Jets (SIJ) and are shown in Figure 19 [10]. In Figure 19, red arrows denote fuel flow and black arrows denote oxidizer flow.

Table 3: Duvall et al.'s Five Modes of Combustion [10]

Mode 1	Stable Detonation with a single wave
Mode 2	Stable detonation, two co-rotating waves
Mode 3	Steady Deflagration with counter rotating waves
Mode 4	Unsteady deflagration with no coherent structure
Mode 5	Rapid transition between unsteady deflagration and stable detonation
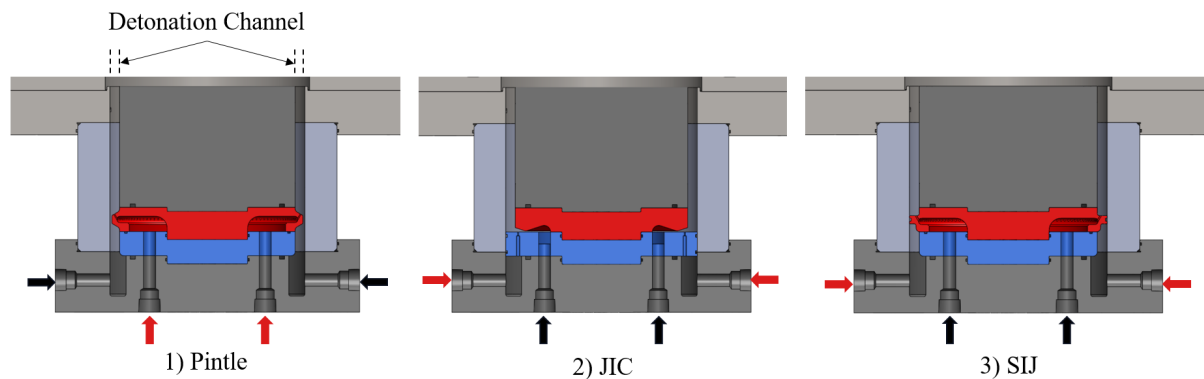
Fig. 19 RDE cross sections highlighting the 3 different injection geometries [10]

The Pintle injector has the oxidizer move around a contour into the detonation chamber. Taken as a whole, this contour creates an annular slot with the outer wall of the detonation channel. Fuel is then injected through equally spaced, circular holes in the upper face of the Pintle contour. Fuel is injected at a non-90-degree angle [10]. The JIC geometry has fuel entering from circular

38

holes axially oriented along the floor of the channel that are each paired with radially oriented injection holes for the oxidizer. The pairs of injection holes are aligned radially (so that the fuel jet is aimed directly in the path of the oxidizer jet) and are 90 degrees opposed [10]. Lastly, the SIJ geometry has fuel and oxidizer injected similarly to the Pintle geometry. However, the SIJ has oxidizer enter through jets instead of an open slot. Furthermore, the jets for the oxidizer are offset with the fuel jets so only a portion of the exit areas overlap [10].

The mode in which the geometry operated in depended mostly on the mass flow and momentum flux ratio of the injection scheme. Equation 10 defines momentum flux as the product of the fuel or oxidizers ratio of specific heats, static pressure, and Mach number at the injection interface into the chamber. Ultimately this value is a measure of momentum and its ratio, defined in Equation 11, between the fuel and oxidizer is a useful metric for comparing injector characteristics [10].

$$q = \gamma p M^2 \tag{10}$$

$$J = \frac{q_{fuel}}{q_{Ox}} \tag{11}$$

Momentum flux can be calculated if the Mach number of the flow at the injection throat is known. Mach number can be found experimentally if the pressure in the chamber and plenum is known via isentropic relationships. Understandably this is an estimation, as injectors with near sonic injection speeds will not generally be isentropic. If the pressure in the chamber is not known Duval et al. proposed a time averaged numerical method [10]. In the case of an unknown or uncertain chamber pressure, the numerical method using experimental results also offers a way to estimate the pressure once the Mach number is known. However, again this would rely on isentropic relations and be subject to the same error [10].

Results from Duval et al. of the three injection schemes varied. The Pintle geometry operated in Modes 1,4, or 5 while the JIC operated in Modes 1, 2, or 4, and the SIJ in Modes 1, 3,

or 4 [10]. Their results showed that the Pintle injector and JIC injector detonated most readily at similar optimum momentum ratios around 0.5-0.6. Both these schemes also had different air/fuel plenum pressure ratios at these momentum ratios. The difference likely stemmed from the JIC being choked across a larger operating regime than the Pintle due to different area ratios of the injector holes [10]. The SIJ scheme performed much differently than either of the other two with Mode 1 momentum flux ratios in the range of 0.12-0.28 [10]. Additionally, the SIJ injector had air/fuel plenum pressures that were disparate. The oxidizer flow was always choked while the fuel flow was only occasionally choked. Best performance was attained when choking conditions were matched [10]. Lastly, the Pintle injector had the best pressure recovery characteristics [10].

Ultimately these results indicated that the best scheme in terms of pressure recovery and detonability was the Pintle geometry. However, the Pintle geometry did not choke across as wide an operating regime as the JIC injector [10]. Choking injector flow is desirable because it decreases the amount of coupling between the detonation and the plenums and increases fill recovery speed. However, choking also increases pressure losses during the injection, which helped the Pintle scheme's pressure recovery. The JIC injector is simpler to manufacture on the small scales of the Micro-RDE when compared to the Pintle scheme and still had similar momentum ratios indicating similar performance [10]. Therefore, JIC schemes were the selected injection scheme for the research by Dechert. From his results, detonation was achieved when momentum ratio was between 0.6 and 1.0 [1]. Changes to the existing JIC scheme will be the initial modification made to Dechert's design in the current research.

Section 2.4.2 Impact of Blowing Ratio and Confinement on JIC Geometry

To further understand the mixing mechanisms of a JIC geometry Bohon et al. set up an experiment to visualize the flow interaction of a JIC scheme [24]. The injector flow of their

experiment was pre-mixed with a fluorescent dye that when illuminated with a laser, highlighted

the flow behavior [24]. The main fluid in the set up was water and the fluid parameters (Reynolds

number, momentum flux, blowing ratio, and blockage ratio) of the bulk flow and dye flow were

matched to characterize Hydrogen-Air interactions in a real RDE [24]. A diagram of the

experiment is shown in Figure 20. The corner directly upstream of the dye jet was called the

concave corner and was either rounded or left sharp during experiments [24]. To translate this set-

up to the Micro-RDE, the dye jet would be analogous to the fuel injection, and the main flow

would be analogous to the oxidizer flow [1]. However, it must be noted that in the Micro-RDE

the fuel was injected radially, where in this experiment the fuel/jet flow was injected axially. This

has an impact on the applicability of the blockage ratio used in this experiment compared to the

Micro-RDE.
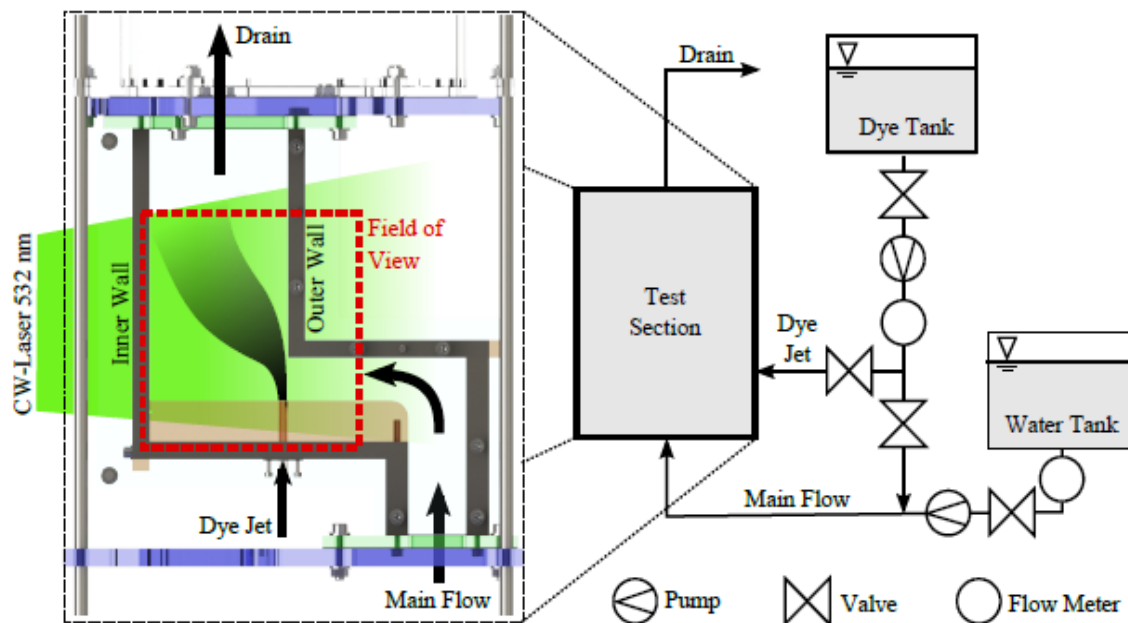
Fig. 20 Bohon et al. Experimental set up [24]

In addition to the standard JIC geometry, where the fuel is injected into the bulk flow inside

the detonation channel, Bohon et al. also moved the dye injection further into the bulk flow to the

right in Figure 20, past the concave corner [24]. This resulted in a "confined" geometry that

injected the jet before the bulk flow entered the detonation channel. This kind of injection modification is similar to one made in the current research.

In their characterization of the flow, Bohon et al. used the momentum flux ratio, blowing ratio (R), and blockage ratio [24]. Blowing Ratio was defined as a reduction of the momentum flux ratio that could be applied because the densities of the fuel and oxidizer were the same [24]. While the blockage ratio helps characterize the obstruction of the cross flow by the jets. Both ratios are defined in Equations 12 and 13. In Equation 12, u_{jet} and u_{bulk} are the velocities of the jet and bulk flow respectively. In Equation 12, l_{jet} is the distance between subsequent jet ports in the RDE channel, d_{jet} is the jet diameter, Δ is the channel gap, and d_c is the RDE diameter. These parameters were matched by Bohon et al. to characterize Hydrogen-Air flow parameters in a nominal RDE chosen for their research [24].

$$R = \sqrt{\frac{u_{jet}^2}{u_{bulk}^2}} \tag{12}$$

$$\frac{\Delta}{d_c} = \frac{l_{jet}}{d_{jet}} \tag{13}$$

As part of the experiment, blowing ratio was varied by increasing the velocity of the jet flow which subsequently changed the flow interaction. The effect of which can be seen for the unconfined case in Figure 21 [24]. In addition to this, Figure 21 also highlights that the mixing zone of the two flows could be characterized by two counter rotating recirculation zones, labeled as Region I and Region II [24]. As the blowing ratio increased the jet trajectory penetrated further into the cross-flow changing which recirculation zone had the most impact on the flow behavior [24].
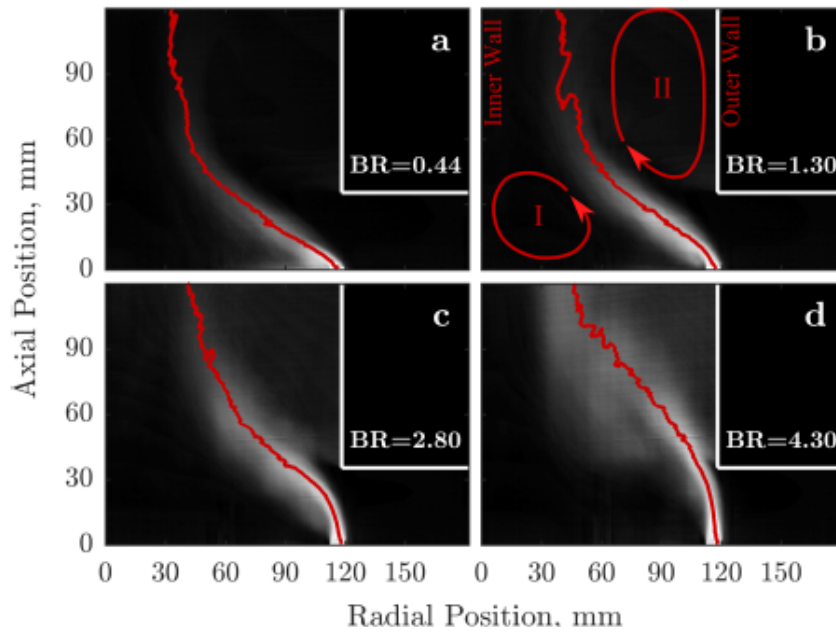
Fig. 21 Mean scalar fields for various R [24]
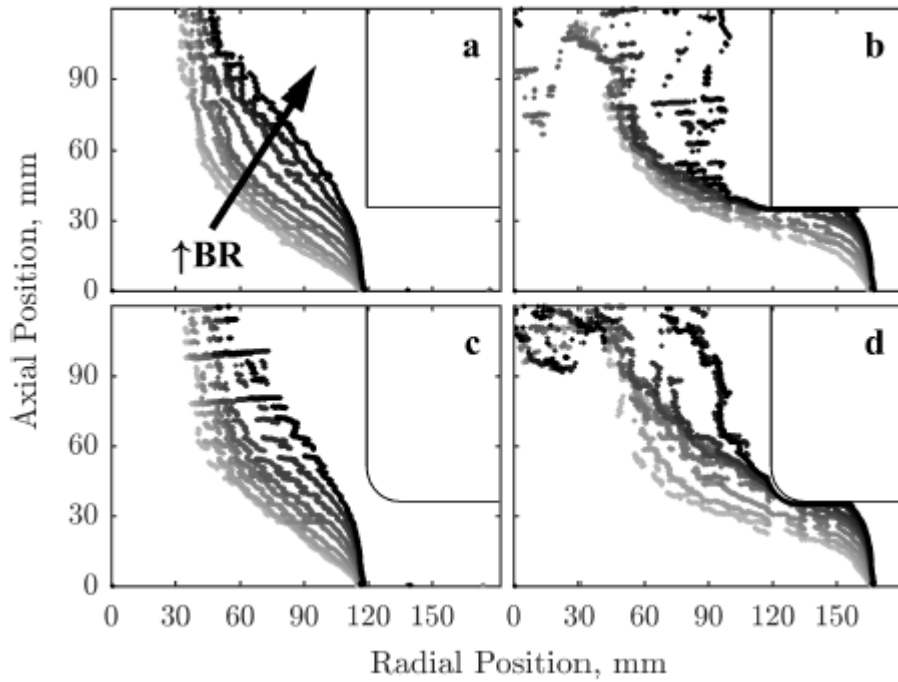
Fig. 22 Trajectories of maximum scalar for a sharp corner with (a) standard and (b) advanced hole positions, and for a rounded corner with (c) standard and (d) advanced hole positions. Darker markers indicate increasing R. [24]

Because the parameters in this experiment were matched for a specific Hydrogen-Air RDE, the specific range of R values defining the flow behavior will change for a different RDE [24]. However, the general trends in between the limits of R should be consistent as the parameters of interest are non-dimensional [24].

A summary of how changing the blowing ratio, confining the jet flow, and rounding the concave corner can impact the flow behavior can be seen in Figure 22 [24]. The impact of moving the jet into the confined condition is in panels 3b and 3d. The most important change in this new configuration was that even low blowing ratios fully penetrated the bulk flow [24]. Furthermore, the main flow feature became the confinement wall. In cases where the jet flow could not reach the confinement wall it simply followed the path of the bulk flow. However, when the blowing ratio was high enough to reach the confinement wall and impinged, the trajectories got entrained into the Region II recirculation zone [24]. Rounding of the concave corner influenced the degree of flow separation which in turn influenced the flow interaction with Region II [24].

Lastly, Figures 23 and 24 show how the mixing percentages of the dye jet into the bulk flow changed with blowing ratio and a rounded/sharp concave corner. In these figures it can be seen that the non-confined case retained its strong jet core and did not move as far into the recirculation regions as the confined case did. Moderate to high blowing ratios appeared to have helped the mixing in-plane for both configurations [24]. However, in the un-confined case very large blowing ratios weakened the recirculation zones and therefore may not be beneficial past a certain value point. Changing to the confined location also changed the main mixing mechanism to the entrainment of fluid by the shear layer [24]. As a result, the sharp corner was able to keep the well mixed flow closer to the floor of the RDE than the rounded corner, suggesting a more favorable environment without a rounded corner. Out of plane mixing increased in the confined case due to the flow impinging on the wall. In order to see this, the blowing ratio had to be high

enough to fully penetrate the cross flow [24]. This observation was particularly significant for the

Micro-RDE's implementation of a confined fuel injection scheme. As was just stated, it was

critical that the injected jet be able to fully impinge on the opposite wall in order to extract the best

mixing behavior. However, the new Micro-RDE injection scheme is confined on all sides which

may limit the benefits of out of plane mixing observed.
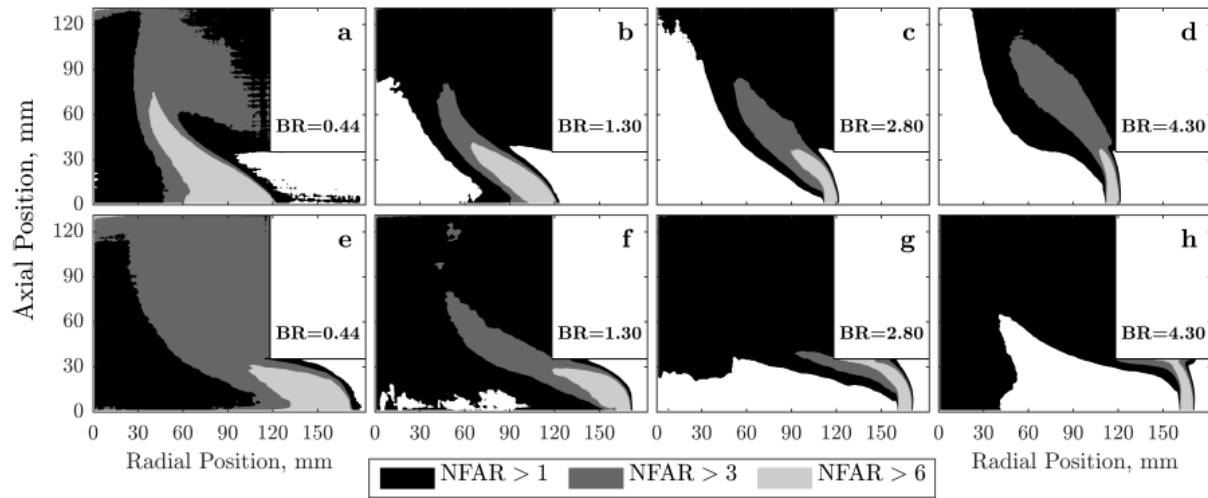
Fig. 23 Normalized Fuel Air Ratios (NFAR) for standard (a-d) and advanced
hole positions (e-h) with increasing blowing ratios for a Sharp Corner [24]
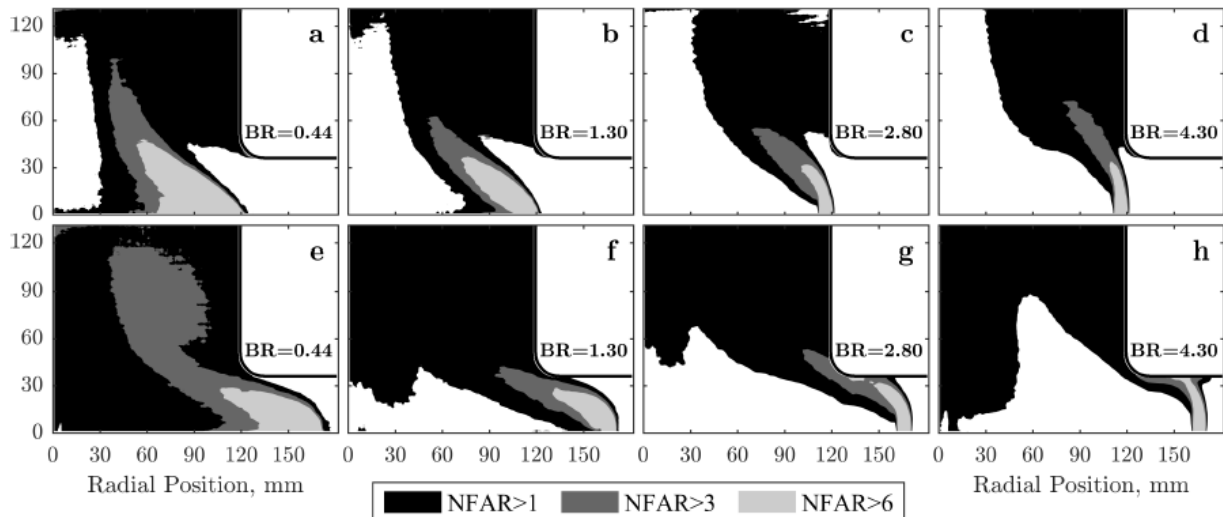
Fig. 24 Normalized Fuel Air Ratios (NFAR) for standard (a-d) and advanced
hole positions (e-h) with increasing blowing ratios for a Rounded Corner [24]

Section 2.5 Detonation Initiation/Ignition in an RDE & Impact of Channel Pressure

A critical aspect of RDE operation is initiation of the detonation, called ignition. A difficult or intermittent ignition may indicate poor operability, however, as was found in the current research, the space of detonable conditions before and after ignition are not always the same. As a result, conditions that may be suitable for detonation may not necessarily be suitable for ignition. Dealing with this non-linear behavior is one of the many challenges associated with RDE design. Regardless, the small channel gaps and fill heights of the Micro-RDE would work against both the detonability during ignition and operation. In an attempt to ameliorate the high potential for instabilities in the initial design, Dechert chose an ethylene (C_2H_4) and nitrous oxide (N_2O) mixture [1]. This mixture had a small cell size, on the order of 1 mm, and a low detonation initiation energy, on the order of 1 J, to help with ignition of the detonation [23]. This low initiation energy allowed the detonation to be started via a spark plug located inside the channel [1]. Dechert's results then indicated that instability was present in part due to the protrusion of the spark plug and the presence of the ¼" access hole into the channel [1].

Therefore, to improve stability, changes to the ignition mechanism were required. One such design is an initiator tube or pre-detonation device which could replace the spark plug. This device sends a small detonation wave into the chamber to start the reaction and does not need to protrude into the chamber like a spark plug does [8]. Other options included optimizing channel pressure and its interactions with injector performance [25].

Section 2.5.1 Channel Pressure Interactions on Wave Propagation and Injectors

One of the major factors impacting the detonability of a given mixture is the channel pressure. In the Micro-RDE, Dechert analyzed how changes in channel pressure impacted detonability by comparing operating maps and pressure data for different exit areas [1]. Figure 25

shows the channel pressure impact on detonability for two exit nozzles with annular gaps (ϵ) of 0.14mm and 0.40mm [1]. The channel pressures plotted corresponded to the pressure before detonation and therefore characterized which environment led to detonation, not the environment that existed during detonation.
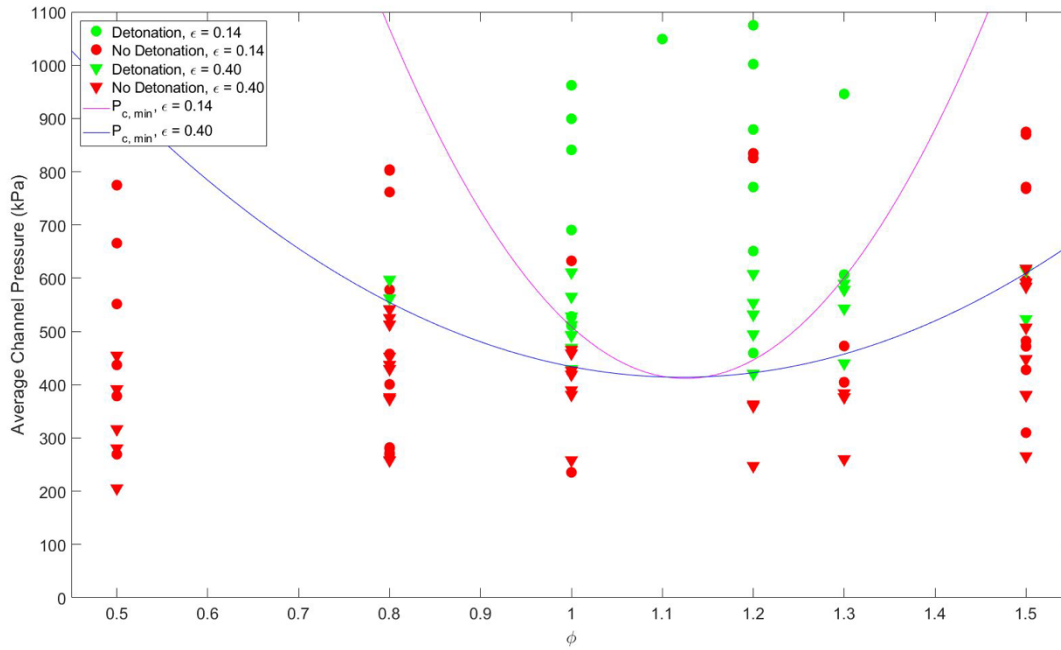
Fig. 25 Channel Pressure influence on detonability for both $\varepsilon = 0.14$mm and $\varepsilon = 0.40$mm nozzles for various equivalence ratios [1]

In Figure 25 the channel pressures where the mixture would detonate had a parabolic shape [1]. This was due to the decrease in the cell size as stoichiometric conditions are approached [23]. Therefore, formation of the detonation wave structure was more probable. As the equivalence ratio moves away from an equivalence ratio of one, the cell size increases, and formation is no longer as probable. However, if the pressure also increases, then the cell size will decrease, and the effects of pressure and equivalence ratio may counteract. This resulted in the parabolic shape in Figure 25 [1].

The influence of the two different nozzles are not as straightforward. The $\varepsilon = 0.14$ mm created a smaller exit area and therefore increased the channel pressure more for a given mass flow

compared to the $\varepsilon = 0.40$ mm nozzle [1]. In the stoichiometric argument above this would imply that the smaller gap nozzle would allow for a larger range of detonable equivalence ratios. However, as shown in Figure 25, the larger gap nozzle allowed for a wider range of detonable equivalence ratios [1]. Dechert explained that this was the result of channel pressure interaction with the injectors. The higher chamber pressures of the 0.14 mm un-choked the injector holes by decreasing the pressure ratio across them [1]. The un-choked injectors then did not recover as well after the passage of the detonation wave and the range of operable equivalence ratios subsequently decreased [1]. This counter-intuitive interaction highlights the importance of balancing the benefits of increased pressure on cell size with injector dynamics and design.

Po-Hsiung et al. also looked into the dynamics of channel pressure on injector performance as well as wave propagation speed [25]. To characterize this interaction, the authors estimated the pressure in the chamber after detonation with Chemical Equilibrium with Applications (CEA) calculations using a deflagration model to achieve a low-end estimate on the pressure after detonation [25]. Experimental results were then compared to these estimations. Both the chamber pressures, estimated and reported, were for during detonation, not before detonation. The results were broken into categories based on if the flow was choked at the injectors, un-choked, or choked at the exit plane [25]. Figure 26 and 27 summarize their results. In the figures, the CEA calculations were lower than experimental values as expected due to the deflagration model [25]. Additionally, a parabolic relationship between exit nozzle area and detonation channel pressure existed. Figure 26 shows that the conditions where the injectors switched from choking to non-choking modes varied with mass flow and equivalence ratio, but always occurred as exit area was decreased and channel pressure increased [25]. In Figure 27 it can be seen that choking at the exit occurred at higher channel pressures than the other two cases suggesting even more severely un-choked injectors under that condition [25].

Furthermore, the parabolic shape suggested that the injectors become un-choked for exit areas equal to and slightly larger than the critical throat area [25]. Therefore, calculations on expected chamber pressures should be performed to ensure an acceptable range of pressure ratios will be encountered by the injectors during operation. In addition to choking at the injectors, the authors also looked at how chamber pressure affected detonation wave speeds [25]. These results are shown in Figure 28. Again, a parabolic relationship was found, implying that the mechanisms for this interaction are like the mechanisms seen previously. Additionally, the highest detonation wave speed occurred at the lower channel pressures [25]. This was likely due to the injectors being choked at lower pressures and thus allowing for better injection recovery and better local mixing of reactants.
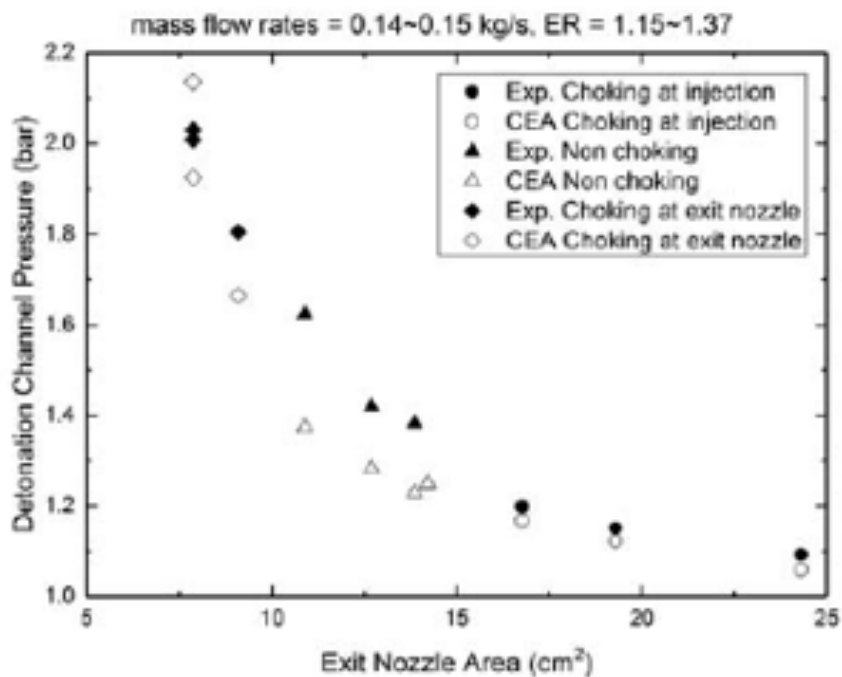
Fig. 26 Comparison of channel pressure for choking and non-choking
conditions at injection plane [25]

(a)

mass flow rate = 0.15kg/s, ER = 0.4

(b)

mass flow rate = 0.15kg/s, ER = 1.17~1.25

(c)

mass flow rate = 0.19kg/s, ER = 0.68~0.82

(d)
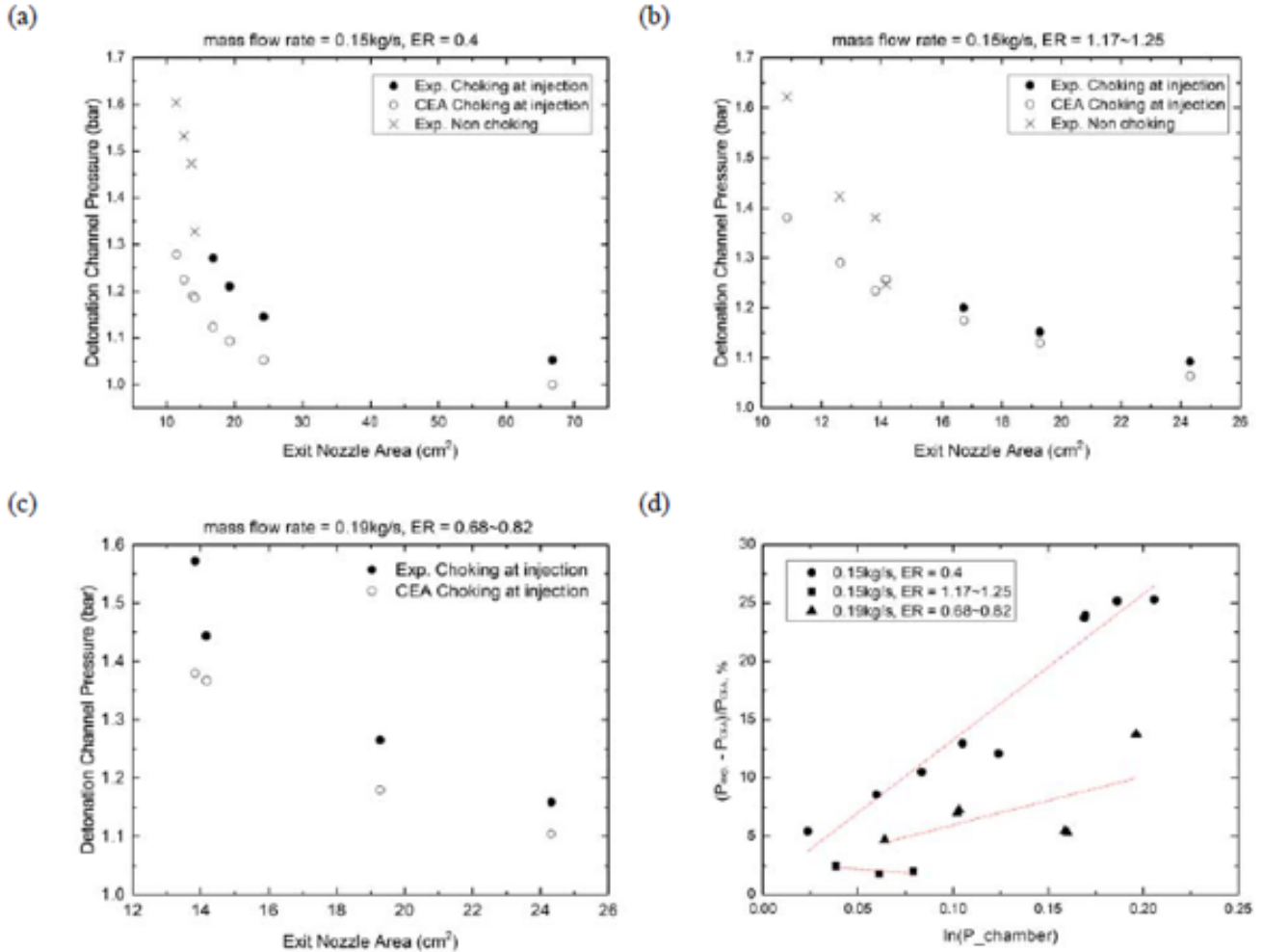
Fig. 27 Comparison of experimental and theoretical channel pressure [25]

Lastly, the authors observed that during high channel pressure operation the wave entered a counter rotating propagation mode and concluded that this behavior was causing the decreased wave speeds [23]. This behavior is also similar to that found by Dechert [1]. The similarities of these results further support the assertion that the injectors were becoming un-choked during operation of the Micro-RDE [1,25].
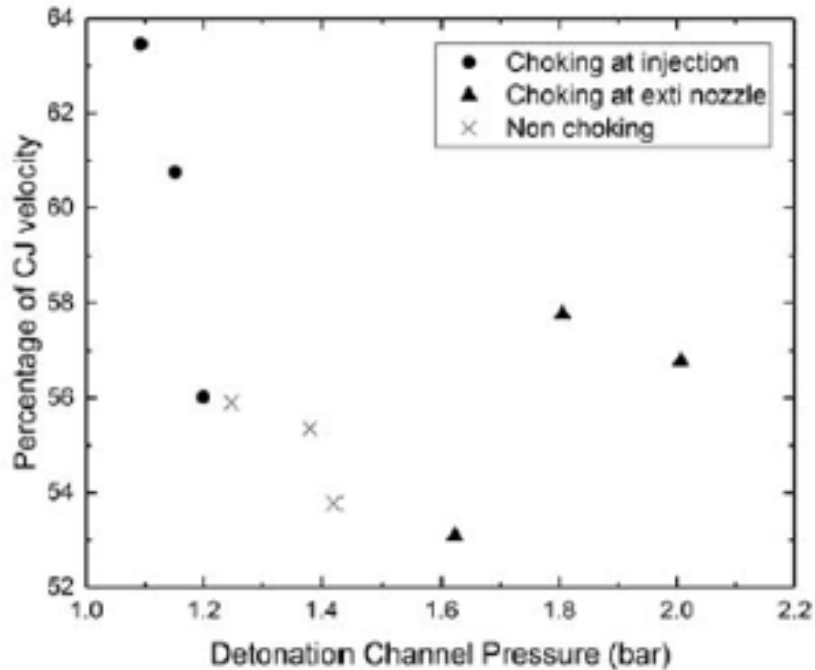
Fig. 28 Impact of channel pressure on wave velocity [25]

Section 2.5.2 Pre-Detonation Devices

As examined by Dechert, the protrusion of the spark plug and hole used to place it into the channel interfered with the propagation of the wave [1]. Although the interference may help transitions to detonation by offering an obstacle on which to establish the reaction, the repeated observations of "clapping" suggested it posed an impediment to single wave operation [1]. An alternative to the spark plug is a pre-detonation device, or "pre-det", which operates by initiating a small detonation outside of the RDE and sending it into the chamber. Figure 29 shows a schematic of a pre-det used by George et al. [27]. The reactants impinge in the mixing junction and are then ignited via spark plug. The ignited mixture then undergoes deflagration to detonation transition in the initiator tube section and is channeled as needed into the RDE chamber at the entry point [27]. Pre-det designs commonly enter the RDE chamber tangentially. However, normal injection is also possible [16,27].
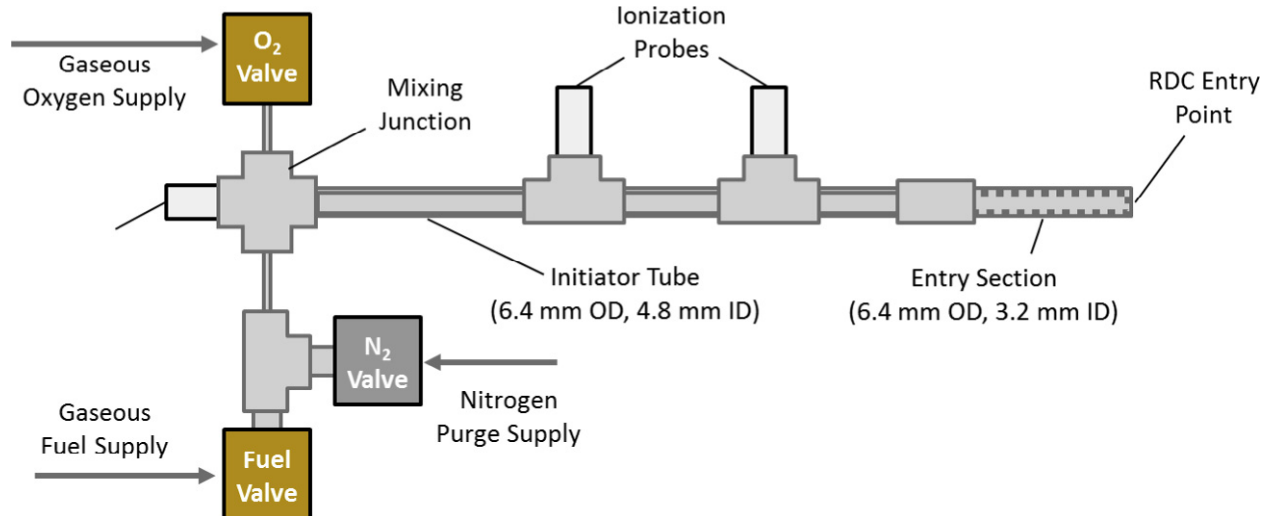
Fig. 29 Schematic of initiator/pre-det assembly [27]

Pre-det devices may use various combinations of reactants, but reactive combinations such as hydrogen and oxygen are commonly used [27]. For successful transmission into the chamber of an RDE, the pre-det wave must diffract into the larger volume while encountering a different mixture composition (in the case of the reactants being used differing from the pre-det to the RDE). George et al. found that when considering this diffraction, critical pre-det tube diameters are on the order of 10 mm for hydrogen and oxygen mixtures [27]. Ultimately this is a function of the cell width of the reactants used, and therefore a function of the pressure and equivalence ratio. For example, stoichiometric hydrogen-oxygen reactants at 1 atm have a cell size of around 2 mm [23]. Therefore a 1/8" tube (~3 mm), such as the one proposed in the current research, is a reasonable size to propagate the detonation through. Importantly, that calculation was done for stoichiometric mixtures of hydrogen and oxygen at 0.1 MPa (1 atm). If the equivalence ratio were to move away from one, the cell size would tend to increase, however the 1.38 MPa injection pressure used in the current research would tend to significantly reduce the sizes well below the 3 mm tube diameter.

George et al. also outlined effects of pre-det mixture and RDE size on the propagation of the initiation wave for hydrogen-oxygen and ethylene-oxygen mixtures [27]. Figure 30 displays that the most energy was deposited via the detonation wave at equivalence ratios near 2.5 for hydrogen-oxygen mixtures. Ethylene-oxygen mixtures did not have an optimum equivalence ratio but had little improvement above ratios of 3.0 [27]. Both reactant combinations deposited around 5-15 J [27]. Given that ethylene-oxygen mixtures need less than 1 J to initiate, higher than stoichiometric equivalence ratios would not be needed for the current research and thus minimum cell sizes can be used [1, 23, 26]. Smaller channel widths increase confinement of the wave upon entering the chamber and subsequently decrease expansion. This in turn preserves the strong post shock conditions behind the wave for longer. However, overall energy deposition was not enhanced by a smaller channel width [27].

Further considerations on channel width and its impacts on the pre-det must be made in the case of the Micro-RDE. For the small geometries used, the hydrogen-oxygen cell size may be larger than the channel width. However, this is unlikely given that the large injection pressures would decrease the cell sizes well below their stoichiometric and 1 atm value discussed earlier. Furthermore, because initiation energies for ethylene and nitrous oxide are an order of magnitude less than what can be deposited and because the pre-detonation shock wave did not enhance detonability, the proposed pre-det's ability to ignite the mixture is not a concern [23,27]. Lastly, Figure 31 shows the impact of channel pressure and width on energy deposition. In hydrogen-oxygen mixtures increased pressure has a neutral and sometimes negative impact on the amount of energy deposited while ethylene-oxygen mixtures increase energy deposition at higher pressures [27].
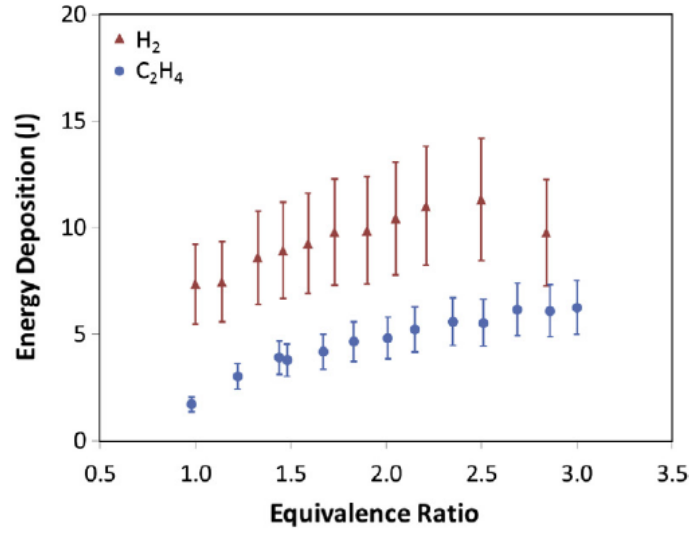
Fig. 30 Energy deposition for a range of equivalence ratios [27]
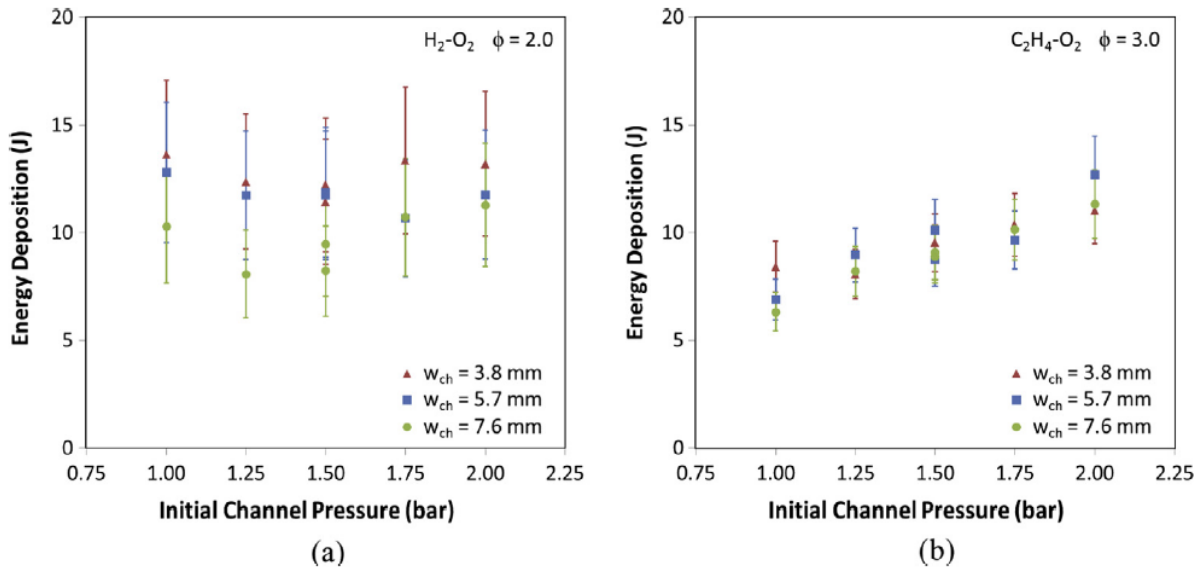
Fig. 31 Estimated energy deposition for (a) Hydrogen-Oxygen and (b) Ethylene-Oxygen mixtures for various channel widths and pressures [27]

III. Methodology

With the background covered, the changes made by the current research to the Micro-RDE and supporting testing apparatus to improve its wave speed and stability can be presented. In Section 3.1 the pertinent design aspects from the previous work are reviewed along with the new modifications made to the injection scheme geometry and the new components required. Erosion and protrusion into the detonation channel when using a spark plug ignition method motivated a switch to using a pre-detonation device. In Section 3.1 the details on the integration of this pre-detonation device to the facility and testing apparatus, along with the subsequent iterations on hardware to mitigate erosion damage, is presented. Flow control of the fuel and oxidizer was required to manipulate the mass flow and equivalence ratio. The devices used, along with their issues, are detailed in Section 3.2. Lastly, instrumentation such as pressure and temperature sensors and the high-speed camera used to observe and document the Micro-RDE are documented in Section 3.3. Throughout each section uncertainty analysis of the techniques used to produce the data in Chapter 4 is presented.

Section 3.1 RDE Design and Changes: Injection, Ignition, and Erosion

The original Micro-RDE design by Dechert is presented in Section 3.1.1 [1]. Dechert concluded that the injection scheme and ignition method were the primary areas of concern when looking to improve wave stability and behavior [1]. Non-ideal local mixing and hardware damage from erosion around the spark plug created a desire for a modified injector geometry and a less intrusive ignition device. Therefore, changes were made to the Jets in Crossflow (JIC) injection scheme and the spark plug was replaced by a pre-detonation device. These topics are in Sections 3.1.2 and 3.1.3 respectively. However, in order to implement these changes, a new fuel and oxidizer manifold was designed along with a new outerbody to accommodate it. Issues with

erosion when using the pre-detonator device required iteration on the new hardware. These changes are covered in Section 3.1.4. Furthermore, Section 3.1.5 discusses how the switch to using a pre-detonator device necessitated additional facility integration to access the required hydrogen and oxygen gas. To operate the pre-detonator, the LabView control program was updated, which is also outlined in Section 3.1.5. Lastly, Section 3.1.6 covers how aerospike nozzles were used to counteract area changes from erosion. This section will also discuss the significant erosion issues of the nozzles.

Section 3.1.1 Previous Micro-RDE Design

The first iteration of the Micro-RDE was built by Dechert from five main parts sized in accordance with the criteria outlined by Bykovskii et al [1, 7]. Referring to left image in Figure 32 and starting from the top of the RDE cross section and moving down, the following parts were designed: a connection plate (red), an oxidizer manifold (orange), a fuel manifold (green), and an outer body (blue) [1, 7]. Table 2, in Chapter 2, summarized the geometric parameters these pieces created when assembled. Gaseous nitrous oxide and ethylene were used as the oxidizer and fuel respectively. The 24 oxidizer injection holes were located inside the oxidizer manifold and opened into the oxidizer plenum inside the connection plate. To reduce pressure losses, the injector hole diameters started at 0.17 mm and then changed to the designed injection diameter of 0.11 mm as they entered the 2 mm wide detonation chamber formed between the fuel manifold and outerbody. In the middle of the RDE, the fuel manifold interfaced with the ½" ethylene supply line and had 24, 0.4 mm diameter fuel injection holes drilled radially into the detonation chamber. Both types of injection holes (0.11mm and 0.4mm) were sized to choke flow across mass flows of 0.025 kg/s to 0. 075 kg/s without back pressuring supply lines above the flow controller limit of 2.2 MPa [1].
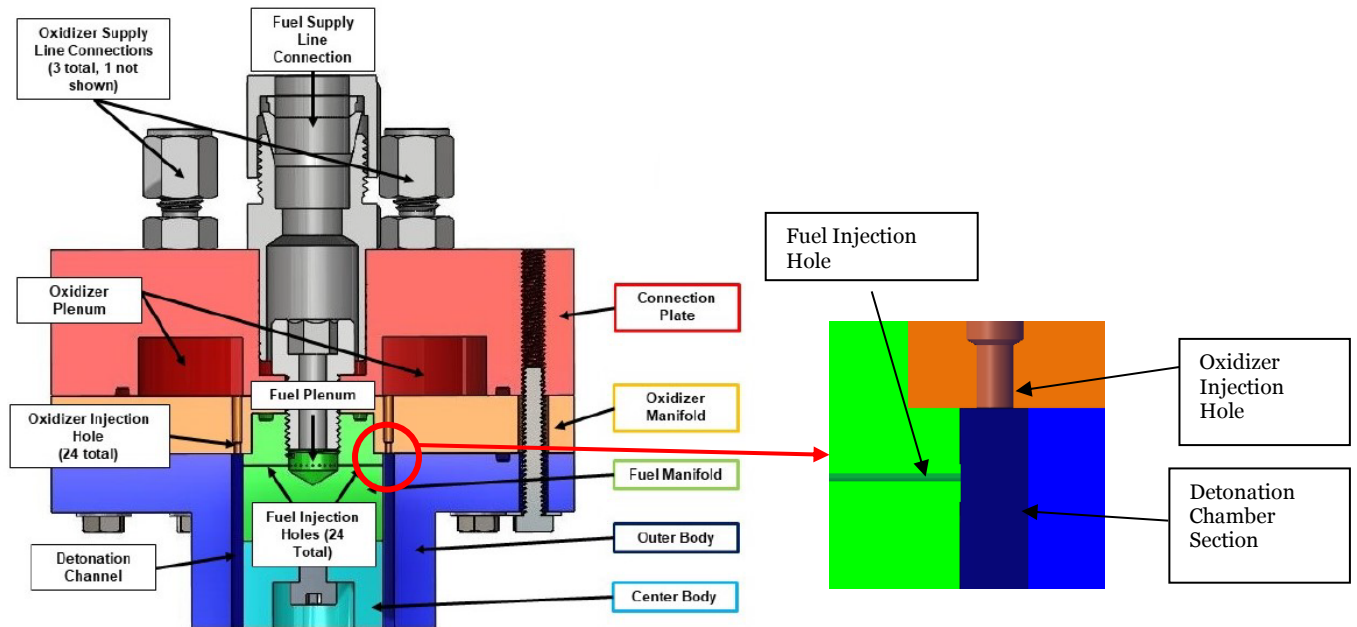
Fig. 32 Cross Section view of old Micro-RDE set up with injection geometry highlighted. Modified from Dechert [1].

Inside the detonation chamber, the oxidizer and fuel flow were injected in a Jets in Crossflow (JIC) scheme at 90 degrees placing the mixing zone of the reactants inside the 2 mm channel. Figure 32 highlights this geometry in the image on the right. During assembly of this configuration, the fuel and oxidizer holes had to be carefully aligned to ensure proper impingement of the jets. Lastly, the centerbody was attached to the fuel manifold. However, the centerbody alone did not back pressure the channel adequately and the RDE was unable to initiate detonation [1]. In response, an aerospike nozzle replaced the centerbody to reach an adequate pre-detonation static pressure [1]. Multiple nozzle diameters were designed and used to vary the exit area and control channel pressure. For further detail on the full build up and design of this iteration of the Micro-RDE, the reader is referred to Dechert [1].

Section 3.1.2 New Injection Scheme Design

With the injection scheme shown in Figure 32, the observed wave frequency was nominally 13 kHz. With a 28 mm channel diameter this corresponded to 1140 m/s or ~50% CJ speed given the estimated CJ velocity of nitrous oxide and ethylene of 2200 m/s [1]. Such a low percentage of CJ velocity meant the detonation was on the verge of an acoustic wave and strongly suggested that the wave was not seeing an ideal mixture locally [1,7]. Poor mixing was likely due to the injector refresh time of ~75 μs (corresponding to the 13 kHz wave frequency observed). Such a short period limited the time available to sufficiently mix the reactants before the wave completed a rotation. Further consider that the mixing process was taking place in the detonation chamber where fresh reactants were free to be diluted with recirculating products, it was not surprising the mixing quality was suboptimal. Therefore, to improve the detonation wave's stability and increase the resultant wave frequency, the mixing/injection of the reactants was modified.

The modification to the injection scheme moved the point of fuel injection from inside the detonation channel to inside each individual oxidizer hole. Figure 33 illustrates this. In the new injection geometry, each of the 24 fuel injection holes were placed within their respective oxidizer injector about 1 mm from the entrance to the detonation channel. As can be seen in the cross section, the angle of cross flow was maintained at 90 degrees. In this manner, the mixing zone for each injector started within the oxidizer injection holes which allowed partial pre-mixing prior to entering the channel. Additionally, the relocation created a confined space in which the reactants initially mixed. As discussed in Chapter 2, this confinement had the potential to positively improve the mixing quality of the reactants due to increased flow turbulence from impingement on the opposing surface [23]. A deeper recession of the point of cross flow into the oxidizer injector would create a larger pre-mixed volume and therefore have an increased risk of flame holding at the injectors. Testing did not show such issues at the current location and therefore a deeper

recession remains an option.

To accommodate the point of cross flow's re-location, the original fuel and oxidizer manifolds were re-designed into a single part and the RDE's outerbody was modified to fit around this new part. Combination of the manifolds allowed the small, 0.4mm injection hole diameter to be machined while still maintaining an ability to interface with the previous design's connection plate. However, the new interface between the manifold and outerbody required two new O-rings to seal off fuel and oxidizer from the oxidizer plenum. The O-ring cut locations are also visible on the cross-section view shown in Figure 33. Additionally, because the fuel holes were now drilled through each individual oxidizer hole, the issue of potential misalignment of the fuel and oxidizer holes during assembly of the RDE was eliminated [1].

Figure 33 also has a photo of the Micro-RDE with the outerbody removed to further demonstrate the new configuration. As can be seen, there are two types of injector holes highlighted. Facing in the axial direction are the main injectors, which open into the detonation channel and flowed the fuel and oxidizer pre-mixture. Second are the radial fuel injector holes. These particular holes, visible in the figure, are a result of the machining process and were not intended to feed any reactants to the RDE. Referring to the cross section in Figure 33, any flow from these holes were sealed off by the O-rings once placed inside the outerbody. The combination of partial pre-mixture, confinement, and perfect alignment offered by the new design was believed to improve the local mixing quality and also reduce the mixing height. Which in turn would improve the waves ability to operate stably and closer to the designed 80% CJ velocity.

Connection Plate

Fuel Injection Hole

Oxidizer Injection Hole

Outer Body

Relocated fuel injection holes 24 total

Combined Fuel and Oxidizer Manifold

Aero-Spike Nozzle

Detonation Chamber Section

Main Injectors flowing fuel/oxidizer pre-mixture into chamber

Aero-Spike Nozzle

Oxidizer Plenum formed in Connection Plate

New Combined Fuel/Oxidizer Manifold

Fuel Injector Drill Holes. Sealed by two O-Rings in outerbody (not pictured).

Fig. 33 Cross section view highlighting relocated fuel injection holes (top) and outerbody-less picture of combined fuel and oxidizer manifold installed on connection plate.

Section 3.1.3 Spark Plug Ignition Method and Erosion with new Injection Scheme

Initial testing of the modified injection scheme utilized the same NGK 5869 ER9EH spark plug as Dechert [1]. Use of the spark plug method required a ¼" threaded hole which opened directly into the detonation chamber. This hole was centered approximately 21mm above the injection holes in the previous RDE design, and this location relative to the injectors was kept consistent on the new outerbody. Figure 34 shows the new RDE outerbody with the spark plug seated into place along with a cross section view showing the location relative to the injectors. The spark plug was fired by a 5ms, 5V signal to a 40kV ignitor coil. The 5ms signal was initiated manually by an operator in the facility control room which allowed multiple ignition attempts for a given test run. This differed from previous testing by Dechert where the spark plug was fired electronically by the control software [1]. This updated program is discussed in Section 3.1.5.
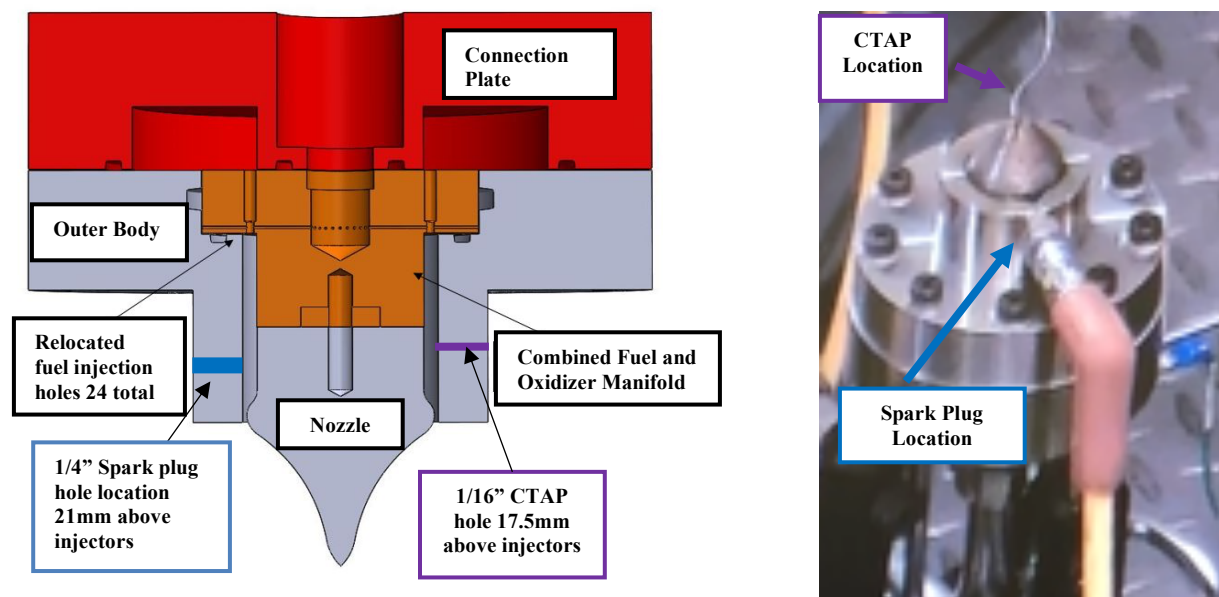
Fig. 34 Cross section view of new Micro-RDE set up highlighting the location of the ¼" spark plug and 1/16" CTAP holes (Left). Image showing how spark plug seated into outerbody (Right).

The 1/16" CTAP hole was located 160 degrees counter clockwise from the spark plug hole and was kept at approximately 17.5mm above the injectors to remain consistent with its previous

location in the old design. The CTAP tube was secured into its insertion hole via JB Weld. Options such as hot welding and brazing were not feasible due to the 1/16" diameter tube quickly melting before the outerbody could heat up sufficiently. Multiple detonation tests were possible on the cold weld solution, but it did require occasional re-application to re-seal the tube. It was found that like the spark plug, if run times were kept short (below one second), the JB Weld was more likely to survive a detonation event without issue.

Putting the spark plug inside the chamber was found to be a necessary step to achieving detonation in the original RDE, and as such was initially continued for this research [1]. Unfortunately, doing so resulted in prominent protrusion of the spark plug into the chamber. It was not uncommon for a spark plug to experience significant damage after a single detonation, causing a need for frequent spark plug replacement [1]. A damaged spark plug is shown in Figure 35 next to a new spark plug highlighting the extent of damage.
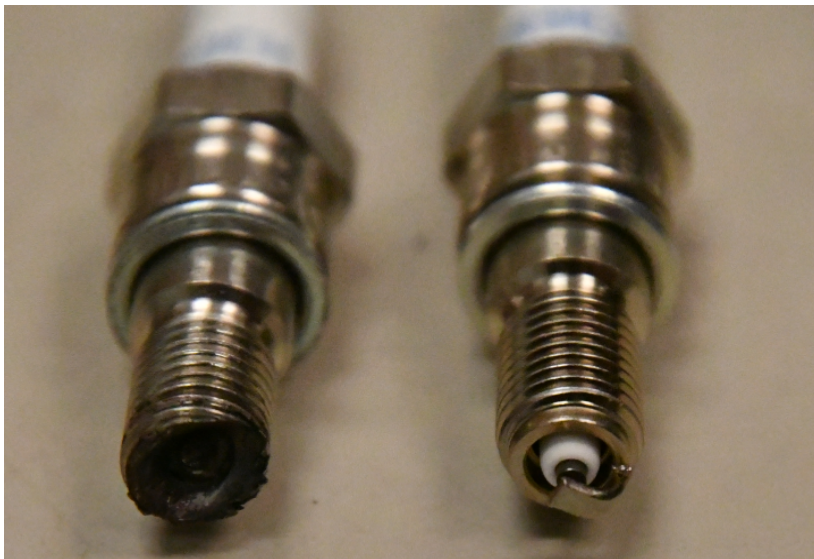
Fig. 35 Erosion/damage of spark plug after detonation. Eroded spark plug
(left) new spark plug (right).

Initially, it was believed the main concern of this protrusion was interference with the wave's propagation path around the detonation chamber. However, after a limited testing campaign on the new hardware (combined fuel and oxidizer manifold injection scheme and new

outerbody) the spark plug was found to consistently erode the outerbody and nozzle near the ¼"

entry hole as seen in Figure 36. Erosion was observed to be the result of the spark plug protrusion

becoming heated by the exhaust gases to the point that it would begin to burn. High speed imagery

showed that this burning could begin as early as 0.1s into a detonation event. Compounding the

issue, the mass flow controllers needed a test duration on the order of a few seconds to properly

recover, discussed in detail in Section 3.2. Therefore, it became a compromise between flow

recovery and erosion damage to use test durations between 0.3 and 1.0 seconds. However, even at

these run times, there was still a potential for erosion damage depending on how earlier into the

run the spark plug began to burn, as the burning would create significantly more heat transfer.

Figure 36 shows an example of a major erosion event after a 2.44 second detonation. In

this case the spark plug ended up melting itself to the outerbody after completely melting away the

section of outerbody above it. This was the longest test duration run, and as such was an extreme

result. Run times less than a second saw significantly less erosion. Figure 37 shows an outerbody

with mild erosion after a series of runs with durations between 0.3-1.0 seconds. As can be seen,

even the mild erosion events from shorter runs were enough to significantly alter the detonation

chamber area, ultimately impacting the RDE operation in a manner difficult to accurately quantify.

Interestingly, the CTAP hole showed only a limited amount of erosion damage as noted in Figure

41.
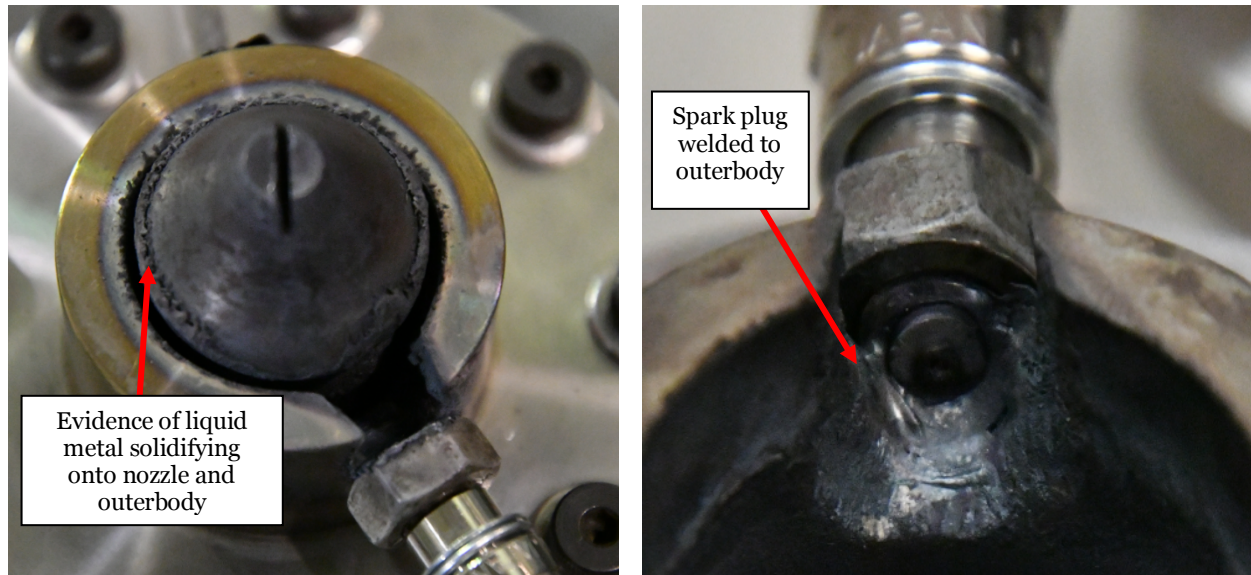
Fig. 36 Outerbody erosion damage after 2.44s run. Evidence of liquid metal solidifying on exit edge and nozzle throat (Left). Spark plug welded to outerbody (Right).

The nozzle in Figure 36 shows evidence of solidified metal via the presence of rough deposits around the throat. Additional deposits around the exit of the outerbody were also indications that there was liquid metal present. Figure 37 also shows the same deposits and erosion in the milder case but only in the vicinity of the spark plug hole. The lack of extreme erosion on other sections of the outerbody away from spark plug hole in Figure 37 meant the heating required to erode and melt the steel was occurring mainly at the spark plug. As a result, starting at the spark plug, a chain of events would occur, where a growing region of the outerbody wall became liquefied as the spark plug burned. In turn, the heat that was being taken in by the metal to liquid phase change was allowed to be used to increase the liquid metal's temperature. At the higher temperatures the liquid metal could more easily melt the neighboring material increasing the rate at which the melted area grew as the run continued.

This sequence of events was consistent with the high-speed video where the spark plug's hot spot could be seen to continuously grow larger and brighter throughout a run. Significantly, this meant that it was the burning spark plug and subsequent liquid metal that lead to the

catastrophic damage observed, not the detonation wave. This was further supported by the survivability of the hardware when run times were kept just short enough that the burning spark plug did not have enough time to melt the outerbody material around it. Therefore, it was decided that if the spark plug was removed, then the metal may last longer before melting (if at all) and the run times without catastrophic hardware damage might be extended. This led to an early switch away from the spark plug to the pre-detonator.
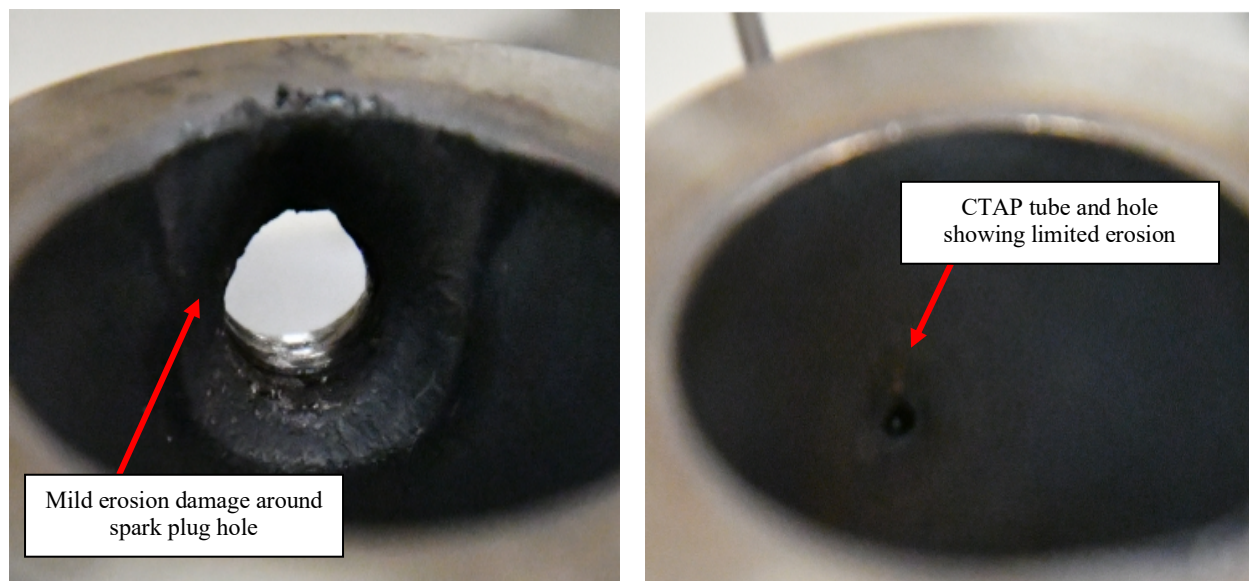
Fig. 37 Mild erosion around ¼" spark plug insertion hole centered 21 mm above injectors (left) and 1/16" CTAP entry hole 17.5 mm above injectors (right).

Section 3.1.4 Pre-Detonator Ignition Method

As discussed in Section 2.5.2 a pre-detonator, or "pre-det", is a device which creates its own native detonation that can then be used as a means to initiate detonation in the RDE channel. The pre-detonator offered an alternative to the spark plug with the main advantage of a smaller access hole and a flush entry into the channel. Figure 38 shows the pre-detonator device and its injectors, spark plug and connector, and 1/8" detonation tube. For the current research, a small volume of hydrogen and oxygen mixture at a designed equivalence ratio of two was used. Both

gases were injected at 1.38 MPa (200 psi) and ignited by a small native spark plug. Since each line

was injected at 1.38 MPa, the injectors were specifically sized for either hydrogen or oxygen.
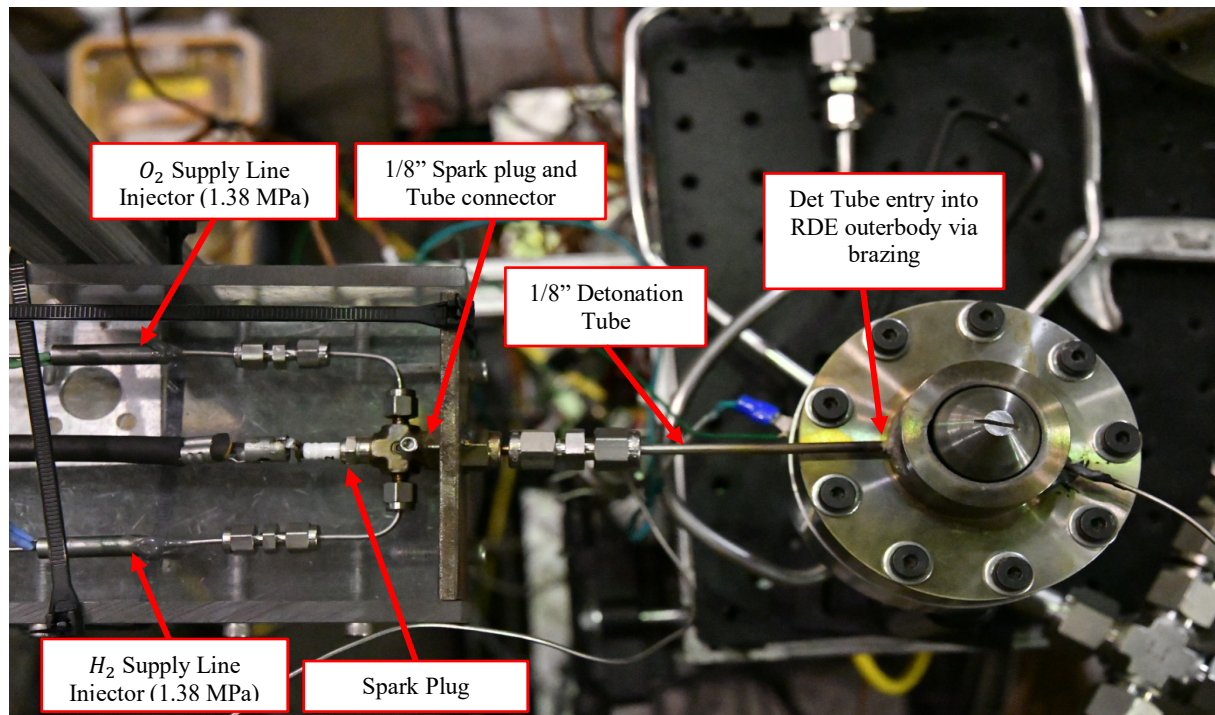
Fig. 38 Pre Detonator Device using $\Phi = 2$ H_2 and O_2 mixture integrated into Micro RDE outerbody via 1/8" detonation tube.

The pre-det was designed by Innovative Scientific Solutions Inc and had been previously

used with 1/4" diameter detonation tubes successfully [8]. The use of 1/8" was done to minimize

the hole drilled into the channel wall and its subsequent recirculation volume. The tube was

inserted into the RDE through a ~1/8" hole drilled through the outerbody centered at an axial

distance 21 mm above the injectors. This height was chosen to be consistent with the spark plug

and was depicted in Figure 34. Where the spark plug hole could be threaded to allow the plug to

be screwed into place, the pre-detonator tube needed to be brazed into place. Hot welding was too

difficult because the unequal heating rates of the 1/8" tube versus the solid, 7.1 mm thick

outerbody. Regardless, it was found that brazing the tube into the outerbody was more than

sufficient to securely hold it in place, even during detonation events. The CTAP location and cold

weld securing method was also kept consistent between the pre-det and spark plug outerbodies.

After successful detonation with the pre-det device it was found that the 1/8" hole still created noticeable flame holding/recirculation and subsequent erosion/melting of the tube and neighboring channel wall. However, the 1/16" CTAP hole did not experience the same erosion damage. Therefore, the pre-det entry hole was drilled to have a diameter of ~1/8" partway into the outerbody that then became 1/16", as seen in Figure 39. It was intended that the 1/16" entry would limit the recirculation volume that was accumulating in the 1/8" hole while still maintaining an ability to propagate the hydrogen-oxygen detonation. However, to prevent quenching and other potential propagation issues at this smaller diameter, the 1/8" hole was maintained 6.1 mm into the 7.1 mm thick outerbody wall, leaving only 1 mm left to be traveled at a 1/16" diameter. The pre-det hole was maintained at 21mm above the injectors. Subsequent testing showed that at this diameter (1/16"), the pre-det could still propagate a detonation into the channel without observed issues and the ignition capabilities of the pre-detonation device were not appreciably impacted. However, the hole still had a tendency to erode during tests. In fact, the erosion appeared to be forcing the 1/16" hole back to a 1/8" hole after one to two runs, limiting the benefits of the modification.

Consistent survivability of the CTAP hole, which was 1/16" all the way through, suggested that hole size was small enough to avoid recirculating enough product gases to cause erosion. Therefore, the erosion on the pre-det hole was likely from the 1/8" tube accumulating enough hot product gases to quickly heat both the tube and the thin amount of metal between the tube and the chamber to the melting point. Two ideas were used to address this. First, the 1/8" tube was recessed further into the outerbody wall, to about half the wall thickness or 3.5mm. This allowed the 1/16" portion to be thicker and further isolated the 1/8" tube from the hot product gases in the chamber.
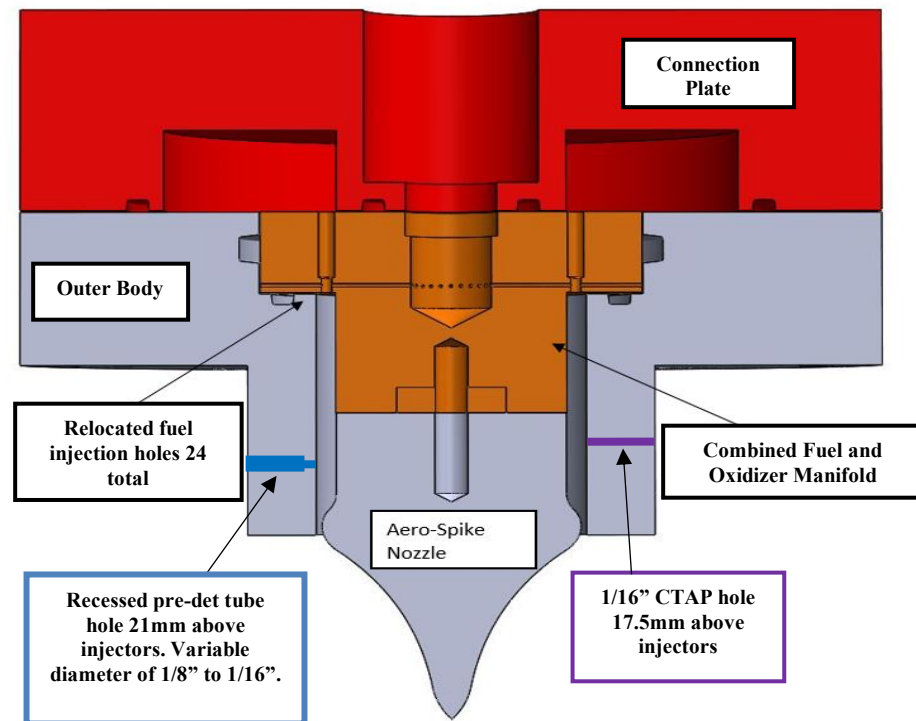
Fig. 39 Cross section highlighting variable hole diameters of the pre-det tube of 1/8" to 1/16" at 21mm above injectors and CTAP location 17.5mm above injectors.

The other idea came from recognizing that in the fill height of the detonation wave there was periodic cooling from the unburnt reactants and the expansion process behind the detonation. Above the fill height, the walls of the detonation chamber would only see product gasses, which while cooler than the detonation itself were still hotter than the reactants. If the pre-det hole could be lowered into where the reactants were, then the amount of heating it saw may be reduced. Mixing lengths and exact fill heights inside the chamber were uncertain, so it could not be said exactly where the wave ran, however; fill height had been previously estimated to be between 3.2-8.1mm. Existing burn patterns also suggested a 2-4mm mixing zone that needed to be added to the estimated fill height. This gave a conservative estimate on where to expect fresh reactants of ~12mm. The lowering and further recession of the pre-det hole is shown in Figure 40 along with the max estimated fill height location assuming a negligible mixing length. Unfortunately, the exact distance of 12mm above the injectors could not be made due to the drill bit anchor not fitting

past the wide portion of the outerbody during drilling. Therefore, to expedite testing, a location of 15mm was used instead to allow easy access of the drill bit at the cost of being beyond the unburnt reactants. Later, an outerbody was made with the hole drilled through the thicker portion of the outerbody to get inside the estimated fill height and is discussed later in this section.
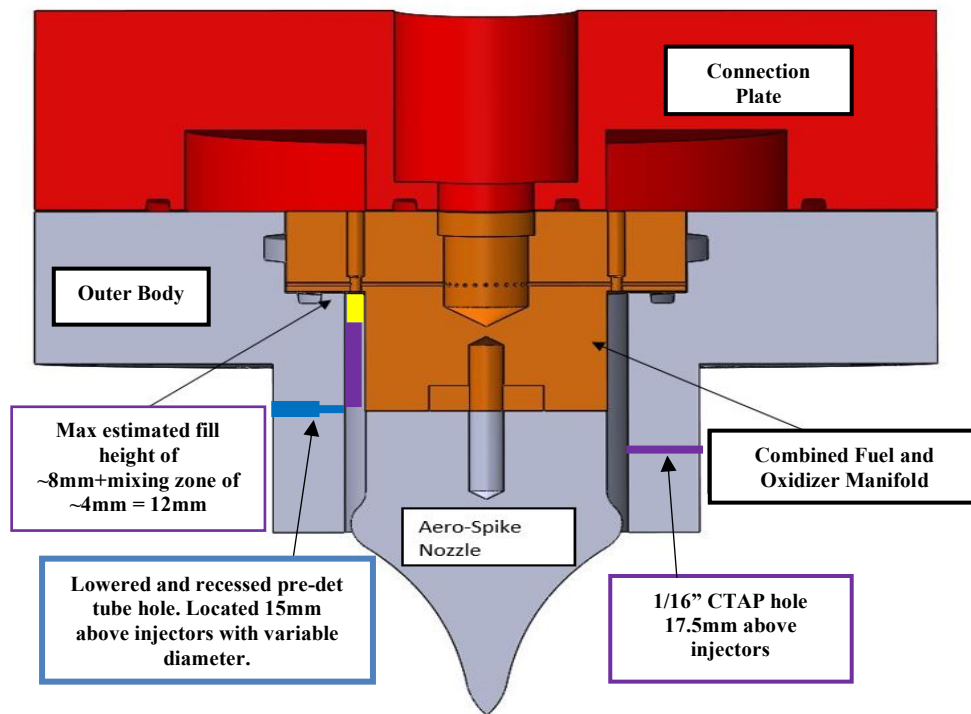
Fig. 40 New lowered and recessed position of pre-det hole with variable diameter now located 15mm above injectors with 1/8" to 1/16" diameter change at 3.5 mm into the outer wall.

Figure 41 shows a picture of an outerbody with the modifications of Figure 40 after a series of detonations. The outerbody pictured also has two pre-det holes, one at the old 21mm location and the second at the new 15mm location. Both holes changed diameter from 1/8" to 1/16" at a radial distance of 3.5mm into the outerbody wall. For the particular outerbody in Figure 41, the upper hole was never used and was plugged on the outside to prevent pressure loss. It was found that the lower hole eroded back to a ~1/8" diameter after use. This was the same behavior as had been seen when the hole was located 21mm above the injectors and suggested that the lower location was still susceptible to erosion. As a result, it was assumed the hole needed to be lowered

further to benefit from unburnt reactant cooling. Additionally, the unused upper hole had less erosion than the one below it. This observation reinforced that erosion was intensified by the presence of the pre-det tube. Lastly, although the outerbody in Figure 41 experienced erosion around the pre-det hole and exit plane, the severity was comparatively less than previous versions and when runs were kept at or below one second, there was little additional damage. As a result, this outerbody was able to be used repeatedly without replacement. A large portion of data collected for the pre-det ignition method was done using the outerbody configuration shown in Figures 40 and 41.
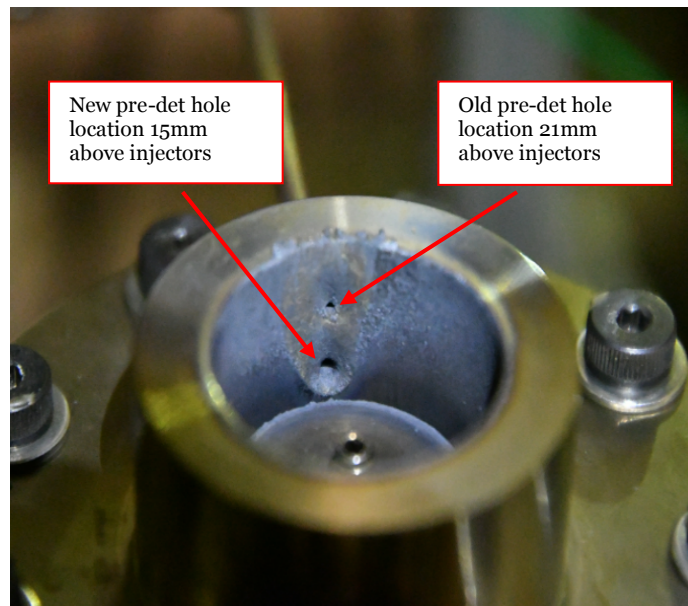
Fig. 41 Steel outerbody with pre-det hole recessed and lowered in channel.
Old hole location (21mm from injection holes) shown on top with new hole
location 6mm below (15mm from injection hole).

To further reduce erosion, new outerbodies were 3D printed by the University of Dayton Research Institute (UDRI) out of Inconel 625. While the primary source of erosion was from the recirculating hot spots melting the metal, another possibility was that the high temperatures at these locations were heating the steel such that its tensile strength could no longer withstand the detonative static pressures of 1.15-1.38 MPa. This would cause local failure points anywhere there

were significant hot spots, potentially explaining the observed damage. Under this assumption, prevention of erosion could be accomplished by keeping the outerbody wall material at a tensile strength that was strong enough for the detonation chamber pressures and temperatures. Therefore, it was beneficial to evoke the improved tensile strength of Inconel 625 at elevated temperatures over the 304 Stainless Steel, despite the higher melting point of 304 stainless steel (1725 K compared to Inconel 625's melting point of 1625 K). For example, nominal tensile strength for 304 Stainless Steel at 1170 K is 75 MPa. Whereas, Inconel 625 maintains a tensile strength of 280 MPa at 1170 K [30, 31]. Although it is uncertain exactly what temperature the channel walls were heated to, these values indicate the potential for a four-fold increase in tensile strength by moving to Inconel at an assumed wall temperature of 1170 K.

Figure 42 shows the Inconel outerbody pre-det and CTAP holes after a 1.3 second detonation. The Inconel outerbody only used the recessed pre-det tube modification and the pre-det hole was at the original position 21 mm above the injectors. Like the stainless versions of the outerbody the lower half of the detonation channel exhibited limited to no erosion, indicating lower heat transfer likely from the cooling from unburnt reactants. At a higher axial station, approximately 15mm above the injectors and higher, there was evidence of erosion on the outerbody as seen in the figure. However, it was noticed that the depth of erosion around the pre-det hole was noticeably less than on the stainless-steel versions. Further, it seemed that most of the erosion "damage" was in fact material that had melted off the nozzle and re-solidified onto the outerbody's wall, and the Inconel material underneath appeared mostly undamaged. This was supported by the extensive erosion of the nozzle. Despite the improved survivability, this specific run resulted in the pre-det hole becoming eroded shut. As a result, the outerbody was unusable without re-drilling another hole. This result was novel and only occurred once. These observations suggested that the increased strength of the Inconel was helping to limit erosion. However, the re-

71

solidified material showed that liquid metal, likely from the nozzle, was responsible for the blocked pre-det tube. Therefore, melting metal was still an important factor and likely constituted the primary design concern.
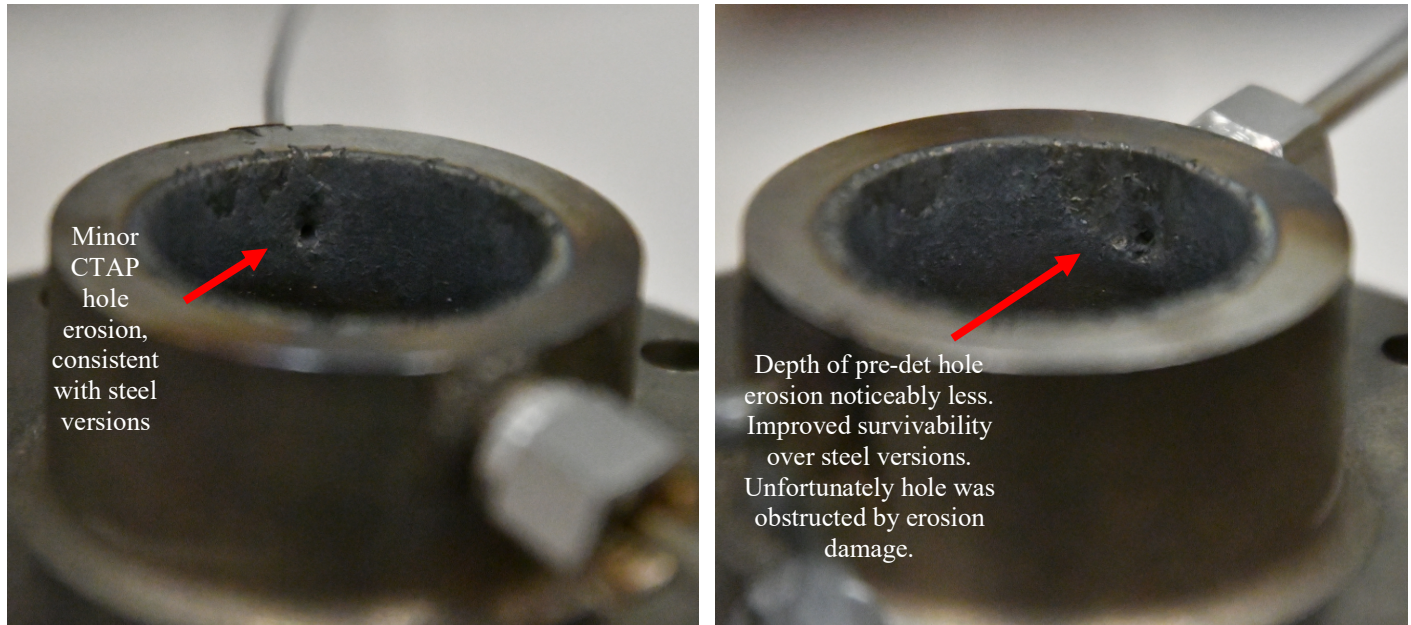
Fig. 42: Inconel Outerbody with pre-det hole and CTAP 21mm above injection holes after 1.3 second detonation.

The pre-det location 15 mm above the injectors was still above (axially) the cool, unburnt reactants. In response, a lower location was drilled at 5.5 mm above the injectors in a second Inconel outerbody made by UDRI. This location was well inside the estimated 12 mm mixing and fill height zone and would benefit from the Inconel construction. This configuration is shown in Figure 43. To reiterate, the intention of the lower hole location was to use the cooling from the unburnt reactants to reduce the wall temperatures near the inevitable hotspot created by the pre-det hole. The same diameter changes from 1/8" to 1/16" were used. The length for the 1/16" section was kept at 3.5 mm to ensure the same chance of properly propagating the detonation into the channel. The CTAP hole location was placed 17.5mm above the injectors to match older versions. Testing with the new outerbody suggested the new pre-det location did not negatively impact the

device's ability to ignite the RDE.
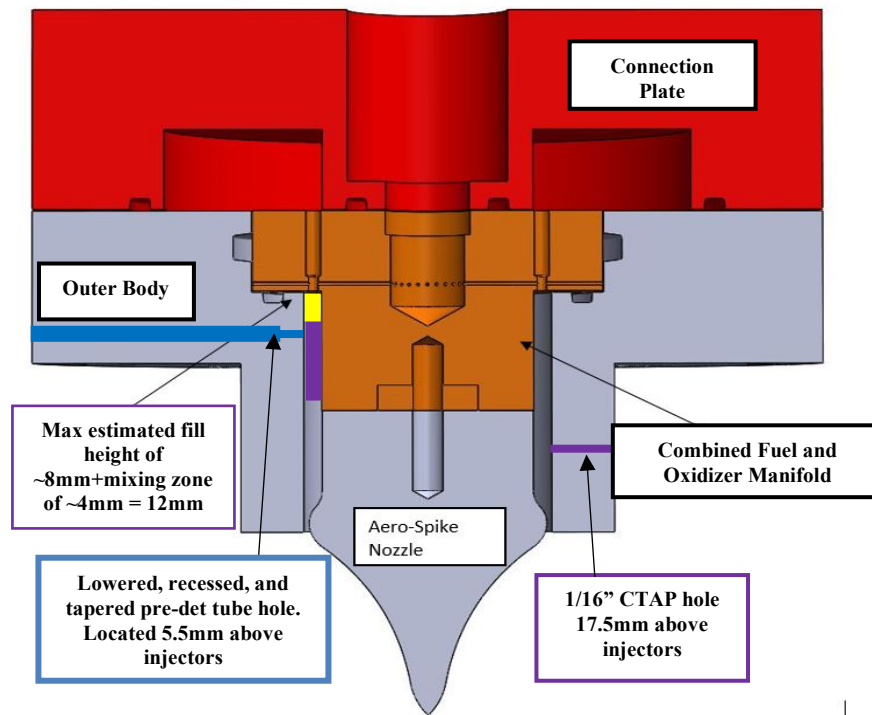
Fig. 43 New lowered and recessed position of pre-det hole with variable diameter now located 5.5mm above injectors with 1/8" to 1/16" diameter change at 3.5 mm into the outer wall.

Three initial detonations were achieved on this outerbody configuration with durations of 0.7, 0.9, and 1.0 seconds. The outerbody's condition after these three runs is shown in Figure 44. As apparent in the figure, this new pre-det hole location had survived significantly better than other versions. It should be noted that the longest run, at 1.0 seconds, was shorter than the 1.3 second run previously discussed with the higher hole location. As a result, the lack of damage may be a function of the shorter run times. Regardless, the pre-det hole and neighboring wall's lack of erosion suggested there was improvement.

Limited erosion damage was also observed at nozzle's throat axial location. Erosion in this region also appeared to cause some damage to the CTAP hole, however this damage was not any more or less than already seen on previous versions. High speed imagery of the runs showed that

when erosion did occur it was not catalyzed by a local hotspot near the pre-det hole or CTAP hole as was the case in previous versions. Instead, any erosion was the result of the nozzle, which is discussed in depth in Section 3.1.6. Further, the outerbody's Inconel construction showed the same improved resistance to erosion near the nozzle that was discussed earlier and shown in Figure 42. Which supported the claim that the Inconel's improved tensile strength was benefiting the RDE. The marked improvement of the pre-det hole's condition at 5.5mm suggested that issues with erosion were now isolated to the survivability of the nozzles.

Fig. 44 A) CTAP and B) Pre-Det Hole after three detonations of duration 0.7, 0.9, 1.0 seconds. Pre-Det hole located 5.5mm above injectors.

Section 3.1.5 Facility Integration and Control of the Pre-Detonation Device

To operate the pre-detonation device in Figure 38, it had to be properly integrated both to the testing facility and the RDE. First, it had to be shown that the detonation generated by the device could be successfully propagated into the channel. Hydrogen and oxygen have been shown to have cell sizes on the order of 2 mm at 1 atm and $\Phi = 1$ [22]. However, ISSI had configured the pre-det to operate fuel rich with an $\Phi = 2$, which would increase the cell size from 2 mm. However,

the higher operating pressure of 0.4-1.4 MPa worked to decrease the cell size [22]. Therefore, it was initially unclear if the detonation would successfully propagate through the smaller, 1/8" diameter tube. Furthermore, the device originally had a ¼" connector attached to the spark plug which was usually mated to a ¼" tube. Therefore, a step-down connection was added so that the ¼" detonation tube could attach to the 1/8" tube entering the RDE. When this was tested it was found that the detonation was quenching inside the ¼" to 1/8" step down. Therefore, a new connector was made to interface directly the spark plug and 1/8" detonation tube. This version of the pre-det is the one shown in Figure 38 and was able to propagate a detonation successfully, and repeatedly into the RDE.

Next, the two injectors had to be opened and closed and the spark had to be fired remotely via a LabView program managed from the facility control room. As mentioned previously, both injectors were supplied by 1.38 MPa of pressure, and each was sized so that if they were simultaneously opened and closed the resultant mixture would be at an equivalence ratio of two. Therefore, the injectors had to be sent the same open and close signal, followed by a signal to the spark plug. Firing of the spark plug while the injectors were still open would increase the risk of damage to the mechanical actuators inside, and therefore was avoided. To open and close the injectors, a new 5V trigger signal was wired into the National Instrument data acquisition (DAQ) controller and sent out to close a 12V power supply circuit. The power supply circuit was connected to the injectors and would provide the power needed to actuate them to open as long as the circuit was closed. Once the 5V signal was stopped, the 12V power supply circuit would open and the injectors would shut off.

The pre-det's spark plug was fired in much the same was the previous spark plug set up. As a result, the already available 40kV ignition coil was simply connected to the pre-det's spark plug. The connector between the pre-det spark plug and the 40kV coil had a higher resistance than

the connector used for the NGK 5869 ER9EH spark plug to account for the smaller required current. The same 5ms, 5V signal used to trigger the coil in the old spark plug set up could then be used directly when operating the pre-det.

Figure 45 shows a schematic detailing a general sequence of control signals sent out from the control room LabView program during a typical test run using the pre det device. The signal sequence used to operate the pre-det also included two 5V signals sent out to the nitrous oxide and ethylene solenoid valves. These signals would actuate the last chance valves and allow the fuel and oxidizer to flow into the RDE as detailed by Dechert [1]. From the diagram, the oxidizer valve would open first, followed 200ms later by the fuel valve. These two valves would then stay open for a set amount of time measured from when the oxidizer signal was sent. After this time both 5V signals would stop and the valves would close. Total fuel and oxidizer flow times varied as needed but were kept longer than 1500ms to allow adequate time to manually fire the pre-det and run a detonation. Anytime between when both valves were opened to when they were both closed, the pre-det's firing sequence could be initiated.

The 100ms sequence for the pre-det included sending the 5V signal to the 12V of power circuit to actuate the pre-det injectors open for a set amount of time allowing oxygen and hydrogen to fill the tube into the RDE. Afterwards this signal stopped, a set delay time was added, after which the 5ms spark signal fired the spark plug. The firing sequence could be repeated as soon as it was finished which allowed multiple manual firings during a single run. The control variables in the sequence were how long the injectors opened for and how long the delay was between when they closed and when the spark fired. The spark plug signal was always set to 5ms. Trial and error revealed a 100ms sequence of 70ms open/20ms delay/5ms spark yielded the most consistent detonations from the pre-det. The LabView code and signal sequence was also backwards compatible with the spark plug ignition method. In that case, the timing on the open and delay

times could be set to 0ms to allow just the 5ms spark signal to be sent out. All other signals would run as described above.
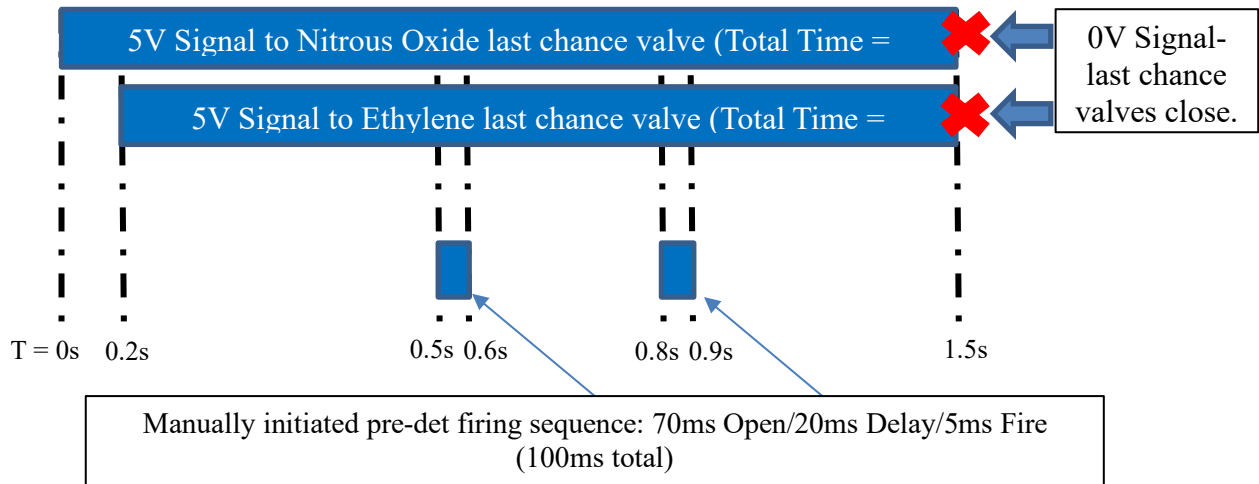
Fig. 45: Typical LabView firing sequence with 1.5s total time and two user triggered fire sequences

Section 3.1.6 Use of Nozzles for Ignition Channel Pressure Control and Resultant Erosion

Detonation channel pressure prior to ignition was a critical factor in successful detonation. Previously, Dechert found that there existed a minimum pressure needed prior to ignition for a given mass flow and equivalence ratio [1]. As will be discussed in Chapter 4, this was a manifestation of the channel pressures influence on the injector stiffness. While the flow controllers could manipulate the mass flow and equivalence ratio before ignition, another tool was needed to manipulate the channel pressure, particularly on runs after erosion damage had caused changes in the exit. Aerospike nozzles, such as the one shown in Figure 33, were implemented by Dechert as a means to do so and this technique was carried over into the current research as well [1].

The nozzle acted to control the chamber pressure by restricting or widening the exit area over channel area ratio, ε, as needed to back pressure the channel to a detonable level for a given

mass flow. Nozzles were sized according to the gap they created at the throat/exit with the channel wall. The nozzles used in the current work had sizes of 0.50mm, 0.625mm, and 0.75mm. With a channel gap of 2mm, these nozzle sizes corresponded to area ratios of ε = 0.26, 0.33, and 0.39, respectively. Each of these ratios ensured the flow was choked as it exited the RDE by keeping channel pressures above the ~0.2 MPa critical pressure (twice atmospheric pressure).

Significantly, the channel pressure was sensitive to small changes in the exit area. To illustrate, consider the Equations 14 and 15, where A_{th} is the area created by the nozzles at the exit, COR is the channel outer radius of 14 mm and Δ_N is one of the gap distances, in meters, listed above. Under the assumption of choked flow, which was valid for all test conditions, it can be seen that a change of gap distance of just 0.25mm created a +/- 33% change in effective exit area or equivalently a 33% change in channel pressure for a fixed mass flow. This sensitivity led to issues with maintaining pressure in the target window when erosion occurred. Any erosion of the outerbody and/or nozzle could result in a different effective exit area than was designed. This was particularly acute when using the spark plug ignition method due to the more severe changes in effective exit area that resulted. Therefore, test points that had pre-ignition channel pressures within the pressure window could be moved outside the threshold in following runs if the outerbody sustained even slight erosion damage near the throat.

$$A_{th} = \pi((COR)^2 - (COR - \Delta_N)^2) \tag{14}$$

$$A_{th} = A^* = \frac{\dot{m}}{P_t}\sqrt{\frac{T_t\gamma}{R}}\left(\frac{2}{\gamma+1}\right)^{-\frac{\gamma+1}{2(\gamma-1)}} \tag{15}$$

Varying the nozzle sizes based on observed pre-ignition channel pressures was done to account for this phenomenon and keep the RDE detonating without replacing hardware. In cases where the majority of the area change resulted from the used nozzle, it could simply be replaced. There were also cases were the solidified metal from erosion could decrease the effective area and

increase the chamber pressure above what was detonable. In these cases, a larger throat gap, or smaller diameter nozzle, was required to increase the effective exit area. The nozzles had an equivalent impact on the operation despite the difference in physical size, so long as the pressures for a given mass flow/equivalence ratio were similar, i.e., effective flow areas were matched. Channel pressures during detonation were not directly manipulated.

During testing it was found that the nozzles were particularly susceptible to erosion, and the level of erosion was directly related to the length of the detonation duration. Two examples of eroded nozzles are shown in Figure 46. The nozzle on the right was after a detonation of 1.3 s, whereas the nozzle on the left was from a detonation with 0.60 seconds. It was found that when either the spark plug or pre-det hole began to burn it would cause the portion of the nozzle nearest the hot spot to melt as well. For detonations that had run times under one second, erosion would be limited to just the area of the nozzle closest to the burning pre-det hole/spark plug. For test runs longer than around one second, a second hotspot would usually begin to form 120-180 degrees opposed from the pre-det hole. With enough time both hot spots would grow as ablative metal was convected around the channel by the detonation's oblique shock, and eventually encompass the entire channel circumference. By this point the entire nozzle circumference would begin to melt equally. This condition usually resulted in an erosion pattern similar to the right-hand picture of Figure 46. Whereas shorter runs would look more like the left-hand picture when only the first hotspot had time to form.

Fig. 46 Side by side comparison of nozzles after a 0.60 second run (left) and a 1.3 second run (right) highlighting the effect of the hot spot growth on severity and location of erosion.

In Figure 47, a 1.4 second run is shown to illustrate the progression of erosion. A hotspot region first formed around the pre-det hole as shown in the T = 0.296s picture. At this point the hotspot is around the same brightness as the actual detonation wave, suggesting that both regions were from burning of the same reactants: nitrous and ethylene. This would mean the hotspot was simply a recirculation zone of unburnt fuel and oxidizer at this time. By the T = 0.502s mark, a second hotpot had formed ~180 degrees away from the first. The location of the second hotpot was inconsistent from run to run, but generally formed at some point in all runs with enough time. As can be seen in the T = 0.502s picture, the hotspots have also formed points where the brightness is significantly more than the detonation wave. It was believed that the difference in brightness indicated that these spots corresponded to the melted metal which would be very bright orange or white in color. By the T = 0.907s frame, nearly the entire channel has become white with bright spots, indicating that now the entire nozzle throat area is melting/burning.

Also, in this picture are two bright columns exiting the channel. These were locations

where the outerbody had begun to melt significantly at the exit creating exhaust flow pillars full of debris. Of note, the outerbody for this run was the same as shown in Figure 41 and experienced new erosion damage along the outer body's exit wall. This can be seen in the post run image in Figure 47. Lastly, the T = 1.010s image shows the peak erosion intensity for this run. Here, the video has become nearly completely saturated by the intense brightness. From this point on the level of melted/burning metal begins to decrease, a result attributed to the decreasing chamber pressure from the now increased exit area created.

At the point corresponding to the T = 1.010s picture in Figure 47, the melting nozzle would have the liquid portions at the lower axial stations blown axially toward the exit. This sloughing of material from the lower portion of the nozzle is what led to the shape shown in the right picture of Figure 46. As discussed, eroded nozzles caused progressive changes in RDE's channel gap and throat area as the detonation occurred. Subsequently, the amount of back pressure being created during the run was a function of the nozzle's condition. This impacted the RDE's operation in a manner that will be discussed more in Chapter 4. The sequence of events shown in Figure 47 were another indication that much of the catastrophic erosion damage was catalyzed by the presence of hotspots either from the outerbody, nozzle, or both. This only reinforced the motivation for the design iteration presented in Section 3.1.4.
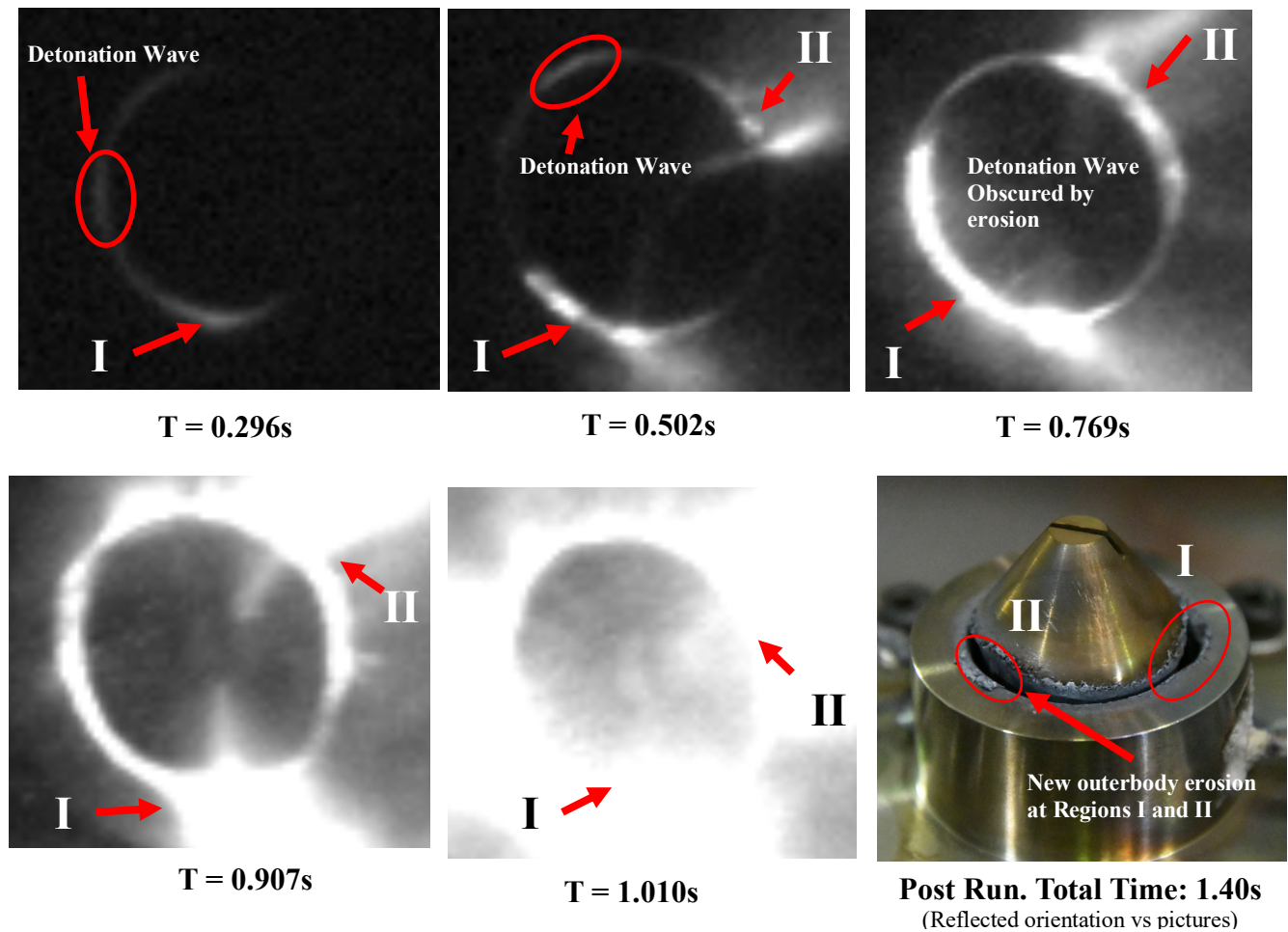
Fig. 47 Five step progression of nozzle erosion during a 1.4s run. Region I and Region II denote the location of the pre-det hole and CTAP hole respectively. Detonation location highlighted where visible.

Like the nozzles, the combined fuel/oxidizer manifold would experience erosion with varying levels of severity. Figure 48 shows two eroded nozzle and manifold combinations, both were documented after a single run. For reference, the image on the right corresponds to the run shown in Figure 47. Interestingly, although the image on the right of Figure 48 was only 1.4 seconds, it presented a more severely eroded manifold than the run in the left image which had a duration of 2.2 seconds. The difference in erosion severity was believed to be attributed to the nozzle on the right becoming loose on its securing screw, which allowed it to be lifted slightly during the run. Subsequently, a recirculation volume between the two parts was allowed to form. Once this recirculation zone was established, the detonation became anchored there. The

discrepancy between the two manifolds also highlighted the importance of mitigating recirculation volumes at the nozzle attachment point. Parts with damage as severe as shown in the right of picture of Figure 48 required immediate replacement. Whereas a manifold with the damage shown in the left image of Figure 48 could continue to be used.

Lastly, the manifold on the left of Figure 48 exhibited a dark band near the injectors, above which the metal appeared to have the type of damage associated with melted/eroded metal. Due to the cooling from the unburnt reactants, it was assumed that where this transition between melted and non-melted metal occurred indicated how far up the unburnt reactants flowed. This band could therefore either indicate the wave's axial position along the channel, or it could indicate the mixing zone. In the case where the unburnt section indicated the wave's axial location, it could also be
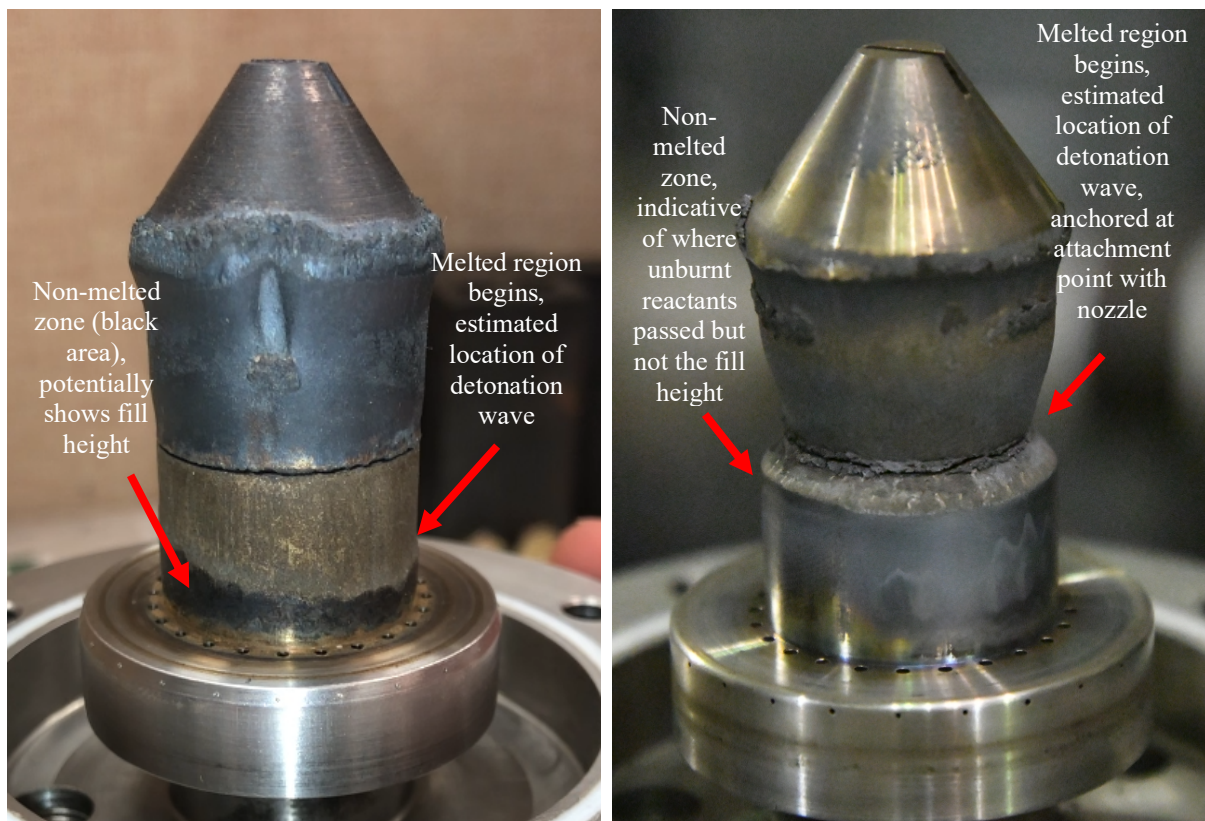
Fig. 48 Comparison of fuel and oxidizer manifold erosion damage after a 2.2 second run (left) and 1.4 second run (right) with estimated locations where the detonation ran.

used to estimate the fill height. However, in the case where it indicated the mixing height, the fill height could not be determined directly. For example, in the right-hand picture of Figure 48, the damaged metal section did not begin until the center attachment point. In this case the detonation had anchored itself along the seam between the nozzle and fuel/ox manifold, and therefore the unburnt section below the seam was not directly representative of the fill height. This made using burn patterns to estimate fill height inconsistent.

After the design iteration discussed in Section 3.1.4 it became clear that the relocation of the pre-det hole had improved the outerbody's survivability leaving the manifold and nozzle as the weakest link. One method to improving erosion resistance was to construct the fuel/oxidizer manifold and nozzle out of a more heat resistant material such as Inconel or ceramic carbide. The benefits of Inconel over stainless steel were presented in Section 3.1.4 and would only be beneficial so long as the melting point was not exceeded. Should the nozzle and manifold exceed Inconel's melting point, Ceramic Carbide could be used. This material had a melting point of 3100K, ~1275K higher than the 1725K melting point of the 304 stainless steel used initially. Such an improvement would most likely keep any erosion restricted to the outerbody which had shown demonstrative improvement. Furthermore, without the additional heat transfer from the melting nozzle and manifold it was believed the erosion on the outerbody would be subsequently reduced. Unfortunately, this option was not able to be implemented at the time of writing this document.

Section 3.2 Mass Flow Control

To characterize the impact and potential benefits of the changes made to the injection scheme and ignition method, data on the mass flow rate and equivalence ratio of each run was needed. Mass flow controllers were used on both the ethylene and nitrous oxide feedlines to set and control the flow rate into the RDE as well as the equivalence ratio. Accurate and reliable flow

control and measurement capabilities were important because together they directly defined the space in which operability was tested. Therefore, Alicat Scientific volumetric flow controllers were chosen for their accuracy and fast control time. These controllers were used to set and measure the mass flow into the RDE. The specifications of these controllers are reviewed along with how they were operated in Section 3.2.1. Characteristic data acquired from the flow controllers are presented in Section 3.2.2 in preparation for their use in the findings of Chapter 4. Section 3.2.3 covers the issues encountered while using the Alicat flow controllers and the alternative methods employed to recover mass flow data. The efficacy of the recovered data is also reviewed.

Section 3.2.1 Flow Controllers and Operation

The mass flow controllers used for the current work were the 500 and 2000 Standard Liter Per Minute (SLPM) MCRQ High pressure Mass/Gas Flow Controllers from Alicat Scientific. The performance specifications for each flow controller are shown in Table 4. All specifications were obtained from the flow controller's operating manual or from Dechert [1]. The 500 SLPM controller was used on the ethylene control line and was chosen for its ability to control the desired mass flow range of 1.26 g/s to 10.31 g/s of C_2H_4. This flow range corresponded to a volumetric flow rate (at standard conditions) of 1000–8180 cm^3/s or 60-500 SLPM. The 2000 SLPM controller was placed in the oxidizer feed line and was calibrated to handle flows up to 2500 SLPM to accommodate the desired oxidizer flow rates of 21.56 g/s to 71.22 g/s for N_2O to achieve equivalence ratios from 0.5 to 1.5. This mass flow range was equivalent to a 10900-36000 cm^3/s or 660-2175 SLPM. Both controllers were calibrated and tuned for their specific gas (C_2H_4 or N_2O) from the manufacturer [1].

Both flow controllers had advertised response times of 100ms and were calibrated by Alicat

with PID tuning to achieve this response. Another specification of interest was the estimated pressure drop across the controller at full scale, venting to atmosphere. For the oxidizer controller, the pressure drop was 197 kPa (28.6 psid) and 44.8 kPa (6.5 psid) for the ethylene controller. These pressure drops are used in the discussion of the control issues in Section 3.2.3. Lastly, these controllers had an operating pressure limit of 2.2 MPa. This limit drove the hole size requirements on the injection scheme and also limited the bottle pressures of both the oxidizer and fuel [1]. These also will be used for the discussion in Section 3.2.3.

Table 4 Alicat MCRQ Flow Controller Specifications [1]

Fuel	
Operating Range	167-8330 cm^3/s
Maximum Pressure	2.2 MPa
Accuracy	$\pm$ 167 cm^3/s (2% of Max Flow Rate)
Oxidizer	
Operating Range	833-41700 cm^3/s
Maximum Pressure	2.2 MPa
Accuracy	$\pm$833 cm^3/s (2% of Max Flow Rate)

Each of the controllers were commanded via a USB connection to a laboratory computer that had Alicat's proprietary Flow Vision software. The Flow Vision software allowed an operator to set in the desired flow rates on the controllers, manipulate PID values for transient response tuning, and log data of pressure, temperature, and mass flow. Figure 49 shows an example picture of a control panel for an individual controller. PID values were kept at their calibrated settings for all testing and were set to give a <100ms response time. Mass measurements were used as the closed loop feedback output. During operation the controllers would have their desired flow rate values entered into the set point window and the open valves button would be selected. Standard liter per minute units were used to input flow rates. Once the controllers were opened, only the facility valves were required to be opened in order for flow to move from the supply bottles to the

RDE. Further details on the facility control apparatus are available in the work by Dechert [1].
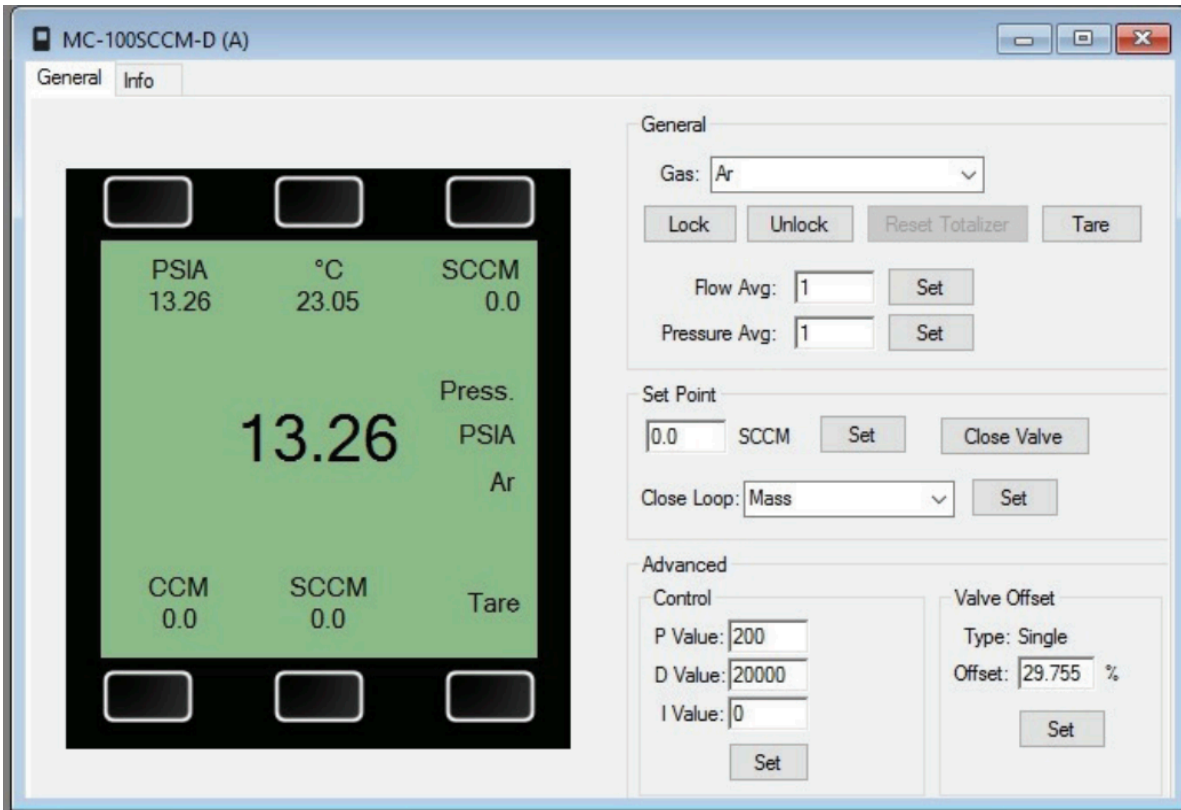
Fig. 49 Example Alicat Flow Vision control panel for an individual controller. Gas set to Argon.

Standard Liters Per Minute, or SLPMs, were the units used to input desired flow rates into the controllers. Although liters per minute are a measure of volumetric flow rate, SLPMs are standardized by the density of the controller's calibrated gas, i.e., ethylene or nitrous. Therefore, if the controller gas setting corresponded to the gas it flowed, the SLPM readings measured mass flow. In order to test over the desired range of mass flows and equivalence ratios, a set of test matrices converting between SLPMs and kg/s were made to quickly set up the controllers. Eleven of these matrices were created in total, one for each equivalence ratio from 0.5 to 1.5 at intervals of 0.1. Equations 16 and 17 show how a desired mass flow, in SLPMs could be determined from total mass flow in kg/s and equivalence ratio. Densities of 1.965 kg/m^3 and 1.252 kg/m^3 were used for N_2O and C_2H_4 respectively. The stoichiometric mass fraction of ethylene and nitrous

oxide combustion, $\left(\frac{F}{A}\right)_{st}$, was 0.1062. These were determined by dividing the molecular weights, in $\frac{g}{mole}$, of each gas by 22.4 L and employing the one-to-one conversion of grams per liter, $\frac{g}{L}$ to kg/m^3. For example, a test condition with total $\dot{m}$ of 0.05 kg/s and Φ of 1.0 could be put through the equations below to find a desired oxidizer $\dot{m}$ of 0.045 kg/s and a fuel $\dot{m}$ of 4.8 g/s, which was equivalent to 1380 SLPMs of N_2O and 230 SLPMs of C_2H_4. Flow measurements were made by the controllers approximately 0.5 m upstream of the RDE. This led to a delay between measured and actual flow into the RDE of approximately 0.1 seconds in the fuel flow and 0.02 seconds in the oxidizer flow based on the nominal Mach numbers calculated in Section 3.3.1.

$$\dot{m}_{fuelSLPM} = [\dot{m}_{total}(\frac{\Phi * \left(\frac{F}{A}\right)_{st}}{1 + \Phi * \left(\frac{F}{A}\right)_{st}})] * [\frac{60000}{\rho_{C_2H_4 \cdot STP}}] \; SLPMs \tag{16}$$

$$\dot{m}_{oxSLPM} = [\dot{m}_{total}(\frac{1}{1 + \Phi * \left(\frac{F}{A}\right)_{st}})] * [\frac{60000}{\rho_{N_2O_{STP}}}] \; SLPMs \tag{17}$$

Section 3.2.2 Flow Rate Data Acquisition

As was mentioned, the controllers had a data logging feature built into the Flow Vision software. Data logging was an important capability because it allowed the flow rate histories to be known during a test run. In the absence of logging, the conditions had to be assumed based on the values set into the controllers. Pressure, temperature, and mass flow data could all be sampled from the controllers. Data sampling rate could be adjusted manually in milliseconds, however there was an option for the program to "poll device as fast as possible". This option was selected to capture as much detail as possible on how the mass flow responded to the detonation. Analysis of the data showed that the fastest sample rate was 28 Hz. Data was logged passively for as long as the logging feature was selected. Stored data was put into a .csv file that could be loaded into Excel

or MATLAB to create plots of a run's mass flow time history. Two examples of such a plot are shown in Figure 50. In the figure, the flow rates from each controller are plotted for quick comparison. The top graph shows the flows in kg/s, which required two y-axes because there was an order of magnitude difference in flow rate between the fuel and oxidizer. The bottom graph was plotted in SLPMs which only required a single y-axis. Graphs such as Figure 50 also highlighted some of the key features associated with a typical data log containing a detonation. Of interest were locations where the flow rate settled before and during detonation and the clear mass flow drop off from the detonation's backpressure. These features are discussed at length in Chapter 4.

Flow Vision polled each device's outputs in an alternating sequence which impacted the effective sample rate. For example, if temperature, pressure, and mass flow data were selected for polling by the software, the 2000 SLPM controller would be polled for temperature, then the 500 SLPM controller would be polled for temperature, next it would return to the 2000 SLPM controller and poll pressure, and so forth. This created longer effective sample times between data points of a particular output than if only one output type was selected. As will be discussed in Section 3.3, pressure and temperature data were collected separately and therefore only mass flow data was needed from the controllers. The alternating sequence meant that for a particular controller the effective sampling rate was half that of the set rate, or 14 Hz.
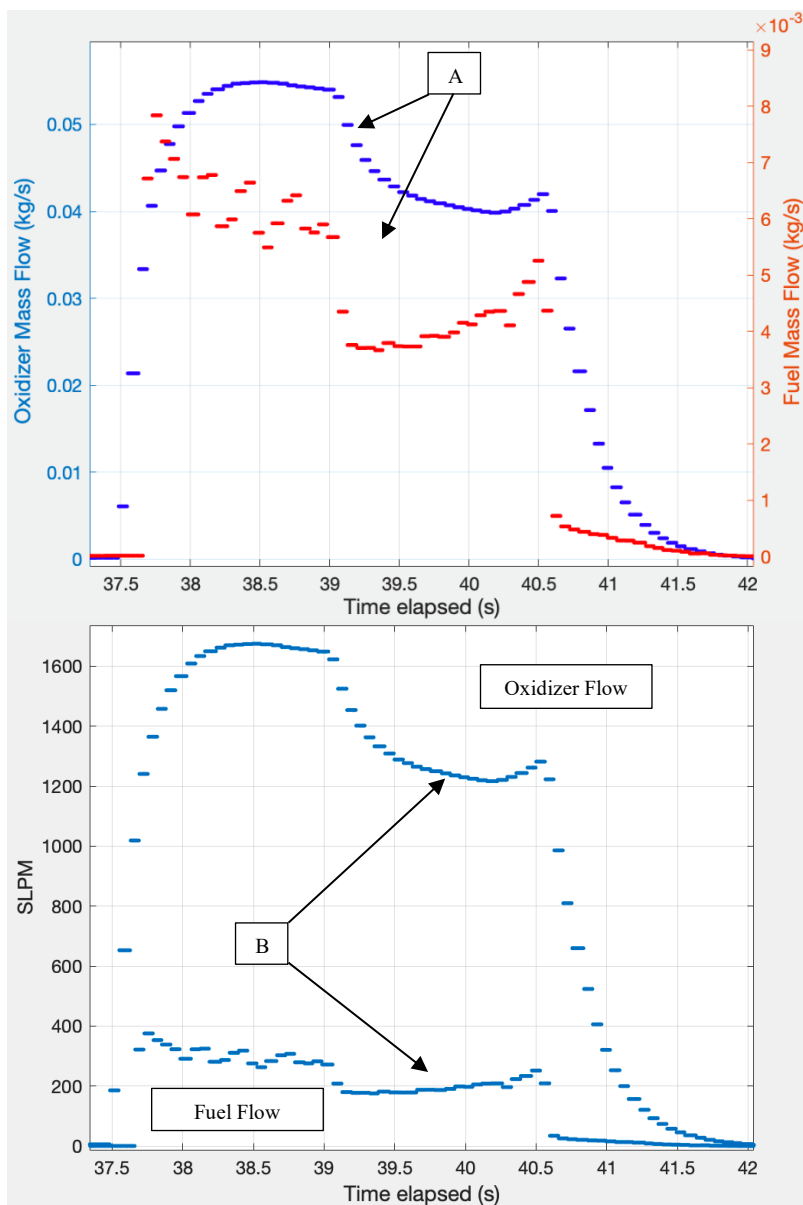
Fig. 50 Example mass flow time histories in both kg/s and SLPMs for a run with a detonation. [A] shows flow rate drop due to detonation beginning. [B] highlights flow rate values during developed detonation.

Section 3.2.3 Flow Control Issues

During the testing process two issues with the mass flow controllers were encountered. First, it was found that the sampling rate was not consistent. For about 30% of the runs collected the data was sampled at approximately 4 Hz instead of the usual 14 Hz (effective speed accounting

for the alternating polling sequence), despite the controller being set to "poll the device as fast as possible". As a result, much of the mass flow behavior was unobservable and determining the pre-ignition and post-ignition mass flow conditions was imprecise and inaccurate. Figure 51 shows an example of a run with low sampling rate and no detonation. Runs without a detonation did not have the mass flow drop associated with the detonation pressure rise. Therefore, these flow histories had a higher likelihood to have observable behavior because they were in a steady condition for longer. Sometimes the timing was right that the device sampled during the detonation period. This would be confirmed based by comparing the pressure measurements taken at the same time as the mass flow sample point. Pressure data is discussed in more detail in the next section.
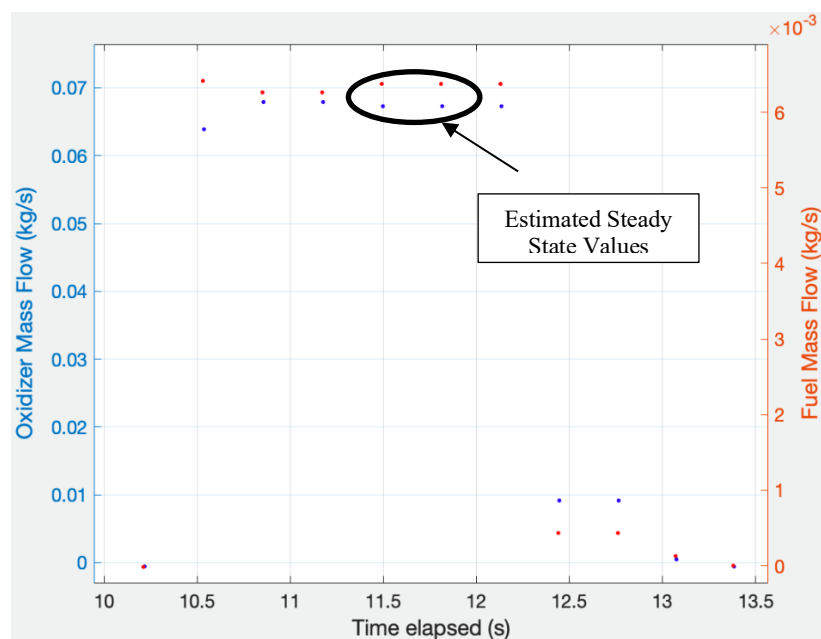
Fig. 51 Mass flow history with a sampling rate of 4 Hz. No detonation and circled data points correspond to those considered representative of steady state values.

To recover better mass flow data from the runs with a low sampling rate, an analysis method was employed using the pressure and temperature data from the oxidizer and fuel plenums. Details on how pressure and temperature data was collected is presented in Section 3.3.1. In following method, the two flow paths being sent through the fuel and oxidizer injectors were considered. The corresponding plenum conditions were assumed as the total conditions. As will

be discussed in Section 3.3.1, this assumption was appropriate. Using Equation 18 and treating the plenum to injector flow path as a simple converging nozzle, an estimated mass flow could be determined. Required values were the total conditions (P_T and T_T), specific gas constant and ratio of specific heats of the fuel or oxidizer (R and γ), and the effective flow area at the end of the injector ($C_D * A_{inj}$). A Mach number through the effective area was also required (M_{inj}).

Prior to detonation, Mach one could be assumed through both injectors. This was because the plenum pressure to chamber pressure ratios, $\frac{P_c}{P_T}$, were always well below the critical ratio of ~0.55. Therefore, if the static pressure through the injectors was used, it would have had to be even lower. The critical ratio was approximately the same for both C_2H_4 and N_2O and could be calculated with Equation 19. During detonation, the unsteady pressure changes at the injectors made direct application of this method inappropriate because steady flow was assumed in its derivation. Therefore, Equation 18 was only analytically accurate for flow prior to detonation. Other methods were used for conditions during detonation and discussed later in this section.

$$\dot{m}_{inj} = \frac{C_D A_{inj} P_T}{\sqrt{T_T}} \left(\sqrt{\frac{\gamma_{gas}}{R_{specific}}} \right) M_{inj} \left(1 + \frac{\gamma_{gas} - 1}{2} M_{inj}^2 \right)^{-\frac{(\gamma_{gas}+1)}{2(\gamma_{gas}-1)}} \tag{18}$$

$$\frac{P_c}{P_T} = \left(1 + \frac{\gamma_{gas} - 1}{2} M_{inj}^2 \right)^{\frac{-\gamma_{gas}}{(\gamma_{gas}-1)}} \tag{19}$$

To use Equation 18, the effective flow area ($C_D * A_{inj}$) was needed. As a result, the injector discharge coefficients, C_D had to be found for the injector geometry. This presented an issue because without mass flow data the C_D could not be determined from the available instrumentation. To circumvent this, reliable mass flow data sets taken at 14 Hz from the Alicat controllers were used as baselines with which to get estimated C_D values. Furthermore, due to the discharge coefficient's dependence on mass flow several values were calculated at various flow rates to

determine variability of values over the applicable range of flow rates. These discharge coefficients were found to vary $\pm6\%$ for the oxidizer flow path and $\pm10\%$ for the fuel flow path over an observed combined mass flow range of 48 g/s to 73 g/s. The variation was attributed not to uncertainty from the pressure transducers, which were small and presented in the next section, but to the inherent unsteadiness of the mass flow measurement. Figure 52 plots the mass flows and corresponding discharge coefficients for both the fuel and oxidizer and illustrates the variability of the C_D's over the range of mass flows. To counteract the scatter in Figure 52, two average values, based on the set of points shown, were calculated. This was done for both the fuel and the oxidizer.

Table 5 shows three example cases which implemented the method just described to find mass flows at a specified point in time prior to detonation. Total pressure and temperature values used in Equation 18 had to be properly aligned in time to ensure the mass flow corresponded to the proper values. Further details on pressure and temperature measurements are presented in Section 3.3.1. Each case in Table 5 had the corresponding 14 Hz mass flow data values used to solve for the discharge coefficients shown in Figure 52. Average discharge coefficients of 0.70 for both fuel and oxidizer were used. Only test points from the same fuel/oxidizer manifold were used in finding respective C_D values to keep manufacturing differences and erosion effects on geometry separated. As can be seen from the table, the estimated values were within 5% of the measured values. This level of accuracy was considered adequate, and as a result the method was used for all test points prior to detonation that did not have corresponding flow measurements taken at the desired 14 Hz. Percent errors of the full data set were all below 10%.
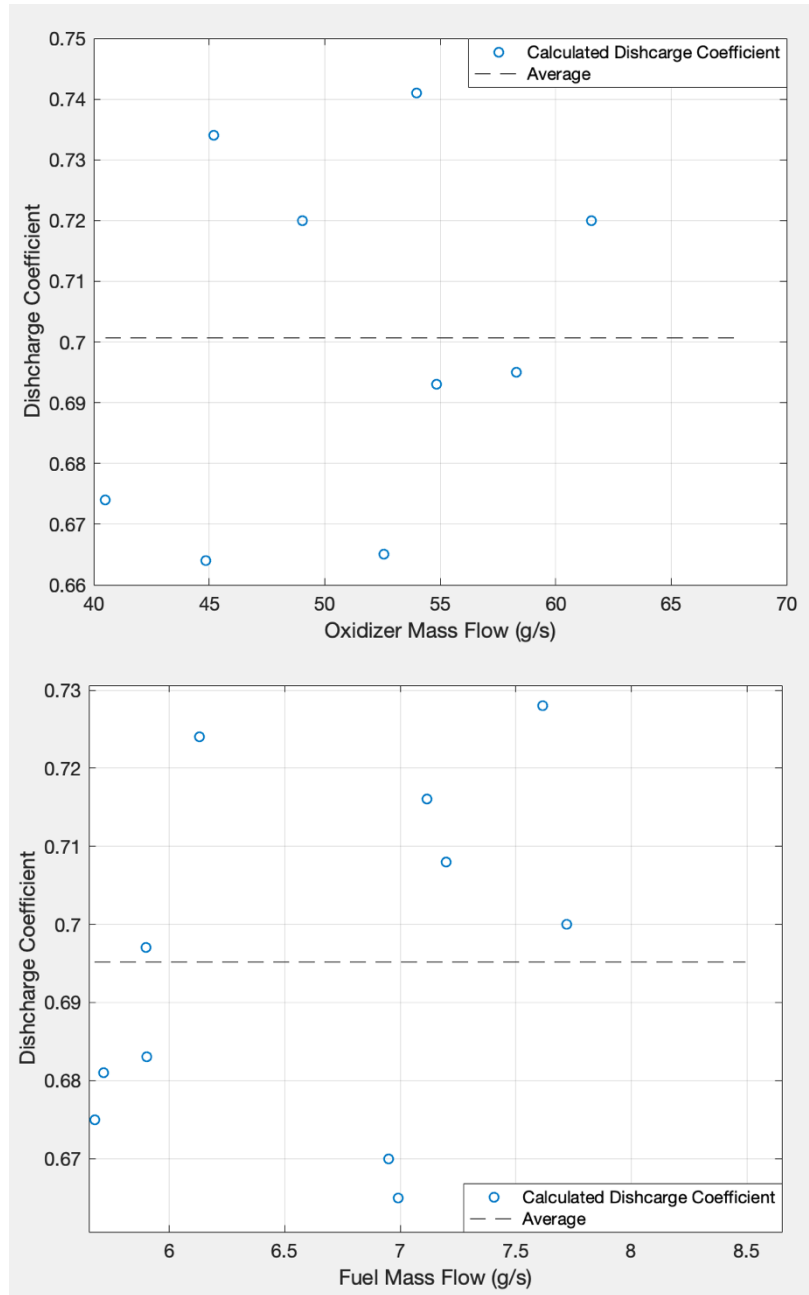
Fig. 52 Mass Flow versus C_D scatter plots with average value lines of 0.70 for Oxidizer (Top) and Fuel (Bottom).

Detonation events created unsteady pressure conditions at the injectors. The increased pressure from the detonation at the injectors also unchoked the flow through them, invalidating the Mach one assumption previously used. Furthermore, the unsteady behavior meant injection Mach number and effective injection area were variable in time and were subsequently

unknowable with the pressure measurements available. As a result, Equation 18 could no longer be used directly. However, average static pressure in the chamber during detonation was known from the CTAP measurement (details in Section 3.3.1). While this static pressure was not the static pressure in the injectors, its ratio with the total pressures was still a measure of the pressure differential responsible for the mass flow through the injectors. This meant that available 14 kHz mass flow data during detonation events, and their corresponding $\frac{P_C}{P_T}$ ratios could be used to create scatter plots and least squares regression lines that could estimate points with unknown flow rates.

Table 5. Comparison of pre-detonation mass flow measurements from Alicat devices and corresponding estimates from Equation 18. Estimated C_D values backed out from baseline cases shown.

Pre-Detonation	Alicat Ox Measurement (SLPM)	Alicat Fuel Measurement (SLPM)	Est. Ox $C_D = 0.70$ (SLPM)	Est. Fuel $C_D = 0.70$ (SLPM)	Percent Error (Ox)	Percent Error (Fuel)
Case 1	1237	279.7	1277	279.8	3.2%	0.0%
Case 2	1520	275.1	1496	282	1.6%	2.5%
Case 3	1775	333.4	1792	348.5	1.0%	4.3%

Such a process was used to create Figure 53 which demonstrates the potential use for this method. Data on the graph came from the same fuel/ox manifold and therefore was a subset of the full data. A least square regression (LSR) line is shown in the figure and represents the set of predicted values given an arbitrary pressure ratio. Due to the averaging of the CTAP measurement, only measurements from periods of near constant pressure were appropriate for generating the regression line. Periods of changing pressure, either due to a detonation establishing itself or erosion changing the exit area, meant the corresponding CTAP pressure reading was no longer giving an accurate average, and the resultant ratio would not represent the proper relationship. This truncated the set of usable points.

From Figure 53, it was seen that the LSR method yielded a maximum error of 6% for the oxidizer and 15% for the fuel when compared to known values. Due to the necessary truncation of

the data set, the available points did not cover a wide enough range of $\frac{P_C}{P_T}$ ratios to estimate all the

available test points without extrapolation of the LSR line. The error values and extrapolation

issues were consistent across the other data sets from other fuel/ox manifolds.
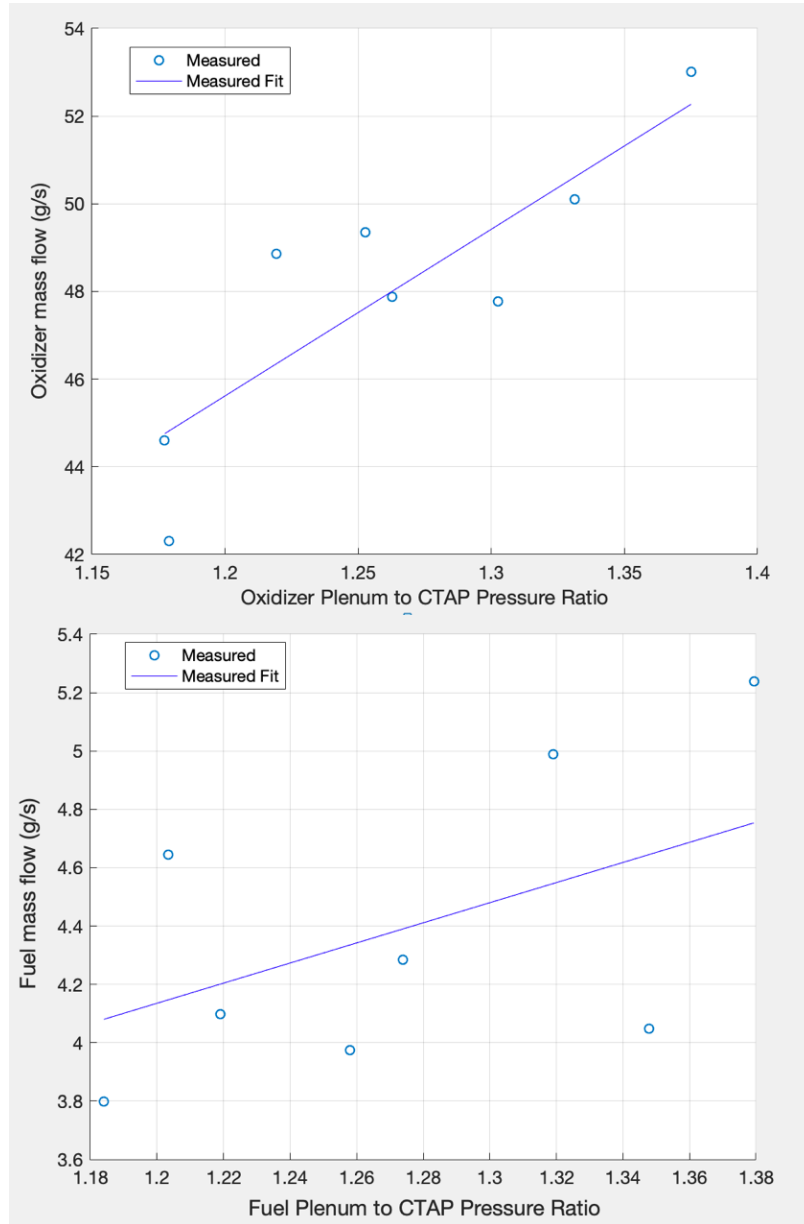
Fig. 53 Mass Flow versus $\frac{P_C}{P_T}$ scatter plots with Least Square Regression fit
for Oxidizer (Top) and Fuel (Bottom).

To avoid extrapolation, the detonation's unsteady pressure effects on the injectors were neglected so that a similar, but less restrictive, empirical relationship using the functional forms of Equation 18 and 19 could be derived. To attain the desired relationship, Equation 19 was re-written to solve for the square of the Mach number M_{emp}^2 as a function of the ratio, $\frac{P_c}{P_T}$. The resultant Mach number was not a physical Mach number, but an empirical factor that could then substituted into Equation 18. The resulting mass flow relationship had the same functional form as was used in the cold flow analysis and was similarly dependent on P_T, T_T, $\frac{P_c}{P_T}$, $(C_D * A_{inj})$, R and γ. The difference was the empirical nature of the measured $\frac{P_c}{P_T}$ ratio and $(C_D * A_{inj})$ factor. The pressure and gas properties were known, but the new empirical effective flow area $(C_D * A_{inj})$ factor still needed to be found using known mass flow values. This process mimicked the one used to determine C_D in the non-detonating case.

The $(C_D * A_{inj})$ term scaled the empirical Mach number factor based on known baseline data. While the factor was $C_D * A_{inj}$, only the C_D value was manipulated so that the A_{inj} values remained equal to the physical injector area. To find adequate C_D values, the L2 norm of a vector containing the percent difference between measured mass flow data and empirically calculated mass flow at the same conditions was minimized. This was done for both fuel and oxidizer flows to produce two C_D values. Once the C_D values that minimized the error were known, the mass flows of test points without measured data could be found using known pressure and gas properties like in the cold flow method. Discharge coefficient pairs (oxidizer and fuel) were determined from mass flow measurements which used the same fuel/oxidizer manifold, similar to the cold flow analysis as well.

Table 6 shows an example data set and corresponding empirical estimates from a single fuel/oxidizer manifold. Oxidizer values were found to be within 10% of measured values. Fuel

error minimization was less ideal with one case having an error of 17%. This was expected because the fuel injectors location inside the oxidizer injector likely caused complex flow behavior at its exit during the detonation cycles. However, as seen in the table, all other values were less than 11%, with the majority well below that.

Table 6. Post-detonation mass flow measurements and corresponding estimates from the empirical forms of Equations 18 and 19.

Post Detonation	Alicat Ox Measurement (SLPM)	Alicat Fuel Measurement (SLPM)	Est. Ox $C_D = 0.55$ (SLPM)	Est. Fuel $C_D = 0.44$ (SLPM)	Percent Error (Ox)	Percent Error (Fuel)
Case 1	1619	194.0	1704	227.4	5.25%	17.21%
Case 2	1292	222.5	1365	201.0	5.62%	9.66%
Case 3	1362	182.0	1339	188.9	1.71%	3.77%
Case 4	1530	251.0	1513	222.9	1.12%	11.19%
Case 5	1459	239.0	1507	213.8	3.29%	10.53%
Case 6	1462	205.3	1458	205.9	0.26%	0.29%
Case 7	1507	190.4	1458	203.8	3.36%	7.03%
Case 8	1492	196.4	1392	192.9	6.64%	1.79%

Lastly, Figure 54 shows four scatter plots summarizing the detonating mass flow example data. The top two plots show the empirical estimates of measured data, the same data as in Table 7, overlaid with the measured values that were plotted in Figure 53. The LSR fit lines from Figure 53 are also included in Figure 54. From these two plots and the table of errors, it was clear that the empirical method had consistent agreement with both the LSR fit and measured values, confirming that the functional form of Equations 18 and 19 were valid so long as the empirical C_D factors could be appropriately found. Additionally, the empirical function could use any arbitrary $\frac{P_C}{P_T}$ ratio input so long as the C_D value could be assumed independent of $\frac{P_C}{P_T}$. This assumption was checked by truncating the range of the ratios used in the determination of the C_D values. Resultant discharge coefficients remained the same, which meant independence was a reasonable assumption and

extrapolation was appropriate within conservative bounds. Ultimately, the empirical function method was preferred over the LSR fit and was used for all cases where there was an absence of measurements from the Alicat controllers. The bottom two plots added in the estimates of test points that did not have measured values, and thus represented extrapolated values. It is restated that the data shown in Figure 54 was a subset of the full data set selected because it was tested on the same fuel/ox manifold.
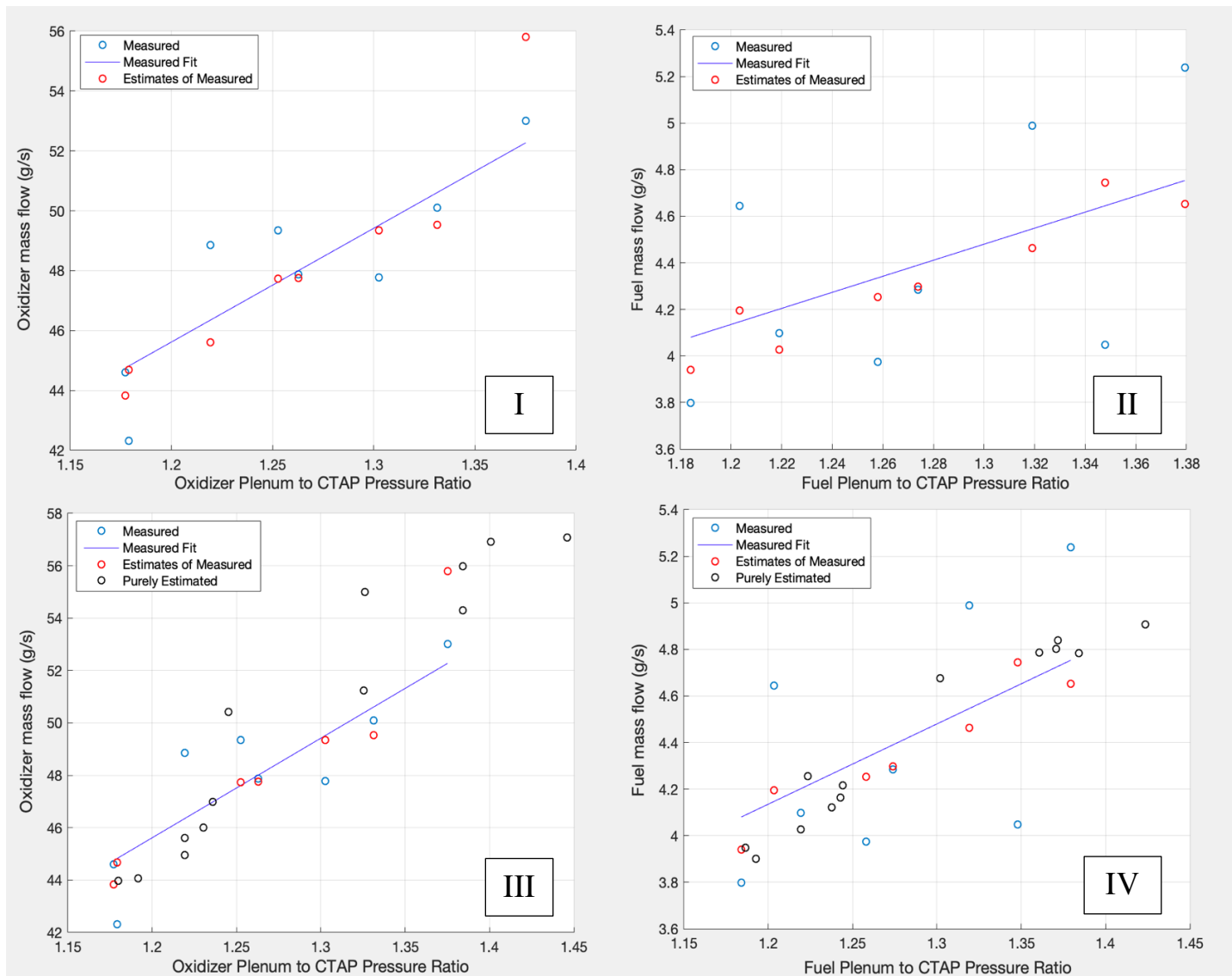
Fig. 54 Summary of Mass Flow vs $\frac{P_c}{P_T}$ methods. Graphs **I** and **II** plot measured values with LSR fit in addition to empirical function estimates of the measured values. Graphs **III** and **IV** add in the empirical function estimates of points without measured values.

The second mass flow control issue was that the Alicat controllers could not adequately adjust the flow rates during a detonation. Figure 50 shows that when a detonation occurred the mass flow decreased significantly. As a result, the detonation mass flows were always significantly lower than requested. Figure 50 also shows that the mass flows appeared to begin increasing over the course of the detonation. Other runs showed revealed this did not always happen and when it did was the result of erosion increasing the exit area and decreasing the channel pressure. This in turn allowed the controllers to flow at a higher rate, further details are reserved for Chapter 4. This was a suboptimal behavior and presented a fundamental challenge to characterizing the operating space of the Micro-RDE because desired conditions could not be achieved directly.

The reason this occurred was due to the pressure differential across the Alicat controllers. During detonation, the pressure downstream the controllers could be increased to ~1.70 MPa. Typical upstream pressures were ~1.90 MPa, leaving a 0.20 MPa differential across the controllers. Accounting for pressure losses anywhere from 0 to 200 and 50 kPa for the 2000 SLPM and 500 SLPM controller respectively, there was likely a differential less than 0.20 MPa on most runs. This presented a problem because for a given mass flow adjustment, the control valve on the Alicats must open more when the pressure differential across it is small versus when it is large. After discussion with Alicat technicians it was found that a 0.17 kPa differential at an upstream pressure of 1.9 MPa would result in a 99% duty cycle on the 2000 SLPM controller's valve. The same issue occurred for the fuel controller as well. Therefore, the controllers were not responding adequately to mass flow drops such as the one shown in Figure 50 because their valves could not actuate appropriately. This meant desired mass flows and equivalence ratios could not be reliably reached during detonations.

Pre-ignition conditions had typical pressure differentials of 0.55 MPa, which were large enough to allow the controllers to manipulate the flow. This meant that pre-ignition conditions

could be controlled to a greater degree than detonation conditions. Furthermore, it was found that varying the desired pre-ignition conditions was able to produce variations in the post detonation conditions. However, these variations were not predictable and therefore the actual range of conditions observed were limited by what could be produced in this indirect way. It was through manipulation of the pre-ignition conditions that all the operating conditions presented in Chapter 4 were obtained.

Section 3.3 Instrumentation

In addition to measuring mass flow, pressure and temperature data along with high-speed imagery of the detonation channel were taken to characterize the pre and post detonation conditions. The general instrumentation used for the current work was nearly identical to that used by Dechert [1]. Therefore, only the aspects of the instrumentation relevant to the results presented in Chapter 4 are discussed. The pressure and temperature sensors, their location relative to the RDE, the type of data collected, and the methods used to analyze that data are covered in Section 3.3.1. Following, in Section 3.3.2, are the details regarding the high-speed camera and its corresponding imagery which was integral to identifying the detonation wave modes. Lastly, the analysis method used to extract wave speed from the high-speed video is presented with a discussion of its uses and limitations. Each type of data produced by the instrumentation discussed helped inform how the new injection and ignition changes to the Micro-RDE impacted its operating envelope and the character of the detonation wave inside it.

Section 3.3.1 Pressure and Temperature Sensors

As documented by Dechert, pressure sensors were placed in three locations: one in the oxidizer supply line, one in the fuel supply line, and one in the detonation channel [1]. Sensors

placed in the oxidizer and fuel supply lines measured instantaneous static pressure and were located between the corresponding last chance valves and the RDE as shown in Figure 55. Both locations had approximately 0.5 m of tubing between them and the connector plate and used high speed OMEGA PX429-500A5V pressure transducers. These sensors sampled data at 1000 Hz and had an accuracy of $\pm$0.08% over a range of pressures from 0-3.45 MPa. The third pressure sensor was an Omega PX429-250A5V connected to the RDE's detonation channel via a long 1/16" tube. This transducer also sampled at 1000 Hz with an accuracy of $\pm$0.08% but only over a range from 0-1.7 MPa. Further specifications for the sensors are presented in detail by Dechert [1].

Assuming negligible losses between the sensor's location and the oxidizer and fuel plenums, readings from the supply sensors represented the plenum pressures feeding the RDE. Furthermore, it was assumed the static pressure measurements were effectively the total pressure and used as such in the mass flow analysis presented in Section 3.2.3. However, for this to be an accurate assumption the flow velocity had to be assumed to have a low enough Mach number to keep the ratio defined by Equation 19 close to one, where P_c was now P_{static}. To check the assumption's validity, Equation 20 could be employed assuming isentropic flow between the sensors and the fuel/oxidizer injectors. The flow area used at the sensor location was $1.27E10^{-4} \ m^2$ based on the ½" tubing at that location. Before detonation, the injectors were choked and therefore the injection areas of $3.11E10^{-6} \ m^2$ and $2.25E10^{-5} \ m^2$ for the fuel and oxidizer respectively could be used as the required A* values. The resultant Mach numbers were attained from iteration and found to be 0.0144 and 0.105 at the fuel and oxidizer sensors respectively. These produced $\frac{P_{static}}{P_T}$ ratios $\approx$ 1, confirming the assumption for the pre-detonation condition. During detonation the injectors would unchoke having the effect of slowing the flow velocity in at the pressure sensors. Therefore, the pressure readings at the plenums were effectively total conditions during detonation as well.
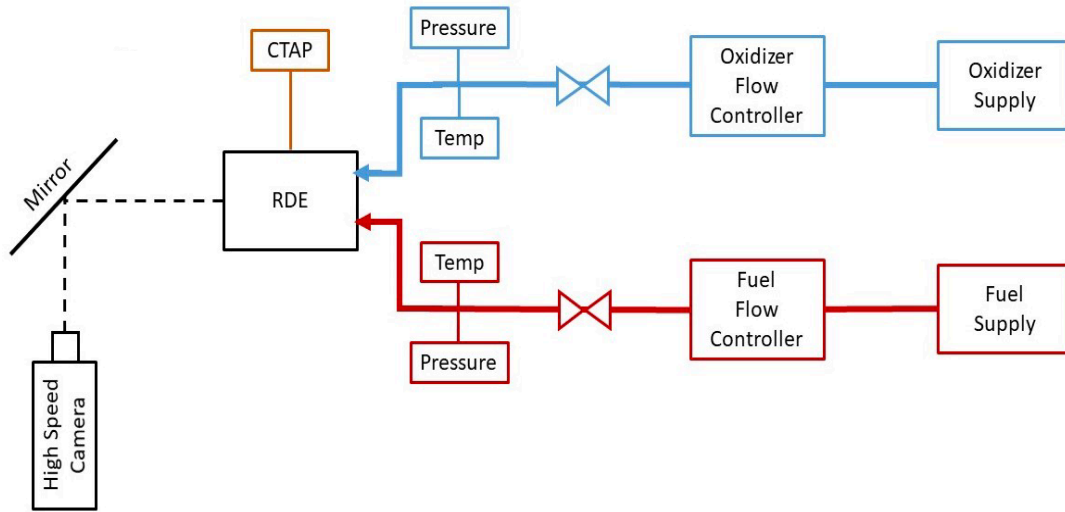
Fig. 55 Schematic of RDE Instrumentation [1]

$$\frac{A}{A^*} = \frac{1}{M}\left(\frac{\gamma_{gas}+1}{2}\right)^{\frac{-(\gamma_{gas}+1)}{2(\gamma_{gas}-1)}}\left(1 + \frac{\gamma_{gas}-1}{2}M^2\right)^{\frac{\gamma_{gas}+1}{2(\gamma_{gas}-1)}} \tag{20}$$

By connecting the Omega PX429-250A5V to the channel with a long tube, a capillary tube average pressure (CTAP) reading was created. This type of reading had the high frequency pressure fluctuations caused by the detonation wave damped out in the long tube before reaching the pressure transducer. Consequently, this represented the average static pressure in the channel, not an instantaneous pressure. During pre-detonation conditions, where high frequency disturbances from a detonation/acoustic wave were absent, the average pressure reading was approximately equivalent to the instantaneous pressures in the channel.

As discussed previously, the mass flow estimation method used during detonation conditions required a $\frac{P_C}{P_T}$ ratio to determine an empirical Mach number factor. Along with the sensors in the fuel and oxidizer supply lines, the CTAP pressure allowed this ratio to be found. Furthermore, a sustained increase in CTAP pressure was indicative of successful detonation inside the channel, which was useful in determining if a detonation occurred or not in a given run. The

CTAP reading could also be used to back out the Mach number and total pressure in the detonation chamber. This was possible because the ratio of the channel area to exit area was known (prior to erosion damage). Therefore, during pre-detonation conditions, where isentropic flow was still an appropriate assumption, Equation 20 could yield the channel Mach number. With this Mach number, Equation 19 provided the $\frac{P_{static}}{P_T}$ ratio in the chamber. Then P_T was solved for using the P_{static} CTAP measurement. Such analysis was useful in determining how much pressure loss was incurred through the injection scheme and the pre-ignition Mach numbers/channel pressure range that yielded successful detonation. Area change due to erosion could also be estimated by comparing pre-detonation CTAP pressure from runs with the same mass flow and equivalence ratio before and after erosion damage.

During detonation conditions, the average static pressure was measurable from the CTAP. Therefore, the exit area to channel area ratio could be used to determine the channel Mach number assuming non-isentropic effects from reacting gasses were negligible. This would then yield an estimate on total pressure during detonation. However, erosion complicated measurements of the exit area.

In combination, the three pressure sensors could be used to produce graphs such as the one shown in Figure 56 which plotted oxidizer pressure, fuel pressure, and CTAP pressure together. These graphs were used to collect the total pressure values used in the mass flow estimation methods from Section 3.2.3 and helped determine when ignition attempts, and denotations occurred. Referring to Figure 56, the beginning and end of each run was clearly visible. Per the command sequence from Figure 45 in Section 3.1.5, the start of every run began with the oxidizer line opening. Two hundred milliseconds later, the fuel line would open, and its pressure would increase followed by the CTAP pressure. CTAP readings would lag shortly behind the fuel and oxidizer pressure due to the inherent damping/averaging effect of the sensor set up. The end of

each run was characterized by a sudden drop in both the fuel and oxidizer plenum pressures as the supply valves were closed. Again, CTAP pressures lagged behind. Using the time stamps corresponding to these events, a beginning and end time for each run could be defined along with when the spark plug/pre-detonator was fired and if those attempts resulted in a detonation.

Every run with a detonation had a significant sustained pressure increase in all three pressure measurements, as shown in Figure 56 beginning at 2.5 seconds. Therefore, the start of a detonation could be found with relation to the start of the run. This time difference could then be correlated to the mass flow data plots shown in Figure 50 to identify when in the mass flow data, the detonation began. Ignition attempts, or firings of the spark plug/pre-det device, were identifiable in the pressure histories by the presence of a sharp spike in oxidizer pressure. Occasionally the CTAP pressure would also spike. If a pressure spike in either the oxidizer reading alone or both the oxidizer and CTAP readings occurred, but was not sustained, it was concluded a detonation briefly occurred but died out. Fuel pressures did not spike because the fuel injector lines were small and long enough to damp out the brief pressure fluctuation of a spark/pre-det attempt.
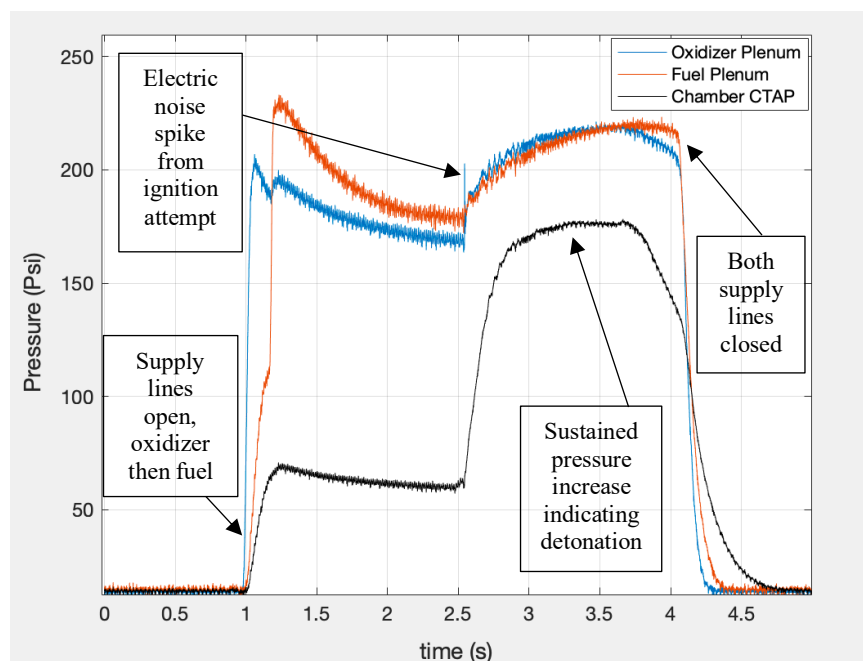
Fig. 56 Oxidizer, fuel, and CTAP pressure history.

As will be discussed in the next section, high-speed imagery had time stamps for each frame. Therefore, the time difference between an arbitrary point during a detonation and when the detonation began, as determined from Figure 56, could be used to line up the video with the pressure data. Doing so required that the initial ignition event be recorded on video so that its time stamp was known. Once data from pressure sensors, mass flow devices, and high-speed imagery were aligned the mass flow and equivalence ratios for each run could be found via calculations using data from the same point in time. Doing so created the operating envelopes used in Chapter 4 to determine how the new injection and ignition methods impacted the Micro-RDE. Mass flow and equivalence ratio values also helped correlate wave behavior and frequency to specific operating conditions.

Temperature data was collected via two K type Omega thermocouples placed in the same locations as the pressure transducers in the supply lines, as shown in Figure 55. From Dechert, these thermocouples had an operating temperature range of 233-343K with an accuracy of $\pm 2K$ [1]. Temperature data was not as useful or informative as pressure data for the current work. However, using the same argument as was used for pressure, the temperature measurements were the total temperature for the fuel and oxidizer at the thermocouple's location if the tubes were further assumed to be adiabatic. Ultimately temperature data from these two sensors were used for the calculations performed with Equations 18-20.

Section 3.3.2 High-Speed Imagery

High-speed imagery from a Phantom v711 camera was used to observe the detonation channel and document the detonation wave behavior. This camera provided video at 128X128 resolution with a max frame rate of 210,526 frames per second, which was equivalent to a new frame every 4.75 μs. At this rate, if the wave reached the desired peak frequency of 20 kHz, the

wave would progress around the channel in 10 frames. An exposure of 1-1.2 μs was used for nearly all the video collected. Consistent with Dechert, the camera was placed on a tripod next to the test stand and pointed at a mirror placed above the RDE. The mirror was used to keep the camera away from the exhaust gasses of the RDE [1]. To illustrate the orientation of the camera and RDE, Figure 57 shows a diagram of the camera's location and a picture of the mirror. Additionally, a side by side comparison of two images produced by the camera is shown to illustrate the orientation produced. The right image was taken with an exposure of 1.2 μs and frame rate of 210,000 fps during a detonation event. The left image was taken with an exposure of 40 ms and frame rate of 24 fps when no test was taking place. Both had a resolution of 128X128 however the image on the right has been zoomed in to make the wave and channel location clearer. The left image also showed how the CTAP and pre-tube were oriented within the frame of the videos and was used as a reference when looking at images such as the one on the right of Figure 57.

To trigger the high-speed video such that it was aligned with the rest of the RDE's control sequence, the same 5V signal sent from the DAQ controller to fire the spark plug/pre-detonator was also sent to the Phantom v711. This meant that once the spark plug/pre-det was fired the camera would begin to record. In the event that the spark plug/pre-det was fired multiple times during the same run, the camera would still be triggered, but only by the first signal. Successive signals did not re-trigger or stop the camera from recording. Recording would stop when the pre-set amount of time had passed after the trigger signal. If a detonation occurred on a successive ignition attempt, there was a delay that would need to be accounted for when corresponding the video frames of interest to pressure and mass flow data.
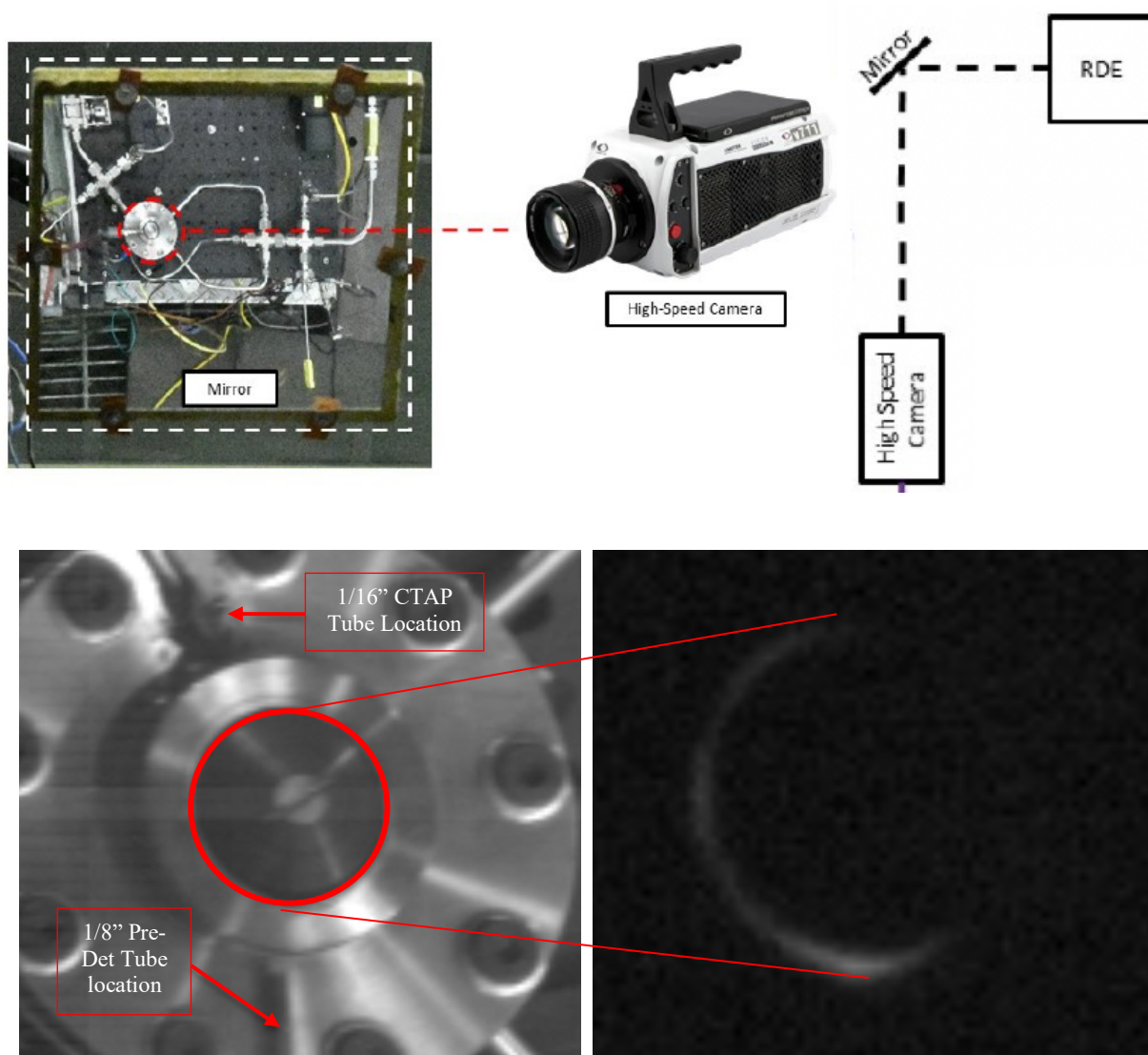
Fig. 57 Orientation of high-speed camera and mirror with respect to RDE
and resultant framing with a standard picture (left) and frame from
corresponding video (right).

High-speed video was used to determine wave speed by hand counting frames and then employing Equation 21. This method constituted finding a sequence in the high-speed video where the wave rotated the chamber five times. The number of frames it took to do so was then divided by the five to get an average number of frames per rotation. This average value was then used in the equation to get an estimated wave frequency based on the camera frame rate of 210,562 fps. Figure 58 shows a single rotation in a set of high-speed images taken from a run using spark plug ignition. Pictures I to IV occurred over a total of 14 frames. Figure 58 also has a color picture of

the RDE in the same orientation as the high-speed pictures for reference. Using Equation 21, the sequence in the figure yielded a wave frequency of 15 kHz. In practice, four more rotations would have been counted to get the average number of frames as discussed earlier. The frames per rotation were able to be determined within ~0.25 of a frame per rotation leading to an uncertainty of ±300 Hz. Lastly, five rotations generally occurred in 70-80 frames, which meant each time the frequency was determined it was done so over a time span of 330-380 μs. Wave frequency measurements were therefore not an average for the entire run but rather an approximation of instantaneous frequency. Continuous measurements over the whole run were not feasible with this method.

$$f = \left(\frac{\#Average\ frames\ per\ rotation}{Camera\ framerate}\right)^{-1} Hz \qquad (21)$$
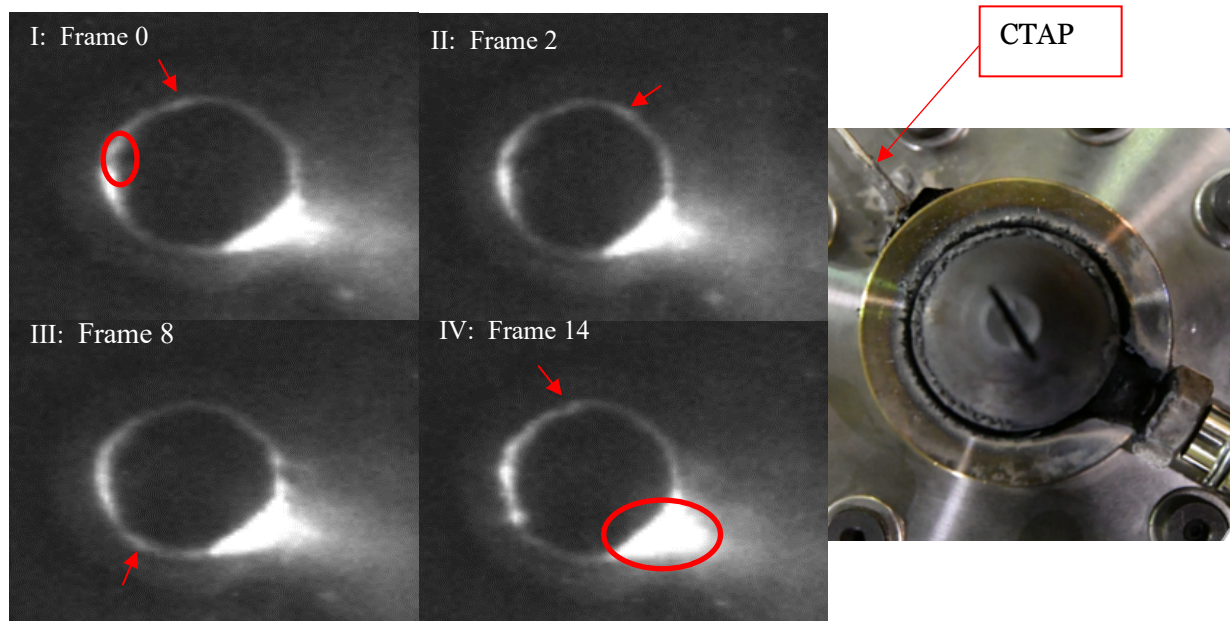
Fig. 58 High-speed photo sequence showing a single rotation of the detonation wave. Color photo in the same perspective as shown. Arrows denote location of detonation wave; ovals highlight zones consistently brighter than wave.

More sophisticated methods of determining wave speed were considered so that continuous measurements could be possible. One such method was described by Boller et al. [29]. In their

approach, a MATLAB code took in the video data and determined the brightest pixels in each frame. The radial location of these pixels could then be tracked frame to frame and the frequency could be determined [29]. Unfortunately, this required that the detonation wave be the brightest pixels at all times. As can be seen in Figure 58, this simply was not the case particularly when bright images from erosion were present. Additionally, the presence of clapping modes and intermittent wave failure meant the required algorithm was too complicated for the scope of this work. Therefore, the more simplistic method described above was implemented.

High-speed video was also used to determine the mode of wave behavior. A significant aspect of the work done was to describe how the changes made to the RDE impacted the stability of the detonation wave. As discussed in Chapter 2, wave stability does not have a universally agreed upon definition in the RDE research community. Therefore, the definition for stability in the work presented here will be described as the wave's ability to propagate consistently in a single or multiple wave mode with a consistent direction of rotation. Clapping modes, alternating wave direction, counter rotating waves, intermittent wave failure, galloping modes and acoustic/deflagrative modes were considered unstable, even in the event that the RDE persisted in one of these modes. Stability defined by the wave speed's percentage of the CJ velocity was an alternative definition. However, as will be shown in Chapter 4, the RDE was capable of reaching a stable condition under the definition above, while failing to be stable with respect to CJ velocity. Therefore, to better resolve the potential influence of the changes, the percent CJ speed is acknowledged as a supplemental metric but not as the main metric by which to describe stability of the detonation wave. Other popular definitions of stability fall under the same argument.

To determine wave behavior, the high-speed video was manually observed at various points within the video and the behavior was documented. Due to the high frame rate, a one second detonation would have a video that would take ~2 hours to watch at 30 frames per second.

Therefore, it was not feasible to ensure that every frame was observed, however the behaviors were found to have time scales on the order of several hundred to several hundred thousand frames. As a result, identification of the modes was possible in a feasible amount of time by skipping hundreds to thousands of frames and identifying variations in the modes. Using this method multiple behaviors were able to be observed, the categories for which are defined in Chapter 4.

A consequence of the high frequency of the Micro-RDE in combination with the varying mass flow conditions encountered during detonation was that a single detonation event usually consisted of multiple modes. Furthermore, it was not uncommon for the unstable modes to exist in combination with one another. Therefore, a single run had the potential to yield multiple operating conditions with corresponding wave modes and speeds. In response it became desirable to find a mode with consistency of at least 200 frames. The time stamps associated with the frames relative to when ignition occurred could then be used to associate the wave behavior with pressure and mass flow data. The minimum number of frames of 200 was determined so that the time frame was resolvable by the pressure and temperature sensors.

In practice, a mode with a consistency of 15,000 frames or more and which occurred after the CTAP pressure had stabilized, was preferable. These guidelines kept the mode within the sampling rate of the Alicat devices (14 Hz) and helped ensure that the CTAP measurement was valid. If novel wave behavior was encountered that lasted for less than 15,000 frames, the 200-frame minimum could be used so that pressure and temperature data would be available for correlation. That temperature and pressure data could then be used to get estimated mass flow via the methods of Section 3.2.3. Such an estimation would be subject to the ~10% error associated with those methods assuming the CTAP value was accurate. If a novel wave mode was observed during a period of transient pressure and occurred too quickly to be observed by the controllers, estimation of the conditions causing the behavior would become difficult and likely be inaccurate.

Therefore, if such an instance was encountered the wave mode would not be correlated to mass flow and equivalence ratio.

IV. Results and Discussion

Using the new hardware and instrumentation discussed in Chapter 3, the Micro-RDE's behavior pre and post detonation was characterized and compared with previous work to determine how the new injection and ignition methods affected operability and wave mode stability. In Section 4.1 the need for two maps, an ignition and operating map, incorporating mass flow estimations and measurements are discussed and compared to previous work. Both the spark plug and pre-detonator results are detailed. Section 4.2 reviews the observed wave behavior from both data sets through discussion of wave mode and frequency. Throughout the section, assessments of the operability and stability of the observed waves are made with respect to the old design. Lastly, Section 4.3 highlights parameters of interest that were found to have an observable impact on the RDE's ignition and operating behavior. Mechanisms for how these parameters had an impact are discussed. Section 4.3 finishes with analysis of the estimated fill height.

Section 4.1 Characterization of Micro-RDE Operability: Ignition and Operating Maps

To make comparisons of the operability, the regime where the new injection scheme would detonate needed to be found. This was approached by testing mass flows from 0.025 kg/s to 0.075 kg/s with the spark plug and pre-detonator ignition methods. A limited range of equivalence ratios between 1.1 and 1.2 were tested with the spark plug and an expanded range of ratios from 0.8 to 1.4 was tested with the pre-detonator. Pre-detonator data was collected on both the outerbody configurations shown in Figures 40 or 43. Differences between pre-det hole location did not have an observable impact on detonability. Different outerbodies were found to have small differences in exit areas, however average pre-ignition chamber pressures and mass flow data provided a good way to track these variations. As a result, data from both outerbody configurations are presented together.

Maps showing the space of requested mass flow and equivalence ratio were developed and preliminary comparisons to previous work were made. However, the mass flow control issues discussed in Section 3.2.3 necessitated the use of estimated mass flow and equivalence ratios instead of the requested values. Section 4.1.1 covers the preliminary operating maps and the impact of the flow control issues for the spark plug data set. Section 4.1.2 covers the same topics but for the pre-detonator data. Section 4.1.3 discusses how replotting the operating map with measured mass flow required two types of maps, an ignition map and an operating map. It then presents the ignition and operating spaces for the spark plug set followed by the pre-detonator set. Trends and uncertainty in the operating and ignition maps and their comparison to previous results from Dechert are also discussed [1].

Section 4.1.1 Operating Space Based on Requested Values in Spark Plug Data

Mass flow and equivalence ratio are significant parameters in operability of an RDE because they have direct influence on whether or not a detonation wave can form. If the mass flow is too low the wave will not be able to sustain itself. If the equivalence ratio is too rich or too lean, then the mixture may exist outside the flammability limits of the reactants, keeping combustion from occurring. Further, detonation cells are a function of equivalence ratio, and most mixtures have a minimum cell size at a specific equivalence ratio (usually near stoichiometry) away from which cell size will increase [22]. Therefore, certain mixtures may be within flammability limits, but the resultant detonation cell structure may be too large to propagate in the geometry of the RDE. It was the goal of the testing to define enough unique points so that the equivalence ratio and mass flow boundaries could be found. To search for these boundaries, the mass flow and equivalence ratio were varied by requesting specific mass flows on the flow controllers. Once

found, the boundaries could be compared to previous work by Dechert to make an assessment on the impact of the new injection scheme [1].

Initially the new injection scheme was used with the spark plug as the ignition source. The 0.75mm gap nozzle which created an $\varepsilon = 0.39$ area ratio was installed in the RDE for these tests. In this configuration, 32 test points were collected. From these an operating map showing which test points resulted in detonation was made. If a mass flow and equivalence ratio pair detonated once it was considered detonable, even if other attempts at the same conditions did not. To stay consistent with the operating maps created in previous work, the values used to define mass flow and equivalence ratio were based on the mass flows requested out of the controllers. These values will be referred to as requested values. Use of requested values assumed that the flow controllers kept the fuel and oxidizer flows reasonably close to the set points before and after detonation. This assumption was used by Dechert as well [1]. Figure 59 shows the operating map along with a map from the previous research [1]. The 0.75mm gap nozzle which created an area ratio of 0.39 was used by Dechert to generate the operating map in Figure 59. Not all 32 test points are visible in Figure 59 because the same requested mass flow and equivalence ratio points were tested multiple times. Of the 32 test points, there were only 17 unique requested mass flows and equivalence ratios, corresponding to the 17 data points on the map. This left 15 cases of repeated test conditions. However as will be shown, these repeated data points did not necessarily represent the same conditions and repeatability of a single condition was therefore not readily determined.

Comparing the maps, the new injection scheme appeared to create a similar operating mass flow range as the previous one when Φ was 1.2. In both maps, requested mass flows from 0.040 kg/s to 0.075 kg/s were detonable. As the equivalence ratio dropped to 1.1 in the new map, the mass flow range decreased to 0.045-0.065 kg/s. When Φ was 1.0 there was a smaller detonative range than when Φ was 1.2. This suggested that seeing less detonability as Φ moved away from

115

1.2 in the new data was consistent with the old data. This also implied that there may be an optimum Φ around 1.2 which was consistent with the old data as well. However, the limited nature number of data points made further conclusions difficult.
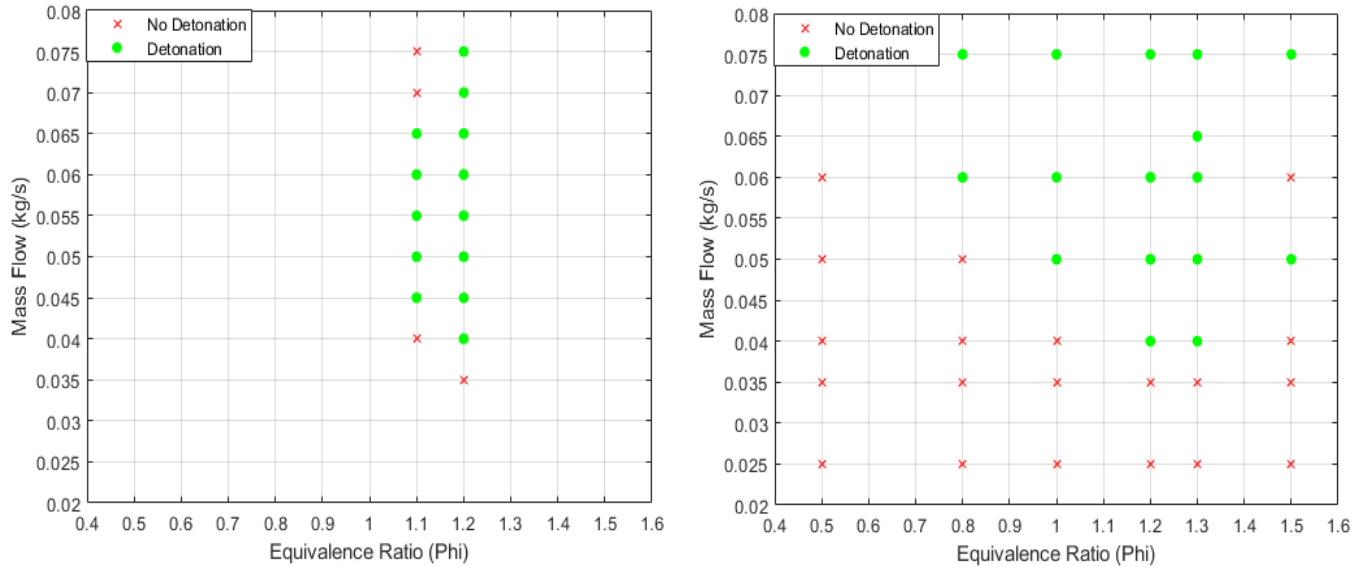
Fig. 59 Operating maps with spark plug ignition for **a)** Re-designed injection scheme. Mass flow and equivalence ratios are set values, not observed values and the $\varepsilon = 0.39$ nozzle was used. **b)** Original JIC scheme [1].

Section 3.2.3 discussed that the requested values on the controllers were not the same values as were measured, and that this difference was even more pronounced during detonating conditions. This threw into question the validity of the operating space defined in Figure 59. To determine the severity of the issue, mass flow data acquired from the logged measurements of the Alicat controllers (referred to as *measured* values) and the mass flow estimation methods of Section 3.2.3 (referred to as *estimated*) were used to make the plots in Figure 60. These graphs show the requested mass flows versus the measured and estimated values for both ignition and operating conditions.

Mass flow data in Figure 60 was extracted by aligning the mass flow and pressure histories of the same run. Figure 61 takes the mass flow and pressure histories from Figures 50 and 56 (each

from the same run) and aligns them in time to illustrate this process. For ignition conditions, data was taken immediately before detonation began. If no detonation occurred, ignition data was taken during a period of steady mass flow and pressure (not shown in Figure 61). Operating mass flows were taken from data after ignition and was further restricted to where the CTAP pressure was steady. Instances where data was taken during unsteady CTAP pressures are discussed in Section 4.3. Data extracted from this process was then used to in analysis such as that presented in Figure 60. The plots of Figure 60 include error bars on the observed mass flow values. Ignition and operating mass flows that were measured by the controllers were subject to the accuracies defined in Table 4, which were equal to $\pm0.16\%$ error in kg/s. Whereas, mass flows estimated by backing out the average discharge coefficient were subject to an averaged $\pm5\%$ error and mass flows correlated by the empirical $\frac{P_c}{P_T}$ relationship had an averaged $\pm10\%$ error. Section 3.2.2 reviewed the details for the different estimation methods.

Considering only the values that were measured, and not estimated, Figure 60 showed that actual flows were similar to the requested values at the point of ignition. For example, oxidizer flow had an average percent error of 1.5% from the requested values while the fuel flow had an average percent error of 6.9%. Most fuel flow values were higher than requested, and this was believed to be due to the operating sequence of Section 3.1.5 firing the spark plug before the fuel controller had time to settle the flow. The oxidizer controller tended to have a larger pressure differential across it, and therefore was able to settle its flow faster. During detonating conditions, the percent errors increased to 13.1% and 22.3% for the oxidizer and fuel flows respectively. Both graphs showed that error from requested values increased as requested values increased. Error increased with increasing requested values because higher flow rates resulted in larger plenum pressures during detonations. This lowered the pressure differential across the controllers and further diminished their ability to track the requested value.

Fig. 60 Observed mass flows versus requested mass flows based on measured and estimated data before and after detonation. Spark plug data.

Fig. 61 Pressure and mass flow time histories aligned in time. Shows how ignition and operating pressures and mass flow values were extracted for a given run.

Section 4.1.2 Operating Space Based on Requested Values in the Pre-Detonator Data

With the pre-detonator installed a new sweep of requested equivalence ratios from 0.8 through 1.4 was performed over a mass flow range from 0.025-0.075 kg/s. Successful detonations were elusive, even at mass flows and equivalence ratios that had previously detonated. This made it difficult to maintain an ordered approach to sweeping the desired operating space. Instead, the

data was collected in a hunt and peck method, searching for any test point that would result in detonation. Once one was found, deviations centering on that test point were made to find additional points. It was later discovered that the inconsistent repeatability of the same test point was due to the inconsistency in the actual flow conditions from the controllers and the changes to exit area from erosion of the outerbody and nozzle.

Section 3.1.6 reviewed that nozzles influenced the ignition channel pressure by setting the exit area. However, depending on the specific outerbody, the current level of erosion on that outerbody, and the level of erosion on the nozzle, the resultant exit area was not equivalent to what was expected based on the nozzle diameter. As a result, the chamber pressure for a given mass flow and nozzle size was inconsistent from run to run. This further complicated inconsistencies in testing conditions. Therefore, in an effort to combat the changes to the exit area without having to replace the entire outerbody hardware, nozzle sizes were varied to maintain channel pressures inside a window of 345 kPa to 550 kPa. This window was chosen based on the growing bank of successful detonations with similar pressures. Nozzles with area ratios of $\varepsilon = 0.26$, 0.33, and 0.39 were used. See Section 3.1.6 for further details on how nozzle diameter impacted exit area. The implications of channel pressure and mass flow are discussed further in Section 4.3.

Forty requested conditions were tested with the pre-detonator. Of the 40 conditions, 20 were found to result in successful ignition over a range of mass flows from 0.050 kg/s to 0.075 kg/s. Figure 62 summarizes the requested test points in an operating map similar to those shown in Figure 59. Like the spark plug data, a single test point usually had several measured/estimated data points that resulted from it, either from multiple runs at those requested conditions or multiple sample points from a single detonation. When compared to the operating map from Dechert, shown in Figure 59, Figure 62 showed that the addition of the pre-detonator pushed the operating window to more fuel lean equivalence ratios with values of 0.9 and 1.0 instead of 1.2 and 1.3 [1].

Additionally, the mass flow range of 0.050 kg/s to 0.075 kg/s in Figure 62 was more restrictive than the ranges of 0.040 kg/s to 0.075 kg/s reported by Dechert. Although these were only requested conditions, the trends were good approximations of the ones presented in Section 4.1.3.
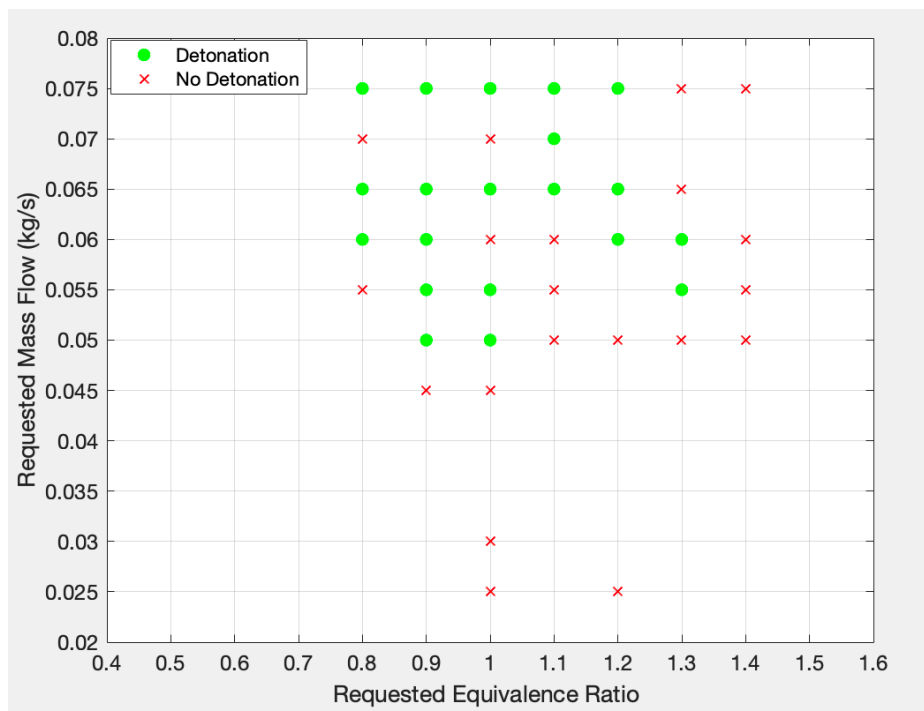
Fig. 62 Operating map with requested values using pre-detonator. Nozzle sizes varied between $\varepsilon = 0.26$, 0.33, and 0.39.

Once again, the estimation methods of Section 3.2.2 were employed to recover mass flow data that was not recorded by the Alicat controllers. Measurement techniques were consistent between the spark plug data set and the pre-detonator data set, and therefore the same measurement error values derived for the spark plug data were used here. With these methods, 93 measured data points were evaluated, 50 of which were taken during successful detonations. Figure 63 plots the same relationship as Figure 60 but with the pre-detonator data. Measured mass flow from Figures 60 and 63 were used to replot Figures 59 and 62 as well, these are presented in the next section.

Starting with the plots for the oxidizer in Figure 63, an average percent error of 3.5% before detonation was found. There was a bias for more mass flow than requested. This was a larger

percent error than in the spark plug data. After detonation, the oxidizer percent error in Figure 63 increased to 18.4% with a bias for less flow than requested. Receiving less oxidizer than requested during detonation was expected due to the increased plenum pressures limiting the controller's pressure differential. However, in comparison to the spark plug configuration which had an error of 13.1%, the new percent error of 18.4% was 5% worse. With respect to fuel flow, ignition mass flows were on average 31% higher than requested. While detonating fuel flows were 32% lower than requested. Both fuel flow percent errors were worse than in the spark plug data, but the pre-ignition fuel flow error specifically had a large 9% increase.

Error from requested values, specifically the ignition fuel flow, may have resulted from the firing sequence triggering the pre-detonator before the controllers had fully stabilized. This was postulated in the spark plug data as well. However, pressure histories showed that even extended trigger delay times resulted in erroneous flows. Additionally, the significant increase in the fuel controller's ignition flow error when compared to ignition flows in the spark plug data, which used approximately the same delay times, suggested that it may have become damaged over the course of testing. In any case, the result was that the actual fuel flow stayed within a window of 6-7.5 g/s nearly independent of the requested flow.

Detonation mass flows showed that the back-pressure effects had increased in comparison with to the spark plug data as well. This was attributed to better sealing of the detonation chamber that resulted from replacing the ¼" spark plug hole with a 1/16" pre-det hole. This change increased the pre-ignition chamber from an average 380 kPa in the spark plug data to an average 460 kPa in the pre-detonator data. Detonation averages also increased from 1.19 kPa to 1.08 kPa. As a result, the back pressure on the controllers was increased and the differential across them was decreased. These effects limited the controller effectiveness and explained the increased percent error seen in the denotation mass flows when comparing the pre-det data to the spark plug data.

<div style="text-align:center">

Before Detonation

After Detonation

</div>
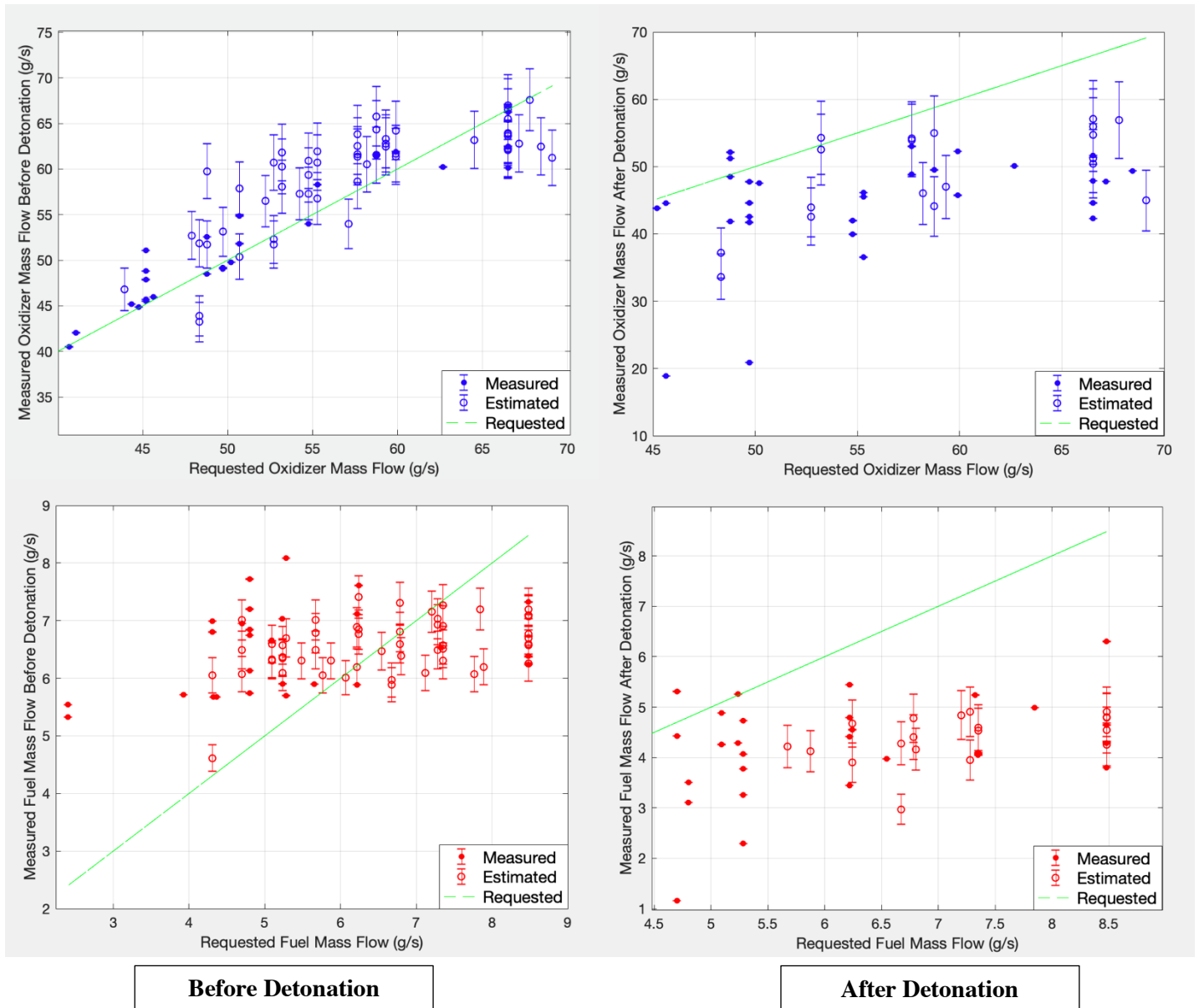
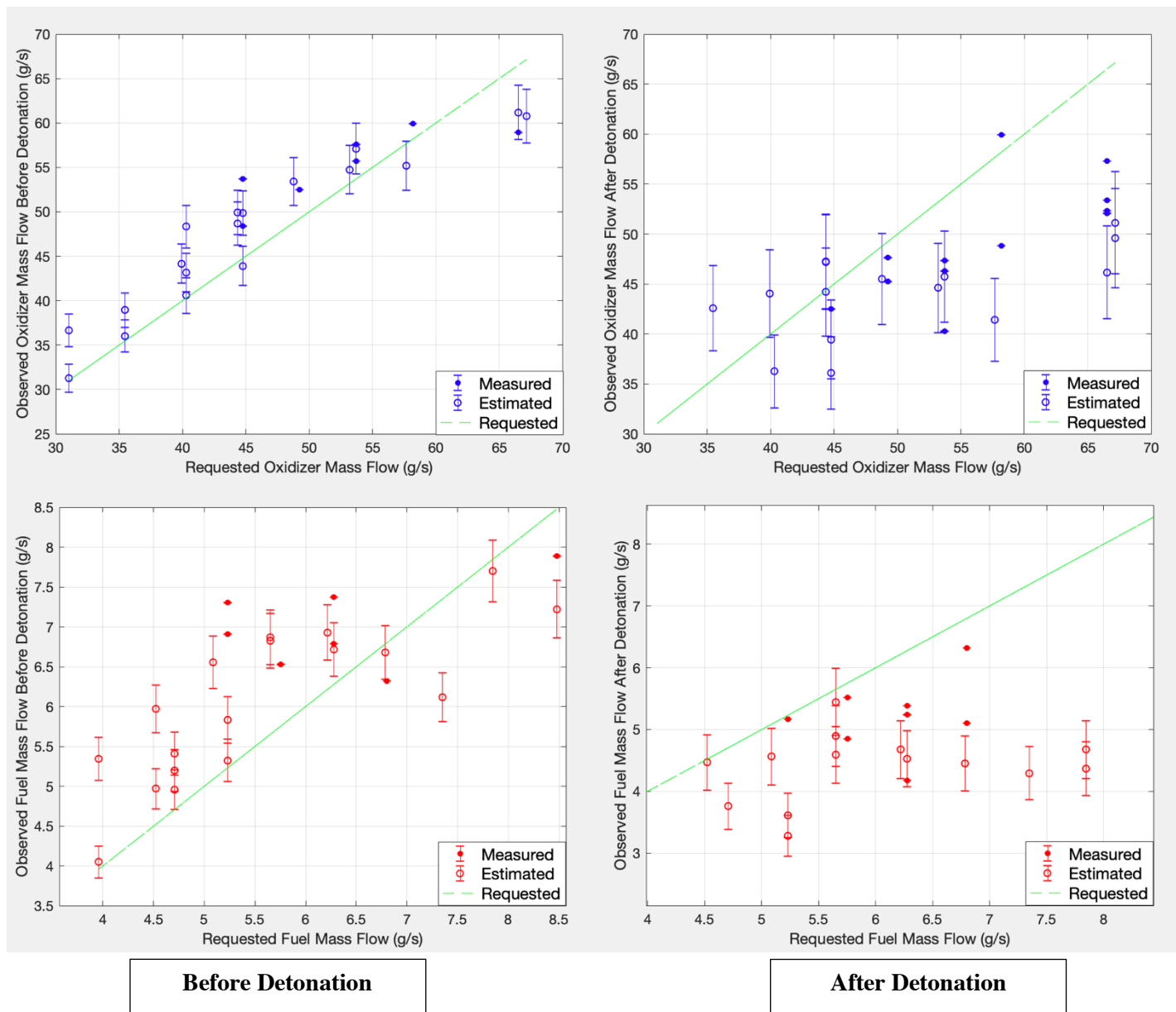**Fig. 63** Observed mass flows versus requested mass flows based on measured and estimated data before and after detonation for the pre-detonator data

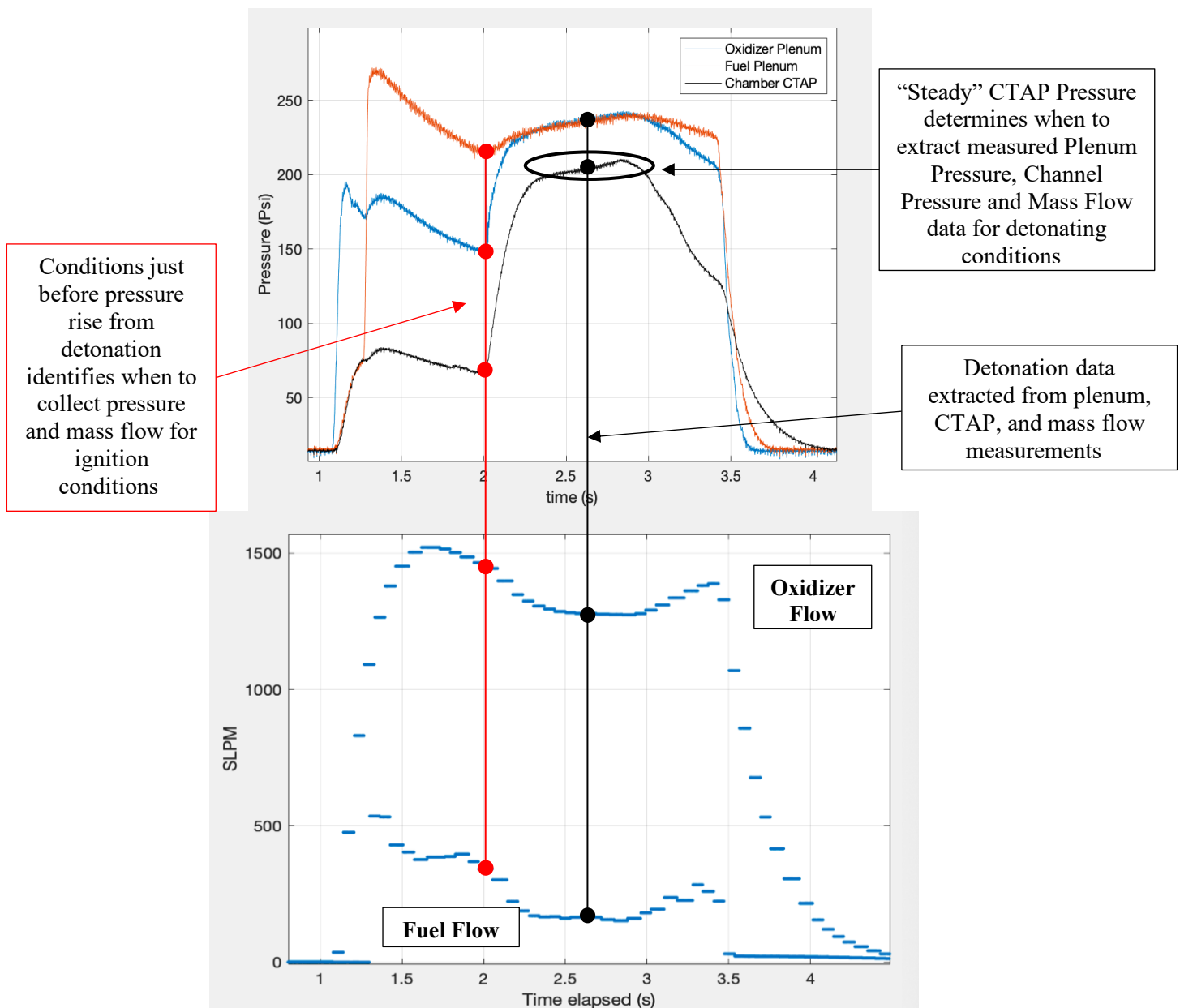**Section 4.1.3 Ignition and Operating Maps with Measured Mass Flow**

It was clear that the requested values did not accurately represent the flow rates seen by the RDE. To account for this, measured and estimated mass flows were used instead of the requested values. Doing so improved the accuracy of mass flow data points in all cases even with the error of the estimation methods considered. Additionally, given the two degrees of freedom from the

independent controllers and feed lines, each test run had its own unique flow condition defined by its new observed fuel and oxidizer measurements. This expanded the data sets from 17 points to 32 in the spark plug case and from 40 to 93 in the pre-detonator case. Furthermore, because there were different sets of observed mass flows before and after ignition that were now captured by the new data set, two new operating maps could be made. One for the ignition conditions and one for the detonating conditions.

The maps for the spark plug data are shown in Figure 64 and Figure 65. The first map represents the set of mass flow and equivalence ratio pairs for ignition conditions and shows which points resulted in successful detonation, and which points did not. This plot will be referred to as the ignition map. The second plot shows the conditions seen during a detonation and will be called the operating map. The errors for the mass flow are the same as were described for Figure 60. For equivalence ratio, implementation of the potential errors of mass flow into the definition of equivalence ratio shown below in Equation 22, showed that in worst case situations errors would double to 0.32%, 10%, and 20% for the measured, analytically estimated, and empirically correlated equivalence ratios, respectively.

$$\phi = \frac{\frac{\dot{m}_{fuel}}{\dot{m}_{Ox}}}{\left(\frac{F}{A}\right)_{st}} \tag{22}$$
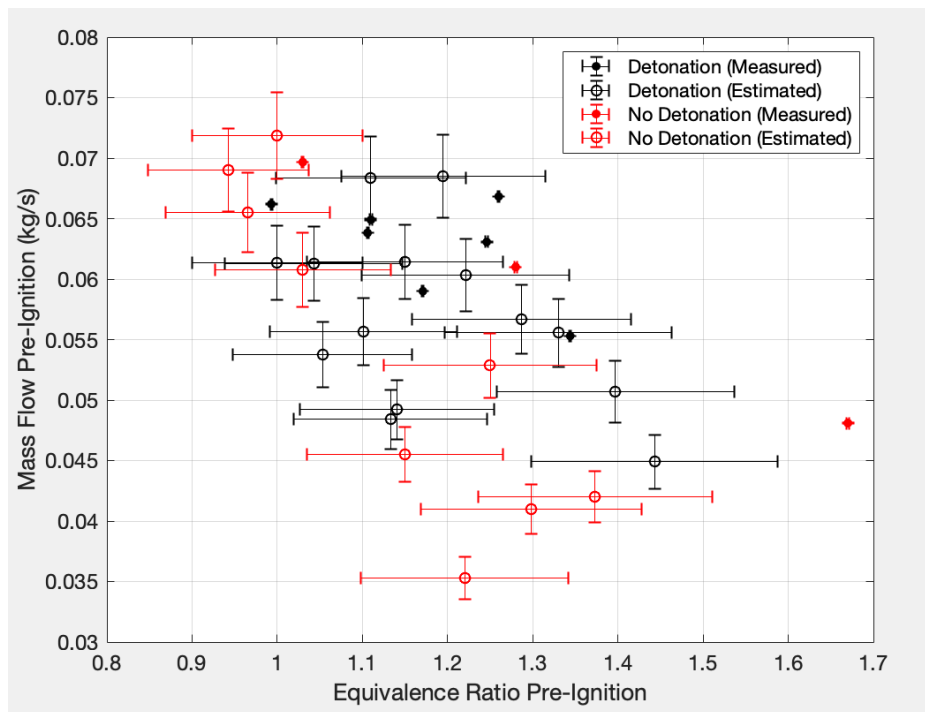
Fig. 64 Ignition Map of new injection scheme with spark plug ignition method using measured mass flow.
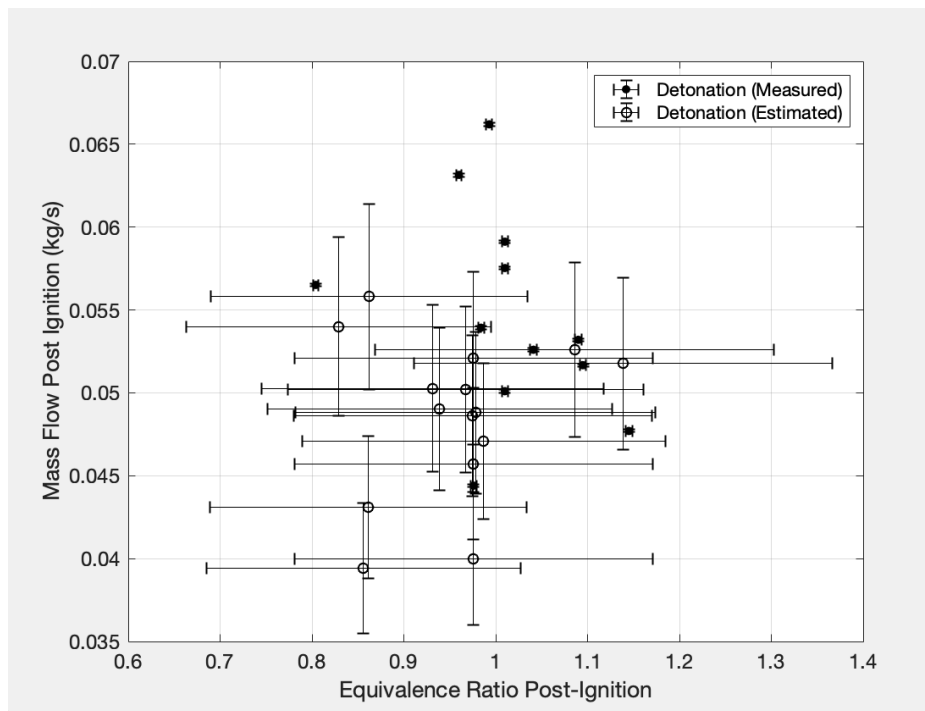
Fig. 65 Operating Map of new injection scheme with spark plug ignition using measured mass flow.

Comparing the operating map in Figures 59 with the ignition map in Figure 64, it was found that the higher than requested fuel flows in Figure 60 pushed the ignition space towards fuel rich equivalence ratios. Furthermore, the ignition map showed that the window of detonable mass flows was approximately 0.045 kg/s to 0.075 kg/s. This mass flow range was in agreement with the operating map in Figure 59, within error. The range of detonable equivalence ratios was from 0.9 to 1.6. Large equivalence ratio error bars significantly expanded this range. When only measured data points were considered it shrank to 1.0 to 1.35. Therefore, in comparison to the operating map from Dechert, the new ignition map had a smaller range of detonable equivalence ratios and mass flows. However, the lack of data points made further interpretation difficult. Further ignition behavior comparison is reserved for later in the section when the larger pre-detonator data set is presented. The overlap of detonable and non-detonable data points were also investigated but results are reserved for Section 4.3.

Examining Figure 65, the detonation's influence pushed the operable mass flows towards more fuel lean and stoichiometric conditions when compared to the ignition map. If only measured values were considered, operating equivalence ratios spanned values of to 0.8-1.15 over mass flows from 0.045 kg/s to 0.065 kg/s. This implied the more fuel lean and fuel rich conditions suggested by the error bars may not be as likely as the more stoichiometric values. Additionally, when error was considered, the mass flow range of the operating space was 0.035-0.065 kg/s. This meant that the low mass flow values, below 0.045 kg/s, were not as likely either. The transition to more stoichiometric conditions at lower mass flows between ignition and detonation was consistent with the mass flow plots shown in Figure 60.

When compared to the operating space reported by Dechert, the operating space of Figure 65 is significantly smaller in both equivalence ratio and mass flow. Again, this was mostly a factor of the range of tested mass flows being much less than used by Dechert [1], and that the operating

map in Figure 65 used measured mass flows and equivalence ratios. Dechert only used the requested values set into the controllers and therefore would not have captured the back-pressuring effects of the detonation discussed so far. Overall the limited range of test points in the spark plug data set limited the depth of analysis on operability of the RDE beyond the inclusion of measured and estimated mass flow values shown in the figures above. Further analysis required the expanded data set from the pre-detonator tests.

Figure 66 shows the ignition map made from the pre-detonator data. Due to the number of data points in the ignition map, successful detonations and unsuccessful detonations were plotted separately in addition to being plotted together. Error bars were implemented using the same values used for the spark plug data. Inspection of the ignition map revealed several interesting characteristics. First, the set of tested conditions backed out from the mass flow and pressure data, for both successful and unsuccessful runs, tended to decrease in equivalence ratio as mass flow increased. To understand why, the ignition mass flow trends in the plots of Figure 63 were considered. In the plots, the ignition fuel flows were consistently between values of 6-7.5 g/s, regardless of requested mass flow, while the oxidizer mass flow tended to follow the requested values. As a result, when total requested mass flows were low, oxidizer flows were appropriately low, but the fuel flows were high. This resulted in fuel rich mixtures at low total mass flows. As the requested mass flow increased, the oxidizer mass flow tracked within 3.5%, but the fuel flow remained in the same 6-7.5 g/s window. In response, the equivalence ratios became more fuel lean as the mass flow increased. By coincidence, at the top end of requested mass flows, a fuel flow rate of 6-7.5 g/s created a near stoichiometric mixture with the subsequent oxidizer flow. The majority of requested test points were at higher mass flows, as can be seen in Figure 62. Therefore, those test points coalesced at equivalence ratios near one with mass flows above 0.06 kg/s. These trends were a consequence of the flow controllers.
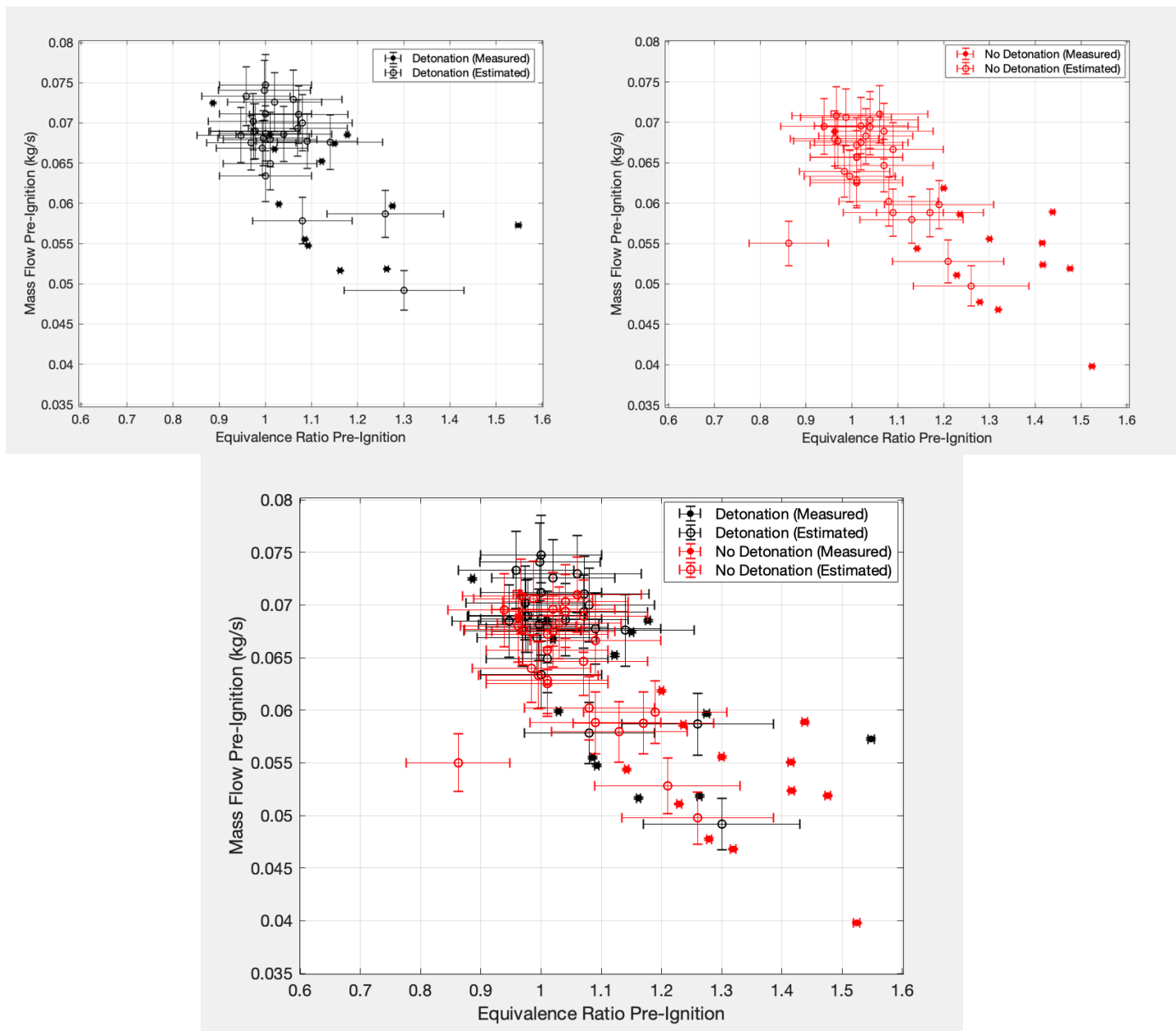
Fig. 66 Pre-Detonator ignition map using estimated and measured values. Map plotted with successful and unsuccessful detonations separately and together.

The pre-detonator data's ignition map had detonable conditions over equivalence ratios from 0.9 to 1.55 and mass flows from 0.050 kg/s to 0.075 kg/s. Fuel rich conditions had lower mass flows than more fuel lean conditions for the reasons just discussed in the previous paragraph. In comparison to the spark plug data, the detonable range of equivalence ratios was wider, but the range of mass flows was smaller. In comparison to Dechert, the range of equivalence ratios was

similar, but the mass flow range was still smaller. The range of detonable tests spanning almost the same range as Dechert was encouraging and showed promise that the ignition space was not compromised by the new injection scheme. The limited range of mass flow was attributed to the flow controller dynamics.

The most significant characteristic of the ignition map was the large amount of overlap of successful and unsuccessful ignition attempts. Unlike the ignition map in the spark plug data, which appeared to have a detonable window forming between mass flows of 0.045 kg/s to 0.065 kg/s and equivalence ratios from 1.0 to 1.35, the pre-detonator data had no distinguishable boundaries. There was some evidence that equivalence ratios beyond 1.4 were too fuel rich for successful detonation as there were multiple test points with no success in that region. However, one successful attempt at the 1.55 and 0.057 kg/s point was recorded. Furthermore, this attempt was measured by the Alicat controllers making it unlikely to be largely affected by measurement error. Therefore, it was determined that had more data points been collected in that area there was likely to be more success. These observations suggested there were other mechanisms determining the ignition behavior beyond the mass flow and equivalence ratio. Such mechanisms include changes to exit area due to erosion and the subsequent impact on channel pressure and injection pressure ratio. Evidence for these factors are discussed later in Section 4.3.

Figure 67 shows the operating map for the pre-detonator data. Error bars were included in line with previous figures. The boundaries of operation were found to extend from mass flows of 0.035 kg/s to 0.068 kg/s between equivalence ratios of 0.6 to 1.4 when all data points were considered. However, the majority of the data was found to focus more inside the window between 0.045 kg/s to 0.065 kg/s and equivalence ratios of 0.7 to 1.1. The operating equivalence ratios therefore centered on a value of 0.85 which was more fuel lean than the spark plug data's stochiometric average. Furthermore, the range of equivalence ratios had been expanded when

compared to the spark plug operating map, with multiple operating conditions extending below the spark plug data's boundary of ~0.7. Interestingly, the new operating map only extended beyond an equivalence ratio of 1.2 when error bars were considered. Therefore, even though the fuel lean regions of the operating space had expanded, the fuel rich space had remained similar between the two data sets. With respect to mass flow, the range of 0.045 kg/s to 0.065 kg/s was consistent with the spark plug data. Lastly, in comparison to the operating map from Dechert, the space in Figure 67 was more fuel lean and had a smaller range of detonable mass flows.
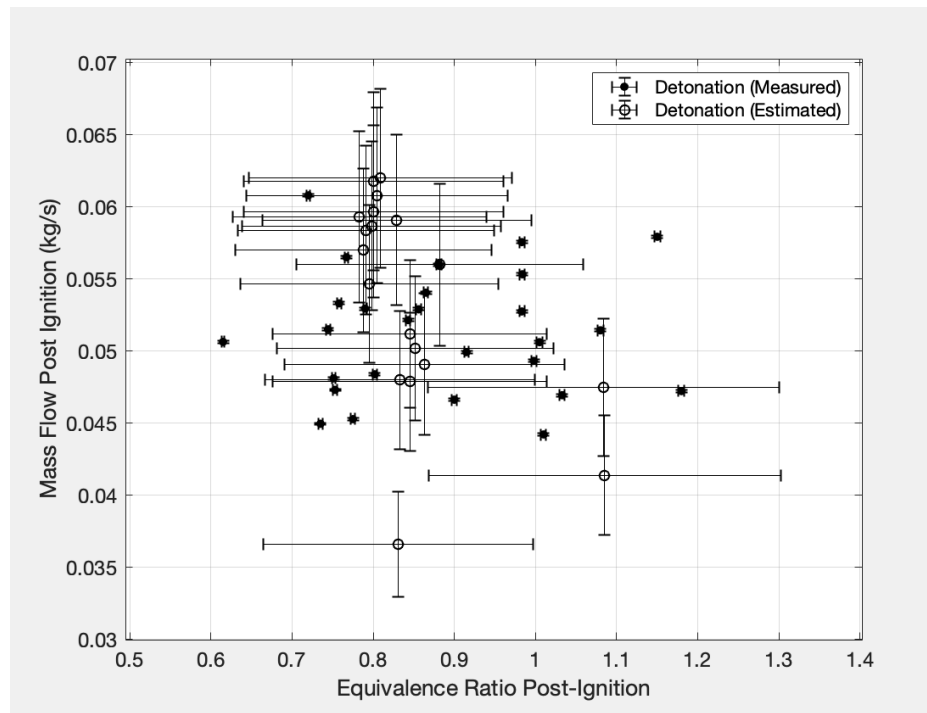
Fig. 67 Pre-Detonator operating map using estimated and measured values.

Once again, it was believed the interplay between the chamber pressures and the flow controllers were the main drivers for the operating map's character, not the injection scheme. As discussed, the average channel pressure had increased when compared to the spark plug data due to the change from a ¼" spark plug hole to a 1/16" pre-detonator hole. The higher pressures led to increased error values when compared to the spark plug data. Referring to Figure 60 and 63, errors during detonation, between the spark plug and pre-detonator set up, increased from 12% to 18%

and fuel error increased from 22% to 32%. The larger increase in fuel error than oxidizer error, in

for the pre-detonator data meant the resultant equivalence ratios trended more fuel lean than the

spark plug data. It was this effect that caused the average equivalence ratios to decrease to 0.85.

Although mass flow errors were greater in both flows for the pre-detonator data, because the

average requested total flow was higher in the pre-detonator data than the spark plug data, the

observed mass flow ranges were approximately the same.

Ultimately, the issues from the flow controllers limited the observable operating space to

what was presented in Figures 65 and 67. As discussed, this was due to the back-pressuring effect

forcing full duty cycle actuation on the flow controller valves. As a result, direct changes to

operating conditions were not possible during detonation as the controllers could not respond.

Furthermore, the differences between requested and measured mass flows would have been present

in the results presented by Dechert as well. Therefore, comparison to the previous requested value

maps was not likely to yield accurate results. This made assessment of the injection scheme

inconclusive. Therefore, further testing with the current flow control design would likely not yield

new information and additional testing with improved flow control is required to expand on the

results shown.

Section 4.2 Analysis of Wave Modes and Frequencies

In addition to improving the operability of the Micro-RDE, the current work was also

concerned with improving the behavior of the detonation wave. Dechert found the wave to

predominantly exist either in a clapping mode or counter rotating mode [1]. These propagation

modes are characterized by the presence of two waves rotating in the opposite direction at or near

the same frequency. When they're frequencies are the same, they pass by each other at the same

two points in the detonation channel giving the appearance of colliding or clapping. When the

frequencies are unequal, the two waves appear as two counter rotating waves where the point of contact rotates as well. These wave behaviors were found to correlate with frequencies around 13-14 kHz, which was 50-60% CJ velocity in the Micro-RDE's geometry and were considered unstable [1]. Dechert hypothesized that the protrusion of the spark plug, poor mixing, and small channel radius were contributing to the prevalence of the clapping mode [1].

Therefore, the current work was interested in the prevalence of clapping and counter rotating modes, along with any new modes, that resulted with the new injection scheme. This would help determine if the new injection scheme had helped improve wave stability. It was also desired to see if removal of the spark plug had an impact on the prevalence of these modes. Furthermore, as discussed in Chapter 3, wave mode stability was defined as consistent propagation in single or multiple wave mode with a consistent wave direction. Wave modes that did not meet this definition were considered unstable. Section 3.3.2 has further details on the motivations for this specific definition. This section will present the observed wave modes and frequencies obtained from analyzing the high-speed imagery. Section 4.2.1 will cover the spark plug's wave modes and frequencies and also introduce the wave mode scoring system. Section 4.2.2 presents the modes and frequencies from the pre-detonator configuration and applies the same scoring system. Comparisons between the two data sets and previous work are made throughout both sections to assess the impact of the new injection scheme and ignition method.

Section 4.2.1 Wave Modes and Frequencies: Spark Plug Configuration

Using the Phantom v711 high speed camera and video processing techniques detailed in Section 3.3.2 wave behavior and frequency was documented for each run with a detonation. Of the 32 test points in the spark plug data set, 17 videos were documented. Some of these cases were obtained from the same detonation, but at different times during the detonation and therefore had

different conditions. In the set of recorded videos, six unique wave modes were observed and had a corresponding frequency range of 13.0 kHz to 16.8 kHz. To ensure that mass flow and equivalence ratio data could be properly correlated to the observed wave modes, the guidelines discussed in Section 3.3.2 were employed. All wave modes in the spark plug data set were able to be correlated to mass flow and equivalence ratio data.

To better analyze the relationship between wave mode, wave frequency, and other operating parameters, such as equivalence ratio and mass flow, a scoring system was developed. This scoring system was numbered from 0-10 and used the definition of wave stability defined in Chapter 3 as a score of 10. From there, observed wave modes were ranked by how "far" away they were from a stable wave mode and a score of 10. Table 7 lists the observed wave modes in addition to their corresponding wave mode score. The modes and scores were developed with knowledge of both the spark plug and pre-detonation test conditions. Only six wave modes were observed in the spark plug data set with the additional modes observed in the pre-detonation data set.

As shown in the table a pure deflagration mode received a score of 0 and a pure clapping mode received a score of 4. If a mode showed a potential to degrade into a deflagration mode it was considered more unstable than those modes which were always detonating. So even though clapping modes were discussed as undesirable, they still represented a detonative mode that was resistant to transitions to a deflagrative mode, and therefore ranked above those modes which were not. However, determination between the scores was ultimately subjective. Referring to Table 7, only modes marked with an * were observed in the spark plug data. Modes observed in the pre-detonator data set were denoted with a ^ and will be discussed in detail in Section 4.2.2. In both data sets, a mode with multiple waves with the same direction was not observed, and so a single wave mode with stable frequency was the pinnacle of wave scores.

Table 7: List of observed wave modes and corresponding wave mode score based on level of detonation instability observed. Higher values are less unstable, score 10 is stable.

Mode Description	Score
Stable single wave mode	10*^
Single wave mode with limited counter rotation and clapping. Potential for wave direction reversal.	9*^
Single wave mode with intermittent counter rotation and clapping. Potential for wave direction reversal.	8*^
Single-wave galloping mode (wave varies frequency within 5 rotations)	7^
Alternating transition between single wave mode and counter rotating two wave mode. Potential for clapping.	6*^
Dominant clapping mode with intermittent single wave rotations	5*^
Pure clapping mode	4*^
Continuous transitions between, counter rotating/clapping/galloping behavior. No deflagration.	3^
1 wave mode that transitions to deflagration then transitions back to detonation in sequence (Repeated DDT events)	2^
No dominant mode with intermittent direction reversal /clapping/ /counter rotating waves and transitions to deflagration	1^
Pure deflagrative mode	0^

*Observed in Spark Plug Data Set
^ Observed in Pre-Detonation Data Set

The six modes observed in the spark plug data were the stable single wave mode, single wave mode with limited counter rotation and clapping, single wave mode with intermittent counter rotation and clapping, alternating transition between single wave and counter rotating two wave modes, a clapping mode with intermittent single wave rotations, and a pure clapping mode. Wave modes such as those with scores of 9 and 8, and 6 and 5 were similar and were differentiated by the persistence of the less stable behavior, with the terminology *limited* implying less instability than *intermittent*. The stable single wave mode (score of 10) and single wave mode with intermittent counter rotation and clapping (score of 8) were the two most frequent modes observed, being documented six times each. Application of the scoring schema in Table 7 to Dechert's description of the wave modes in the original Micro-RDE showed that the previous design never scored above a 6, with most detonations scoring a 4 or 5. Therefore, the newly observed modes

with corresponding scores of 10, 9, and 8 in the spark plug data were novel to the current work and represented an improvement over the previous design.

An objective of the Micro-RDE was to reach operating frequencies above 20 kHz. Previously, the fastest frequency seen in the RDE was 14 kHz [1]. With the new injection scheme, a range of frequencies from 13 kHz to 16.8 kHz was observed. Compared with the previous design's range of 11.7-14 kHz, there appeared to be a marked improvement in frequency. Furthermore, the fastest wave frequency of 16.8 kHz had a corresponding wave score of 10. Initially this was encouraging because it was an example of a stable wave at a frequency much closer to the design goal than previously attained, and implied that high frequencies and wave modes were related. However, analysis of the other frequencies showed that this was an outlier, and that when ignored, the maximum frequency dropped to 15 kHz. Most detonations with the new injection scheme tended to have frequencies between 13-15 kHz, averaging out around the same 14 kHz seen by Dechert. This suggested that frequency and stability were not intrinsically linked, and that while the stability appeared to improve significantly with the new injection scheme, wave frequencies had not seen the same amount of improvement.

To illustrate the trend between wave frequency and wave mode, the wave scores from the spark plug data set were plotted against their corresponding wave frequency, as measured by the methods of Section 3.3.2. The results are shown in Figure 68. From Figure 68, it was clear that a faster frequency, above ~13.8 kHz, corresponded to a more stable wave mode, and a slower frequency, below 13.8 kHz, corresponded to a more unstable wave mode. However, while an unstable wave mode implied a slower frequency, a stable wave mode did not. For example, no wave with consistent clapping behavior (score of 6 or lower) had a frequency above 13.8 kHz, but a wave mode with a score of 10 could have a frequency as low as 13.3 kHz or as high as 16.8 kHz. Therefore, stable wave behavior appeared to be a pre-requisite for higher frequencies and slower

wave frequencies were a pre-requisite for clapping behavior, but higher frequencies were not required to reach the desired stable single wave mode. This was particularly interesting because it suggested clapping behavior was dependent on frequency, but stable single wave behavior was not. Figure 68 also showed that 13 of the 16 points plotted had a score of 8 or higher, which highlighted the clear improvement over the previous injection scheme.
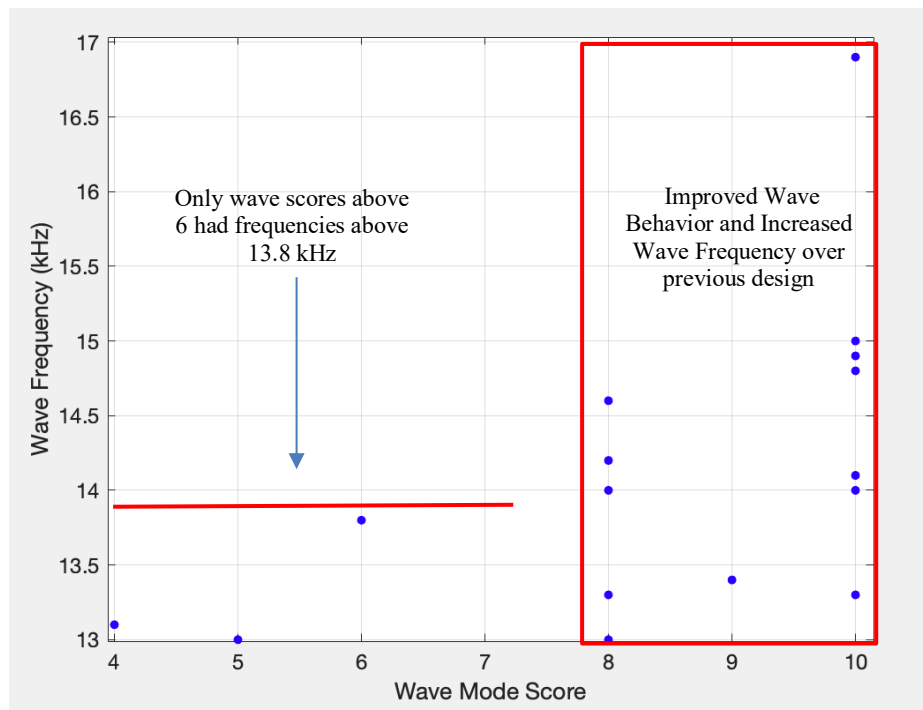
Fig. 68 Plot of wave speed versus wave mode score for spark plug detonations.

To determine if equivalence ratio and mass flow at the point of ignition had impacted the wave modes observed, Figure 69 plotted the ignition map from Figure 64. Error bars were removed for clarity and each wave mode observed in the spark plug data was denoted by a unique symbol. (Some points have multiple symbols overlayed the same ignition conditions. This was because some runs had multiple wave modes associated with it and therefore the same ignition condition could have multiple scores.) Only wave modes with scores of 10, 9, 8, 6, 5, and 4 were observed and therefore only those scores are shown. Figure 69 showed no clear trend in equivalence ratios

and mass flows that would lead to a particular score. For example, wave scores of 10 were observed over a range of mass flows from 0.055 kg/s to 0.067 kg/s and equivalence ratios of 0.99 to 1.33. This was essentially the same ignition space discussed in Section 4.1.1 (when error bars were removed) with a higher minimum mass flow and suggested higher wave modes occurred at higher mass flows. However, the lowest ignition mass flow of 0.045 kg/s, was associated with a score of 8, which meant that favorable wave scores were still achievable at the lower observed mass flows. In general, the limited amount of data points also limited the conclusions that could be drawn, and further analysis is presented in Section 4.2.2 with the pre-detonator data. Operating conditions are analyzed using both the pre-detonator and spark plug data at the end of Section 4.2.2.
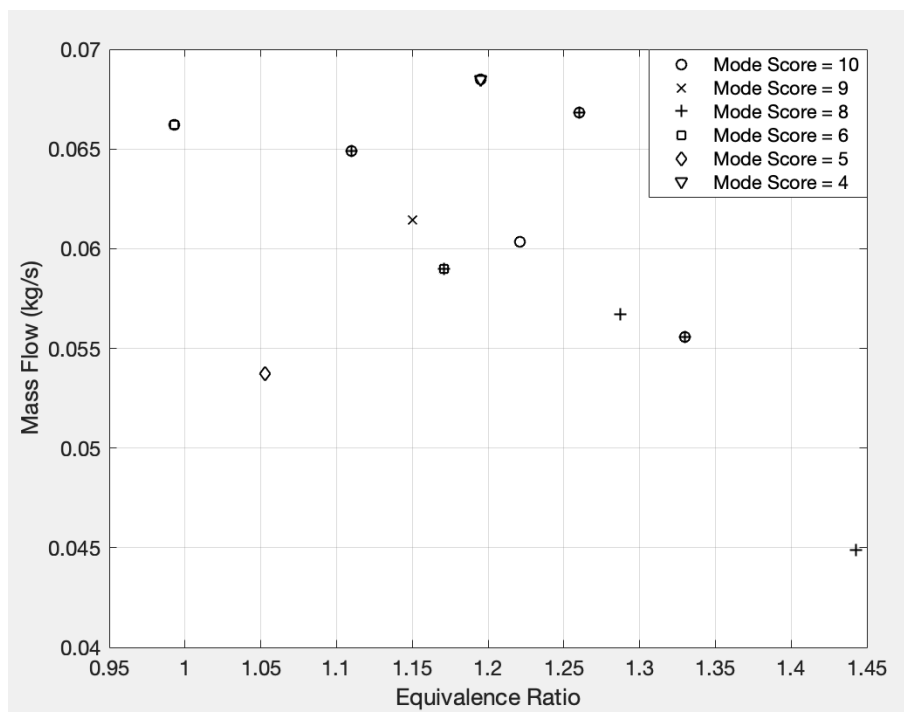
Fig. 69 Ignition map with mode scores overlaid. Wave scores of 10 observed over $0.99 < \Phi < 1.33$ and $0.055 < \dot{m} < 0.067$ kg/s

When the outlier case with a frequency 16.8 kHz was investigated, it was found to have additional irregularities. First, this particular wave behavior was observed during a 2.44s run, which was the longest run of both data sets. Due to the run's duration, it also had the most severe erosion damage. The erosion damage caused low chamber pressures at the point in time where the

wave frequency was measured. For example, the CTAP reading was 670 kPa, which was nearly half of what was usually measured during a detonation. The phenomenon of longer runs causing erosion damage that increased the exit area and decreased the channel pressure was repeated in multiple instances in pre-detonator data. This interaction frequently led to increased wave frequency such as in the case of the 2.44 second run. Further details are reserved for Section 4.3.

Analysis of the high-speed imagery also found that clapping waves did not always pass each other at the spark plug. Furthermore, when the collision location did not coincide with the spark plug, the wave mode exhibited single wave tendencies, and was more likely to earn a wave scores of 5, or 6. In instances where the collision did coincide with the spark plug it tended to not have any single wave behavior and earned a wave score of 4. For the example in Figure 70, an example sequence is shown. In the sequence, the wave was alternating between clapping and single wave modes and had a collision location nearly 60 degrees clockwise from the spark plug location. The variability in the clapping behavior and collision point was distinct from the previous results from Dechert which found that the spark plug location almost always coincided with where the waves met, and single wave tendencies were rare [1]. Therefore, the difference was attributed to the new injection scheme.

In addition, there were instances of the detonation wave appearing to run underneath the spark plug, which sat an axial distance of 11 mm above the injectors at its lowest point. This was the same axial location relative to the injectors as Dechert [1]. A sequence of high-speed images showing a wave potentially running below the spark plug is shown in Figure 71. In the figure, the wave can be seen propagating uninterrupted through the erosion zone caused by the spark plug. Additionally, this erosion zone had completely eroded away the outerbody wall, leaving U shaped gap in the outerbody, shown in the color picture of Figure 71. Despite this, the wave in the chamber was shown to propagate smoothly around the entire circumference and earned a wave score of 10.

It was determined that because the wave's behavior was not influenced by the spark plug as it passed by, it was running underneath it. A lower fill height resulting from the new injection scheme was believed responsible for the lower running wave. More details are presented in Section 4.3.
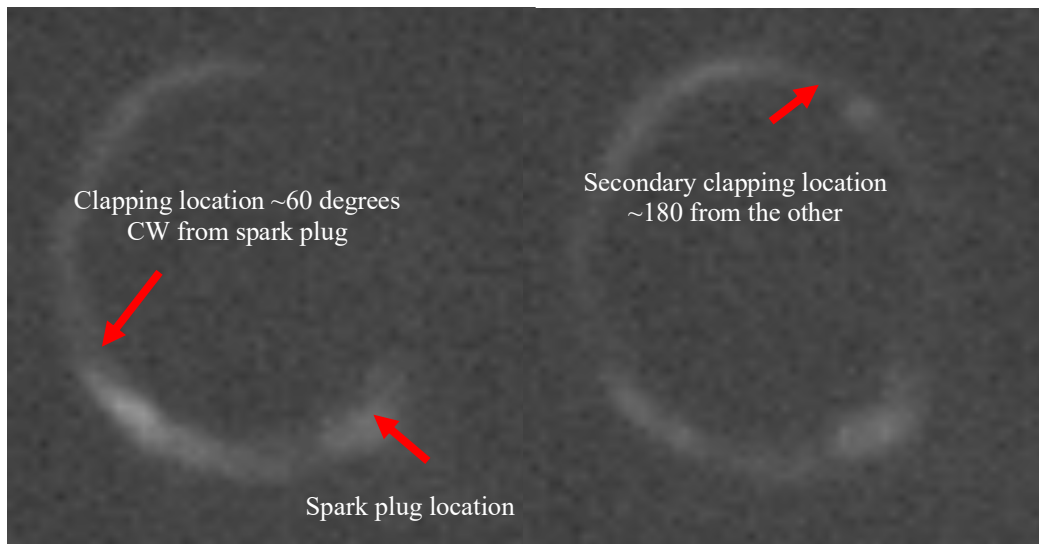
Fig. 70 Two images showing clapping locations not at the spark plug. Imagers were taken when counter rotating waves collided.

Putting the observations of the clapping behavior and instances such as in Figure 71 together suggested that the wave's ability to run beneath the spark plug kept the prevalence and severity of clapping modes down. When the wave did clap on the spark plug, it may have indicated that the wave's location had risen in the channel, allowing it to interact more directly with the spark plug. If this was the case, it explained why instances where the wave clapped on the spark plug were less likely to exhibit single wave tendencies as the spark plug was obstructing the path, as Dechert postulated [1]. Unfortunately, there were no direct measurements of the wave's location. However, burn markings, such as the ones in Figure 48, on fuel/oxidizer manifolds showed supporting evidence that the wave may be propagating at an axial station well below the spark plug. If the wave could be conclusively found to propagate at such a location, it would

suggest the mixing length had been significantly reduced. This would ultimately show that the new

injection scheme had improved the mixing quality. This is expanded on in Section 4.3.
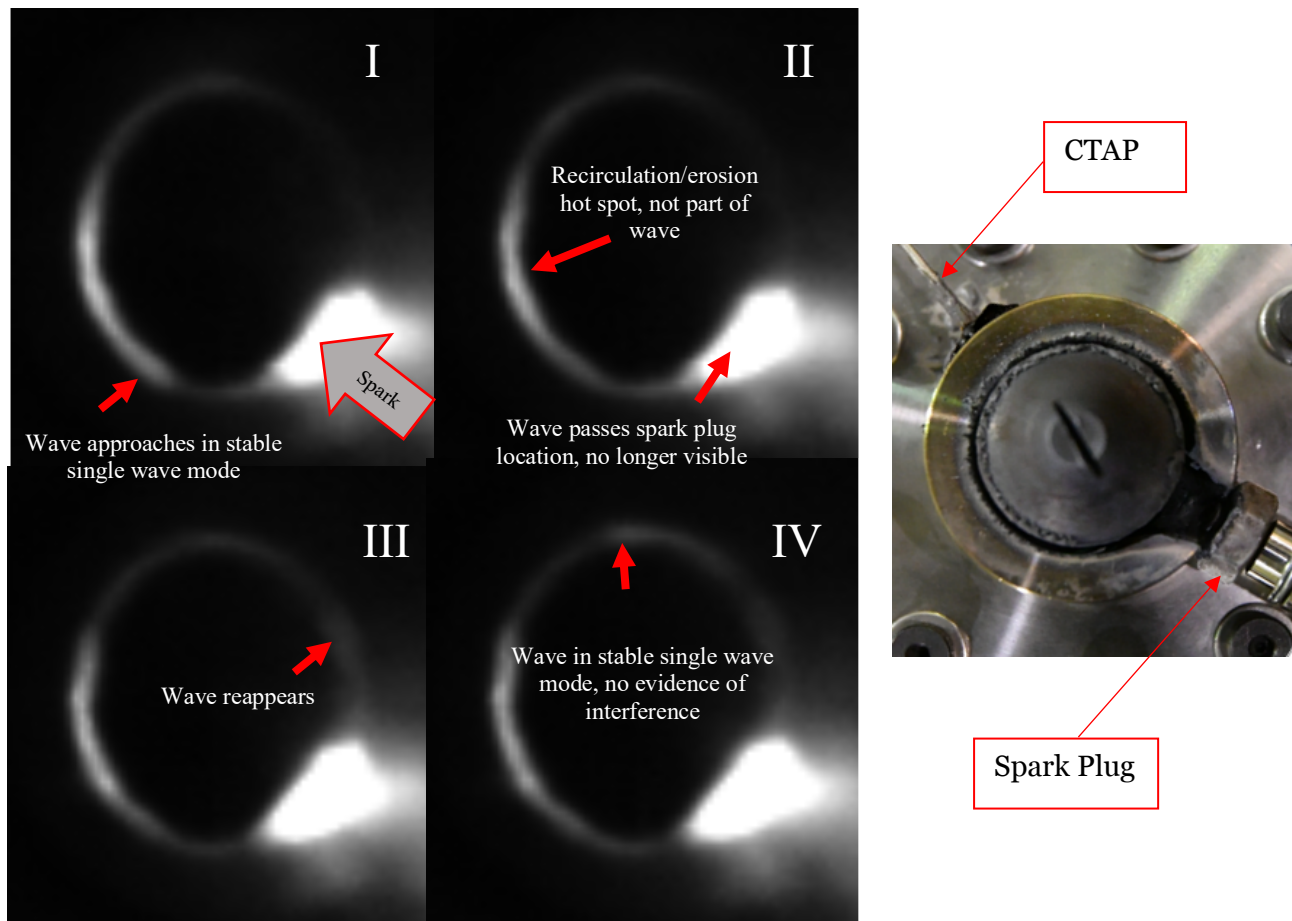
Fig. 71 High-speed photo sequence showing a single detonation wave passing through erosion zone of spark plug unaffected. Three frames between each image. Ovals show wave location, arrows denote location of spark plug and CTAP hole. Reference color photo included.

Section 4.2.2 Wave Modes and Frequencies: Pre-Detonator Configuration

Testing with the pre-detonator resulted in 50 detonation data points. Of which, 48 had

corresponding high-speed video. From the analysis, five additional wave mode categories were

observed, completing the scoring scheme of Table 7. The additional modes were a single wave

galloping mode (score of 7), a mode with repeated transitions between clapping, counter rotating,

and single waves (score of 3), a single wave mode that would transition between deflagration and

detonation (score of 2), a mode without any dominant wave behavior and periodic deflagration

(score of 1), and a pure deflagrative mode (score of 0). These new modes were observed in addition to the modes previously seen in the spark plug data.

With the novel modes classified and included in the scoring system, all 48 scores were compiled to create an ignition map like the one shown in Figure 69 but with the pre-detonator data, and is shown in Figure 72. Overlap of data points in Figure 72 occurred for the same reasons as Figure 69. A wave score of 10 was observed over a range of mass flows of $0.052 < \dot{m} < 0.073$ kg/s and equivalence ratios of $0.89 < \Phi < 1.55$. This was essentially the same range as the set of all detonable ignition conditions and unlike the spark plug data, it was found that the range of mass flows were also in very close agreement (0.052 kg/s vs 0.049 kg/s). This meant that it could not be said higher mass flows tended to lead to high wave scores and that wave modes were mostly independent of mass flow and equivalence ratio.

It was found that no mode below a score of 3 was found outside the ranges of $0.065 < \dot{m} < 0.075$ kg/s and $0.90 < \Phi < 1.20$. This range is highlighted on Figure 72 and suggested that high ignition mass flows and equivalence ratios near stoichiometry prevented deflagrative characteristics because wave modes of 0-2 allowed deflagration but a score of 3 did not. As discussed in Section 4.1.2, stoichiometric conditions at high mass flows were the result of the flow controller dynamics. Therefore, it could not be determined if the range of $0.90 < \Phi < 1.20$ was required to prevent deflagration or simply a restricted window of conditions due to the controllers. However, high mass flows resulted in stiffer injector pressure ratios, which were found to impact the RDE's detonability, and may have prevented deflagration. This is discussed in Section 4.3.
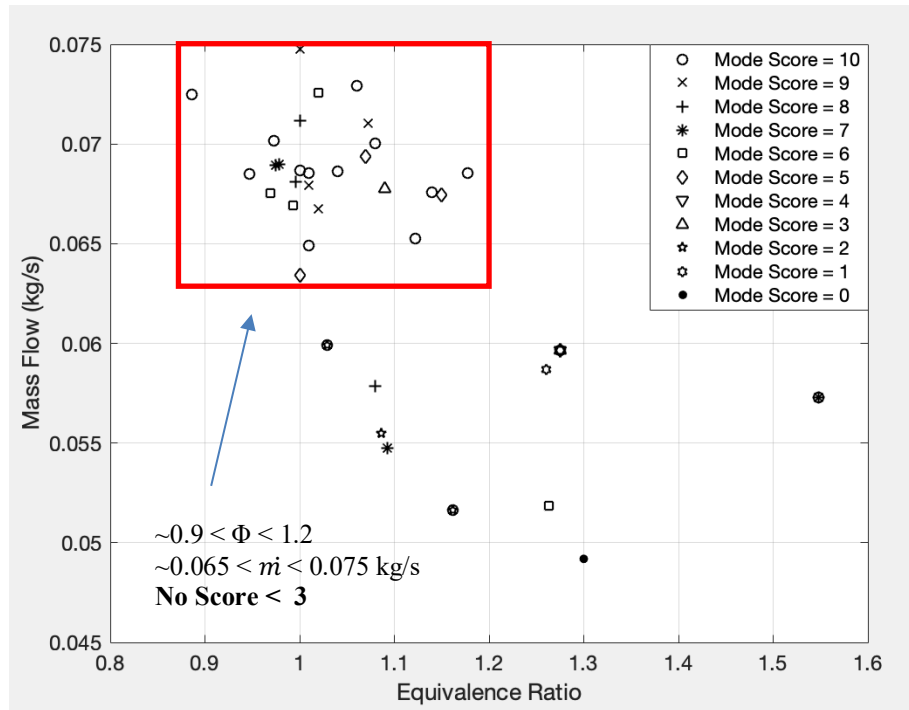
Fig. 72 Ignition map with mode scores overlaid. Wave scores of 10 observed over 0.90 < Φ < 1.20 and 0.065 < $\dot{m}$ < 0.075 kg/s

Average wave frequencies between 12.8 kHz and 16.6 kHz were observed with the pre-detonator. The need for averaging arose due to wave modes with varying wave frequencies (i.e. a score of 7) and is discussed later in this section. This range was similar to what was observed in the spark plug data (13 kHz – 16.8 kHz) and due to the larger number of data points and wider operating map helped to confirm that it was representative of the injector design. Using the wave frequency values, Figure 73 plotted wave mode score and frequency for the pre-detonator data. It should be noted that due to overlapping wave frequency values, not all points are uniquely represented in Figure 73, and the pure deflagration mode was not shown because it did not have a corresponding wave frequency. The trend in Figure 73 was almost identical to the trend seen in the spark plug data except for three outliers, which are highlighted. These data points had wave mode scores of 2, 3 and 7 and each of these modes corresponded to behaviors with wave frequencies that varied rapidly, either from galloping or transitions between detonation and deflagration. The variation was accounted for in the analysis by averaging the range of observed

wave frequencies. As a result, the influence of the high wave speeds had the potential to raise the frequency measurement above what was generally observed depending on the severity of the fluctuations.
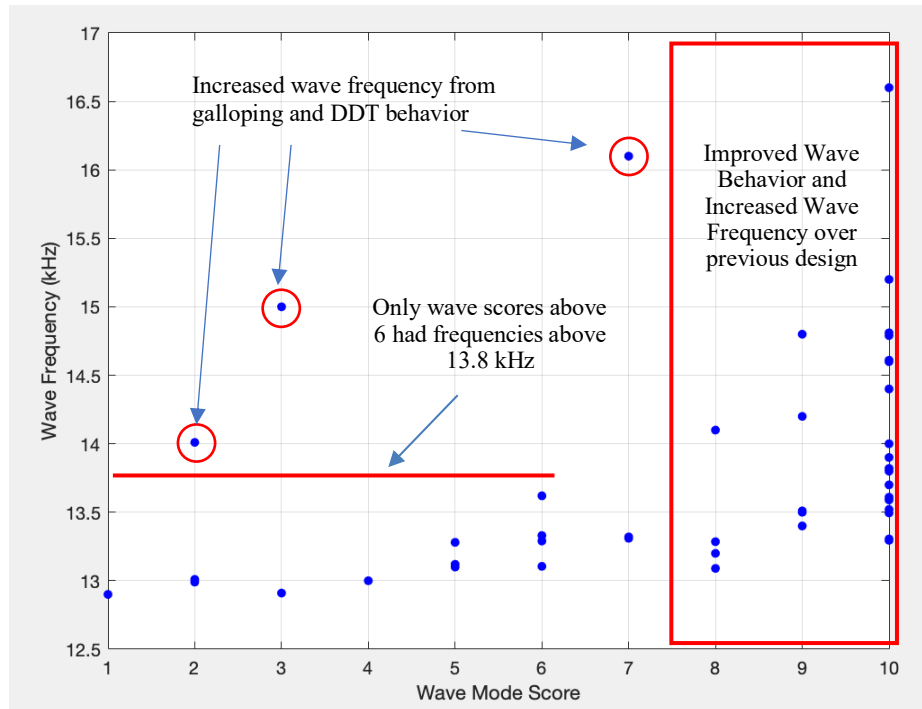
Fig. 73 Plot of wave speed versus wave mode score for pre-detonator detonations. Outlier points are highlighted

Accounting for the outlier cases, the plots of Figure 73 and Figure 68 were in strong agreement, showing that high wave frequency (>14 kHz) occurred only when wave scores were larger than 6. Like before, it was found that when a wave mode was already stable, its frequency was not restricted to a high frequency. The repeatability of these trends implied that the same mechanisms for wave mode and wave frequency in the spark plug data were at play with the pre-detonator installed. Similar to the previous data, longer runs with significant erosion to the hardware had wave frequencies increase and wave modes score improve as the channel pressure dropped. Additional discussion will be presented in Section 4.3.

Figure 73 also showed that in addition to the wave modes unique to the pre-detonator data, all the other wave modes from Table 7 were observed. Furthermore, the distribution of wave modes

was similar to what was seen in the spark plug data with the majority of modes earning a score of 8 or higher. Previously, it was postulated that the spark plug was responsible for clapping modes when the collision point was at the spark plug. It was also suggested that these clapping modes were more likely to earn a score of 4 instead of a score of 5 or 6. With the pre- detonator, clapping behavior had not been eliminated, as seen by the presence of multiple scores of 5 and 6, however the prevalence of a pure clapping modes, with a score of 4, had been diminished. Furthermore, video from the pre-detonator cases with a dominant clapping mode showed that the wave no longer had a preferred clapping point. This was evidence that the spark plug did in fact have an influence on the character of the clapping modes, and likely increased the prevalence of wave modes that would have scored a value of 4.

In most cases, wave frequencies were constant over the time span of 3-4ms (average time frame to complete 5 rotations) used to make the frequency measurement. However, some wave modes exhibited variations in their wave frequency within the time span of a normal measurement. Instances of this behavior were limited to modes with scores of 2, 3 and 7, which were also the outlier cases highlighted in Figure 73. The variations in frequency seen in these modes could be severe, with a range of 13.1 kHz - 19.1 kHz over the course of a few rotations observed in one instance. Such behavior could sometimes be attributed to unique circumstances.

For example, Figure 74 shows the pre and post run condition of the nozzle and fuel/ox manifold after the specific run which resulted in wave frequencies between 13.1 kHz – 19.1 kHz. The wave mode score given to this particular run was a 7, on account of the galloping behavior. High speed video from the run showed that the galloping behavior did not occur until after a significant amount of erosion had occurred in the channel. As a result, the eroded hardware was

believed to have excited the galloping mode. However, exactly how the change in geometry led to the galloping was unclear. It was possible the varying channel gap created by the erosion of the interface (highlighted in Figure 74) between the nozzle and fuel/ox manifold allowed more detonation cells to form. As a result, when the wave was at the axial location of the interface, the additional cells in the wave front allowed the wave to propagate faster. Additionally, the unique channel shape caused by the erosion could have led to added confinement of the wave on the top and bottom and the additional triple point interactions increased its speed. However, the behavior was only observed once as the resultant damage to the hardware precluded additional tests. Therefore, it was not determined if this channel shape consistently resulted in galloping behavior.
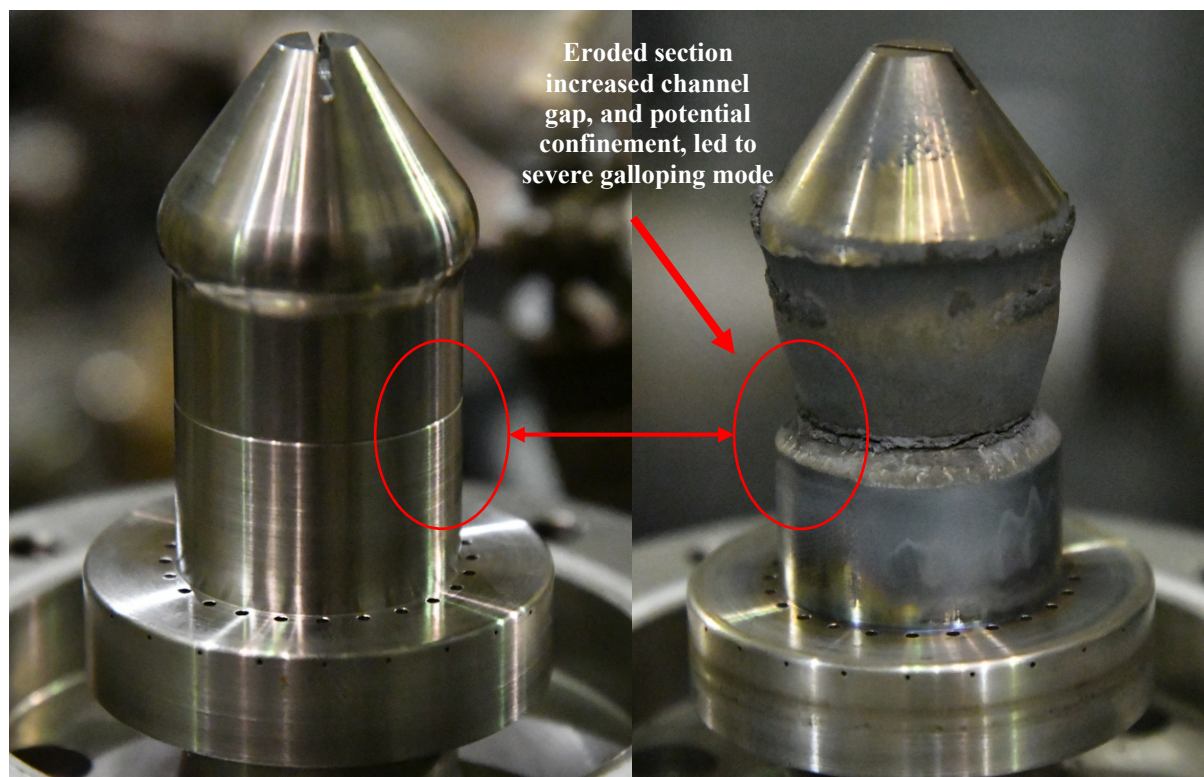
Fig. 74 Fuel/Ox manifold and nozzle after single detonation that resulted in a severe Galloping mode with Frequencies between 13.1-19.1 kHz.

Other examples of a modes with varying frequency were those that transitioned between deflagration and detonation. For example, a wave mode with score of 2 corresponded to a single wave that would decay to pure deflagration and then transition back to a detonation. In this mode,

it was found that the wave could have a frequency of ~14 kHz immediately after transitioning from deflagration to detonation. As it propagated as a detonation, the wave would begin to decay in frequency to around 13 kHz at which point it would enter a deflagrative mode again. It is known that when flame fronts transition to detonation via a DDT process they are initially overdriven [11]. It was believed that the overdriven behavior boosted the wave speed beyond what was sustainable for the given conditions for that particular run and as such it decayed back into a deflagration. This created the variations in frequency seen in waves with this mode. As reflected in the wave scores, such frequency fluctuations (in scores of 2, 3 and 7) were generally a sign of instability. This was why the pure galloping mode (score of 7), which did not have clapping, or any counter rotating behavior was ranked below other modes with those behaviors, i.e. scores of 8 and 9.

From the discussion above, a common characteristic of unstable wave modes was varying wave behavior within the wave mode. This transitory behavior made it difficult to begin distinguishing wave modes at the more unstable conditions, however the presence of deflagration was used as an objective line between them. For example, in a wave mode with a score of 2, there was single wave behavior present, but the wave would periodically dissipate into a deflagration. However, a wave mode that scored a value of 3 had more variations in the wave behavior, such as clapping and counter rotations, as well as lower wave frequencies but never degraded to a deflagration. Therefore, the mode that avoided deflagration was considered more stable even though it had more variation and on average slower wave frequencies.

Delineation between detonation and deflagration was based solely on observation of the high-speed video which allowed for significant subjectivity in wave scores. An objective measure used to counteract the subjective nature of the classification was the wave frequency. Figure 71 showed that no run had a wave frequency below 12.8 kHz. This was because a wave frequency of

12.5-13.0 kHz corresponded to 50-52% CJ velocity for nitrous oxide and ethylene. Such a low percent CJ velocity resulted in an acoustic wave. Therefore, if a frequency of 13.0 kHz or lower was found it was closely investigated to determine the extent of deflagration evident in the video. Additionally, in cases where no wave was observable with which to measure frequency, classification of a deflagrative mode was obvious.

Besides the single wave galloping mode, which had a wave score of 7, all new modes in the pre-detonator set were less stable than previously observed with scores from 0-3. The presence of low scoring wave modes not seen in the spark plug data was attributed to two possibilities. First, the low number of data points in the spark plug data limited the opportunity for these modes to be captured. This coupled with the fact that only a few wave were found with a score of 0-3 in the larger pre-det data set suggested that the new modes were simply unlikely with the current set up. The second explanation was that the more fuel lean conditions in the pre-detonation data led to a higher instance of unstable wave modes.

To check the second explanation as well as potentially explain general trends in wave scores with respect to operating conditions, the *post ignition* mass flows and equivalence ratios (using both the spark plug and pre-detonator data) were plotted with various wave scores in Figure 75. The figure is broken into four groups based on wave scores from 0-3, 4-6, 7-9, and 10. Error bars on mass flow and equivalence ratio were removed for clarity, but are the same values shown in Figures 65 and 67. Similar to the ignition condition analysis in Figures 69 and 72, operating mass flow and equivalence ratio were found to not have a clear influence on the wave modes. To illustrate, a box around a window of conditions from 0.04 kg/s $< \dot{m} <$ 0.06 kg/s and $0.7 < \Phi < 1.2$ was able to encircle most test points in four all cases. This meant different wave modes were not a strong function of mass flow or equivalence ratio. However, it was noticed that for wave modes with a score of 8-10 (fames c and d), mass flows were generally higher than the other modes. This

phenomenon was consistent with the explanation that high mass flows led to stiffer injection which improved wave behavior and is investigated further in Section 4.3.
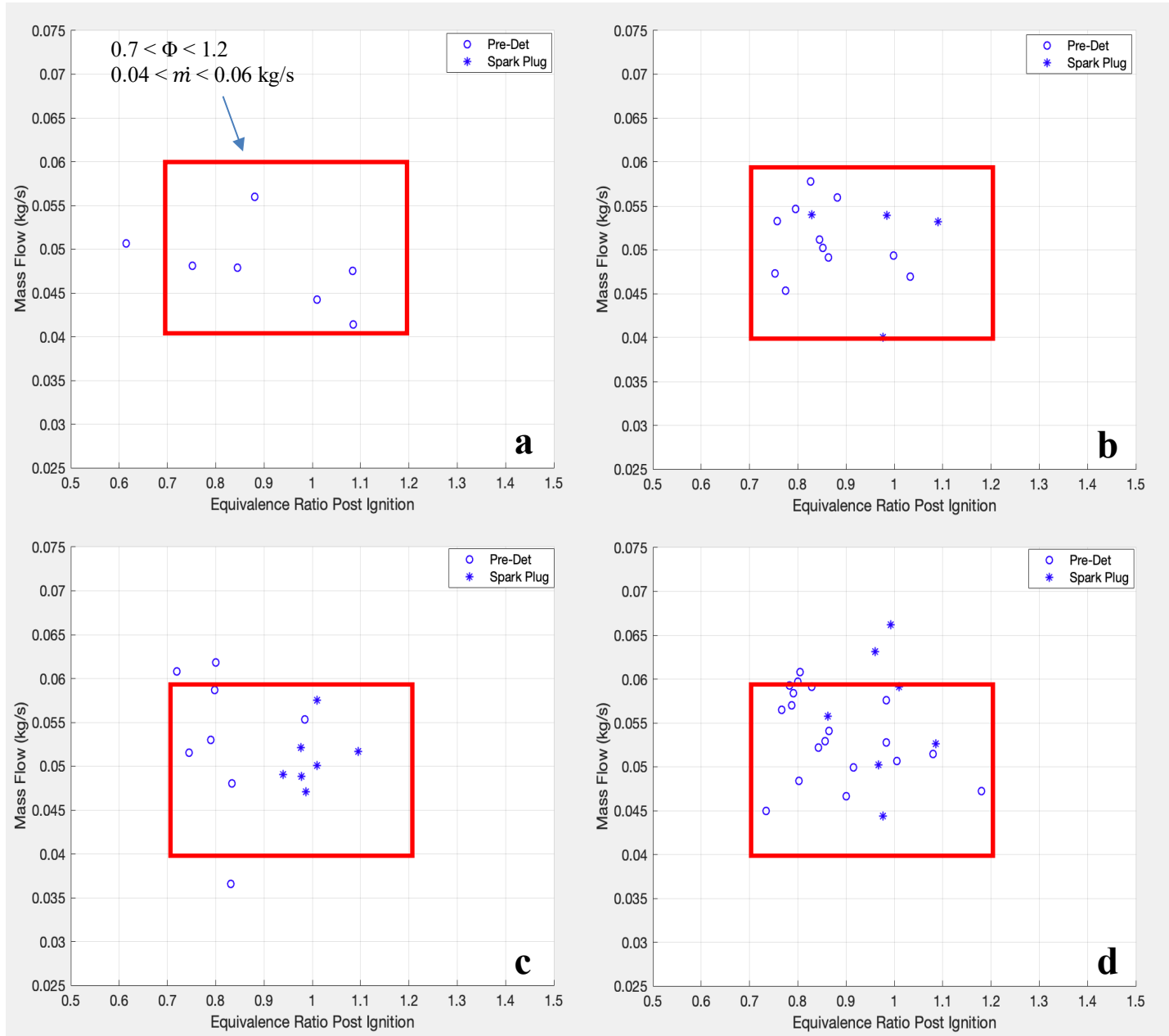
Fig. 75 Operating maps for different wave scores. **a)** Scores 0-3. **b)** Scores 4-7. **c)** 8-9. **d)** Score10. Box highlights the same window in each.

A significant observation from the high-speed imagery was the sequence of events that would lead to transitions between single wave behavior and clapping/counter rotating behavior. In order for a single wave mode to transition to a clapping or counter rotating mode a second wave

had to form within the channel. In the high-speed video, it was observed that this second wave would form from reacting gasses that had decoupled from the main detonation wave front, usually from interaction with recirculating gasses, erosion hot spots, or the spark plug (if present). Once separated from the wave, the deflagrating gasses would be pushed in the direction opposite the original detonation, relative to the detonation, by the trailing expansion waves. If these reacting gasses then encountered enough unburnt reactants, they would begin propagating on their own opposite the original wave. If the original detonation wave was moving slow enough to allow the newly forming wave enough time to establish a proper detonation structure, a secondary wave would result.

If the new wave was significantly weaker than the original wave when they met, it would be reabsorbed/dissipated by the main wave. However, if the secondary wave had a strong enough structure to survive the passing main wave, it would have access to more time and fresh reactants and gain more strength for when they passed again. At this point the waves would be in a counter rotating mode. Given enough iterations on this process the secondary wave could become established enough to persist in a weaker, counter rotating wave for many revolutions. However, if the secondary wave continued to gain strength, it would eventually match speeds with the original wave, at which point a clapping mode would form. The clapping mode would then persist for as long as both waves were of equal strength. Figure 76 shows a sequence demonstrating the transition from a single wave mode to a counter rotating mode. The sequence ends with both waves at similar, but still unequal strengths.

The process described was seen to run in reverse, from two waves to one, and offered a mechanism for reversals in the wave's direction. For example, if the original wave was disrupted after repeated passes with a counter rotating wave and broke down, then the remaining wave would have a propagation direction that was opposite from the main wave. As a result, the new single

wave mode would rotate opposite of from the original single wave mode. Wave reversals were commonly accompanied by brief periods of clapping and counter rotating, which suggested that this mechanism was related to reversals and explained why direction reversal was usually present in wave modes dominated by clapping and counter rotation.

By analyzing the sequence of events described above, a potential reason for the lack of high frequency waves with clapping behavior was found. In the initial stages of the process, where the deflagrating gasses were starting to propagate in the opposite direction, if the original wave disrupted the growing secondary wave before it was adequately established it would dissipate. This sequence of events demonstrated that the clapping behavior had a dependence on wave frequency and that there was an optimum wave frequency, at which, clapping and counter rotating modes could most easily form and persist. From Figure 73 that window appeared to be from 13 kHz -13.5 kHz. At frequencies above this, the primary wave would pass any counter rotating secondary waves too quickly for them to form. At frequencies below this range the wave would not be able to continue to propagate without transitioning to an acoustic mode or deflagration.

It's worth noting that the fresh reactants being used by the newly forming wave, directly behind the main wave, were unlikely to be from the injectors, due to the blockage/back pressuring of the main wave. Therefore, the unburnt reactants had to come from passing through the main wave unburnt. This indicated that the local mixing directly in front of the main wave was nonideal and therefore clapping modes were also a sign of poor mixing. Poor mixing has a direct influence on the velocity deficit from CJ speeds, which would in turn influence ability of the clapping mode to establish itself the first place as described above. This coupling would also explain why clapping behaviors were less common at higher wave frequencies, as the faster frequency would also imply better local mixing. Such complexities are the result of the coupled nature of the mixing and wave frequency to clapping behavior.

There were wave modes with limited to no clapping behavior at frequencies below 13.5 kHz. Therefore, as had been stated earlier, frequency was not the only factor at play. Additional factors to consider were mixing quality and the number of irregularities in the channel, such as erosion patterns, hot spots, recirculation zones, and spark plug protrusions that could initiate decoupling of reacting gasses from the wave front. If a single wave propagated at a lower frequency but never encountered anything to decouple enough reacting gasses to make a second wave, clapping would likely not occur. Also, these low frequency single waves may have had good mixing quality which would prevent clapping as well, however because good mixing would also be expected to increase the frequencies it was not a full explanation for the low frequency.

Therefore, there had to be other factors that drove the observed trends. In an attempt to determine these factors, Figure 77 plotted three operating maps, one showing test points with frequencies above 13.8 kHz, another with frequencies below 13.8 kHz and a third with only those tests with frequencies above 15 kHz. Again, error bars on mass flow and equivalence ratio were removed for clarity. Figure 77 showed that there was not a significant difference in mass flow and equivalence ratios that produced wave frequencies above and below 13.8 kHz. However, faster wave frequencies (higher than 15 kHz) appeared to correlate with more stoichiometric mixtures and mass flows above 50 g/s. Initially this was thought to be the result of cell size minimization near stoichiometric conditions, however further analysis found that this was in fact the result of the mechanism increasing the frequencies, not the cause. A better mechanism is presented in Section 4.3.
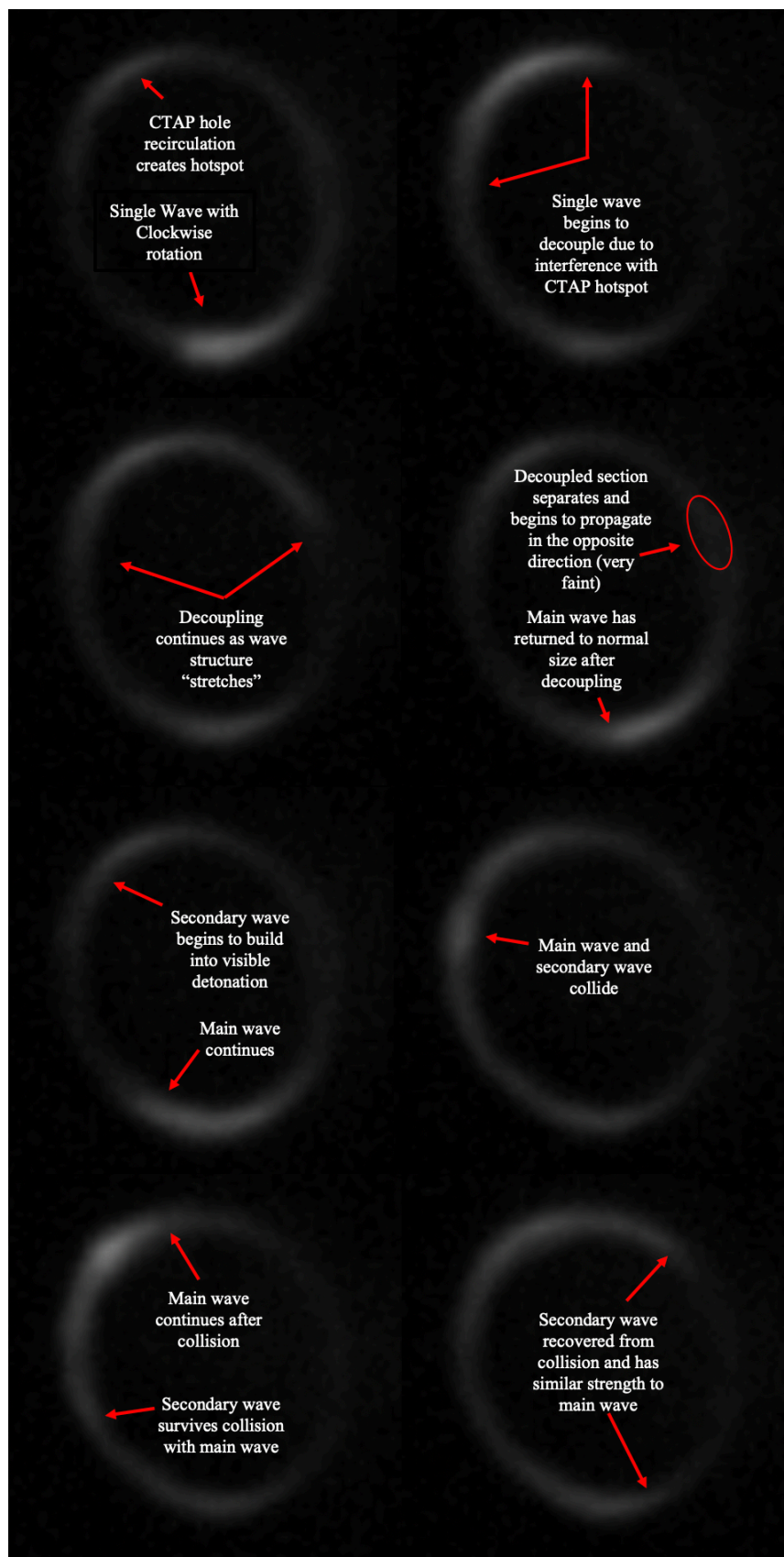
Fig. 76 High speed imagery showing transition from single wave to counter rotating/clapping behavior via decoupling of reacting gasses from main wave.
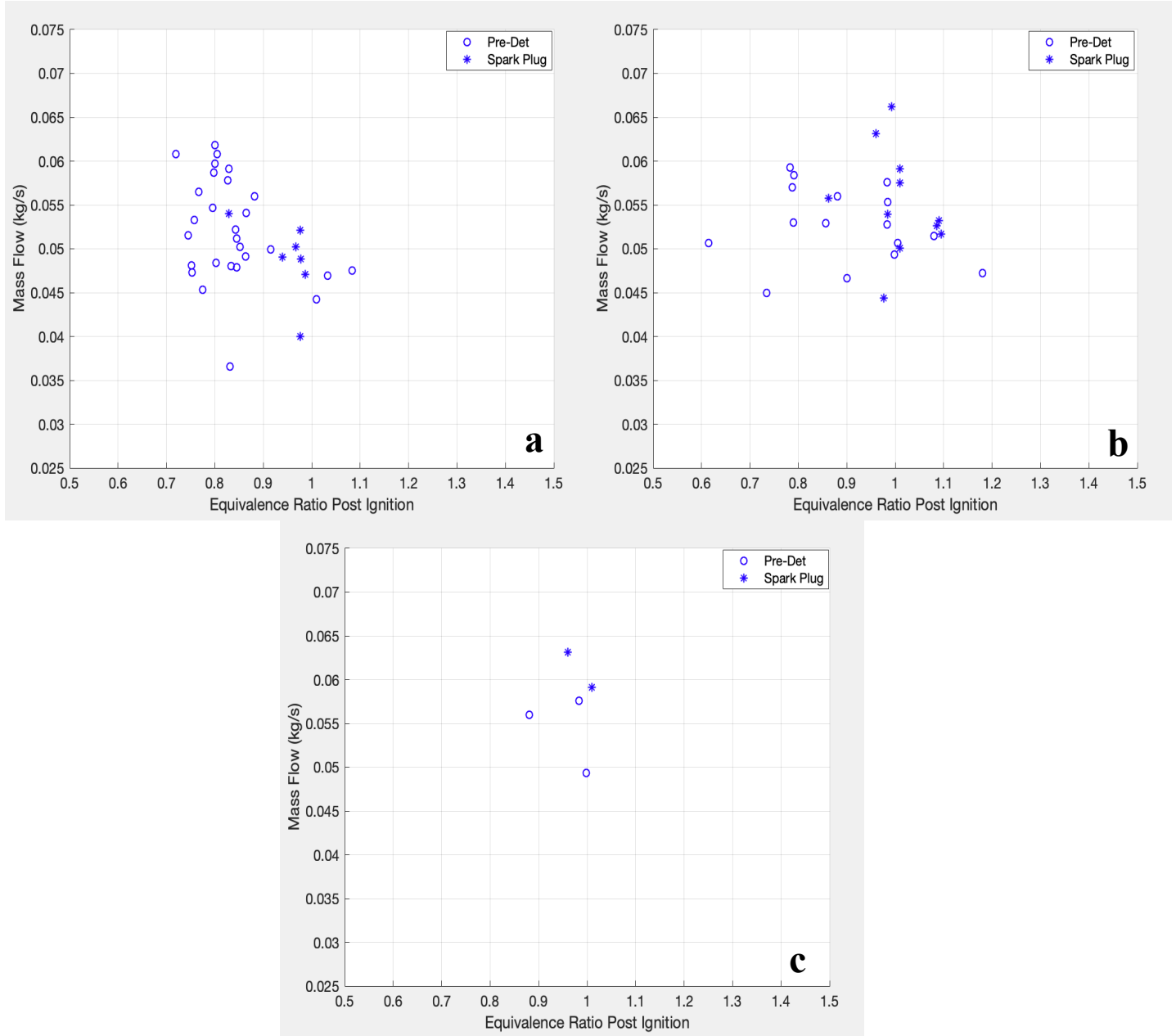
Fig. 77 Operating maps for different wave frequencies. **a)** Below 13.8 kHz. **b)** Above 13.8 kHz. **c)** Above 15 kHz

When all the wave modes were considered, the data showed that the new injection scheme and removal of the spark plug had made an improvement over the design used by Dechert [1]. Of the 48 videos, 21 of them showed evidence of a stable single wave mode. When wave modes with score of 9 and 8 were included, allowing for a minor amount of non-stable behavior, this number

went up to 30 out of 48. Compared to the previous design which never scored above a 6, when the scoring of Table 7 was applied, wave mode stability appeared to be significantly improved. Additionally, much of the benefits to the wave behavior were already observed in the spark plug data. Therefore, the injection scheme change was the main factor for the changes observed. However, removal of the spark plug helped limit pure clapping modes, and as Chapter 3 reviewed, improved hardware durability. Figures 69, 72, and 75 showed that reasons for the trends in wave score were not immediately obvious when cross referenced with the ignition and operating space of mass flow and equivalence ratio. Therefore, in order to determine the parameters which had an impact on which wave mode was seen further analysis was performed and is presented in Section 4.3.

With regard to wave frequency, 19.1 kHz was the fastest recorded value in the pre-detonator data. However, this occurred during a severe galloping wave mode that was believed to be the result of the novel erosion pattern shown in Figure 74 increasing the channel gap. When only wave modes without galloping or varying frequency were considered, the fastest frequency dropped to a value of 16.6 kHz. This example, like the fastest example in the spark plug data, also had a wave mode score of 10 and occurred after erosion had increased the exit area enough to drop chamber pressures significantly to ~745 kPa. Waves in eroded channel geometries were difficult to reproduce and frequently could not be used on subsequent tests. As a result, high frequencies were not reliably repeated. Therefore, limiting the frequency data to just those points which occurred with the RDE geometry intact and as designed, the fastest frequency became 15.0 kHz. The average frequency with these restrictions became 13.8 kHz. Both of these values were consistent with the spark plug data. The invariance in wave speed between both data sets supported that the spark plug was not impacting the wave frequency, only the wave mode, and only those modes with clapping behavior. When cross referenced with the operating spaces in Figure 77,

higher wave frequencies were found to coalesce around stoichiometric conditions and mass flows above 50 g/s. However, as will be shown in Section 4.3, stoichiometric conditions were the result, not the cause of the mechanism changing the wave frequencies.

In conclusion, the frequency data from both the spark plug and the pre-detonator suggested that the wave frequency could positively impact the wave mode, but a more stable wave mode did not necessarily increase the wave frequency. So, while the wave behaviors were observed to improve significantly in special cases, the general wave frequencies were not much closer to the 20 kHz design than were already seen by Dechert [1]. This was ultimately due to the interrelationship between the mixing, decoupling mechanisms, such as the spark plug, recirculation zones, and erosion, and the fill height. Further details on how the fill height impacted the results are presented in the next section.

Section 4.3: Parameters Impacting Ignition Performance and Wave Behavior

Some parameters were found to have an observable impact on the RDE's operation. By studying the impact of these parameters and their potential mechanisms, future changes to the RDE's design that could further improve operability and stability could be conceptualized. First, Section 4.3.1 discusses ignition specific parameters such as average chamber pressure and plenum to chamber pressure ratio which were found to influence the variability in successful and unsuccessful detonation. Using data taken from detonating cases, Section 4.3.2 investigates the changes to wave speed and mode that occurred in special instances where the channel pressure dropped during detonation. Section 4.3.3 then takes the relationships induced by the pressure drop and relates them to the estimated fill height and equivalence ratio as potential mechanisms for the wave frequency and mode. The section concludes with a discussion on the comparison of fill heights between the new injection scheme and the one used in previous work.

Section 4.3.1 Impact of Chamber Pressure and Injector Stiffness on Ignition Performance

The ignition maps in Section 4.2 showed that there was significant overlap of equivalence ratios and mass flows for successful and unsuccessful detonations. This made the operating space of the RDE uncertain and the conditions leading to successful ignition unable to be identified. However, a more informative ignition space was ascertained from the analysis of the pre-ignition mass flow, chamber pressure, and equivalence ratios. Data from both the pre-detonator and spark plug sets are presented in the following discussion. Throughout it should be noted that ignition conditions differed from the corresponding detonation, or operating conditions. The observations on the ignition space are specific to ignition conditions.

Figure 78, shows the average chamber pressures, as measured by the CTAP, as a function of the measured mass flows for both the pre-detonator and spark plug set ups. Both measured and estimated mass flows are shown, and their error bars were removed for clarity. Additional lines representing the expected chamber pressures and mass flow for a given nozzle size are also shown. These lines were calculated using the compressible mass flow equation shown in Equation 18. Average channel pressure was assumed equivalent to the cold flow's total pressure and a choked condition at the nozzle exit was assumed for all cases. Nozzle sizes used during testing were $\varepsilon =$ 0.26, 0.33, and 0.39, where ε was the nozzle throat to channel area ratio (denoted A_{th}/A_{ch} on figure). A smaller nozzle ratio corresponded to a larger physical nozzle and had a steeper slope on Figure 78. Therefore, larger nozzles would produce a higher chamber pressure. Not all points in Figure 78 fell onto the lines corresponding to the nozzles used. This was due to a difference between the actual exit area and the one assumed based on the nozzle diameter. Differences were either due to manufacturing tolerances or erosion from a previous run, or a combination of both. The variation in where the data points landed in these graphs illustrated how the nozzle sized used for a particular

run was not an accurate way to determine the exit area for that test runs. True exit area for a specific test point could be found by fitting the appropriate area line through it.

In Figure 78, successful attempts were present throughout the range of pressures and mass flows. However, there was a growing prevalence of failed ignition attempts along lines of decreasing area ratios. This trend was visible in both graphs. In the pre-detonator data set, the space bounded by the $\varepsilon = 0.39$ and $\varepsilon = 0.33$ lines, and mass flows from 0.055 kg/s to 0.075 kg/s, had 13 ignition attempts. Of which 10 were successful, for a success rate of 77%. Whereas in the space bounded by the $\varepsilon = 0.33$ and $\varepsilon = 0.26$ lines, over the same mass flow range, had 44 attempts with 19 successful attempts for a success rate of 43%. When mass flows below 0.055 kg/s were considered, the success rate for the region between the $\varepsilon = 0.33$ and $\varepsilon = 0.26$ dropped to 21%. The region between the $\varepsilon = 0.39$ line and $\varepsilon = 0.33$ line had no data points below 0.055 kg/s.

In the spark plug graph, the same trends were found but the mass flow range began at 0.045 kg/s instead of 0.055 kg/s. Success rates at mass flows above 0.045 kg/s and between the $\varepsilon = 0.39$ line and $\varepsilon = 0.33$ line were 87% and between the $\varepsilon = 0.33$ and $\varepsilon = 0.26$ lines were 58%. Therefore, the spark plug produced higher ignition success over a larger mass flow range than the pre-detonator. Had the spark plug data set had more data points, its percentages may have dropped in line to the pre-detonator set and more testing would be required to be sure.
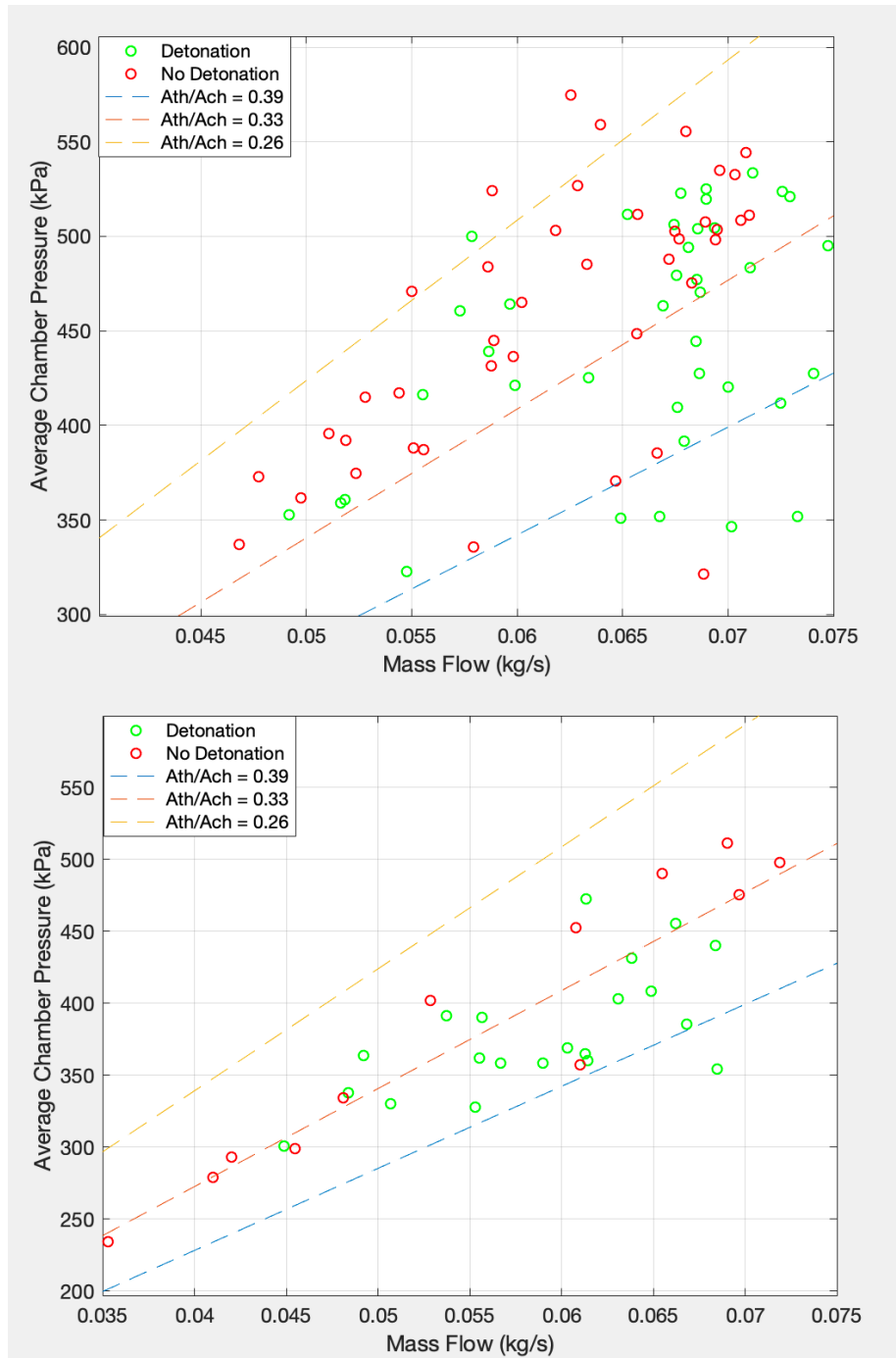
Fig. 78 Plots of average CTAP channel pressure as a function of measured mass flow. Top: Pre-detonator data. Bottom: Spark Plug Data.

Overall, the graphs showed there was a moving range of optimal chamber pressures and mass flows that was dependent the size of the exit area ratio. Mass flows above 0.055 kg/s with pressures along the $\varepsilon = 0.39$ line up to the $\varepsilon = 0.33$ line appeared optimal for the pre-detonator. The

spark plug's optimal space allowed lower mass flows but remained between the $\varepsilon = 0.39$ and $\varepsilon = 0.33$ lines. As a result, rates of successful ignition could be improved by ensuring area ratios were always within these bounds. Larger area ratios than used may prove beneficial as well. For example, the region below the $\varepsilon = 0.39$ line in the pre-detonator set had a success rate of 80%. To show why certain area ratios impacted the detonability, the plenum to chamber pressure ratios, P_f/P_c, and P_{ox}/P_c for the fuel and oxidizer were plotted in Figure 79. Duval et al. and Dechert both used these ratios as a measure of the injector's stiffness which had an influence on a flow field's ability to recover after a passing detonation [1,10]. Stiffer injectors recovered faster and therefore were generally beneficial to ignition dynamics. Based on this, different nozzle sizes were expected to have a direct impact on injector stiffness. For example, a smaller exit area ratio would increase channel pressure at a fixed mass flow and therefore lower the plenum to chamber ratios, lowering the injector stiffness. This assumed both injectors and nozzles were choked which was a valid assumption for all pre-ignition cases. As a result, it was beneficial to find which level of injector stiffness was required in the Micro-RDE.

Figure 79 showed that for both the spark plug and pre-detonator the successful detonation attempts generally occurred at P_f/P_c, and P_{ox}/P_c8 ratios above three. Starting with the spark plug data, there was a significant improvement in detonability when P_{ox}/P_c exceeded 2.9. As P_{ox}/P_c increased above to 4.1, successful detonation was found at P_f/P_c, ratios of 3.4 to 4.4. Those points with a higher P_f/P_c, ratio than P_{ox}/P_c were found to be more fuel rich. When the reverse was true, conditions were more fuel lean. Therefore, the successful data points at higher P_f/P_c, ratios than P_{ox}/P_c ratios were reflecting the successful fuel rich equivalence ratios tested in the ignition map. A near linear trend in the ratios was observed and was highlighted. Trend lines such as this were examples of lines of near constant equivalence ratios. Figure 80 plots P_{ox}/P_c with equivalence ratio to illustrate for both data sets. For the spark plug, detonations along this trend line were

successful and had equivalence ratios between 1.10 and 1.27. Therefore, equivalence ratios of 1.10

and 1.27 in addition to P_{ox}/P_c and P_f/P_c, ratios above 3.0 were a reliable set of conditions to

attempt detonation at when using the spark plug. However, additional success at equivalence ratios

at 1.3 and 1.4 meant the range of detonable equivalence ratios was not restricted to 1.10 and 1.27

so long as the pressure ratios were high enough.
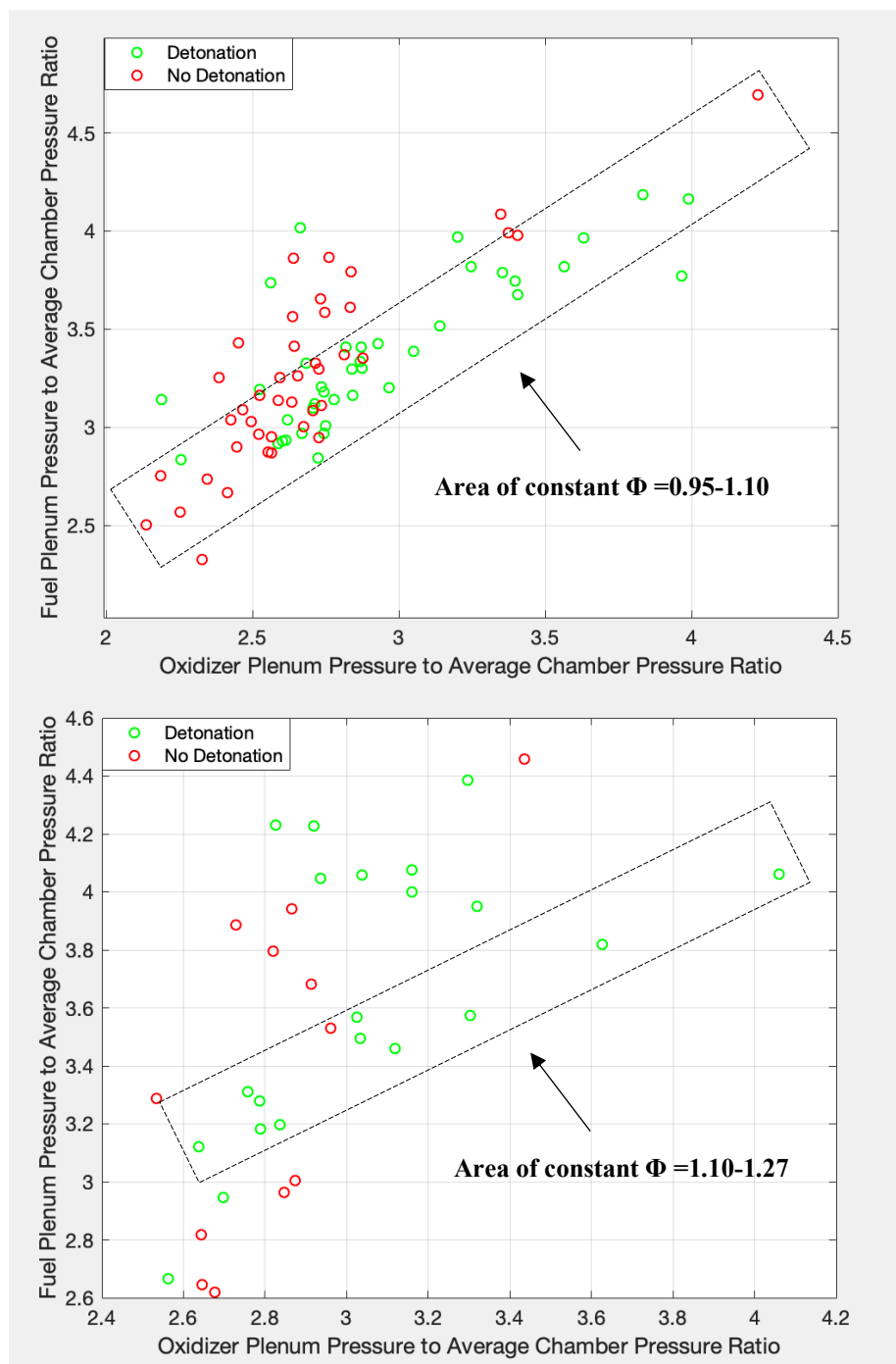
Fig. 79 Plots of fuel plenum pressure to chamber pressure ratio to oxidizer plenum to chamber pressure ratios (Top) Pre-detonator. (Bottom) Spark Plug. Areas of near constant equivalence ratio highlighted.
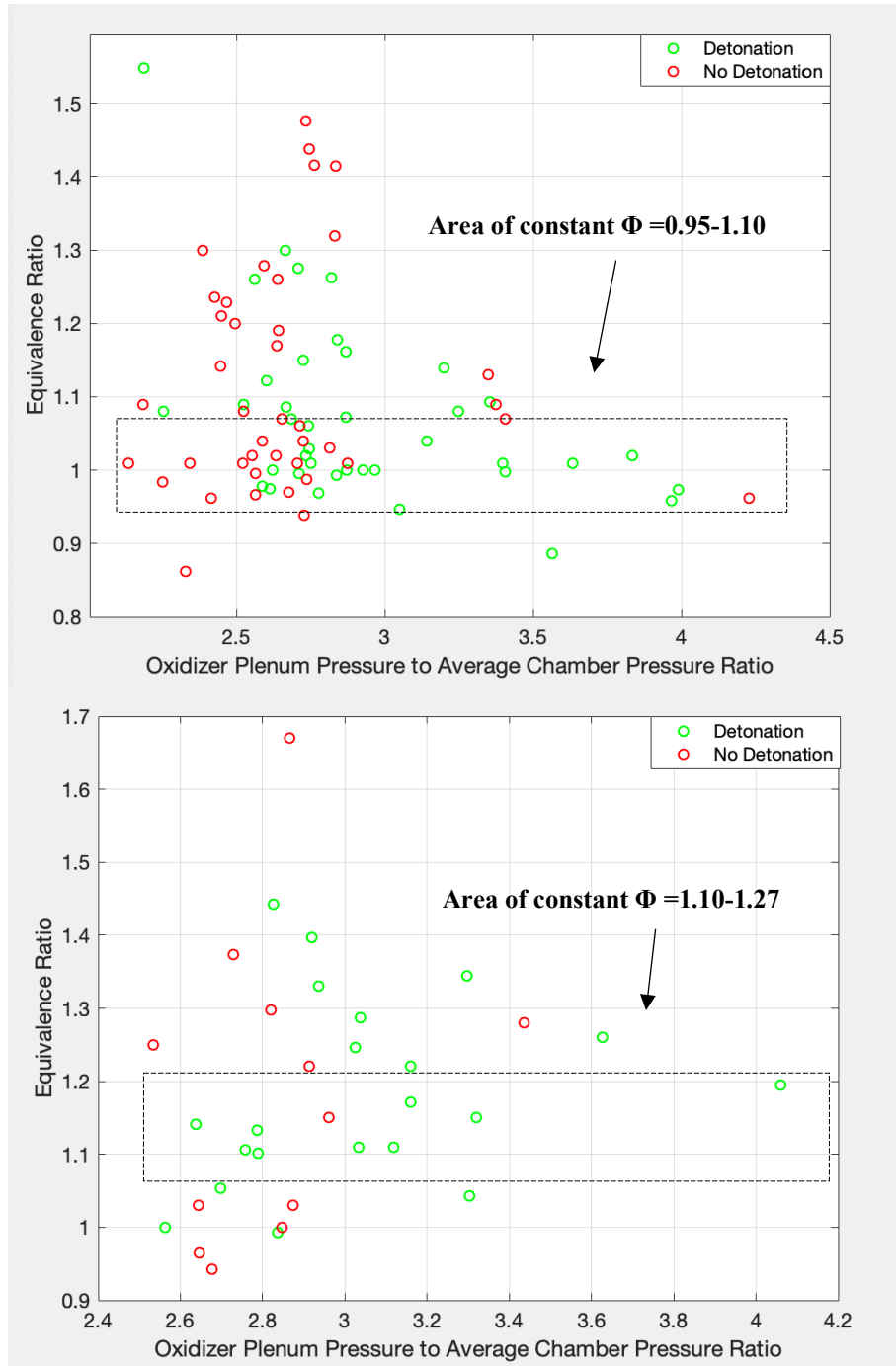
Fig. 80 Plots of oxidizer plenum to chamber pressure ratios and equivalence ratio. (Top) Pre-detonator. (Bottom) Spark Plug. Areas of near constant equivalence ratio highlighted.

In the pre-detonator data, ignition attempts clustered much more closely along a constant line of equivalence ratios between 0.95 and 1.10. Along that line, successful detonation did not occur until P_{ox}/P_c increased above 2.5 and P_f/P_c increased above three. From there the chance of detonation was intermittent until P_{ox}/P_c increased above 3 and P_f/P_c increased above 3.5. For the

data points along the 0.95 to 1.10 equivalence ratio line, 73% successfully detonated once ratios of 3.0 and 3.5 for the oxidizer and fuel were passed. Most of the data points not on the 0.95 to 1.10 equivalence ratio line occurred at pressure ratios below 3.0 and 3.5 for the oxidizer and fuel respectively. Therefore, it was not clear if failure to detonate was the result of the equivalence ratio or pressure ratios. Regardless, there was definitive evidence that the current injection scheme with the pre-detonator was reliably detonable at stoichiometric conditions and P_{ox}/P_c and P_f/P_c ratios above 3.0 and 3.5 respectively. More tests are required to determine detonability at other equivalence ratios. Pressure ratios were higher in the pre-detonator data than the spark plug data because of the higher average channel pressures in the pre-det set up required a stiffer injector to achieve the same recovery.

Combining the conclusions from both Figure 79 and 80 revealed that ignition conditions were optimized when the proper injector stiffness was achieved. For the limited range of equivalence ratios tested, ideal pressure ratios were found at or above 3.0 and 3.5 for the oxidizer and fuel. It is currently unclear if the lower limit of mass flow could be extended by maintaining the pressure ratios at these values or if a new boundary independent of injector stiffness would play a role. Duel choking conditions at the injector and nozzle meant the desired mass flow and equivalence ratio set the plenum pressures while the exit area ratio set the channel pressure. Independent manipulation of the nozzle exit area once a mass flow is fixed is then a potential a method to keep the chamber pressure ratio in the desired range. Therefore, it is hypothesized the pressure ratios found here will apply until the nozzle can no longer be choked. The chamber pressure will then become a function of the injectors and the ignition dynamics would be expected to change.

Lastly, when compared to Dechert, the required P_{ox}/P_c and P_f/P_c ratios of 3.0+ in the new injection scheme were significantly higher than the reported ratios in the old scheme which ranged from 1.2 to 3.0 [1]. This is shown in Figure 81 which shows where the highest injector pressure ratios seen by Dechert would have been in the new data [1]. The difference was ultimately attributed to the change in injector geometry. By moving the fuel injector into the oxidizer injector, the amount of flow blockage was significantly increased over the scheme previously used, which injected fuel directly into the chamber. Therefore, the added flow blockage required substantially more plenum pressure for a given channel pressure to achieve the required fill height into the channel for ignition.
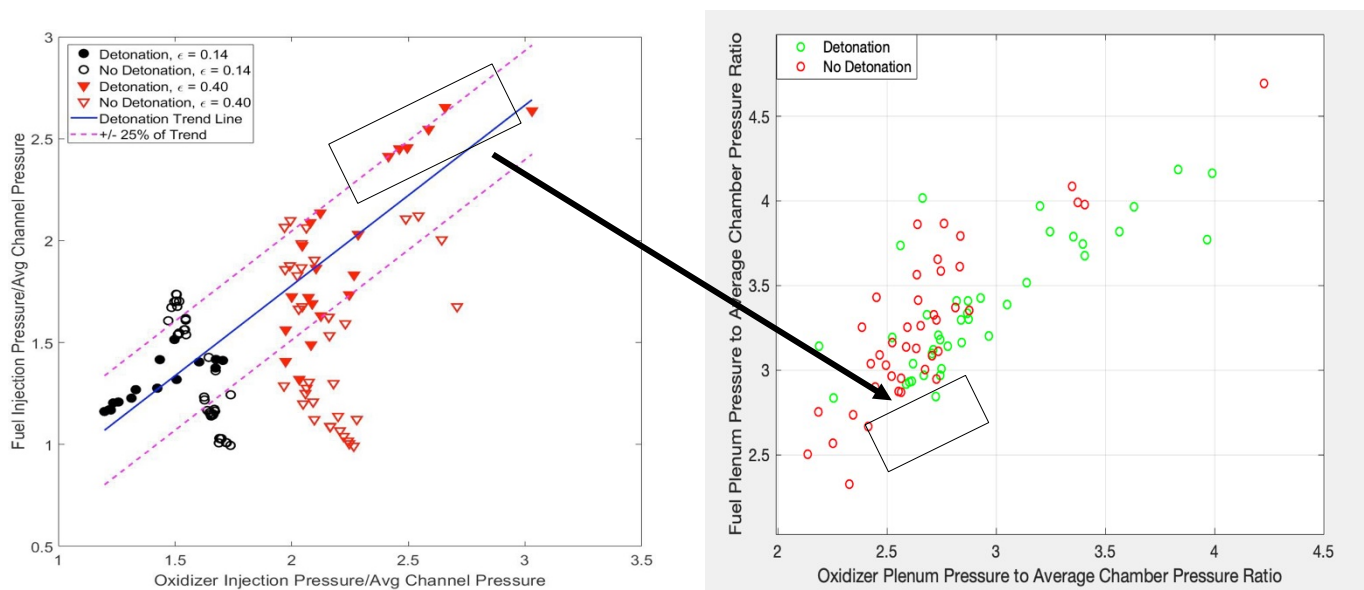
Fig. 81   Plots of oxidizer and fuel plenum to chamber pressure ratios illustrating increased injector stiffness required in new injection scheme. Left figure from Dechert [1]. Right figure from pre-detonator data in current work.

Section 4.3.2 Impacts of Channel Pressure Drop during Detonation on Wave Behavior

In the results from post ignition, detonating conditions, it was observed that the channel pressure, as measured by the CTAP sensor, would drop during runs with a detonation longer than approximately one second. Of the available data, seven cases were observed with such a pressure

drop. Table 8 shows the conditions and behavior for all seven cases including the measured mass

flow, measured equivalence ratio, average wave frequency, wave mode score, nozzle area ratio

(ε), estimated area ratio (discussed later in this section), CTAP pressure, and CTAP pressure before

pressure drop (Initial pressure). Each case in the table had three or two points extracted from a

single run and each point for a specific run is listed from least to greatest pressure loss. The number

of data points was dependent on the length of the run during pressure drop and if corresponding

high-speed imagery was available for a given set of pressure and mass flow values. Use of CTAP

pressure during periods of pressure drop was subject to the measurement delay inherent to the

CTAP design. As a result, the pressure values shown were likely to be overestimated. Initial

pressure was measured directly before sustained pressure drop occurred.

Table 8. Parameters of the seven cases with pressure drop.

Case #	Mass Flow ($\dot{m}$) (kg/s)	Equivalence Ratio (Φ)	Wave Frequency (kHz)	Wave Mode Score	Nozzle Area Ratio (ε)	Estimated Area Ratio (ε)	CTAP Pressure (kPa)	Initial Pressure (kPa)
1-1	**0.045**	0.735	**14**	10	0.39	0.28	**1370**	1380
1-2	**0.047**	0.900	**14.6**	10	0.39	0.33	**1210**	1380
1-3	**0.049**	0.998	**16.1**	7	0.39	0.44	**945**	1380
2-1	**0.053**	0.856	**14.4**	10	0.26	0.40	**1100**	1310
2-2	**0.056**	0.881	**15**	3	0.26	0.51	**938**	1310
2-3	**0.058**	0.983	**16.6**	10	0.26	0.68	**752**	1310
3-1	**0.058**	1.01	**14.6**	8	0.26	0.48	**1030**	1220
3-2	**0.059**	1.01	**15**	10	0.26	0.52	**979**	1220
3-3	**0.063**	0.960	**16.8**	10	0.26	0.77	**671**	1220
4-1	**0.050**	0.915	**13.3**	10	0.26	0.30	**1430**	1440
4-2	**0.051**	1.08	**14.8**	10	0.26	0.35	**1270**	1440
5-1	**0.044**	1.01	**13.0**	2	0.14	0.31	**1210**	1220
5-2	**0.047**	1.18	**14.6**	10	0.14	0.40	**992**	1220
6-1	**0.052**	0.976	**13.3**	8	0.39	0.36	**1250**	1260
6-2	**0.053**	1.09	**14.8**	10	0.39	0.40	**1110**	1260
7-1	**0.054**	0.829	**13.1**	4	0.39	0.39	**1170**	1180
7-2	**0.056**	0.862	**14.1**	10	0.39	0.47	**1020**	1180

Cases of pressure drop were of interest because in all seven cases, the wave frequency was found to increase. Additionally, all frequencies above 15 kHz occurred during a period of pressure drop. As a result, decreasing the channel pressure appeared to be a mechanism that reliably increased wave frequency. The pressure drop's impact on wave mode was less consistent but is also discussed in this section.

For each case of pressure drop, there were accompanied increases in the mass flow. This can be interpreted from Table 8, but to further illustrate Figure 82 shows both a pressure and mass flow history graph that corresponds to Case 1. In the pressure history, the point where the channel pressure dropped is indicated at the $T = 2.8$ second mark. In the mass flow history, at approximately $T = 2.9\text{-}3.0$ seconds the flow rates began to increase. Sudden increases in mass flow, like in Figure 82, were only observed when there was chamber pressure loss during detonation. Therefore, it was believed that the two effects were interconnected. The slight offset in time (2.8 vs 2.9-3.0) was believed to be from the delay time of the controllers reacting to the change in pressure.

Initially it was assumed the flow controllers were driving the flow rate changes as it made sense for them to increase mass flow in response to the detonation. However, this did not explain why the CTAP and plenum pressures decreased at higher mass flow into the channel, as that would increase the plenum pressures, assuming the exit remained choked. Therefore, the drop in pressure was independent of the controllers. A better explanation was found by considering changes to the exit area. Based on the amount of erosion shown in Section 3.1.6 coupled to the chamber pressure's sensitivity to the exit area (see Equations 14-15), it was expected that erosion was changing the exit area during longer runs. The sequence of events would occur as follows: heating from a long detonation (>1 s) led to erosion that increased the exit area and decreased the channel pressure (as measured by the CTAP). Then the plenum pressures dropped and the pressure differential across the flow controllers increased. With increased differentials, the controllers were able to partially

correct the flows to the requested values. This further confirmed that the reason the controllers did

not respond well during detonation was due to the deficient pressure differentials across them.
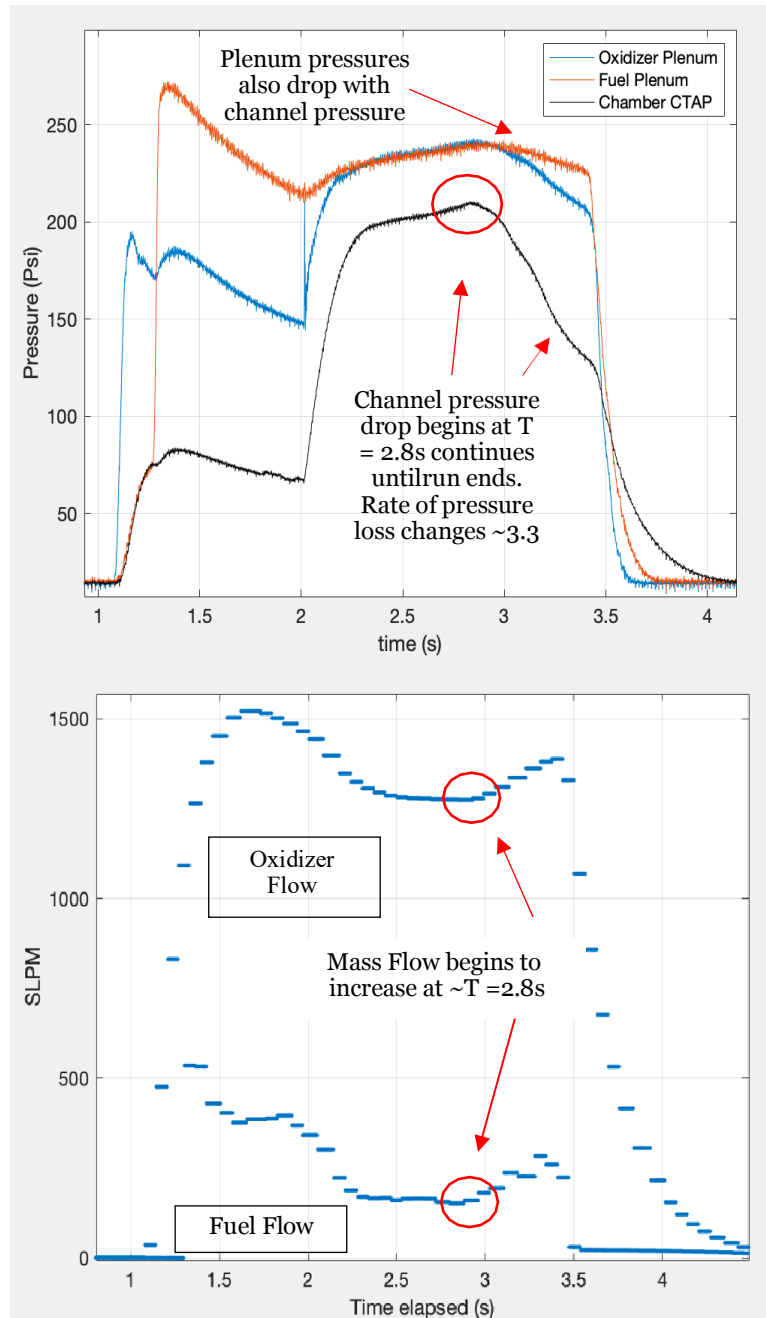
Fig. 82 Pressure and mass flow histories from the same detonation with sudden channel pressure drop. Corresponds to Case 1.

Attributing the pressure loss to erosion also explained why runs of one second or longer experienced pressure drop but shorter runs did not. As explained in Section 3.1, longer runs tended to erode the hardware enough to change the RDE's geometry. Additional confirmation was found when high speed video showed that channel pressure drops coincided with peak erosion intensity.

Figure 83 shows multiple high-speed images taken at different points in time. These are the same images as were used in Figure 47, but the time stamps have been aligned with the corresponding pressure and mass flow data shown in Figure 82. From T = 2.3s until T = 2.5s in Figure 84, the CTAP pressure was steady. During this period, the video showed that erosion intensity was low. However, at T = 2.8s, which was the initial point of pressure loss, there was a noticeable increase in erosion visible in the video. By T = 3.0s, Figure 82 showed a steep rate of pressure loss and at the same time, the video showed that there was a severe amount of erosion. Due to the random nature of the erosion, there were also instances where the nozzle's shape would change such that the exit area decreased. When this occurred the CTAP pressure would increase. This was observed several times, including in the run shown in Figure 82 from T = 2.5s to T = 2.8s. Pressure increases were usually followed by a decrease in pressure because the continued erosion eventually increased the area. Therefore, it was concluded that the pressure drop was the result of increased area from erosion of the nozzle and outerbody.
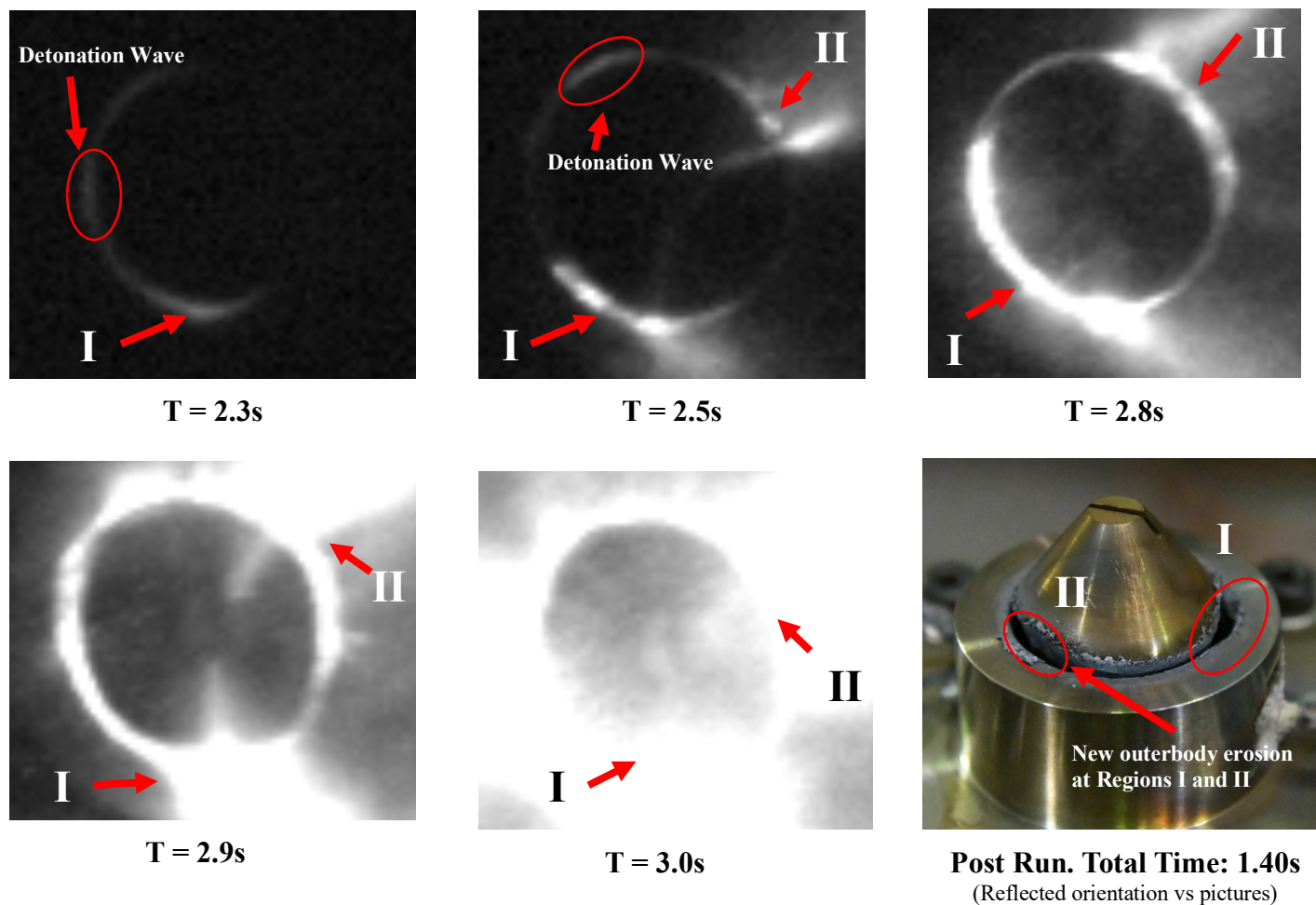
Fig. 83 Five step progression of nozzle erosion during run shown in Figure 76. Time stamps aligned with Figure 76. Region I and Region II denote locations of significant area change.

To estimate the area changes that occurred in each case, CTAP pressure and mass flow data from all seven cases were plotted in Figure 84. In addition, the same lines of constant throat to channel area (ε) plotted in Figure 78 were used. However, because the lines in Figure 78 were for ignition conditions and Figure 84 plotted operating conditions, the total temperature and ratio of specific heats (T_T and γ) were changed to 4000 K and 1.16 respectively. These values were based on post detonation conditions for an N_2O and C_2H_4 CJ detonation at a representative $\Phi = 1$ and initial pressure and temperature of 410 kPa (60 psi) and 295 K. Post detonation conditions were solved for using NASA's Chemical Equilibrium Program (CEA). Therefore, the lines of constant exit area ratio in Figure 84 were estimates only.
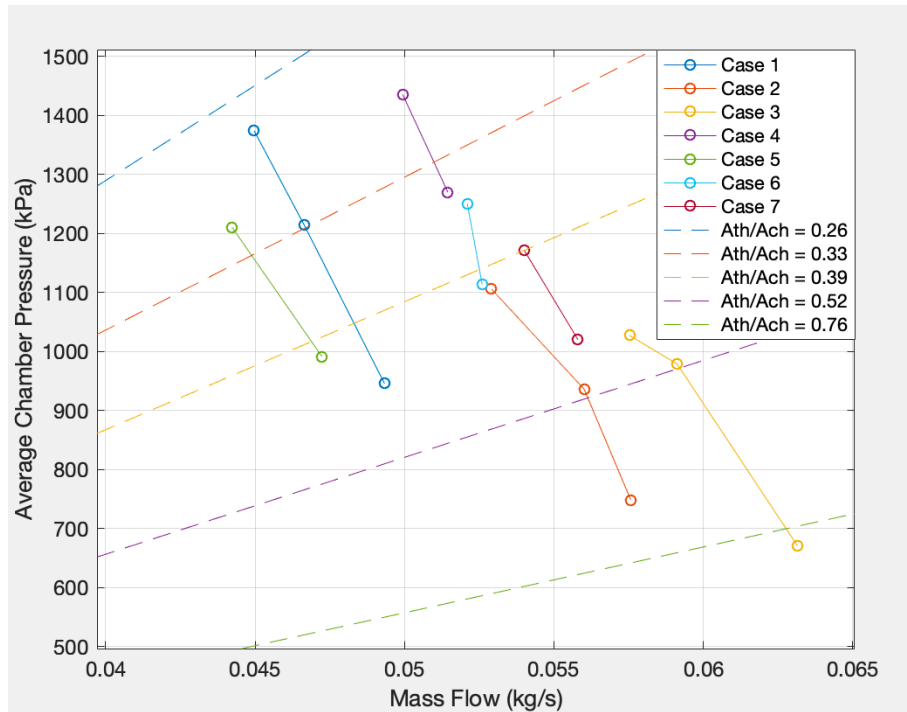
Fig. 84 Average channel pressure as a function of measured mass flow for the seven cases with pressure drop. Lines read from low to high mass flow demonstrate area change.

Following each line from a point of lowest mass flow to highest (mass flow increased as pressure dropped for all cases), Figure 84 showed the exit area ratio increased over the course of the detonation in all cases. To capture the amount of area change, two additional lines of $\varepsilon = 0.52$ and 0.76 were added. Again, these values were calculated using the total temperature and ratio of specific heats discussed above and therefore were estimates useful for showing the relative amount of area change incurred over the course of the seven cases. For example, Case 3 was shown to increase its estimated ratio from $\varepsilon = 0.52$ to 0.76, which was an increase of 46%. Both cases 1 and 2 also had similar sized changes in area. Cases with only 2 data points had smaller changes, which was expected as they were associated with less pressure drop. Due to the CTAP measurement delay, changes to the pressure were likely larger than what was shown. This would only further increase the amount of area change shown.

When Figure 84 was compared with Table 8, it was found that the nozzle area ratios were not in line with the corresponding lines of constant ε. This was because starting points for some

170

runs (i.e. Cases 2 and 3) were extracted after erosion had influenced the area and that there were variances in the amount of erosion on the nozzle and outerbody for a given run (i.e. Case 1). The approximate nature of the ε lines used in Figure 84 also impacted the observed differences. Overall, the photos in Figure 83 combined with the consistency and estimated amount of area change from Figure 84 strongly supported the claim that changes to exit area due to erosion were responsible for the observed pressure drop.

As mentioned at the beginning of this section, every instance of pressure drop showed an increase in wave frequency. However, when data points without a channel pressure drop were included in plots of frequency and chamber pressure, there was not a clear trend as it was expected there would be. In order to properly see the influence of the pressure drop, data from the same run needed to be compared. This was because wave frequency was a function of many coupled variables. When the channel pressure dropped due to erosion, the sudden change in a single variable made its impact observable. Furthermore, to get the proper relationship, the change in CTAP pressure from its value before the pressure drop was used. This was done because the CTAP pressure sensor did not accurately measure the channel pressure during periods of change, but the difference from the run's specific steady state pressure was believed to scale more appropriately.

Figure 85 plots the CTAP pressure difference just described against the corresponding wave frequency for the seven different detonations. Each case had its own set of two or three data points taken during the pressure drop. Figure 85 showed that for every case, the more the pressure dropped, the more the wave's frequency increased. Furthermore, the observed trend was approximately linear for all cases with a slope of +4 kHz for every 500 kPa of pressure drop. Using the same data points, Figure 86 plotted the mass flow against the pressure change and confirmed that as the pressure change increased so did the mass flow. Mass flow changes did not coalesce on the same line as the frequency trend. This was likely a function of the specific pressure differential

on the controllers for a given run impacting the starting mass flow value for each data set prior to the pressure drop. Changes in mass flow varied + 2-5 g/s for every 250 kPa of pressure drop. The variability was again attributed to the interplay with the specific differential across the controllers. Mass flow trends were also not observable in data without a pressure drop included.
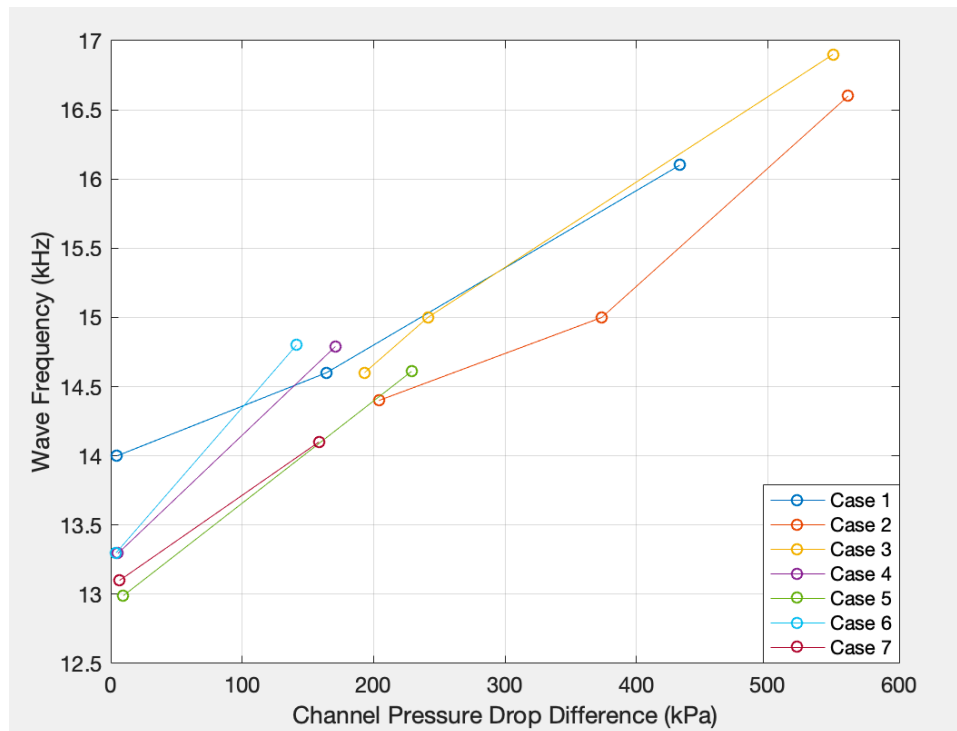
Fig. 85 Wave Frequency as a function of channel pressure drop. Pressure drop measured as difference from pressure prior to the drop and the pressure at the point of interest

In addition to influencing the wave frequency, pressure drops also had an impact on the wave mode. Figure 87 plots the evolution of wave modes with increasing pressure drop for all the cases. The figure showed that two of the seven cases lowered their wave score as the pressure drops increased. For example, Case 1 had a score of 10 and frequency of 13.5 kHz but transitioned to a galloping mode with a score of 7 but average frequency of 16.1 kHz. The second case, Case 2, dropped into a highly unstable galloping mode with a score of 3 and a frequency of 15 kHz, but bounced back to a score of 10 and frequency of 16.6 kHz. Furthermore, Case 2 was able to recover into the second fastest wave frequency recorded with a score of 10, surpassed only by Case 3 which

had a frequency of 16.8 kHz and score of 10. Both cases never dropped to a mode with dominant

clapping behavior (scores 4-9), but instead to a mode with dominant galloping behavior. In

addition, whenever a wave score improved it did so to a mode with less or no clapping behavior.

This meant waves which improved did so through limiting the prevalence of clapping and only

degraded to a non-clapping mode.
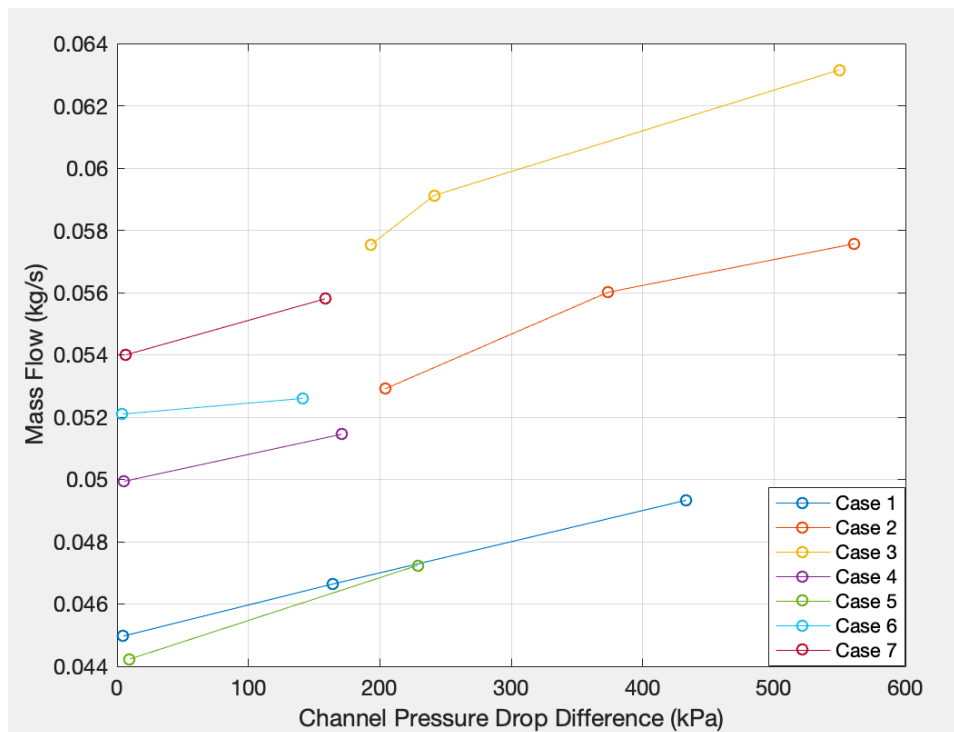
Fig. 86 Mass flow as a function of channel pressure drop. Pressure drop measured as difference from pressure prior to the drop and the pressure at the point of interest.

These trends agreed with the discussion from Section 4.2 where clapping behavior was

found to reduce at higher frequencies but that faster frequencies did not guarantee a higher wave

mode score. This also explained why certain unstable wave modes, such as galloping, and

deflagration were present in some cases. These modes were believed to be not reliant on the same

mechanisms that clapping modes were, and as a result, increased wave frequency from the

decreased pressure would not prevent them from occurring. Galloping modes were also correlated

to runs which had significant erosion inside the channel and nozzle such as was shown in Figure

74. Therefore, the cases where wave score degraded to a galloping mode may have not been related to the changes in mass flow and pressure but rather the extent of erosion present for that particular run. This would be reasonable considering erosion was required for the pressure to drop to start. If true, and erosion enabled the change in wave mode, then the effect of pressure drop would have been universally positive with respect to wave frequency and wave mode.
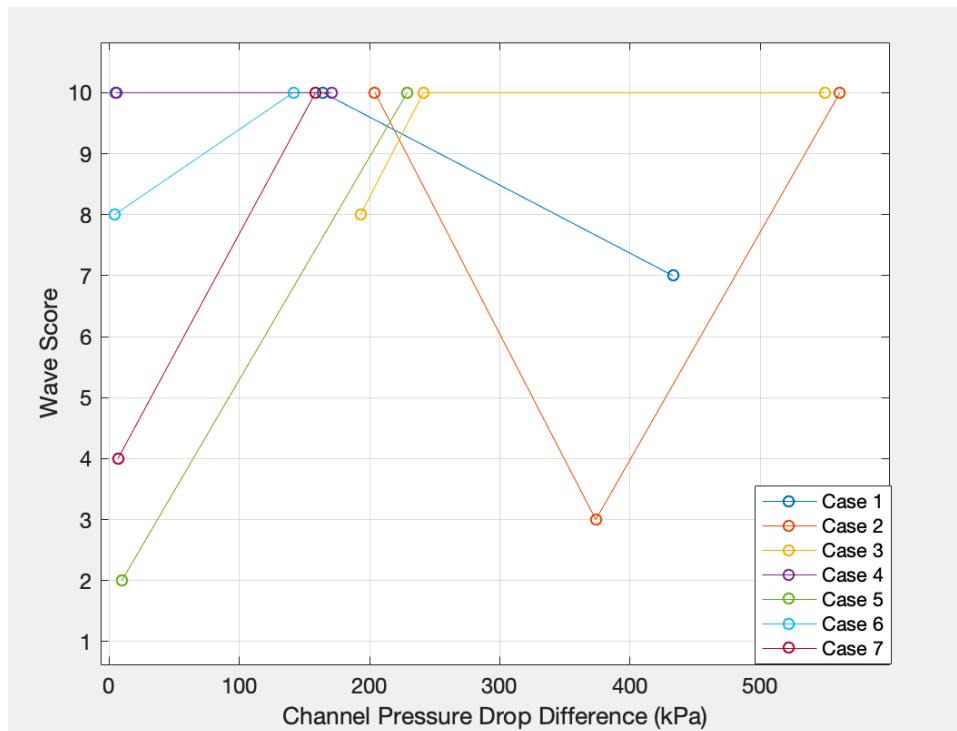
Fig. 87 Channel pressure drop influence on Wave Mode Score. Pressure drop measured as difference from pressure prior to the drop and the pressure at the point of interest in kPa.

Additional parameters that had a consistent impact on the wave behavior were difficult to ascertain. This was because the window of conditions at which detonation occurred was small, as seen in the operating maps in Figures 65 and 67. As a result, the effect of various operating parameters was not well observed. Channel pressures, measured when no pressure drop occurred, had a limited relationship with both frequency and wave mode as mentioned. Plenum pressure to chamber pressure ratios were also found to have little to no trends with respect to wave mode and frequency. Temperature of the RDE walls was another factor which may have led to increased

wave speeds. As discussed, the increases in wave speeds only occurred in longer runs with significant erosion of the steel and Inconel outerbodies. As a result, the RDE structure would have been extremely hot which would have limited the heat loss from the detonation to the walls. The lower heat loss would allow more energy to be put into the detonation which would allow higher wave velocities. Unfortunately, temperature measurements of the outerbody walls were not available. Therefore, it was important to identify the mechanisms occurring during the channel pressure drop because it was the only parameter which had a measurable and consistent impact on wave behavior.

Section 4.3.3 Mechanisms for Observed Wave Behavior during Pressure Drop

In order to determine the mechanism behind the frequency changes when the channel pressure dropped, multiple parameters had to be considered. These parameters included cell size, fill height, equivalence ratio and injector stiffness. Table 9 below summarizes expected trends when the channel pressure dropped. For example, larger cell sizes would have a negative influence on wave frequency and stability. This was due to their inverse dependence on pressure causing them to grow as the pressure dropped. Injector stiffness was expected to have a positive impact on wave stability, but only an indirect influence on wave frequency. However, plots of injector stiffness based on plenum pressure to channel pressures showed a limited relationship. Fill height, defined as the axial height of fresh reactants injected in front of the detonation wave was expected to have a positive impact on both wave mode and wave frequency due to its ability to add to the amount of detonation cells inside the detonation wave front. Equivalence ratio was also expected to have a positive impact on wave frequencies when at stoichiometric conditions. Therefore,

equivalence ratio and fill height were investigated further as they both represented potential mechanisms.

Table 9. Expected trends of various parameters during cases of pressure drop.

Parameter	Response to Decreased Pressure	Response to Increased Mass Flow	Responses' Impact on Wave Stability	Responses' Impact on Wave Frequency
Cell Size (λ)	Increases	Independent	Negative	Decreases
Fill Height (h)	Increases	Increases	Positive	Increases
Equivalence Ratio	Independent	Increases	Independent	Increases near optimum value
Injector Stiffness (P_{plenum}/P_{ch})	Increases	Independent	Positive	Indirect

Due to the generally lean conditions during detonation, the flow controllers would correct the flows to more stoichiometric mixtures when the pressures dropped. This would lead to smaller cell sizes and help to increase the wave frequency. When equivalence ratio was plotted with mass flow in Figure 77, this trend was found to a small degree. To investigate the pressure drop cases specifically, Figure 88 plotted both equivalence ratio as a function of pressure drop and wave frequency as a function of equivalence ratio. The dual plots showed that the fastest wave frequencies did in fact occur between equivalence ratios of 0.96 and 1.0 during periods of pressure drop. However, like the other variables, the trend between wave frequency and equivalence ratio was minimal when data points without a pressure drop were included. It was also found from inspection of Figure 88 that not every run with a pressure drop became stoichiometric. This was because the mixture was ultimately a function of the differential across the controllers not the decreased pressure. Therefore, equivalence ratio was not believed to be strong a mechanism candidate.
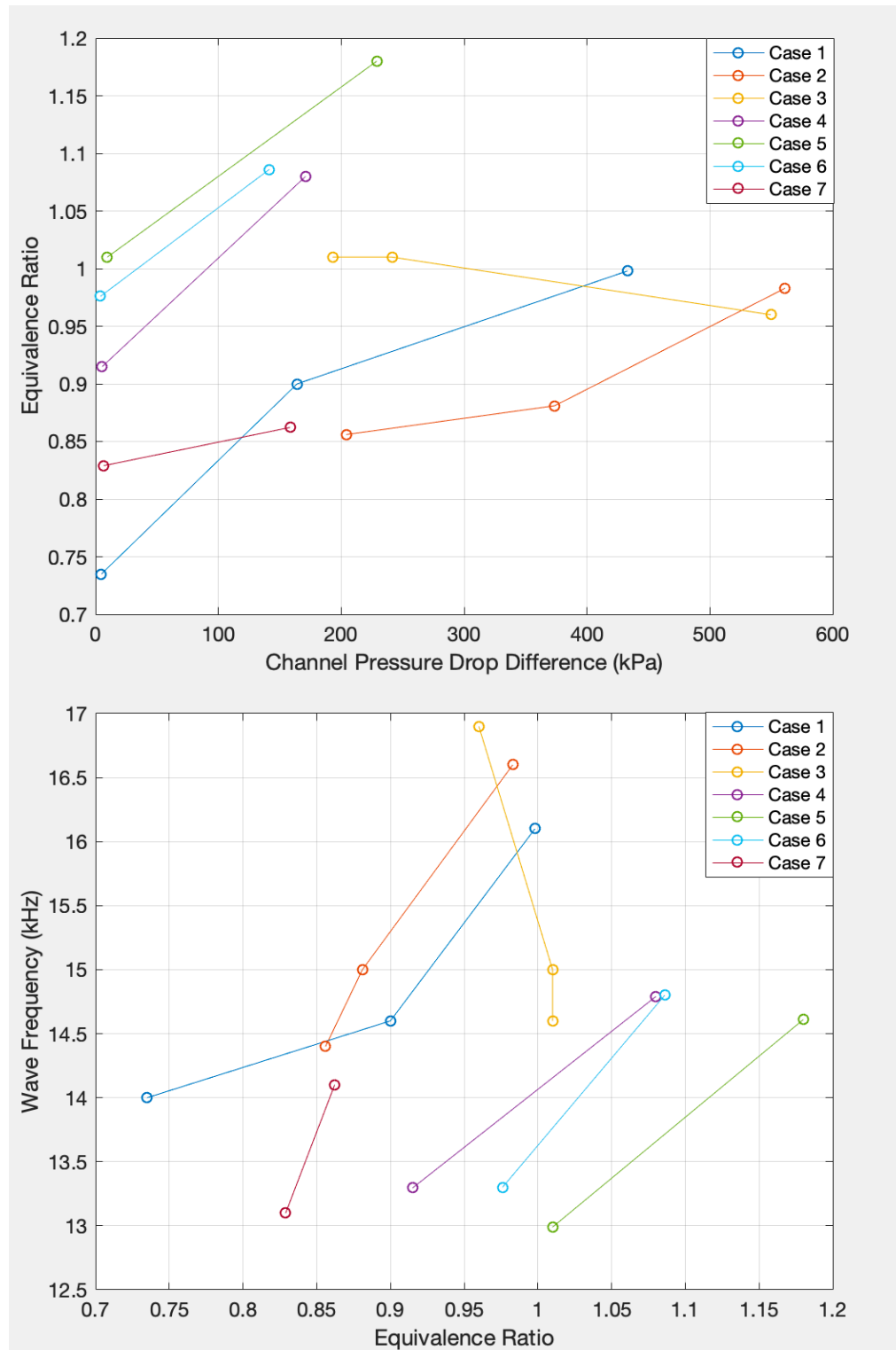
Fig. 88 Dual plots of equivalence ratio as a function of channel pressure drop and wave frequency as a function of equivalence ratio.

The fill height was a critical component in the design of an RDE and was a measure of how much reactant gas was injected in front of the detonation wave. Holding all else constant, fill height was expected to decrease as frequency increased, as there was less time for the injectors to fill the channel at higher frequency. However, this ignored other factors contributing to the fill height, such as pressure and mass flow and considered wave frequency independent of fill height, which was not true. For example, the fill height determines how many detonation cells can exist inside the detonation wave [7, 19, 20]. More cells inside a detonation front increases the frequency of triple point collisions as described by Shepherd [19]. When the frequency of triple point collisions increases, the amount of time it takes the transverse waves to propagate across the corresponding incident wave decreases. Then, because the velocity of the incident wave decays, and there is less time between collisions, the minimum incident wave velocity increases. This increases the wave front's overall average velocity and frequency. Thus, the wave frequency has a dependence on fill height.

Another argument that increased fill height increases the wave frequency comes from Bykovskii et al. who proposed that there was a range of optimal fill heights as determined by Equation 4 [7]. Keeping in mind that Bykovskii et al. defined stability with relation to the detonation's wave speed, better adherence to the proper fill height would translate to a faster and more stable wave [7]. Approximated fill heights prior to pressure drop for the new injection scheme are presented later, but were found to be between 2-3 mm. These fill heights were below the Bykovskii correlation which predicted fill heights between 3-12 mm for the Micro-RDE geometry [1,7]. This meant that increases to the fill height would result in better adherence to the values proposed by Bykovskii et al.

To approximate how both mass flow and channel pressure changes impacted the fill height in the current data, the ideal gas equation was used to perform an analysis similar to the one used by Dechert [1]. The same assumptions used in that analysis were used here for consistency between results, namely: there was no pre-burning of the reactants, the pressure was uniform across the entire fill volume, and the fill temperature was equal to the plenum temperatures [1]. Using the ideal gas equation of state, fill height was derived from solving for the approximate volume of the injected reactants knowing the gas constant and mass flow and estimating the temperature and pressure. With that volume, the geometry of unburned reactants inside the channel was approximated as a triangular prism of width 2 mm, length 88 mm (circumference of channel), and height equivalent to the fill height. Wave frequency was used to determine the amount of time to be multiplied by the mass flow rate to solve for the number of moles inside the volume. To estimate the fill pressure, a factor of 3 between average channel pressure and the pressure in the gas in front of the denotation was used. This factor was derived by Bykovskii et al. based on experimental data from various RDE channel geometries and therefore was not necessarily accurate for the Micro-RDE. However, it was consistent with the method employed by Dechert [1,7]. As there were no temperature measurements in the channel, the total temperature values of 290-295 K from the plenums were used.

Figure 89 plots the fill height versus mass flow in addition to fill height versus estimated fill pressure. Data from both the spark plug and pre-det data sets are included. Only data points with approximately constant CTAP measurements and flow controller measured mass flow values were used in the fill height calculations shown in Figure 89. This was done to help the accuracy of the approximation. The estimated fill height range with the new injection scheme was 2 - 3 mm, with an average of ~2.4 mm. The three data points using the spark plug resulted in values of 2.66, 2.66, and 2.52 mm. This agreed with the general assessment that the spark plug set up had more

pressure relief in the chamber due to the ¼" hole and therefore resulted in lower operating pressures. These lower pressures led to higher-than-average fill heights when compared to the pre-detonator set up.

The relationships in Figure 89 also showed that decreases in pressure and increases in mass flow both increased the fill height. The slope of the fill height versus mass flow trend was approximately +0.6 mm for every 10 g/s of mass flow increase. With respect to pressure, it was +1 mm for every 150 kPa drop. These trends were expected based on the dependencies in the ideal gas law analysis. When the wave frequency was plotted as a function of fill height, shown in Figure 90, there was no clear relationship, either decreasing or increasing. This was attributed to the small range of fill heights and frequencies, from 2-3 mm and 13-14.8 kHz respectively, in the restricted pressure data set used. For example, using the trends just discussed, a change of 1 mm, obtained from the range of fill heights shown in Figure 90, could potentially occur from a pressure change of ~150 kPa. Referring to the trends from Figure 85, a pressure drop of 150 kPa would correlate to a frequency change of only 1.2 kHz. Therefore, it was reasonable to not see a trend in Figure 90. Additionally, the set did not include data points where a sudden pressure drop occurred and therefore neglected the cases with the largest frequencies. This implied that to see the influence of a fill height on the wave behavior the points taken during pressure drops needed to be considered, regardless of the potential inaccuracy from their CTAP measurements.
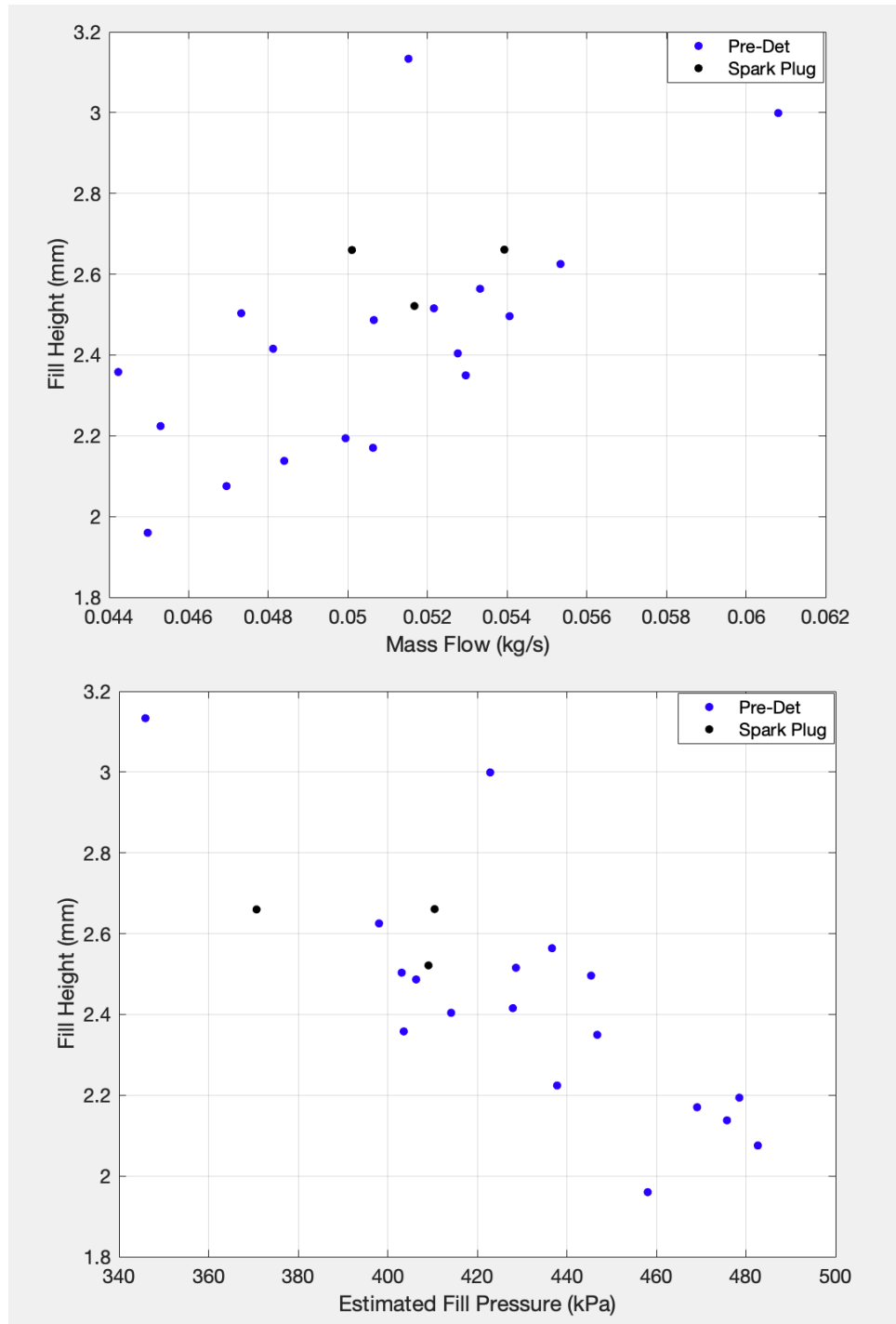
Fig. 89 Fill Height as a function of mass flow and estimated fill pressure. Fill pressure was assumed three times lower than average channel pressure.
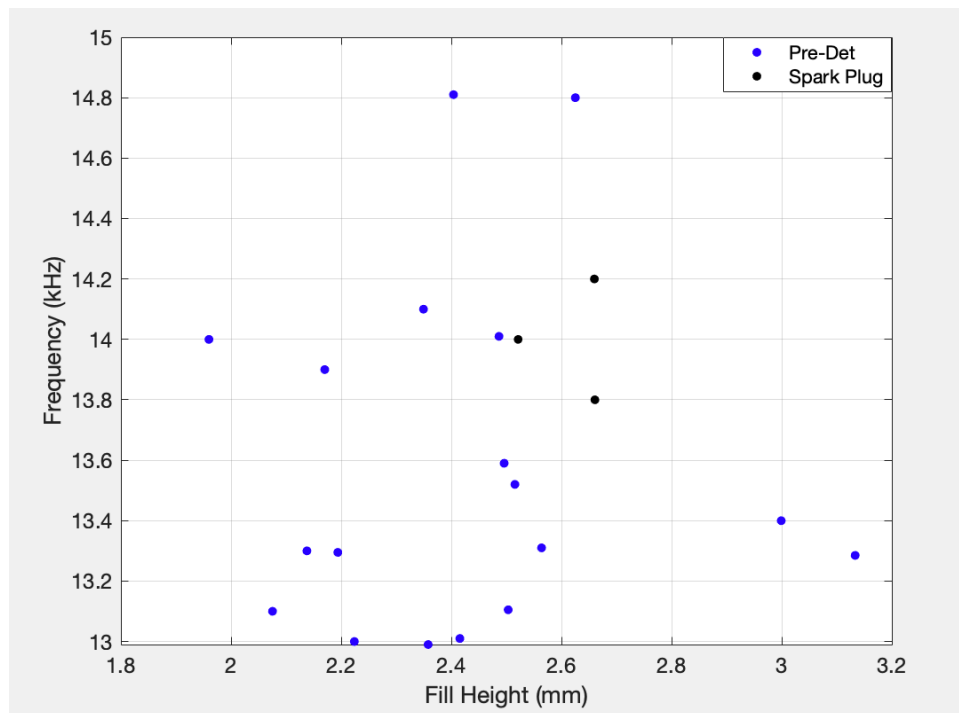
Fig. 90 Frequency as a function of fill height. Data taken during constant CTAP measurements. Limited relationship observed.

To better see if increasing fill heights increased frequency, Figure 91 plots frequency as a function of estimated fill height but with data taken from cases with pressure drop. It was determined that the non-steady CTAP pressures from these data points would have overestimated the channel pressure during periods of rapid pressure loss. This would have underestimated the subsequent fill height estimation, and thus was a conservative estimate of the relationship with frequency, which was acceptable. Each case in Figure 91 increased in fill height, with estimates ranging from 2 mm to 4.6 mm over frequencies from 13 kHz to 16.8 kHz. Cases 4 and 6 showed little fill height growth, however their mass flows both changed less than 2 g/s over less than 180 kPa of pressure change as seen in Figure 86. As a result, their fill heights would not be expected to change much in the ideal gas law analysis. Furthermore, their fill heights were underestimated by the CTAP and it was expected if a more accurate pressure measurement was used larger changes would have been observed. Four of the five fill heights associated with a frequency above 15 kHz were larger than the largest fill height shown in Figure 90. The one fill height that was not larger

had a value of 2.7 mm and was therefore smaller than only two of the fill heights shown in Figure 90. It was concluded that the pressure drop cases were associated with larger than average fill heights, which did trend towards higher frequencies in all cases. This meant that fill height was likely the mechanism driving the increases in frequency.

To further show fill height was a mechanism for the trends in wave mode as well as frequency, the interactions between the channel geometry and fill height had to be considered. When the fill heights measured during constant pressure cases were related to wave mode score in Figure 92 it was found that all points which had a wave score of 10 had a fill height below 2.5 mm. Furthermore, these high scoring wave modes were not associated with high frequencies. As seen in Figure 92, all modes with a score of 10 were at or below 14 kHz except one, which was at 14.8 kHz and had a fill height of 2.4mm. No wave modes in this data set shown had a frequency above 15 kHz.
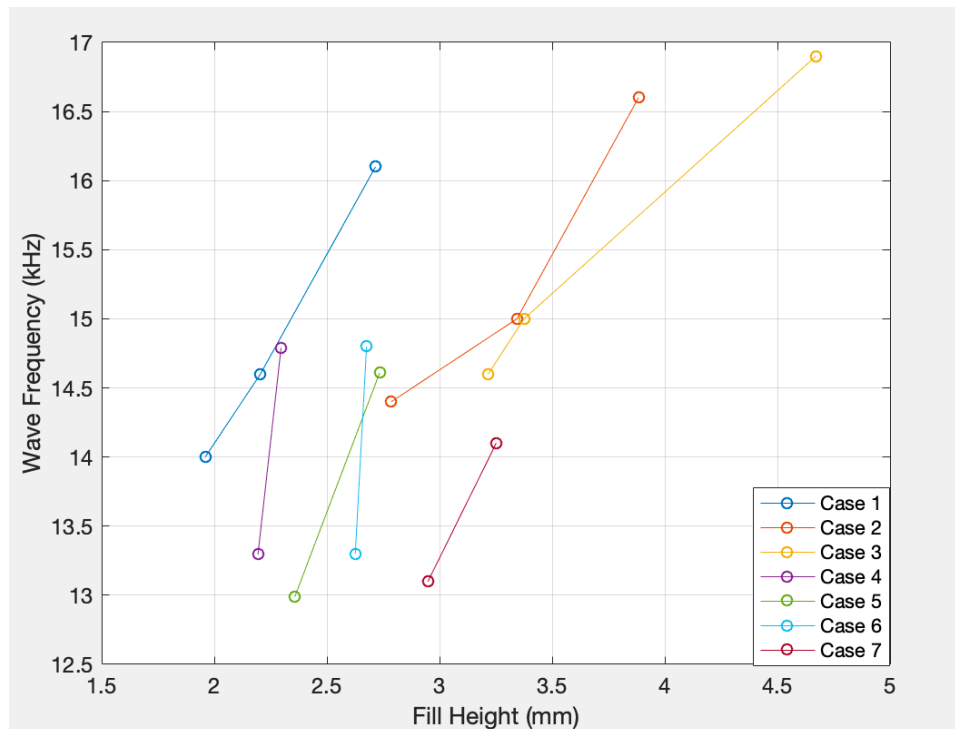
Fig. 91 Frequency as a function of fill height. Data taken during periods of pressure drop.

This observation was consistent with the trend of lower fill heights having a lower frequency and explained cases with a high wave mode score, but a low frequency. In these instances, the smaller than average fill height led to lower frequencies and the lower wave location avoided decoupling mechanisms that would have increased the chances of a clapping mode. Only wave modes observed during pressure drops exhibited both high frequency and high wave scores. Such waves were believed to be the result of both high fill height and little to no erosion/irregularities in the channel to incite instabilities. As discussed, when the high fill height occurred with erosion irregularities the mode tended to degrade into more unstable galloping modes. Therefore, to optimize wave mode and frequency, a smooth channel with limited erosion and high fill height was required.
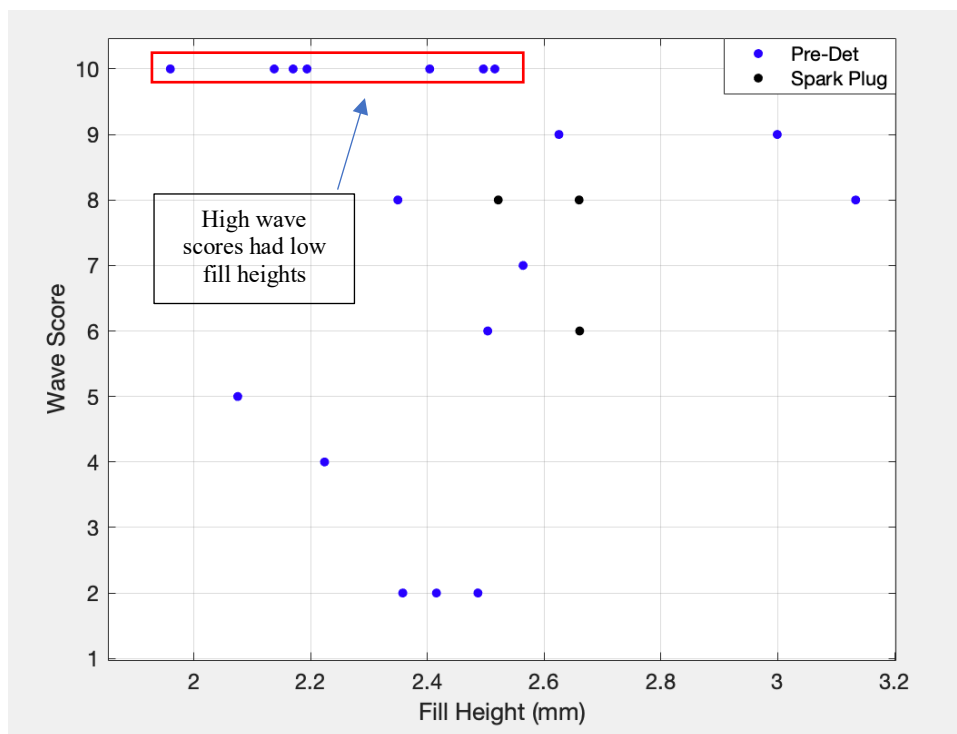
Fig. 92 Wave mode score as a function of fill height. Data taken during constant CTAP measurements.

Lastly, when compared to Dechert, who had found a fill height range of 3.2 – 8.1 mm, the estimated fill heights in this section were significantly smaller [1]. Lower fill heights were

expected with the new injection scheme as the mixing length of the reactants was reduced by introducing the fuel to the oxidizer prior to the detonation chamber. Additionally, images taken after detonation were also used to estimate fill height from the observable burn patterns. Figure 93 shows two of these images, and the burn pattern of interest was measured at 4/32" or 3.2 mm at its smallest and 8/32" or 6.4 mm at its largest. Considering the estimated values were between 2 mm and 3 mm the burn pattern was indicating a larger fill height than estimated. However, the estimation method employed assumed a factor of three between average channel pressure and fill pressure. This factor was derived using experimental data from RDEs using different geometries and mixtures than the Micro-RDE. As a result, the estimated fill heights were not the most accurate and were only an order of magnitude approximation. Therefore, the slightly larger fill heights presented were not unreasonable and were in fact in decent agreement with the estimated values considering the method used. This added validity to using burn patterns to determine the wave's location. Additionally, such small fill heights implied that the number of cells inside the wave was low. For example, using the range of estimated cell sizes of 0.5 mm to 1.75 mm, the potential number of cells inside the detonation wave varied from one 1-12 cells [1]. This supported the
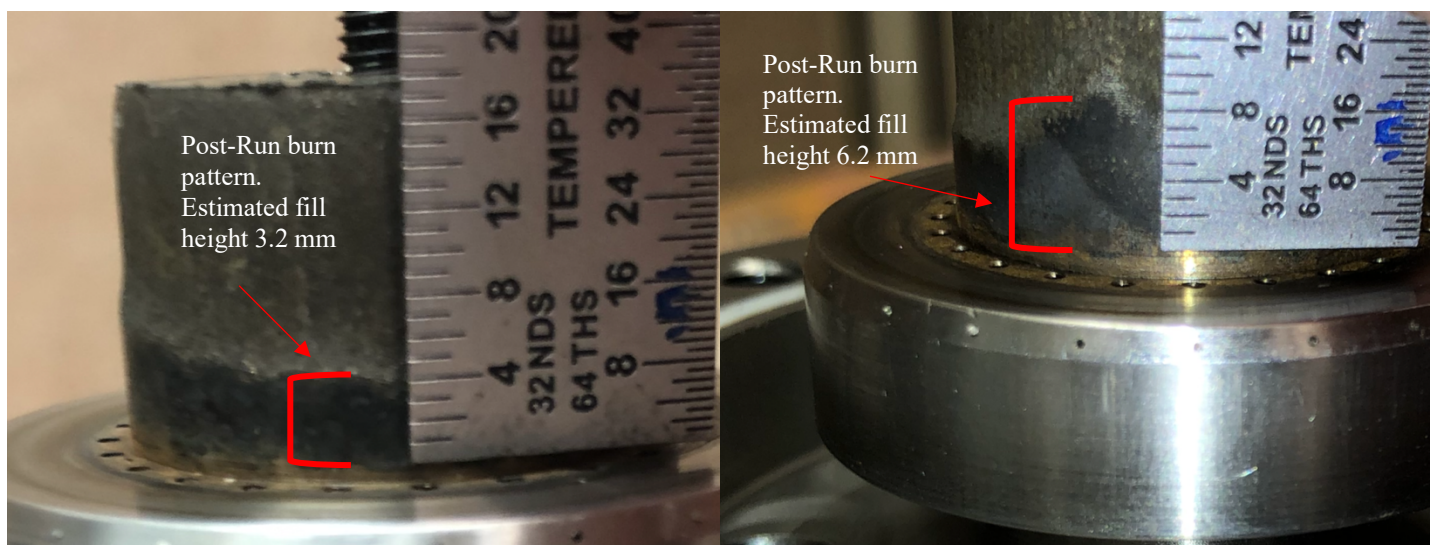
Fig. 93 Pictures of Fuel/Ox manifold after detonation. Visible burn pattern corresponding to approximate fill heights between 4/32" to 8/32" or equivalently 3.2 mm to 6.4 mm.

argument that increases to fill height would benefit the wave behavior through the addition of cells in the wave front and why low fill heights were quickly susceptible to instability. Therefore, one of the differences imposed by the new injection scheme would be an increased minimum mass flow to accommodate the naturally lower fill heights.

Increases in wave frequency were observed every time the channel pressure dropped. From the discussion above, this was the combined result of increases in mass flow and decreased pressure causing increases in the fill height and more stoichiometric mixtures. Both factors occurred simultaneously when the pressure dropped, which made it difficult to determine the extent of their effect individually. However, fill height was considered the primary mechanism. The consistency with which these processes were able to increase frequency revealed potential design improvements focused on optimizing them. For example, variable nozzle geometries or exit areas could be a fruitful avenue to controlling channel pressure and fill height, and thus be a means of reliably manipulating frequency. This would also be helpful in manipulating the plenum to chamber ratios which were found to be important in ignition. It may be possible to use frequency manipulation to actively adjust wave modes out of less stable clapping modes if the mechanisms for clapping are truly dependent on wave frequency as predicted in Section 4.2. Additionally, as was discussed in Section 4.3.1, conditions conducive to successful ignition did not always lead to optimized operating conditions. Therefore, such manipulation could present a means of optimizing both ignition and operation. Further design improvements, and ideas for future work are detailed in Chapter 5. Lower fill heights than in the previous design also increased the minimum mass flow required to achieve a desirable fill height.

V. Conclusion

In an effort to develop a small scale RDE that operated on the limits of detonability a "Micro-RDE" with a channel diameter of 28mm, a channel gap of 2 mm, and channel length of 30 mm was designed by Dechert to achieve a 20 kHz operating frequency at mass flows between 25-75 g/s [1]. Dechert showed that detonation was achievable at this size and mass flow. However, the wave modes were universally unstable with consistent clapping modes and wave frequencies 30% lower than designed. Poor mixing quality and channel protrusion from the spark plug ignition were cited as the main reasons for the instability and low speeds [1].

The current work focused on improving upon the design by Dechert. To do so, a new injection scheme was designed, built, and tested and the old spark plug ignition method was switched to a pre-detonator. Both modifications were responses to mechanisms believed to be causing the unstable wave modes and low frequencies observed in the previous design. Therefore, the objectives of the current research were to explore the operability of the Micro-RDE with the modifications in place as well as observe changes to wave behavior. Comparisons to the performance of previous work would then inform whether or not the modifications had improved the RDE's ability to achieve its original design goal. The following sections recap the steps taken to implement these changes, the results they produced, and potential avenues for future work.

Section 5.1: Methodology

A new injection scheme was designed to place the fuel feed line into the oxidizer injection holes about 1 mm before the oxidizer injectors opened into the detonation channel. The goal was to decrease mixing length in the channel so that the reactants were better mixed by the time the wave passed. To integrate this injection scheme into the modular design of the Micro-RDE a new combined fuel and oxidizer manifold was designed with an accompanying outerbody.

In addition to the new injection scheme a pre-detonator device was integrated into the RDE's testing apparatus as a replacement for the spark plug. The pre-detonator still required a hole into the channel through which it could send its initial detonation. First attempts at integration used an 1/8" hole located at the same axial location as the spark plug, 21 mm above the injection holes. The injector hole was later placed at lower axial locations to cool it with unburnt reactants and limit the extent of erosion damage. The hole size was also changed from 1/8" to 1/16" to limit recirculation volume. Final designs incorporated an outerbody made of Inconel to further improve erosion resistance and placed the pre-detonator entrance 3.5 mm above the injectors. Subsequent detonations showed these changes increased durability of the outerbody. Nozzles were also subjected to severe erosion damage and did not show evidence of improved durability with the outerbody and pre-det hole modifications. However, limiting run times below one second prevented the most severe cases of erosion. Therefore, limiting run times, or incorporating materials such as Inconel or ceramic carbide for the nozzles, would benefit hardware longevity.

To explore the operability of the RDE, volumetric flow controllers were used on both the oxidizer and fuel feed lines as means to regulate the mass flow into the RDE and set the desired equivalence ratios. Data logging software was used to measure flow histories from these devices. However, intermittent issues with the sampling rate in the resultant histories made their results inaccurate. In response, estimation methods were devised. For cold flow, non-detonating conditions discharge coefficients for specific injector manifolds were determined using accurately measured mass flow data. These discharge coefficients and corresponding pressure data were used to determine mass flow rates. During detonation, discharge coefficients could not be analytically modeled as in the cold flow case. Instead, an empirical fit from data taken during detonating conditions was performed. The empirical relationship was then used to back out mass flow estimates. Both methods adequately reproduced known data and were therefore used when mass

flow data measured from the controllers was not available. The flow controllers were also found to not adequately adjust mass flows back to requested values after a detonation. The back pressure induced by the detonation decreased the pressure differential across the controlling valves such that they were at max duty cycles. As a result, flow rates were static about the conditions created after the detonation back pressured the feed lines. This limited the range of mass flows and equivalence ratios tested.

Pressure and temperature sensors were placed inside the feed lines for both the fuel and oxidizer. Analysis was performed to show that these measurements were adequate total pressure and temperature values. A capillary tube average pressure measurement was used inside the detonation channel to obtain average chamber pressure measurements. Pressure and temperature measurements were required to perform the mass flow estimation methods.

To address the second objective of characterizing the new wave behavior, high speed video of the detonation chamber was used to determine wave mode and wave frequency. Wave frequency calculations were performed by hand because automated algorithms required too much complexity for the scope of the research. A dedicated effort to create such algorithms, or different frequencies acquisition methods, may be beneficial to future research.

Section 5.2: Results

To characterize the operating space and make comparisons to previous work, mass flows from 0.025 kg/s to 0.075 kg/s were tested over a range of requested equivalence ratios. With the spark plug, equivalence ratios between 1.1 and 1.2 were tested. When the pre-detonator was used the range increased to equivalence ratios of 0.8 to 1.4, and therefore constituted the bulk of the data. Maps showing the space of requested mass flow and equivalence ratio test points were developed. It was intended to use these maps to directly compare to similar ones made in the

previous research. However, due to the mass flow control issues, use of requested values was not an accurate representation of the true mass flow and equivalence ratio in the RDE. Furthermore, the flow controllers' inability to regulate to desired test conditions limited the tested space. In addition, conditions at the point of ignition and during detonation were significantly different. Therefore, two maps, using measured mass flows and equivalence ratios, were made. One for ignition conditions, called an ignition map and the other for detonation, called an operating map. These were made for both the spark plug and pre-detonator data sets.

After tests with the spark plug, detonable ignition was found over equivalence ratios of 0.9 to 1.6 at mass flows of 45-75 g/s and detonation was sustained in a range of equivalence ratios from 0.8-1.15 at mass flows of 45-65 g/s. For the pre-detonator tests, detonable ignition was found over a range of equivalence ratios from 0.9 to 1.55 at mass flows between 50-75 g/s. Detonation was maintained over a range of equivalence ratios between 0.6 to 1.2 with mass flows between 35-70 g/s. In both data sets, ignition maps were more fuel rich than operating maps, again due to the pressurizing effect of the detonation on the controllers. The spark plug data was found to be more fuel rich than the pre-detonator data due to higher average channel pressures. In comparison to the previous research, both the ignition and operating maps had a smaller range of detonable equivalence ratios and mass flows, but this was mostly a factor of the controllers limiting the available set of test points, not the RDE's capabilities. Therefore, true comparisons of the operating envelope were limited as it was not clear how much the maps could be expanded had the controllers been able to reach all the desired test points. Ignition maps for both the spark plug and pre-detonator data also showed significant overlap of successful and unsuccessful data points. This suggested other factors were driving detonability beyond the mass flow and equivalence ratio. As a result, the efficacy of the new injection scheme was inclusive until these factors were determined.

In addition to the operating space, the wave mode and frequency was studied and compared to the previous work. Several new wave modes were observed in the spark plug and pre-detonator data sets. Therefore, to make assessments of the modifications' impact, the wave's propagation behavior was quantified. To do so a standard was put forth with which to judge the other observed modes. This standard was defined as a single wave consistently propagating in a one direction with constant frequency. From this definition different wave modes were ranked according to how well they met this standard. This ranking scheme was also applied to the observed wave modes from the previous research. Quantification of wave modes showed that removal of the spark plug significantly decreased the prevalence of lower scoring modes with dominant clapping behavior. Evidence that the wave propagated underneath the spark plug suggested the wave fill height had been lowered by the new injector design, which decreased the prevalence of clapping modes.

Multiple instances of single waves which met the definition for stability (score of 10) were observed over ignition conditions from $0.9 < \Phi < 1.33$ and $0.055 < \dot{m} < 0.075$ kg/s and operating conditions from $0.7 < \Phi < 1.2$ and $0.04 < \dot{m} < 0.06$ kg/s. These ranges showed that wave mode score had a limited dependance on equivalence ratio and mass flow and suggested other parameters were responsible for observed trends. Average wave frequencies up to 16.8 kHz were observed. Peak frequencies reached 19.1 kHz, but were observed in wave modes with more instability, such as galloping behavior. Frequency was found to correlate with stable wave modes, however stable wave modes were not restricted to high frequencies. For example, multiple instances of single waves which met the definition for stability were observed and with frequencies as low as 13.3 kHz. However, no clapping mode was able to reach a frequency higher than 14.8 kHz. Therefore, mechanisms for unstable behaviors such as clapping appeared linked to low frequencies but other unstable behaviors, like galloping were linked to factors such as erosion. Potential explanations of the mechanisms leading to clapping behavior were put forth to explain the frequency dependence.

Frequency, like wave mode score, was found independent of mass flow and equivalence ratio, enforcing the need to identify the parameters influencing the wave behavior.

The consistency of single wave behavior in both data sets supported the objective in developing a new injection scheme to improve wave mode. Wave frequency, with a range of 13.1-19.1 kHz was also improved over the previous range of 11.7-14 kHz. However, when outlier cases were removed, wave frequencies averaged to approximately 14 kHz. Although, these waves were significantly more stable than those measured with the previous injection scheme. So, while an improvement was achieved, the injection scheme was unable to produce wave frequencies at the original design objective of 20 kHz.

The new ignition maps showed prevalent overlap of conditions that did and did not detonate. Therefore, other parameters had to be investigated, beyond the mass flow and equivalence ratio that drove the operability character of the Micro-RDE. The relationship between mass flow and channel pressure showed nozzle sizes played a role in the detonability and that exit area ratios between $\varepsilon = 0.39$ and 0.33 were found optimal for the points tested. Further inspection showed the mechanisms for this behavior was the nozzle's impact on injector stiffness as measured by the plenum pressure to chamber pressure ratios, P_{ox}/P_c and P_f/P_c. Plenum pressure to chamber pressure ratios of more than 3.0 and 3.5 for the oxidizer and fuel respectively were found to greatly increase the probability of detonation. When compared to Dechert, the required P_{ox}/P_c and P_f/P_c ratios of 3.0+ in the new injection scheme were significantly higher than the reported ratios in the old scheme which ranged from 1.2 to 3.0 [1]. This was attributed to the change in injector geometry requiring more driving pressure to achieve an adequate fill height. In this regard, the new injection scheme also provided benefits over the initial design suggesting that premixing is desirable for this Micro-RDE.

Detonations with durations longer than one second led to enough erosion to change the exit area enough that the channel pressure would drop. These channel pressure drops ranged in magnitude from 150 kPa to 600 kPa which was nearly half the original detonation chamber pressure of approximately 1.2 MPa. Every instance of channel pressure drop was shown to increase the wave frequency. This was the result of the pressure change allowing the flow controllers more control authority to begin increasing the mass flow into the RDE's. Increased mass flow and low pressures led to growing fill heights during the runs with pressure drop. Fill heights without pressure drop during the run were estimated to be between 2-3 mm. When the pressure did drop during the run, fill height could increase up to 4.5 mm. Therefore, it was determined that an increase in fill height was the mechanism driving changes in wave frequency during pressure drops. Additionally, unstable waves with clapping behavior improved their mode score with larger fill heights but unstable waves without clapping did not. This meant clapping mechanisms were suppressed at the higher frequencies caused by the fill height changes, while unstable wave modes without clapping were not. Therefore, fill heights also acted as an indirect mechanism for wave mode improvement.

Compared to previous work estimated fill height between 2-3 mm was significantly smaller than the previous design which estimated values between 3.2-8.1 mm [1]. This was strong evidence that the new injection scheme had decreased the operable fill height and therefore had also decreased the mixing height. Doing so allowed the wave to run lower in the channel and therefore avoid potential decoupling irregularities which could cause unstable wave behavior. Low fill heights were consistent with observations that wave was able to run underneath the spark plug and with post run burn patterns.

The existence of stable single wave modes with frequencies between 13.3 – 16.8 kHz and the decreased prevalence of clapping modes showed that the injection scheme changes and use of

the pre-detonator had positively improved the stability of the Micro-RDE. However, mass flow control issues limited the tested operating envelope and subsequent comparisons to previous work. Detonable injector pressure ratios were significantly higher than the previous design and were found to be controllable with changes to nozzle diameter. Fill heights, estimated between 2-3 mm, drove improvements to wave frequency and mode. These fill heights were significantly smaller than the previous work, suggesting that the injector had improved mixing quality as desired. Erosion of the outerbody and nozzles played a significant role in testing, and short run times on the order of one second are most likely necessary even with hardware improvements.

Section 5.3: Future Work

Replacement of the flow control method is required in order to fully explore the operating range of the Micro-RDE. The current work's issues stemmed from the pressure differential across the Alicat controllers decreasing when the detonation back pressured the feed lines. Once this occurred, they were no longer capable of changing the flow rate. Therefore, a replacement flow control scheme must be resistant to pressure increases during the transition from cold flow to detonating flow. One such option are sonic nozzles. These nozzles would be placed into the feed lines, upstream of the RDE and create a choke point where the flow velocity would be sonic. Doing so makes the mass flow controllable by pressure directly upstream of the sonic nozzle. Furthermore, the sonic condition inside the nozzle would prevent pressure communication upstream, and thus allow the mass flow rate to be maintained during the change from cold flow to detonating flow.

The nozzles diameter couples to the upstream pressure to create the mass flow rate, and a sonic condition across the nozzle must be maintained. Therefore, design considerations for sonic nozzles are the nozzles' diameter, the upstream driving pressure, and the downstream pressure. To

maintain the proper downstream pressure and ensure a choking condition, the sonic nozzle must be approximately 60-80% smaller than any other flow area. The resulting pressure downstream of the nozzle also will influence the injector pressure ratios and its impact on ignition must be considered. Additionally, gas upstream of the nozzle must remain in a gas phase, and therefore upstream pressures are restricted according to the temperature and pressures experienced in the feed lines. If sonic nozzles are able to be properly implemented, they will allow accurate and reliable mass flow control and better explore the operability of the Micro-RDE.

Wave mode was a critical aspect of this work and was directly tied to the assessment of the Micro-RDE's ability to achieve its objectives. Observations of the wave were made with high-speed imagery looking down into the channel. While this was adequate for wave frequency and initial characterization of wave behavior, much of the details of the detonation's behavior were obscured. This could be improved if the wave were able to be observed from the side. Then, its location in the channel, and shape could be seen. Doing so would drastically improve characterization of behaviors such as galloping, clapping, and counter rotation. Fill height would also be directly observable, and the influence of different injection schemes would be clearer. Observation of the number of triple points inside the wave front may also be possible which would inform the cell size of nitrous oxide and ethylene and the critical number of cells required to adequately propagate a detonation in a small scale RDE. All of these additional capabilities could directly prove or disprove many of the results and ideas for mechanisms put forth by this work.

To view the RDE's channel, the current outerbody could be replaced by a quartz outerbody. The quartz would then allow high speed imagery directly into the channel. Special camera augmentations would likely be required to ensure the quality of the images. Considerations would need to be made for the quartz's durability to the extreme operating environment of the Micro-RDE. As a result, many outerbodies may be required and very short run times would need to be

maintained. To ensure the integrity of the quartz as much as possible, no holes should be drilled into it for instrumentation. This will limit pressure data from runs, however, only designs which have already been tested and shown to detonate should be used with the quartz outerbody.

Erosion was a consistent issue. It was not clear if the erosion was the result of melting or reduced tensile strength at the RDE's operating temperature. An Inconel outerbody was incorporated to take advantage of improved tensile strength at high temperatures while the nozzles remained stainless steel. This was shown to improve durability of the outerbody, but the nozzles still eroded significantly. Subsequent tests also showed that after repeated detonation erosion still was present on the outerbody. The erosion mechanism was therefore the result of the hardware melting, not failing under stress. Continued efforts to improve durability might then benefit from a material with elevated melting points instead of improved tensile strength. Specifically, it is suggested that the outerbody maintain an Inconel construction, but the nozzle material be changed to a ceramic carbide. The ceramic carbide would offer melting points ~3100 K, significantly higher than the current melting points of Inconel and stainless steel. With improved erosion resistance, testing would be able to be completed without repeated replacement of hardware and the need to account for changes to RDE exit area after runs. Run times could also be extended beyond one second.

Another approach that could reduce issues with erosion is shortening the channel length. The original channel length was chosen based off guidelines from Bykovskii et al. [7]. However, the estimated fill heights of 2-3 mm are significantly smaller than those used when sizing with Bykovskii criterion [1,7]. Using the same guidelines but updated with the new fill heights the channel length could be reduced to 12-15mm. Doing so would reduce flow residence time and decrease the heat transfer to the RDE's outerbody and nozzle.

From the results on the influence of channel pressure changes, potential uses for variable exit area was discovered. If an optimum plenum to chamber pressure is found during detonation to be significantly different from the ratio required to ignite, variable exit area could be implemented so that the ratios are always within the optimal range. Potential designs include an ablative nozzle material. However, this would only be applicable when a larger exit area is needed during detonation than before, which may or may not be the case. Additionally, ablative nozzles would be one time use and therefore not be efficient for testing. A more dynamic design would incorporate an aero throttle which injects air/inert gas into the channel to decrease or increase the effective flow area and thus manipulate the channel pressure. This would require additional testing apparatus infrastructure but could be feasibly integrated into the modular design of the Micro-RDE. For simplicity the injected gas could even be re-routed oxidizer injected well above the reaction zone. Its effect would remain but may react with product gasses to some degree.

Lastly, the increased blockage of the relocation of the fuel injection stream inside the oxidizer steam led to a significant increase in optimal injection pressure ratios. The implication of such differences could be further explored with additional injection scheme designs. This would inform whether stiffer injection is required, or if the benefits of a partial pre-mixture injection scheme could be achieved with lower injection pressure ratios. Lower injection pressure ratios would allow for better pressure recovery and therefore offer a better potential for pressure gain. Coupled with the optical access suggested earlier, additional injection schemes could also be compared to determine how injection stiffness relates to injected fill height.

Bibliography

[1] Dechert, J. R., "Development of a Small Scale Rotating Detonation Engine", M.S. Thesis, Department of Aeronautical Engineering, Air Force Institute of Technology, WPAFB, OH, 2020.

[2] Turns, S. R., <u>An Introduction to Combustion: Concepts and Applications</u>, WCB/McGraw-Hill, Boston, 3rd ed., 2012.

[3] Rankin, B. A., Fotia, M. L., Naples, A. G., Stevens, C. A., Hoke, J. L., Kaemming, T. A., Theuerkauf, S. W., and Schauer, F. R., "Overview of Performance, Application, and Analysis of Rotating Detonation Engine Technologies," *Journal of Propulsion and Power*, Vol. 33, No. 1, 2016, pp.131-143. doi:10.2514/1.b36303.

[4] Wintenberger, E. and Shepherd, J. E., "Thermodynamic Cycle Analysis for Propagating Detonations", *Journal of Propulsion and Power*, Vol. 22, No. 3, 2006, pp. 694-698.

[5] Schauer, F. R., Stutrud, J., and Bradley, R. "Detonation Initiation Studies and Performance Results for Pulse Detonation Engine Applications," *39th AIAA Aerospace Sciences Meeting & Exhibit,* AIAA 2001-1129, Reno, Nevada, 2001.

[6] Thomas, L., and Schauer, F. R., "Buildup and Operation of a Rotating Detonation Engine," *49th AIAA Aerospace Sciences Meeting,* Orlando, Florida, AIAA 2011-602, 2011.

[7] Bykovskii, F. A., Zhdan, S. A., and Vedernikov, E. F., "Continuous Spin Detonations," *Journal of Propulsion and Power*, Vol. 22, No. 6, 2006, pp. 1204–1216, https://doi.org/10.2514/1.17656.

[8] Fotia, M. L., Schauer, F. R., and Hoke, J. L., "Experimental Study of Performance Scaling in Rotating Detonation Engines Operated on Hydrogen and Gaseous Hydrocarbon Fuel," 20th AIAA International Space Planes and Hypersonic Systems and Technologies Conference, AIAA 2015-3626, Glasgow, Scotland, 2015. https://doi.org/10.2514/6.2015-3626.

[9] Dechert J.R, Schauer, F.R., Polanka, M.D., Schumaker, S. A., Sell, B. C., Fotia, M. L., "Development of a Small Scale Rotating Detonation Engine", *AIAA Scitech Forum,* AIAA-2020-0127, Orlando, Fl, 2020.

[10] Duvall, J., Chacon, F., Harvey, C., and Gamba, M., "Study of the Effects of Various Injection Geometries on the Operation of a Rotating Detonation Engine," *AIAA Aerospace Sciences Meeting*, AIAA 2018-0631, Kissimmee, Florida, 2018.

[11] Lee, J. H. S., The Detonation Phenomenon, Cambridge University Press, Cambridge, 2008.

[12] Wintenberger, E. and Shepherd, J. E., "Stagnation Hugoniot Analysis for Steady Combustion Waves in Propulsion Systems." *Journal of Propulsion and Power*, Vol. 22, No. 4, 2006, pp. 835-844.

[13] R. Vutthivithayarak, E.M. Braun, F.K. Lu, "Examination of the Various Cycles for Pulse Detonation Engines", AIAA 2011-6064, *47th AIAA/ASME/SAE/ASEE Joint Propulsion Conference & Exhibit*, San Diego, California, USA, 2011

[14] Heiser, W. H., and Pratt, D. T., "Thermodynamic Cycle Analysis of Pulse Detonation Engines," *Journal of Propulsion and Power*, Vol. 18, No. 1, 2002, pp. 68–76.

[15] Paxson, D. E., and Kaemming, T., "The Influence of Unsteadiness on the Analysis of Pressure Gain Combustion Devices," Journal of Propulsion and Power, Vol 30 Mar 2014, Vol 30, No. 2, p377-383.

[16] Lu, F. K., and Braun, E. M., "Rotating Detonation Wave Propulsion: Experimental Challenges, Modeling, and Engine Concepts," *Journal of Propulsion and Power,* Vol. 30, No.5, 2014, pp. 1125-1142

[17] Sichel, M., and Foster, J. C., "The Ground Impulse Generated by a Plane Fuel–Air Explosion with Side Relief," *Acta Astronautica*, Vol. 6, Nos. 3, 4, 1979, pp. 243–256.

[18] Shepherd, J. E., "Detonation in Gases," *Proceedings of the Combustion Institute*, Vol. 32, 2009, pp. 83–98.

[19] Akbar, R. "Mach Reflection of Gaseous Detonations", Ph.D. Thesis, Rensselaer Polytechnic Institute, Troy, NY, 1997.

[20] Austin, J. The Role of Instability in Gaseous Detonation, Ph.D. Thesis, California Institute of Technology, Pasadena, CA, 2003.

[21] Kudo, Y., Nagura, Y., Kasahara, J., Sasamoto, Y., and Matsuo, A., "Oblique Detonation Waves Stabilized in Rectangular-Cross-Section Bent Tubes," Proceedings of the Combustion Institute, Vol. 33, No. 2, 2011, pp. 2319–2326.

[22] Nakayama, H., Moriya, T., Kasahara, J., Matsuo, A., Sasamoto,Y., and Matsuo, A., "Stable Detonation Wave Propagation in Rectangular-Cross-Section Curved Channels," *Combustion and Flame*, Vol. 159, No. 2, 2012, pp. 859-869.

[23] Kaneshige, M. and Shephard, J.E., Detonation database. Technical Report FM97-8, GALCIT, July 1997, edited Jan 29, 2005. URL [http://www.galcit.caltech.edu/detn_db/html/db_12html] accessed 28 Aug 2020.

[24] Bohon, M., Bluemmner, R., Paschereit, C., Gutmark, E., "Experimental Study of Reactants Mixing in Model Rotating Detonation Combustor Geometries," *53rd AIAA/SAE/ASEE Joint Propulsion Conference,* AIAA 2017-0712, Atlanta, GA, 2018

[25] Po-Hsiung C., Woo Kah L., Sihe C., Huang X., Jiun-Ming L., Chiang T., Khoo B., "Investigation of Channel Pressure Effect on Rotating Detonation Engine," *AIAA Scitech 2019 Forum,* AIAA 2019-0107, San Diego, California, 2019

[26] George, A., Driscoll, R., Anand, V., Munday, D., Gutmark, E., "Fuel Blending as a Means to Achieve Initiation in a Rotating Detonation Engine," *2015 AIAA Aerospace Sciences Meeting*, AIAA 2015-0205, Kissimmee, Florida, 2015.

[27] St. George, A., Randall, S., Anand, V. Driscoll R. Gutmark, E., "Characterization of Initiator Dynamics in a Rotating Detonation Combustor", Experimental Thermal and Fluid Science, Volume 72, 2016, Pages 171-181, ISSN 0894-1777, https://doi.org/10.1016/j.expthermflusci.2015.11.002.

[28] Schultz, E, Shepherd, J., "Validation of Detailed Reaction Mechanisms for Detonation Simulation", GALCIT Explosion Dynamics Laboratory Report FM99-5, Pasadena, CA, 2000.

[29] Boller, S. A., Polanka, M. D., Huff, R., Schauer, F. R., Fotia, M. L., and Hoke, J. L., "Experimental Flow Visualization in a Radial Rotating Detonation Engine," *AIAA Scitech 2019 Forum,* AIAA SciTech Forum, AIAA 2019-1253, San Diego, California, 2019.

[30] Special Metals a POC Company. (2013). *INCONEL Alloy 625*. Special Metals Corporation Group.

[31] North American Stainless. (2020). *North American Stainless Long Products Stainless Steel Data Sheet*. North American Stainless.

REPORT DOCUMENTATION PAGE

The public reporting burden for this collection of information is estimated to average 1 hour per response, including the time for reviewing instructions, searching existing data sources, gathering and maintaining the data needed, and completing and reviewing the collection of information. Send comments regarding this burden estimate or any other aspect of this collection of information, including suggestions for reducing the burden, to Department of Defense, Washington Headquarters Services, Directorate for Information Operations and Reports (0704-0188), 1215 Jefferson Davis Highway, Suite 1204, Arlington, VA 22202-4302. Respondents should be aware that notwithstanding any other provision of law, no person shall be subject to any penalty for failing to comply with a collection of information if it does not display a currently valid OMB control number.
PLEASE DO NOT RETURN YOUR FORM TO THE ABOVE ADDRESS.

1. REPORT DATE *(DD-MM-YYYY)*	2. REPORT TYPE	3. DATES COVERED *(From - To)*

4. TITLE AND SUBTITLE

5a. CONTRACT NUMBER

5b. GRANT NUMBER

5c. PROGRAM ELEMENT NUMBER

6. AUTHOR(S)

5d. PROJECT NUMBER

5e. TASK NUMBER

5f. WORK UNIT NUMBER

7. PERFORMING ORGANIZATION NAME(S) AND ADDRESS(ES)

8. PERFORMING ORGANIZATION REPORT NUMBER

9. SPONSORING/MONITORING AGENCY NAME(S) AND ADDRESS(ES)

10. SPONSOR/MONITOR'S ACRONYM(S)

11. SPONSOR/MONITOR'S REPORT NUMBER(S)

12. DISTRIBUTION/AVAILABILITY STATEMENT

13. SUPPLEMENTARY NOTES

14. ABSTRACT

15. SUBJECT TERMS

16. SECURITY CLASSIFICATION OF:			17. LIMITATION OF ABSTRACT	18. NUMBER OF PAGES	19a. NAME OF RESPONSIBLE PERSON
a. REPORT	b. ABSTRACT	c. THIS PAGE			
					19b. TELEPHONE NUMBER *(Include area code)*